Multiphysics simulation of electroslag remelting process

A thesis submitted to the Montanuniversität Leoben
for the degree of Doctor of Montanistic Sciences (Dr. mont.)

presented by
Ebrahim Karimi Sibaki
Leoben, October 2015

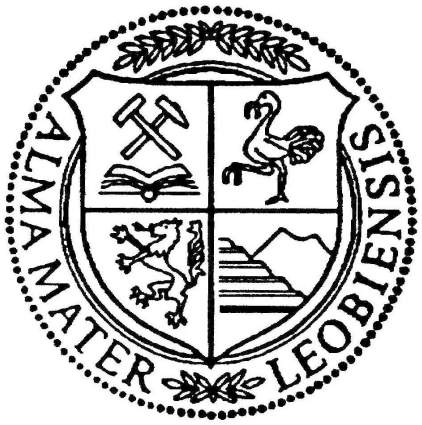

Examiner: Assoz. Prof. Dr.-Ing. Menghuai Wu
Chair for Simulation and Modelling of Metallurgical Processes
Department of Metallurgy

Co-Examiner: Prof. Clemens Brand
Chair of Applied Mathematics
Department of Mathematics and Information Technology

This thesis was supported by the Austrian Federal Ministry of Economy, Family and Youth and the National Foundation for Research, Technology and Development within the framework of the Christian Doppler Laboratory for Advanced Process Simulation of Solidification and Melting.

Eidesstattliche Erklärung

Ich erkläre an Eides statt, dass ich diese Arbeit selbstständig verfasst, andere als die angegebenen Quellen und Hilfsmittel nicht benützt und mich auch sonst keiner unerlaubten Hilfsmittel bedient habe.

Leoben, 23.10.2015

M. Sc. Ebrahim Karimi Sibaki

Affidavit

I declare in lieu of oath, that I wrote this thesis and performed the associated research myself, using only literature cited in this volume.

Leoben, 23.10.2015

M. Sc. Ebrahim Karimi Sibaki

Acknowledgement

I wish to express my gratitude to my thesis advisor, Prof. Menghuai Wu, for giving me the opportunity to do my PhD in his group, for his constructive advice, encouragement, and guidance as well as for his clear-sightedness and enthusiasm in scientific discussions.

My special thanks go to my co-supervisor, Dr. Abdellah Kharicha, for his endless support and encouragement, for his inspiring guidance, and for being an amazing supervisor and mentor.

I am grateful to Prof. Andreas Ludwig for giving me the opportunity to work in his research group. It is an honor and pleasure to work at the chair of Simulation and Modelling of Metallurgical Processes (SMMP).

Prof. Clemens Brand is gratefully acknowledged for being the co-examiner of the thesis.

It has been a great pleasure to write my dissertation in close collaboration with the INTECO melting and casting technologies GmbH. I therefore sincerely thank my colleagues Harald Holzgruber, Alexander Scheriau, Bertram Ofner, Michael Kubin, and Manfred Ramprecht for continuous support and generous advices.

I would like to thank Dr. Jorg Korp for sharing his knowledge and experience with me.

I especially thank my colleagues in SMMP, Dr. Jan Bohacek and Dr. Alexander Vakhrushev for being wonderful source of positive energy, and for unselfish sharing of their knowledge, skills, and time with me. I extend my gratitude to all present and former members of SMMP for contributing to such a nice atmosphere. I therefore thank Georg Nunner, Tobias Holzmann, Josef Domitner, Alexander Antoniu Cernaianu, Jenny Dorner, Sabine Rosenblattl, Klaus Jürgen Otto, Sandra Cihan, Samiullah Baig, Johann Mogeritsch, Mihaela Stefan-Kharicha, Hadi Barati, Andreas Kemminger, Mahmoud Ahmadein, Yongjian Zheng, Jun Li, Guenter Unterreiter, Konrad Schrempf, Tanja Pfeifer, and Lubomir Soukup.

I would like to especially thank my wonderful lifetime friends: Abas Mohsenzadeh, Akbar Hosseinkhani, Saeid Alinezhad, and Saeed Shoaie for their support.

And last, but foremost, thanks to my outstanding family (my father, my mother, and my brothers) in IRAN who always supported me and believed in me.

Kurzfassung

Das Hauptziel der vorliegenden Dissertation besteht sowohl darin fundamentale Zusammenhänge zwischen der Strömung, der Temperatur und des Magnetfeldes während des Elektroschlacke-Umschmelzprozesses (ESU) zu verstehen, als auch die Erstarrung des ESU-Blocks mithilfe von mathematischen Modellen und Simulationen zu beschreiben. Die vorliegende Arbeit ist in neun wissenschaftliche Veröffentlichungen unterteilt und enthält zusätzlich eine ausführliche Zusammenfassung der in den letzten Jahrzehnten entwickelten und eingesetzten mathematischen Modelle. Zur Validierung der numerischen Ergebnisse wird auf entsprechende Experimente eingegangen. Zusätzlich werden Neuerungen, welche sich aus dem Standard ESU Prozess entwickelt haben, diskutiert. Hierunter fallen beispielsweise der ESU Prozess mit Elektrodenwechseltechnik, der ESU Prozess bei Verwendung mehrerer Elektroden gleichzeitig, der CCM Prozess (current conductive mold –stromführende Kokille), der ESRR Prozess (electroslag rapid remelting – Elektroschlacke-Schnellschmelzen), der DESU Prozess (Druck-ESU) und der ESU Prozess zur Herstellung von Hohlblöcken.

Das numerische Modell, welches von Kharicha und seinen Kollegen [Mater. Sci. Eng. A, 2005, p. 129; Steel Res. Int., 2008, p. 632] entwickelt wurde, ist in dieser Arbeit erweitert worden, wodurch es ermöglicht wurde, folgende Studien durchzuführen:

- Betrachtung der Form des flüssigen Metallbades in 2D und 3D Simulationen (Profil des Zweiphasengebietes).
- Analyse der Auswirkung (i) der elektrischen Leitfähigkeit der Schlacke (Flüssig und Feststoff); (ii) der verwendeten AC Frequenz; (iii) der Schlackenbadhöhe und (iv) des Kokillentyps (isoliert oder nicht) auf den elektrischen Strompfad und deren Einfluss auf das Strömungsfeld, die Temperatur und die Erstarrung des Blockes.
- Einfluss der morphologischen Parameter des Kristalls wie beispielsweise der Permeabilität und des primären Dendritenabstands (PDAS) auf das Erstarrungsprofils des ESU-Blocks.
- Einfluss der Bewegung der Grenzfläche Schlacke-Metallbad auf den elektrischen Widerstand und der daraus folgenden Wärmeentwicklung im ESU-Prozess.

- Einfluss der Leistungsunterbrechung während des Elektrodenwechsels auf das Strömungsfeld, die Temperatur und die Erstarrung im Block.
- Einfluss der physikalisch-chemischen Eigenschaften der Schlacke wie zum Beispiel die thermische und elektrische Leitfähigkeit auf die Schmelzrate, das Poolprofil und auf die Form der Elektrodenspitze und Eintauchtiefe der Elektrode.

Folgende wichtige Erkenntnisse konnten gewonnen werden:

- Das Geschwindigkeitsfeld der Schlacke und der Schmelze sind zeitlich abhängig in alle drei Raumrichtungen (transient), wobei das Poolprofil annähernd stationär und achsensymmetrisch ist bei Betrachtung des ESU Prozesses im industriellen Maßstab.
- Das Poolprofil des ESU-Blocks ist sehr sensible auf die interdendritischen Schmelzbewegungen im Zweiphasengebiet obwohl die interdendritische Geschwindigkeit wesentlich kleiner als die Geschwindigkeit der Schmelze oder der Schlacke ist.
- Der Strompfad beeinflusst das Geschwindigkeits- und Temperaturfeld genauso stark wie das Erstarrungsprofil des ESU-Blocks. Zudem ist der Strompfad durch die Kokille nicht vernachlässigbar und muss berücksichtigt werden.
- Keine signifikanten Änderungen des Erstarrungsprofils des ESU-Blocks wurden bei kurzer Leistungsunterbrechung (< 5 min) vorhergesagt.
- Die Schmelzrate, die Form der Elektrodenspitze und die Eintauchtiefe der Elektrode hängen stark von den physikalisch-chemischen Eigenschaften der Schlacke ab. Das Verhältnis der Schmelzrate und der Wärmeentwicklung bestimmen die Form der Elektrodenspitze.

Zuletzt werden Zielrichtungen für weitere Forschungsthemen aufgezeigt.

Abstract

The main goal of this dissertation is to achieve fundamental understanding of the flow, temperature, and magnetic fields in the whole process of the electroslag remelting (ESR) as well as solidification of the ingot through mathematical modeling and simulation. The main content of this thesis is a combination of nine scientific articles. In addition, a comprehensive review of the mathematical models developed over past decades is given. Experiments, especially those used to verify the numerical models, are also reviewed. Furthermore, features of new technologies originated in the standard ESR process such as ESR with electrode change, ESR with multiple electrodes, current conductive mold (CCM), electroslag rapid remelting (ESRR), pressure-ESR (PESR), and ESR for hollow ingots are discussed.

The numerical model, as originally developed by Kharicha and his colleagues [Mater. Sci. Eng. A, 2005, p. 129; Steel Res. Int., 2008, p. 632], was extended in this thesis. With the extended functionalities of the model, it is possible to perform following studies:

- The influence of a modeling in two and three dimensions (2D, 3D) on the predicted shape of the melt pool (profile of the solidifying mushy zone of the ingot).
- Impacts of electric conductivity of slag (liquid and solid), applied AC frequency, slag cap height, and mold type (either isolated or live) on the electric current path, and their influences on the flow field, temperature field, and solidification of the ingot.
- Effects of the crystal morphological parameters such as permeability and primary dendrite arm space (PDAS) on the predicted pool profile of ingot.
- The effect of movement of slag-pool interface on the overall electrical resistance and subsequently generated power in the process.
- The influences of power interruption during electrode change procedure on the flow and temperature fields as well as solidification of the ingot.
- Effects of physicochemical properties of the slag such as thermal and electrical conductivities on the melt rate, shape, and immersion depth of an ESR electrode.

Some important knowledge was obtained:

- The velocity field in the slag and bulk of melt pool is transient and in 3D feature, but the pool profile of the steel ingot is firmly steady and axisymmetric for an industrial scale ESR process.
- The pool profile of the ingot is very sensitive to the interdendritic melt flow in the mushy zone although the velocity magnitude of the interdendritic velocity is notably smaller than the velocity in the bulk of melt pool or slag.
- The electric current path governs the velocity and temperature fields as well as pool profile of the ingot, and the possible current path through the mold is not ignorable.
- No significant change in the pool profile of the ingot was predicted during the short time of power off (< 5 min) through electrode change.
- The melt rate, shape, and immersion depth of an ESR electrode depend strongly on the physicochemical properties of the slag. The ratio of the melt rate to the generated power (power consumption) determines the shape of electrode tip.

Finally, important directions for further research are pointed out.

Contents

1 Introduction

1.1 Background

Electroslag remelting (ESR) is a secondary metallurgical process aiming at further purification after completion of the primary extraction and refining operations. The process, as explained in more detail in Section 2.1, is a method of refining a consumable metal electrode through a molten slag that is electrically heated. It is not clear who invented the process although the earliest recorded reference to the principles of the process had been reported by Nickolai Slavyanov in 1892 [1-2]. Armstrong [3] had conducted experiments on a small scale using a resistance heated slag to aid melting in 1928. Then, Hopkins [4-5] had melted a consumable electrode under a slag blanket in 1935. After World War II, Soviet scientists had developed electroslag welding process to improve metal quality and to mechanize the welding of vertical joints at the E. O. Paton Institute of Electric Welding in Kiev [6]. Furthermore, Soviet researchers published the first monographs on the topic of ESR in 1962, which were translated and published abroad [7]. Over past decades, the process has been developed to produce a variety of ferrous and non-ferrous alloys such as steel, nickel-based, and titanium-based super alloys. Diverse application areas exist for ESR products in tool steel, aircrafts, oil and chemical industries, thermal power station, nuclear power plant, and military technology. Nowadays, million tons of ESR ingots are produced in a wide range of sizes and weights in various countries such as Austria, Iran, China,

Germany, France, Russia, USA, Canada, Italy, Hungary, Slovenia, England, Japan, Brazil, and South Korea [7].

Finely controlled solidification is a remarkable characteristic of the ESR process that leads to production of ingots with superior surface and internal quality. The expensive process of surface machining is not required for ESR ingots with smooth surfaces and they can be directly forged after completion of the ESR process [8].The internal quality is highly dependent on the shape of melt pool, i.e., the depth and thickness of mushy zone. The desired outcome of the ESR process is a shallow melt pool that promotes unidirectional (upwards) solidification of the ingot and subsequent formation of segregation-minimal alloy [9]. The degree of macrosegregation depends on the slope of the solidus/ liquidus isotherms and solidification time that in turn is related to the mushy zone depth. In fact, long solidification time or deep mushy zone results in severe macrosegregation and subsequently inadequate mechanical properties, cleanliness, and yield [10-12]. Therefore, the melt pool profile is often used as an indicator of the internal quality of the ingot. For instance, the pool profile of an ESR ingot is shown in Figure 1.1.

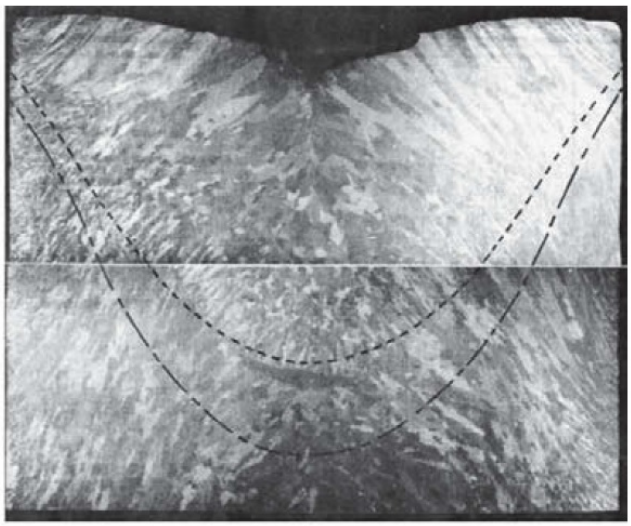

Figure 1.1. Pool profile of an ESR ingot; liquidus (upper line) and solidus (lower line) isotherms are indicated [13].

The pool shape of ingot is governed by operating conditions such as electrical parameters, mold cooling system, slag/alloy properties, etc. which will be further described in Section 3. The complex ESR process involves a range of physical phenomena and their interactions: heat transfer with phase change taking place in melting of the electrode and solidification of the ingot, chemical and electrochemical reactions in the slag, and the interaction between the turbulent flow and electromagnetic field known as magnetohydrodynamics (MHD). Experimental analysis and measurements are quite difficult during the ESR process due to high degree of opacity of materials and involved high temperature (~ 2000 K). Therefore, simulation tools can be applied to get insight into the invisible phenomena. Computational fluid dynamics (CFD) is a very powerful technique that enables us to attain deeper knowledge of the ESR process. That is of key importance for improving the technology, minimizing failure rate, and increasing productivity.

1.2 Objective

The target of this doctoral dissertation is to use numerical methods to investigate the multi-scale/multi-phase/multi-physics ESR process. It is impossible to describe all involving phenomena such as melting, solidification, magnetohydrodynamics (MHD), chemical and electrochemical reactions in one single comprehensive model due to the complexity of the process. Furthermore, it is a major challenge to consider all physical phenomena which occur at different length scales because of limitation in computational resources. Therefore, reasonable assumptions are made for each simulation trial that will be further discussed in Section 3. Here, different sizes of process, from the laboratory benchmark to very large industrial scale, are simulated. Selected simulation examples are given in Section 3.2 through 3.7 to clarify influences of key variables as listed in the following:

1) A full-scale 3D simulation of an industrial scale ESR is performed to investigate the validity of axisymmetric assumption for modeling the flow field and pool profile.

2) The electric current path in the whole system including the mold (either isolated or live mold) at different applied frequency is studied.

3) The influence of electric conductivity of slag (liquid and solid) on the electric current path and hence in the pool profile of ingot is discussed.

4) The importance of slag cap height on the current path is pointed out.

5) The influence of the applied frequency of AC power supply on the hydrodynamics of the process is investigated.

6) The impact of slag-melt pool interface movement on the electric current path and generated power in the slag is studied.

7) The effect of crystal morphological parameters such as primary dendrite arm spacing on the solidification of ingot is studied.

4) Effects of thermal and electrical conductivities of slag (liquid and solid) on the immersion depth, melt rate, and shape of the electrode are analyzed.

7) The model is refined to consider impacts of power interruption on the system behavior during the electrode change procedure.

8) Major chemical and electrochemical reactions taking place in the slag are qualitatively discussed. A one-dimensional model is developed to describe the electrochemical transport of ions in the slag.

2 State of the art

2.1 The ESR process

2.1.1 General description

Hoyle [5] comprehensively described various aspects of the standard ESR process such as required equipment, instrumentation, control, and operating practice. Production of ingot through a simple ESR furnace is shown in Figure 2.1 (a). Furthermore, a schematic representation of the process including major components of electrode, slag, ingot and mold is illustrated in Figure 2.1 (b). Thermal energy is supplied to the process through the Joule heating that results in remelting the primary electrode and formation of droplets. The droplets then pass through the slag and reach the liquid pool. The melt pool solidifies directionally and builds the high-grade ingot in a water-cooled mold.

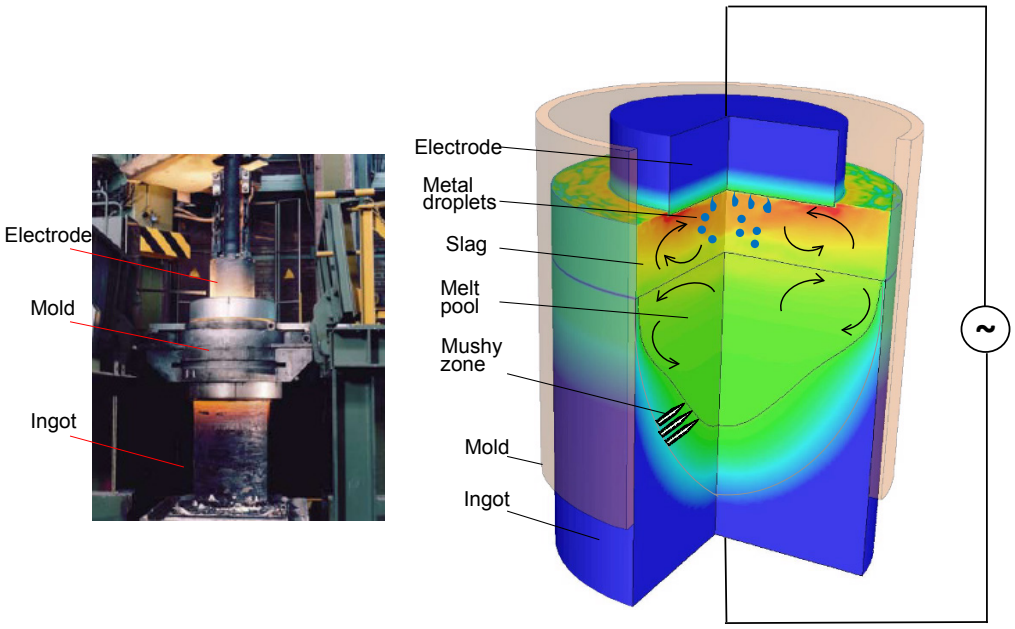

(a) (b)

Figure 2.1. (a) The ESR process (photo courtesy of SCHMOLZ + BICKENBACH Austria GmbH), (b) Schematic representation of the ESR.

ESR molds, typically made of copper, are designed to contain the hot slag bath, to receive and accumulate the molten metal, and to provide a suitably shaped vessel for solidifying ingot. A substantial part of generated heat in the process is transferred through the mold wall to the cooling water. Furthermore, considerable amount of electric current flows through the mold. As such, special care must be taken to design an adequate mold which is capable of fulfilling all the tasks [14-15]. Principally, three different configuration of standard ESR plant exist: plant with retractable baseplate, static (live) mold, and short-collar/moveable (isolated) mold; each has particular fields of application [16].

2.1.2 ESR slags

The slag is the core compound served to clean the metal by removing sulfur and non-metallic inclusions. Several chemical and electrochemical reactions take place in the slag aiming at further purification and refining of the metal [17-18]. The required heat is supplied into the process by passing electric current through the resistive slag layer (Joule heat). Furthermore, the slag protects the molten metal from direct contamination that might come from the surrounding atmosphere. A crust of solidified slag, called slag skin layer, forms a mold lining which separates molten slag and ingot from the mold. Figure 2.2 (a) shows the slag at room temperature (~ 300 K). Additionally, the slag at high temperature (~ 2000 K) during the process is shown in Figure 2.2 (b). For several decades, a large amount of research has been ongoing to explore the mechanism of ESR slags. It is beyond the scope of the current dissertation to address hundreds of books, monographs, and scientific papers which were reviewed elsewhere [19-20].

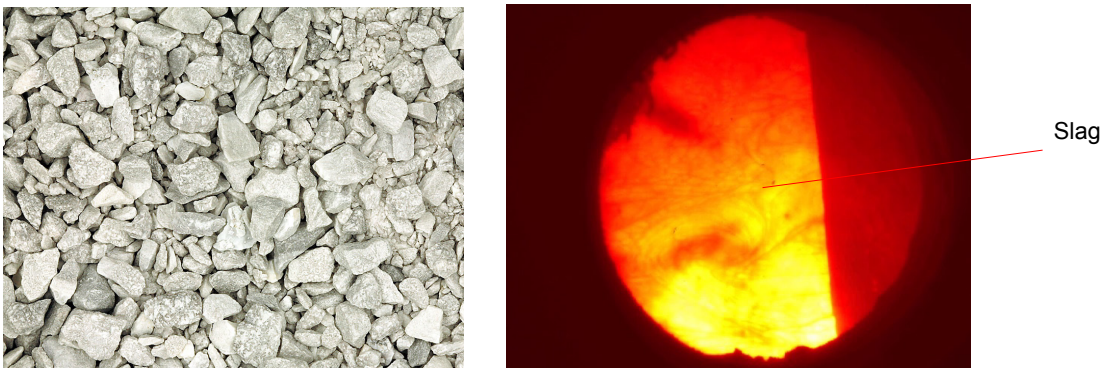

(a) (b)

Figure 2.2. (a) ESR slag at room temperature, (b) ESR slag during operation (photos courtesy of INTECO melting and casting technologies GmbH).

Nevertheless, CaF_2-based slags are generally used since they have high degree of chemical reactivity and low electrical conductivity. A conventional ESR slag is typically composed of a mixture of CaF_2 (30-60 %Wt.), Al_2O_3 (30-60 %Wt.), and CaO (30-60 %Wt.) [2]. Most often, a small amount of SiO_2, TiO_2, and MgO are added to modify reactivity of the slag that in turn influences the final compositions of Al, Ti, or Mg in the ingot [21-24]. Furthermore, the aforementioned oxides can change physical as well as physicochemical properties of the slag such as viscosity, density, etc. [19]. For instance, a lubricative skin layer forms on the surface of a short collar (moveable) mold by addition of SiO_2 to the slag that is in favor of producing ingots with superior surface quality [25]. The physicochemical properties are dependent on both temperature and composition of the slag. Due to the difficulty of measurements at elevated temperature, a large uncertainty of the properties exists [26]. Nonetheless, the following crucial slag properties are required for our CFD modeling which are extracted from literature: electric conductivity [26-33], thermal conductivity [27, 34-35], viscosity [19, 26-27, 36-38], density [2, 19, 26-27, 38-41], specific heat [42], surface tension [19, 27, 41, 43], emissivity [35, 44], and liquidus/solidus temperature [36, 45]. A crude approximation of physicochemical properties of the conventional slags is described in Table 2.1. The variation range is huge. The interested

readers are highly encouraged to consult with the aforementioned references for further information.

Electrical conductivity (Ω^{-1} m^{-1})	80-300
Molecular thermal conductivity (W m^{-1} K^{-1})	0.5-5
Viscosity (Pa s)	0.002-0.1
Density (kg m^{-3})	2500-2900
Specific heat (J kg^{-1})	900-1400
Surface tension (N m^{-1})	0.1-1
Emissivity	0.8-0.9
Solidus temperature (K)	1300-1500
Liquidus temperature (K)	1600-1800

Table 2.1. Variation range of physicochemical properties of the conventional ESR slags.

2.2 Mathematical models

It is of great importance to be able to predict the way in which the operational parameters affect the structure and chemical composition of the final ESR ingot. Willner et al. [46] had performed a multi-regression analysis of measurements to explore the relationship between electrode diameter, power input, feeding velocity, specific power, and pool depth in the ESR. The aim was to derive empirical rules for further optimization of an ESR plant (ϕ 250 mm). One should consider that traditional trial and error approaches are prohibitively expensive especially for production of large ESR ingots. Therefore, it is necessary to develop mathematical models describing transport phenomena occurring in the whole process. Over the past century, numerous mathematical models have been proposed to describe the fluid flow, heat transfer, and mass transfer in the ESR [47]. Here, important aspects of mass transfer in the ESR are briefly discussed. Additionally, extensive reviews of mathematical models of fluid flow, electromagnetism, heat transfer, and solidification in the ESR were given [48-104]. A summary of the review is listed in Table 2.2 according to the investigated phenomena as well as involved domain of modeling. Furthermore, key features of the model for each group of references are briefly described. Most often, modeling results are validated against experiments that are also discussed accordingly.

Involving physics	**Calculation domains**	**Brief description of key model features**	**Ref.**
Only thermal (solidification) field	Only ingot	Quasi steady state pool profile of the ingot and related solidification parameters such as depth of mushy zone, local solidification time (LST), and grain growth angle (GGA) were studied. Radial contraction and thermal stress on solidifying ingot were also studied.	48,49,52, 58,65,70, 97,98
	All possible Regions	Pool profile of the ingot and related solidification parameters such as shrinkage of the ingot, secondary dendrite arm space (SDAS), LST, and GGA were studied. Temperature profile of the electrode, immersion depth and shape of electrode were investigated.	50,51,54, 55,60,61, 95
Only electromagnetic field	All possible Regions	Effects of operational parameters of the process such as diameter of electrode or ingot, applied AC frequency, and slag resistance on distribution of electric current density and generated power were studied.	62,69,72, 85,90,92
Coupled flow, electromagnetic fields	Slag and melt pool	Variations in distribution of electric current density influence the velocity field as well as the movement of slag-pool interface.	53,66
Coupled flow, thermal (solidification), electromagnetic fields	Only slag	The flow pattern is influenced by Lorentz and thermal buoyancy forces, size of droplets, thickness of the slag skin, melt rate of the electrode, and mold current.	56,64,73, 75,77,87
	Only ingot	Macrosegregation and crystal morphological parameters such as PDAS and SDAS were studied.	86
	Slag and ingot	The flow in the slag and melt pool as well as pool profile of the ingot and related solidification parameters such as columnar to equiaxed transition (CET), LST, SDAS, and GGA are dependent on applied current, mode of current (AC or DC), generated power, fill ratio, size of droplets, skin thickness, and movement of slag-pool interface. Macrosegregation, probability of formation of freckles, and distribution of inclusions were addressed.	57,63,67, 68,71,74, 76,78-83, 88,89,93, 94,96,99, 101-104
	All possible Regions	The generated power, feeding velocity of the electrode, melt rate of the electrode, and the size of the system significantly influence thermal field in the electrode and slag.	59,84,91, 100

Table 2.2. A summary of the review of mathematical models for fluid flow, heat transfer, electromagnetism, melting of the electrode, and solidification of the ingot in the ESR.

2.2.1 Electromagnetic field

The flow of the molten slag and liquid melt pool is strongly influenced by the electromagnetic field in the ESR process. As such, an accurate prediction of the electromagnetic field is an important step toward modeling of the process. Dilawari et al. [53] reported a low value for magnetic Reynolds number in the ESR process. Therefore, the effect of flow convection on magnetic field distribution is negligible. However, the movement of slag-melt pool interface and dripping of droplets through the slag dynamically modifies electric current distribution as described by Kharicha et al. [83]. For the sake of simplicity and ignoring effects of slag-pool interface movement and dripping droplets on the global electromagnetic field, it is acceptable to assume that the magnetic field is dominantly in azimuthal direction. Thus, a 2D axisymmetric model can be used to describe electric current distribution in the ESR [79]. Here, two different approaches are suggested to calculate the electromagnetic field: One based on magnetic induction formulation [88, 105], and other one based on vector potential-scalar potential formulation [100, 106-108]. The potential formulation is computationally more expensive compared to the common approach based on electromagnetic induction equation. However, it is very robust and accurate for solving electromagnetic field in the presence of moving boundaries. In addition, it can effectively model the current path including eddy current and mold current (current crossing the skin layer and flowing through the mold). Examples of calculation results are shown in Figure 2.3. The magnetic induction equation was solved to calculate vector field of the electric current density in the slag and electrode as shown in Figure 2.3 (a) where the current was not allowed to flow through the mold [56]. Distribution of electric current density in the electrode, slag, and melt pool is illustrated in Figure 2.3 (b) in which calculation were performed using the vector potential-scalar potential formulation. The movements of slag-pool and slag air interfaces as well as mold current were allowed [94].

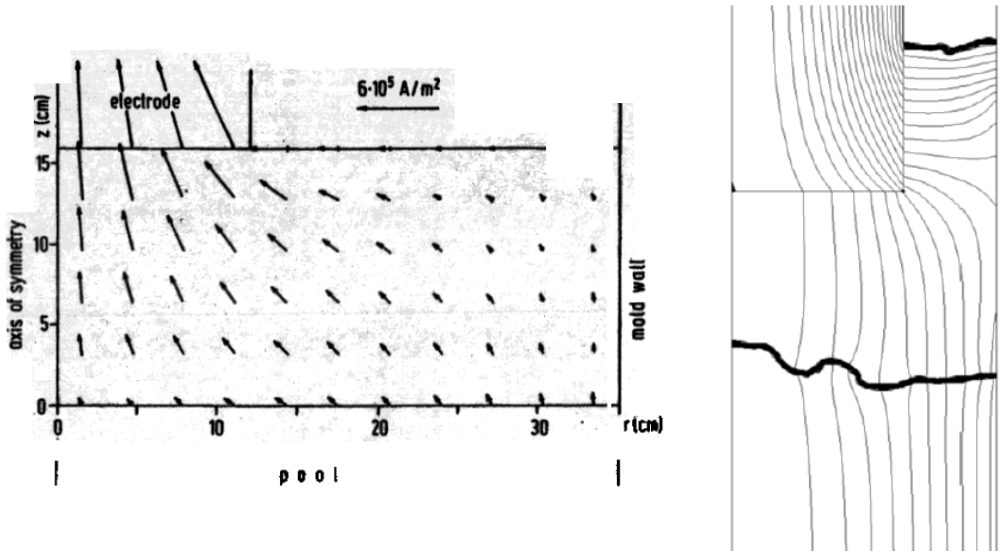

(a) (b)

Figure 2.3. Modeling results of distribution of electric current density are shown: (a) in the slag and electrode using the magnetic induction formulation [56]; (b) in the electrode, slag, and melt pool using the vector potential-scalar potential formulation [94].

After computing the electromagnetic field, distributions of Lorentz force and Joule heat can be obtained which are source terms for momentum and energy equations respectively [105]. The origin of the Lorentz force is the interaction between the electric current and the self-induced magnetic field in the system. Furthermore, the process by which the passage of an electric current through a conductor releases heat is known as Joule or resistive heating.

Considering conservation law of electric current in the slag, Medina et al. [62] solved Laplace equation to establish Ohm's law in the slag where mold current was allowed. Patel [69, 72] expressed the electric current distribution in the slag, electrode, and ingot in terms of a stream function to study effects of electrode/ingot size, applied AC frequency, and amplitude of current on magnetic and joule heating distributions. A parabolic relationship between the voltage drop and electrode diameter was predicted. In addition, Patel [85] presented an analytical solution in the form of Fourier-Bessel functions for distribution of

current density in the slag, electrode, and ingot. Assuming an electrically insulating slag skin, a linear decrease in joule heating and voltage was found by the increase of the immersion depth. Li et al. [90] developed a three dimensional model based on finite element method (FEM) to study distributions of electric current, magnetic field, electromagnetic force, and Joule heat in the slag, electrode and ingot where an electrically insulating slag skin was assumed. Hugo et al. [92] studied distributions of current density and joule heat in which mold current was allowed. Note that electric current path is strongly dependent on operation parameters such as mold type, slag type, applied AC frequency, etc. Here, electric current paths are calculated at different applied frequency and slag cap thickness for static or moveable molds including mold current [109]. Details of analysis are given in section 3.3.

It must be stated that since 2005 our knowledge of the electromagnetic field in the ESR is greatly improved. A comprehensive transient 3D model of the electromagnetic field considering influences of the movement of slag-melt pool interface and dripping of droplets through the slag was presented by Kharicha et al. [83]. Snapshots at different times of distribution of electric current density are shown in Figure 2.4. Note that, performing a 3D calculation including all the aforementioned phenomena such as movement of the interface is computationally very expensive. As such, it is advised to apply the robust 2D axisymmetric models for engineering applications especially for the systems of large scale (> ϕ 500 m ingot diameter).

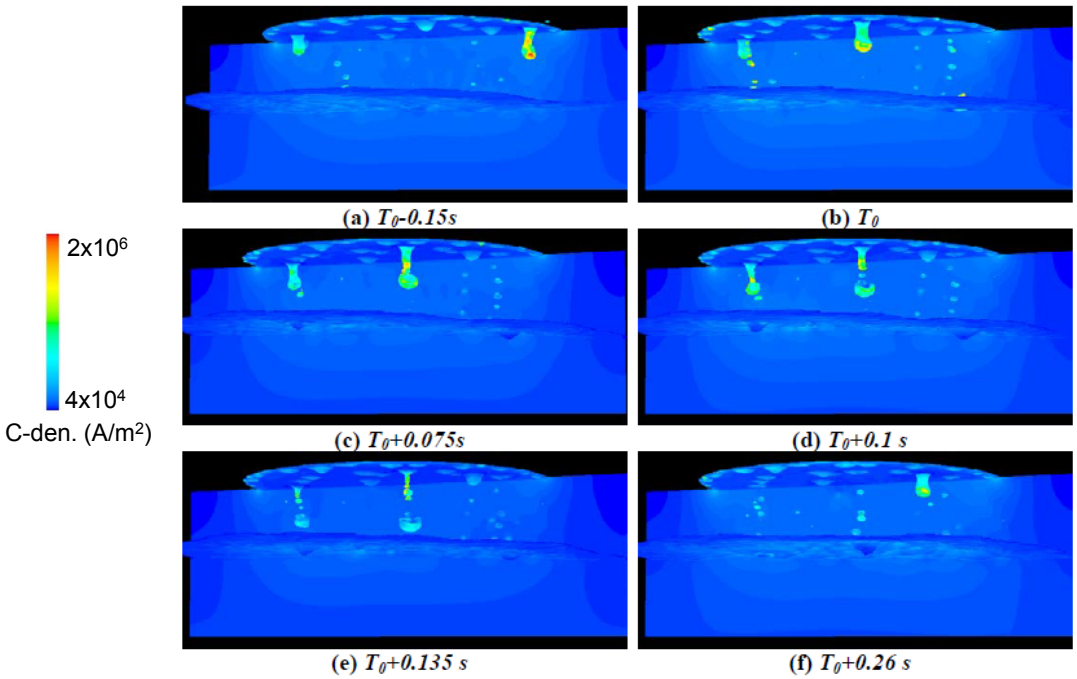

Figure 2.4. Evolution of electric current density (4.10^4-2.10^6 A m^{-2}) during formation and departure of droplets [83].

2.2.2. Heat transfer and solidification

Simulation of the thermal field in an ESR is of principle importance. The pool profile, local solidification time (LST) and subsequently microstructure of the ingot, melting of the electrode, mass transfer parameters (mass transfer coefficient and diffusivity), and thermodynamic information (equilibrium constants and activity coefficients) are governed by the thermal field. Maulvault [48] modeled the temperature field in an ingot to calculate the pool profile at quasi-steady state where modified values of specific heat of alloy were used to include the solidification latent heat. Using similar approach to model temperature field in the ingot, Carvajal et al. [49] provided results for an Al-4.5Cu (%Wt.) alloy produced through ESR. Assuming a region of infinite convection and complete mixing (uniform temperature) in the metal near slag-pool interface, an unsteady model suggested by Basaran et al. [52] to calculate solidification parameters such as the pool profile, depth of mushy zone, and solidification time. Considering slag at steady state and growing ingot

at unsteady state, Ballantyne et al. [54, 110] modeled temperature distribution in the ingot to calculate related solidification parameters. Their results were successfully validated against the experiment as shown in Figure 2.5.

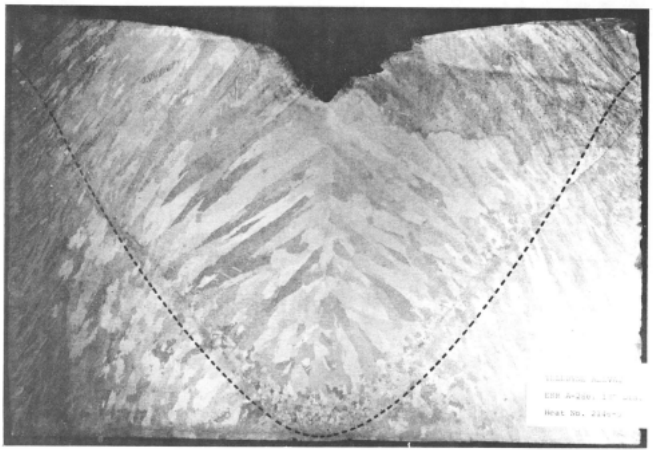

Figure 2.5. Comparison of computed and observed pool profile of an ESR ingot [110].

Attempts have been made to model segregation of components of the alloy including only thermal field in the model. Ridder et al. [55] introduced a combined theoretical-experimental study using a rather simple model to find relationship between pressure drop in the mushy zone (porous media), interdendritic velocity, and species concentrations [105]. Results of experimental measurements for Ni-27Mo (%Wt.) and Sn-15Pb (%Wt.) alloys such as slag temperature or heat transfer coefficients were applied in the model. The solidus isotherm was considered as a moving boundary and no flow was modeled in the melt pool. Jeanfils et al. [58] calculated macrosegregation of multiple components in WASPALOY alloy using Scheil model for solidification of the ingot (no diffusion of components in the solid). The transient temperature field in an ESR ingot was calculated in which modified specific heat values were used to take into account solidification latent heat. The interdendritic flow in the mushy zone was estimated through the Darcy's law. Details of the model was presented by Mehrabian et al. [111].

Nastac et al. [65] proposed a stochastic model to predict the grain structure using the thermal history of a growing ESR/VAR ingot. Li et al. [97] used a coupled cellular automaton and finite element method (CAFE) to investigate grain growth angle (GGA) of growing columnar grains. The tip velocity of dendrite was calculated using Kurz-Giovanola-Trivedi (KGT) model including only solute diffusion undercooling [106]. Their calculated results were in good agreement with the experiment as shown in Figure 2.6. Rao et al. [95] used KGT model for growth kinetic to study crystal morphology and GGA of a steel alloy. They observed columnar equiaxed transition (CET) after examining the ingot. Furthermore, they stated that GGA is smaller at lower melt rate.

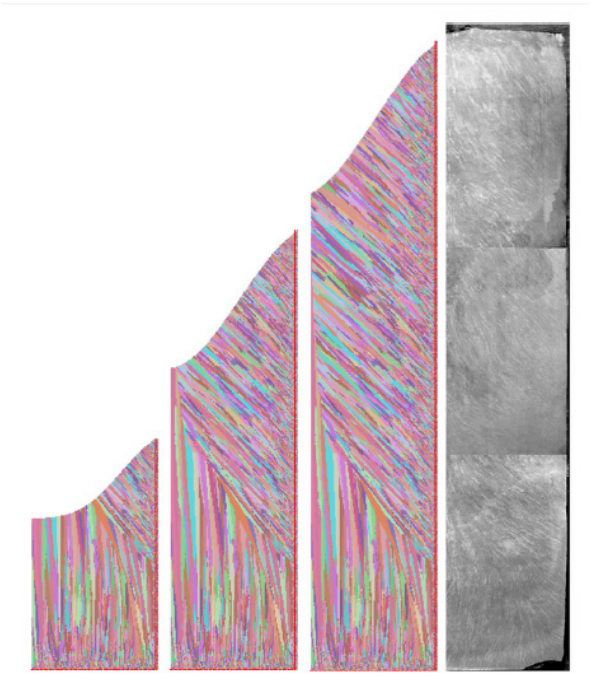

(a) t=1000 s (b) t=2000s (c) t=3000s (d)

Figure 2.6. Calculation results of evolution of the microstructure at the longitudinal section of an ESR ingot is compared with the experiment [97]: (a) t=1000s, (b) t=2000s, (c) t=3000s, (d) experimental results.

Shrinkage of an ESR ingot and subsequent formation of the air gap between the mold and ingot strongly influences the cooling condition of the system. In fact, formation of the air gap alters conduction to a combined convection-radiation heat transfer mechanism. Sanchez

Sarmiento et al. [60] calculated temperature field for a Ni-based ingot considering a variable heat transfer coefficient at ingot-mold interface to model the air gap expansion with ingot cooling. Yang et al. [70] introduced a thermal/elastic finite element based model to calculate stress during solidification of alloy 706. Calculated surface temperature of the ingot was compared with experimental measurements to validate the model. Eickhoff et al [98] assumed a prescribed parabolic temperature distribution in the whole ingot. Then radial contraction of solidifying ingot was calculated to estimate the thickness of air gap and length of full contact between the ingot and mold. For a laboratory scale ESR ingot (~ 200 mm), maximum values of 1.8 mm and 30 mm were calculated for the radial contraction and contact length respectively.

The establishment of relationship between operational parameters and thermal state of the electrode is of primary interest due to numerous chemical and electrochemical reactions occur at the tip of the melting electrode. Mitchell et al. [50] calculated steady state temperature profile of the electrode. They predicted a large temperature gradient at the tip of the electrode that can certainly influence reactivity of active chemical elements. Mendrykowski et al. [51] introduced a one dimensional model to compute the thermal field in the electrode. They found that thermal radiation to the electrode is negligible compared to the heat conduction along the electrode. Tacke et al. [61] proposed an approximation formula for the immersion depth and shape of electrode tip. Furthermore, they investigated the influence of operational parameters and system size on the melting condition of the electrode. Their results were validated against experiments.

Here, it must be stated that further efforts are required to improve our knowledge of the thermal field in the ESR. Nevertheless, the advection of heat by movement of the bulk fluid significantly influences the thermal field in the system. Therefore, it is necessary to include impacts of the flow field.

2.2.3 Coupled models with the flow field

The first numerical model that accounted for the coupling of the flow and electromagnetic fields in the slag and melt pool was reported by Dilawari et al. [53]. They predicted a linear relationship between magnitudes of applied electric current and velocity whereas thermal buoyancy force was ignored. Figure 2.7 shows the pioneering work of Dilawari et al. to compute velocity field in the slag for a laboratory scale ESR process [53].

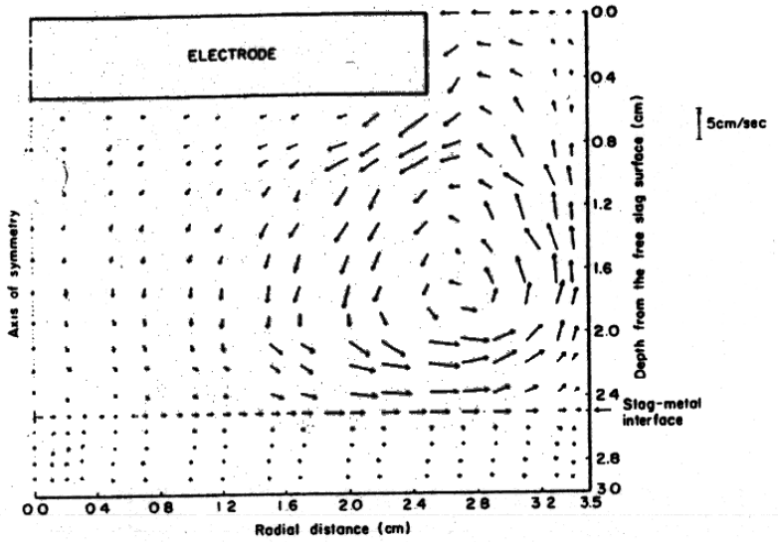

Figure 2.7. The first published numerical results of the velocity field in the slag [53].

Kreyenberg et al. [56] investigated the flow distribution under influences of the Lorentz and buoyancy forces in the ESR slag. It was shown that the buoyancy force could significantly alter the flow pattern in the slag. Jardy et al. [64] modeled the flow, electromagnetic and temperature fields in the slag. They predicted higher melt rate of the electrode when the buoyancy force is stronger than the Lorentz force in the slag.

Over past decades, numerous models coupled with the flow field were proposed to study influence of operational parameters such as ingot size, magnitude of applied current, applied AC frequency, and fill ratio (ratio between cross sections of the electrode and ingot) on the final quality of the ingot. Choudhary et al. [57] calculated the pool profile of the ingot where the coupling between turbulent flow, electromagnetic, and temperature fields in

the slag was taken into account. The importance of fill ratio, the input power, and the immersion depth of electrode were addressed. Furthermore, they stated that the temperature field in the slag is more uniform at large-scale systems [59]. Ferng et al. [63] reported that the applied AC frequency could significantly influence the velocity field in the melt pool. However, a weak effect of AC mode compared to DC mode on the velocity field in the slag was predicted. Viswanathan et al. [67] studied numerically and experimentally relationships between melt rate, input power, and pool profile of the ingot. By the increase of melt rate, a linear increase in the pool depth was reported. Kelkar et al. [68] presented details of analysis of the turbulent flow, temperature, and magnetic fields for the Ni-based alloy 718 produced through ESR process. Furthermore, Rückert et al. [76] analyzed details of calculation results for production of AISI304 ingots through ESR process. Their results were validated against the experiment. Weber et al. [79] predicted that decreasing the fill ratio leads to increasing both the melt rate of electrode and volume of liquid pool. Patel et al. [80] used the commercial software (MeltFlow) to study effect of fill ratio on pool depth of alloys 718 and 304 stainless steel. Results regarding to the heat loss through the slag-mold interface were analyzed. Furthermore, they predicted that increasing the fill ratio leads to decreasing the pool depth of ingot.

Kharicha et al. [88] studied the importance of applied frequency on the shape of slag-pool interface as well as variation in kinetic energy in the slag and melt pool. With the increase of applied frequency, the kinetic energy increases in both the slag and melt pool since larger displacement of the slag-pool interface was predicted at higher applied frequency. Assuming a constant thickness of liquid metal film formed at tip of the electrode (~ 8 mm), Yanke et al. [91] used heat transfer coefficients at slag-electrode interface to predict melt rate of the electrode for alloys IN 718 and WASPALOY. Furthermore, they studied effects of system size, applied current, and thickness of slag skin layer on melt rate and pool depth of an ingot [99]. Kelkar et al. [93] developed a transient model capable of predicting flow

field, temperature field, magnetic field, pool shape, inclusion motion, Rayleigh number, and local solidification time (LST). Their modeling results were validated against the experiment as shown in Figure 2.8.

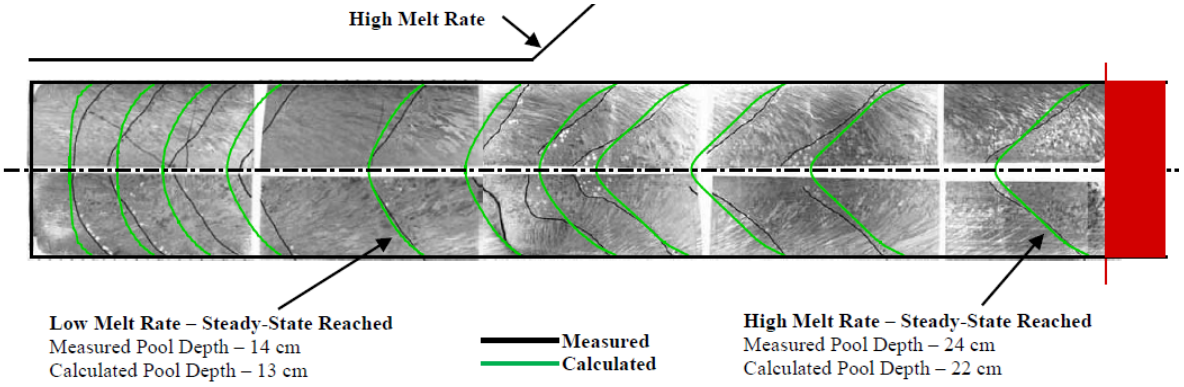

Figure 2.8. Comparison between the transient predicted and measured pool profile of the ingot [93].

Wang et al. [96] proposed a three dimensional model for a laboratory scale ESR process to study the effect of applied current on the general system behavior. The calculated pool profile was validated against the experiment.

Attempts have been made to model solidification parameters of the ESR ingot such as LST, microstructure, and macrosegregation. Yan-wu et al. [71] used vorticity-stream function formulation to model the flow field. They estimated that LST could be longer than one hour at the ingot center (ϕ 950 mm), whereas primary dendrites arm spacing is fairly small (~ 140 μm). Their modeling results were compared with experimental measurements. Krane et al. [86] studied the influence of melt rate on crystal morphological parameters of IN718 alloy. Both primary and secondary dendrite arm spacing were found to increase with the increase of melt rate. Giesselmann et al. [104] developed a combined 2D axisymmetric and 3D model to study an ESR process for production of alloy 718. Furthermore, they observed CET at the central region of ingot. They experimentally measured grain growth angle (GGA) and secondary dendrite arm spacing (~ 120 μm). Jardy et al. [78] stated that the

probability of freckle formation in VAR or ESR can be related to the local Rayleigh number. As shown in Figure 2.9, the area with higher Rayleigh number is more prone to freckles. Thus, an optimum melt rate to produce a high-grade ingot could be achieved when local Rayleigh numbers are kept at minimum values.

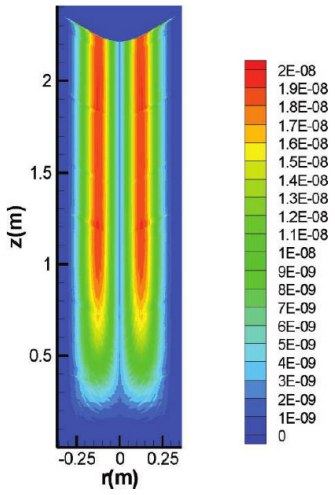

Figure 2.9. Distribution of Rayleigh number for an steel ingot [78].

In fact, the macrosegregation in the ingot is strongly governed by the flow in the melt pool and mushy zone [105]. Wang et al. [101] attempted to model macrosegregation of Ni in AISI 201 stainless steel for a laboratory scale ESR ingot (ϕ 120 mm). As shown in Figure 2.10, they observed a negative segregation at the lower part and a positive segregation in the upper part of the ingot. Their results were validated against an experiment in which the slag was composed of calcium fluoride, 75 mass pct., and aluminum oxide, 25 mass pct. The composition of Ni at the final ingot was analyzed using the method of SPECTROLAB optical emission spectrometer. Surprisingly, they observed a strong macrosegregation that is due to melting of a dual alloys electrode. Furthermore, macrosegregation of multiple components in alloy 625 was studied by Fezi et al. [103] considering effects of mushy zone permeability, ingot diameter, initial composition of the electrode, and applied current.

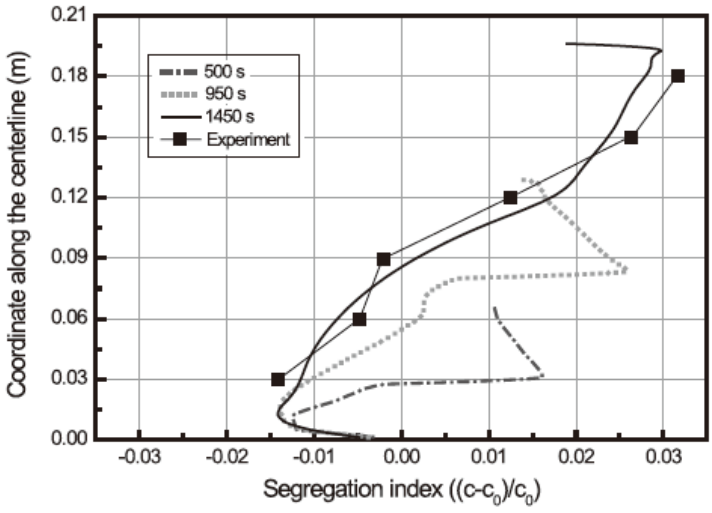

Figure 2.10. Evolution of segregation index along the centerline of an ESR ingot [101].

The electric current path can strongly influence conditions of flow and solidification in the ESR system. Kharicha et al. [66] reported the importance of mold current on the shape of slag-pool interface and distribution of Lorentz force. Furthermore, they pointed out the relationship between slag skin thickness, temperature fluctuation in the slag and the amount of mold current [75, 77]. Increasing the amount of mold current may lead to decreasing the thickness of slag skin. Additionally, the electrode immersion depth affects both the thickness of slag skin and amount of mold current [94].

Slag-pool interface movement as well as formation, departure, and dripping of droplets through the slag significantly influence the hydrodynamic conditions of the process as reported by Kharicha et al. [74]. According to their modeling results, the pool depth becomes deeper when the slag-pool interface was allowed to move [82]. Additionally, effects of size of droplets on the global electromagnetic, flow, and temperature fields in the slag were analyzed [73]. Kharicha et al. proposed a multiphase model to estimate the volume-averaged impact of droplets in the slag and melt pool [81]. Considering the complex interaction between flow, temperature, and magnetic fields in the ESR, Kharicha et al. [83] performed a 3D calculation to study the chaotic flow in the slag and melt pool

during formation and dripping of droplets. Effect of interface energy between slag and melt on the size of droplets and consequently electrical resistance swing in the slag were addressed [87]. Decreasing surface tension leads to formation of small droplets at the electrode tip. Then, they split to smaller droplets in the bulk of slag due to the pinch effect as shown in Figure 2.11.

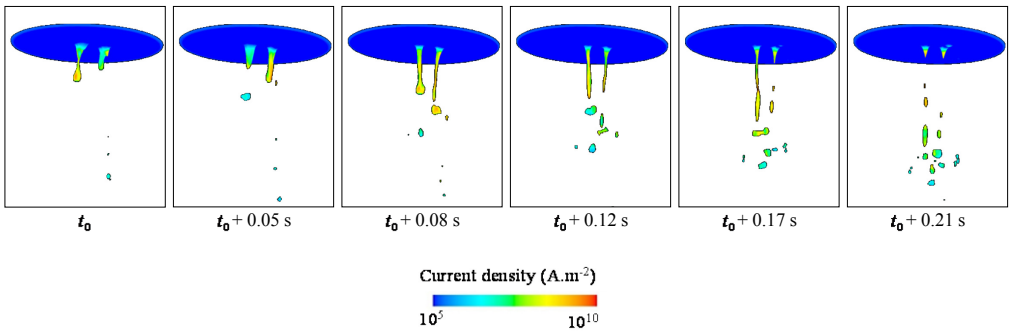

Figure 2.11. Droplet formation and atomisation inside the slag zone [87].

Wang et al. [102] developed a full scale 3D model where a parabolic shape for the tip of the electrode was assumed. They calculated the residence time of droplets in the slag and compared their results with empirical models. The thermal state and melt rate of the electrode are considerably influenced by the flow in the slag. Kharicha et al. [84, 100] studied melting of the electrode tip using the multiphase Volume of Fluid (VOF) model. The importance of electrode feeding velocity, immersion depth, shape of the electrode tip, and release of Joule heat were addressed. They stated that the melting of electrode is an unstable process, thus the immersion depth of the electrode must be controlled to achieve steady state. In the current work, effects of physicochemical properties of the slag on melting behavior of the electrode are analyzed [106, 113].

Attempts have been made to model distribution of non-metallic inclusions in the final ingot ignoring possible chemical reactions. Kharicha et al. [89] studied theoretically and experimentally distribution of inclusions in the ingot. According to modeling results, large inclusions (~ 9 μm) accumulate near the wall of ingot whereas small inclusions (~ 2 μm) are more evenly distributed.

Here, it must be stated that our knowledge of the flow field in the slag and melt pool has been notably improved. Nowadays, a fairly good estimation of the flow field as well as pool profile of the ingot can be obtained using the available CFD models for the ESR.

2.2.4 Species transport

Here, features of species transport as a major phenomenon occurring in the ESR are briefly discussed. Different contributions to species transport are easily recognized in removal and precipitation of non-metallic inclusions in the slag and melt pool, chemical and electrochemical reactions in the slag, and refinement of the alloy through the process.

Chemical reactions taking place within the slag bath or at metal-slag interfaces dominantly influence type of inclusions in the ingot as reported by Mitchell [114]. It was stated that nucleation and growth of inclusions in the ingot might occur which can be avoided by adding more de-oxidants to the melt pool. Furthermore, a careful selection of the composition of slag is essential to increase residence time of droplets inside the slag bath. Kay et al. [115] proposed possible mechanisms of inclusion removal including floatation, absorption, and chemical reaction. They stated that a deep melt pool could efficiently enhance flotation of inclusions. The floating inclusions in the melt pool are absorbed at slag-pool interface. Furthermore, inclusions could be dissolved at high temperature as a consequence of chemical reactions in the slag (e.g. reactions of silicon oxide and aluminum oxide).

Numerous chemical and electrochemical reactions can be carried out in the slag [17, 18]. Reactions are majorly taking place within the slag bath or at slag-metal-gas-mold interfaces [5]. Aluminum-silicon oxides and Sulphur are frequently reacting. A mechanism including a series of electrochemical reactions was postulated for Sulphur removal in the ESR. Minh et al. [116] melted a copper electrode in similar condition as the ESR process. They

suggested a diffusion controlled electrochemical reaction for the Sulphur. Kato et al. [117] studied behavior of oxygen and sulphur during DC melting of electrode in the ESR. They observed that concentrations of Sulphur and oxygen in the final ingot are very dependent on the electrode polarity during remelting. A higher amount of oxygen and lower amount of Sulphur was traced in the ingot produced through the ESR with the negative polarity of electrode.

The pioneering work of Kawakami et al [118-119] described possible electrochemical reactions occurring at the tip of electrode. They observed that the melt rate of electrode is dependent on the electrode polarity in DC ESR process. Mitchell et al [120] pointed out further possible electrochemical reactions after performing a series of experiments to measure electrochemical polarization overpotential. They used the well-known galvanostatic pulsing technique to measure magnitudes of overpotential resulting from concentration polarization at the interface between iron and CaF_2-based slags. A significant change in composition of a pure iron electrode was observed after polarization. A noticeable increase in composition of oxygen in the bulk of the electrode was measured using methods of optical and electron microprobe scans as shown in Figure 2.12. A "dirty" microstructure in the optical picture and areas of oxygen containing materials (probably iron oxide) in probe pictures are illustrated. Additionally, the measured potentials agreed with the results from the electrolytic cell.

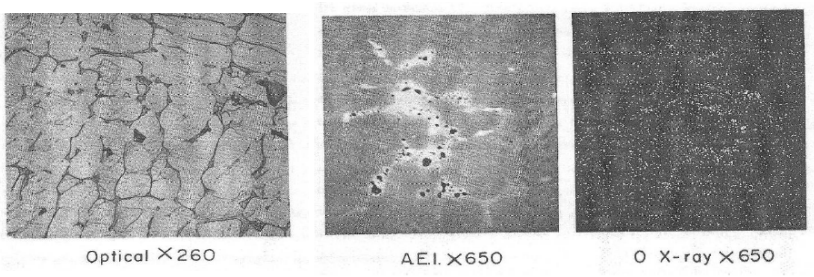

(a) (b) (c)

Figure 2.12. Section through an anodic pure iron electrode after 10 min of polarization in the slag: (a) optical, magnification 260 times, (b) AEI, magnification 650 times, (c) Oxygen, magnification 650 times [120].

Mitchell et al. [121] noticed that addition of a relatively small amount of Al_2O_3 to CaF_2 could significantly decrease the electric conductivity of liquid slag. As a consequence of formation of complex ions such as $AlOF^{-2}$, the mobility of F^- reduces that might describe the variation in the electric conductivity of slag [121].

Loss of alloy elements such as Ti and Al due to electrochemical oxidation was reported as a significant issue during DC operation of ESR process [122]. Reactions of special alloy elements such as Fe or Mn were also studied. Nowack et al. [123] postulated a relationship between current density (direct or alternating current) and potential. Increasing the iron oxide content in the slag or the applied frequency results in decreasing the overpotential. Prange et al [124] measured the magnitude of exchange current density at 1450 °C for an iron electrode immersed into the slag. Furthermore, Schwerdtfeger et al. [125] presented modeling results of curve fitting to describe an electrochemical mechanism of oxidation of titanium and aluminum where iron oxide was considered as the major oxidizer agent for both of those elements. The reaction kinetics of Mn and Fe were analyzed by Fraser et al [126] aiming to find the relevant mass transfer coefficients. They extended their investigation to examine effects of applied frequency and mold type (isolated or live) on the reaction kinetic of Mn. They concluded that experimental results support faradaic reaction of Mn on the interfaces of slag-metal or slag-mold [127]. In the present thesis, an attempt is made to develop the basic model of electrochemical transport of ions in the slag that is fully described in Ref. [128].

It must be stated that modeling species transport in the ESR is still in a very preliminary stage. Extensive dedicated efforts are required to develop high fidelity models considering the coupling between flow, heat, electromagnetic and species concentration fields.

2.3 New ESR technologies

Nowadays, the standard ESR process might be slightly modified to produce ingots with special characteristics. The demand to apply the following well-known industrial processes originated in the ESR is rapidly growing: heavy ESR ingot with electrode change technology, ESR with multiple electrodes, electroslag rapid remelting (ESRR), current conductive mold (CCM), Pressure-ESR (PESR), and ESR for hollow ingot. The distinctive attribute of aforementioned processes are briefly described. Additionally, schematic representations are shown in Figure 2.13.

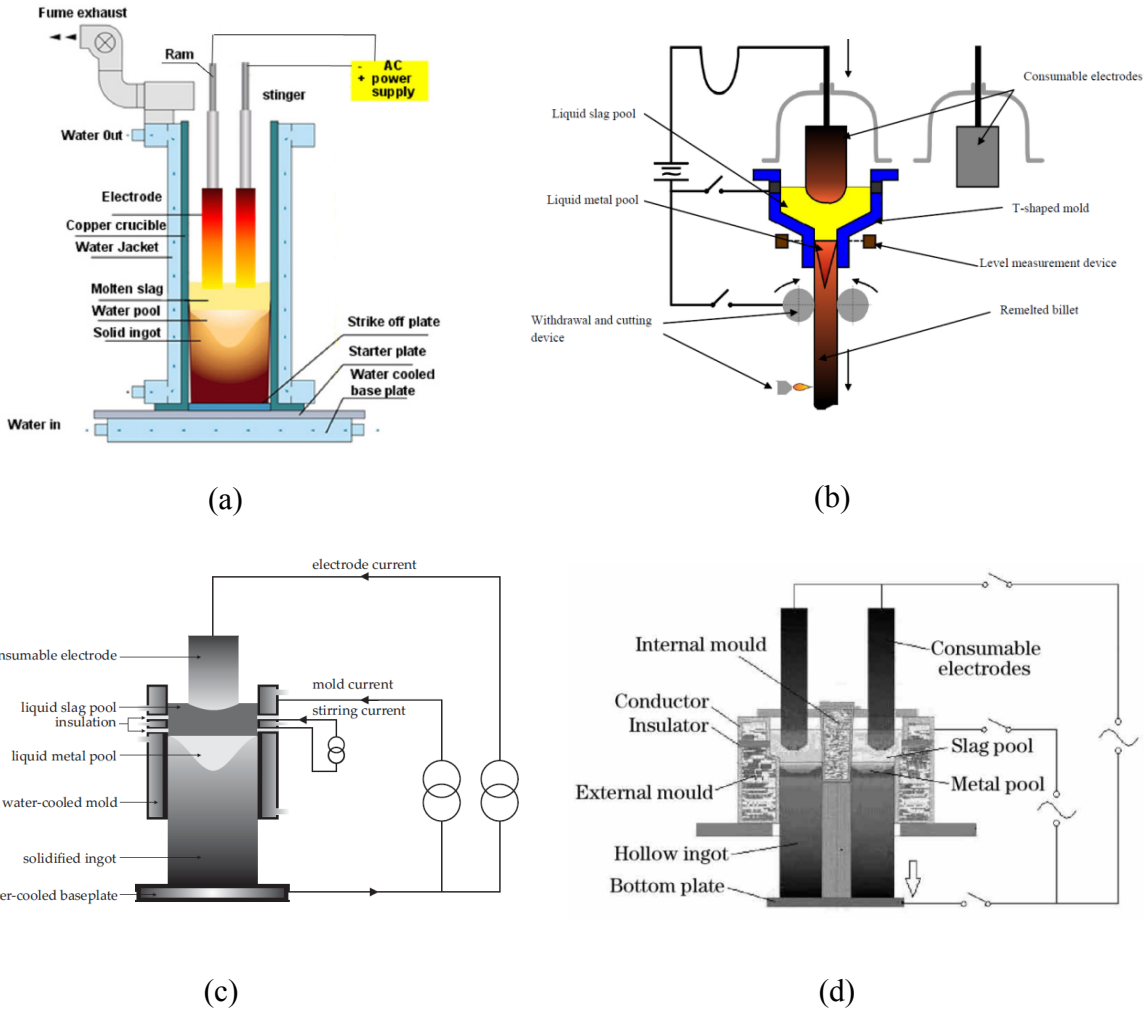

Figure 2.13. Schematic representation of new technologies: (a) ESR with multiple electrodes [133], (b) Electroslag rapid remelting [136], (c) current conductive mold [139], (d) ESR for hollow ingot [150].

2.3.1 ESR with electrode change

Nowadays, the demand for very large heavy ingots (> 100 tons) through ESR process is increased especially in chemical, oil and gas industry. Producing a large ingot by ESR process is quite a long process that might take several days. Manufacturing a large ingot requires electrode change technology in which several smaller electrodes are remelted one after another to produce one big ingot.

The entire electrode change procedure is divided to three steps. Firstly, within a very short time (< 5 min), the electric power is turned off, and a new preheated electrode is prepared to replace the remelted last one. Secondly, the electric power is again turned on. Consequently, the temperature of the new electrode rises to reach the melting temperature. Finally, the melt rate increases until reaching the target melt rate. There are only few reports available on this topic. As stated by Holzgruber [129], no traceable change in ingot internal composition was observed during the power interruption. However, Matushkina [130] reported slight defects of surface during electrode change. Jackson [131] monitored thermal field in mold using thermocouples to analyze heat balances across the ingot during power interruption. It was observed that solidification occurred much more rapidly at the pool periphery rather than in the ingot center. It was also found that gross changes in the structure and composition of ingot are not expected unless power interruption lasts for too long.

Further investigation is required to clarify the influence of power interruption on the process. A very first attempt is made to model electrode change using CFD simulation tools. Details are given in Ref. [132].

2.3.2 ESR with multiple electrodes

Remelting multiple electrodes simultaneously (Figure 2.13 (a)) can increase the production rate of the process with the advantage of little inductance, and lower power consumption

especially to produce large scale or rectangular ingots. Li et al. [133] developed a mathematical model of the ESR system with two series-connected electrodes. Distributions of current density, magnetic flux density, Joule heat, power density, temperature field, and pool profile were analyzed. Dong et al. [134] theoretically studied ESR process with four electrodes. They stated that remelting four electrodes with two sets of bifilar configuration improves the quality of a large scale ingot (Shallow molten pool). As such, it is in favor of manufacturing large ingots to remelt four electrodes configuration rather than single electrode through ESR process.

2.3.3 Electroslag rapid remelting (ESRR) process

In the ESRR process, a T-shaped mold is used including a graphite ring that takes major amount of current through the mold as shown in Figure 2.13 (b). Holzgruber [16] presented details of the process. The first ESRR process with continuous casting concept using automatic manipulator was established in the beginning of 2002 as reported by Alghisi et al [135]. The standard ESR process can ideally control the solidification of ingot and produce homogenous structure with minimum defects. However, the melt rate of electrode is rather low that makes the whole process uneconomical especially to produce small ingot sizes. In substitution, continuous casting is an economical process to produce small ingots such as billets at high casting speed. Unfortunately, deep liquid melt pool forms in the billet ingot of continuous casting that leads to center porosity and segregation. As such, continuous casting is not suitable to produce segregation prone alloys like tool steel or several super alloys.

The electro slag rapid remelting (ESRR) process has advantages of both traditional ESR and continuous casting processes to produce billets. According to industrial praxis, the melt rate (in kg/h) of electrode is strictly chosen as a fraction of (0.6 to 1) ingot diameter (in

mm). Therefore, production of ingots with diameter lower than 400 mm through ESR is very limited and uneconomical despite of their wide application area. Nevertheless, the ratio of melt rate to ingot diameter can be as large as 3 to 10 to produce billets of 100-300 mm using ESRR [136]. The research on the ESRR process is currently ongoing aiming to improve the design of the T-shaped mold, to decrease overall heat loss in the process, and to obtain a higher temperature at metal meniscus (better surface quality of ingot) [137].

2.3.4 Current conductive mold (CCM) process

In the CCM process, a certain amount of input power is introduced to the slag through the mold by applying a stirring current as shown in Figure 2.13 (c). A portion of the originally imposed current is also taken through the mold. In the standard ESR process, the input power, melt rate, pool depth, and ingot surface quality are coupled parameters. The input power and subsequently melt rate of the electrode must be kept sufficiently low to reduce the liquid pool depth. In contrary, a good surface quality of ingot can be achieved when large input power and high melt rate are applied [138]. Nevertheless, a shallow pool depth together with a good surface quality of the ingot can be obtained using current conductive mold (CCM) technology. Holzgruber et al [139] presented details of the process as well as results of several experimental tests. Medovar et al [140] found that applying two power sources in the ESR using CCM technology result in production of ingots with almost flat pool profile. Liu et al. [141] mathematically modeled the CCM process to calculate distributions of current density, Lorentz force, Joule heating, flow, and temperature in the slag bath. Note that, the stirring current intensifies mixing near the mold wall and leads to relatively uniform temperature in the slag bath.

Here, it must be reported that other methods such as using a rotating electrode or using an external magnetic field (EMS) were tested to promote stirring in the slag. Hernandez-

Morales [142] studied theoretically and experimentally effects of EMS on the ingot quality of a laboratory scale ESR using an AC operated device. Since the EMS force is confined near the wall, the microstructure was not considerably modified in the center of the ingot. Wang et al. [143] presented 2D axisymmetric modeling results of the grain morphology for an EMS ESR process. They concluded that EMS could refine the grain size because of excessive stirring. However, the pool depth of ingot might increase considerably. A strong rotational flow (angular movement) can be observed on the slag surface when EMS is applied. One should consider that, the angular movement might be also ignited in presence of an axial magnetic field originated from earth, nearby electric cable lines or a neighboring ESR furnace. Brückmann et al. [144] experimentally studied effects of angular movement of the slag on the quality of the final ingot. The angular movement has severe negative impacts on the internal and surface quality of the ingot. The ingot had an asymmetric pool profile as well as several spiral shaped marks on the surface.

Wang et al. [145] made an attempt to model a laboratory scale ESR considering a rotating electrode. Based on modeling results, they reported a higher melt rate for the rotating electrode compared to the stationary one. Surprisingly, they calculated almost similar pool depths of ingots.

Here, it must be stated that our knowledge on impacts of EMS or rotating electrode techniques is very limited. As such, extreme care must be taken to apply the aforementioned techniques.

2.3.5 Pressure electroslag remelting (PESR) process

A protective hood is used in the Pressure-ESR (PESR) process where the pressure of the gas (generally nitrogen) is very high (25 to 42 atm). The aim of this technology is to

enhance nitrogen solubility in the metal ingot. Nitrogen alloyed steels are corrosion-resistant which are applicable in engine valves, power generation components, drill collars, etc. [5, 146, 147].

Patel et al [146] conducted a series of experiments on a laboratory scale PESR furnace to examine the effect of furnace pressure and additives on nitrogen solubility in a Fe-Cr-Mn alloy. They reported that using additives such as Si_3N_4 to increase nitrogen pick-up requires consistent feeding and uniform distribution in the slag.

Recently, a new method was tested to improve addition of nitrogen to the system through the electrode. Nitrogen gas was blown into the slag through a central hole in the electrode. Yamamoto et al [147] provided details of the experiment. They stated that nitrogen gas could be effectively absorbed at the tip of the remelting electrode.

2.3.6 ESR with hollow ingot process

In the ESR with hollow ingot process, an ESR furnace with multiple electrodes and current conducting mold is used as shown in Figure 2.13 (d). Seamless steel pipes with superior quality in large diameter and thick wall are highly demanded in nuclear power, hydropower, and other energy fields. Medovar et al. [148] discussed the advantages, disadvantages, future and challenges to produce hollow ingots through the ESR. Furthermore, Liu et al [149, 150] studied production of hollow ingots. They presented calculated results of distributions of current density, magnetic force, Joule heating, fluid flow and temperature. Further study is required to design and use hollow ingot ESR furnaces in economical way.

3 Simulation of ESR process

Over past decades, several numerical models were established to investigate the ESR process. Most of them have been discussed in the previous section. In this thesis, transport phenomena in different size of ESR process are numerically studied. Here, only a summary of significant results are provided. Details are given in the publications appending in the last part of this dissertation. The current work is an extension of the model which has been developed by Abdellah Kharicha in Montanuniversität Leoben since 2005. The commercial CFD software, FLUENT-ANSYS v.14.5, was used to simulate the fluid flow, heat transfer, and electromagnetic fields. Numerous external user-defined functions (UDF) were coded and implemented into the software.

The Multiphysics ESR process involves melting, solidification, heat transfer, mass transfer, and magnetohydrodynamics (MHD). It is not feasible to include all the aforementioned phenomena in one single comprehensive model. Based on our purpose of investigation, we might make proper simplification in each calculation. For instance, the solidification of ingot was ignored when prediction of melting behavior of the electrode such as melt rate, immersion depth, and shape of the electrode was the focus of study.

Here, the major achievement is that our knowledge of magnetohydrodynamics (MHD) in the whole ESR, solidification of the ingot, and melting of the electrode has been remarkably improved. Investigation of the species transport in the slag especially due to electrochemical transport of ions has been initiated by developing a one-dimensional numerical model. Finally, an outlook for further modeling activities is given in the section of future prospects.

3.1 General model description and assumption

Here, a general description of the modeling approach including related equations and assumptions is given. For specific investigations on some process parameters such as the melt rate of electrode, the model is refined. More details will be described in the relevant sections. Nevertheless, the related transport equations are numerically solved using the well-known Finite Volume Method (FVM) [151].

The flow in the slag and melt pool is calculated by solving the equations of conservations of mass and momentum [106]. It must be noted that, impacts of solidification, electromagnetic, and thermal fields on the velocity field are modeled by adding source terms to the momentum equation. The thermal buoyancy force is considered using the Boussinesq approximation. The interaction between the electric current and the self-induced magnetic field is the origin of the electromagnetic force (Lorentz force). Furthermore, the drag resistance of the dendrites to the flow in the mushy region is taken into account according to the permeability [152].

The turbulence in the slag and melt pool is considered using shear stress transport model (SST) model. The model is known to effectively blend the precision and robustness of k-ω model in the near-wall region with the bulk liquid k–ε modeling in far field [153-154]. Furthermore, Turbulence is modeled using the Scale-Adaptive Simulation (SAS) approach for some of our specific studies such as a 3D simulation of the ESR [155]. The latter is the improved version of shear stress transport (SST-K-ω) turbulent model which can be dynamically adjusted to resolve structures in a unsteady RANS simulation e.g. in presence of a moving liquid-liquid interface. It is believed that accuracy of results using SAS model is comparable to LES model with the advantage of lower computational cost.

The temperature field and solidification of the ingot are modeled by solving the enthalpy conservation equation [156]. The source terms of Joule heating and solidification latent heat are included. It is of great importance to choose a valid liquid fraction-temperature relationship to model the solidification. Most often, a linear relationship is applied [157]. On the other hand, the steel alloy can be treated as an effective binary Fe-C alloy system in which the alloy element C is very diffusive in both liquid and solid. Thus, the Lever rule [158] is consistent to solidification path (liquid fraction as a function of temperature).

An accurate modeling of electromagnetic field is essential since the flow is driven by the Lorentz force. Two popular formulations of magnetic field exist for modeling: The formulation based on the classical magnetic induction equation [105], and the formulation based on magnetic vector potential-electric scalar potential [106]. The potential formulation is computationally more expensive compared to the common approach based on magnetic induction. However, it is very accurate for solving electromagnetic field in presence of moving boundaries. Additionally, it can effectively model the current path including mold current and eddy current.

Modeling effects of droplets in the ESR is very challenging and controversial. Here, we used a rather simple model considering droplets as mass, momentum, and energy carriers which impact both the melt pool and slag [105].

Sophisticated modeling tools were embedded into the current model to investigate special phenomena occur in the ESR. For instance, Volume of Fluid (VOF) [159] model is applied to study the influence of slag-pool interface movement on the magnetic field. Furthermore, the dynamic mesh technique is used to model melting and shape of an ESR electrode [160-161].

Reasonable assumptions were made to reduce the complexity of the Multi-physics ESR system. Nonetheless, Considering the ESR process as a 2D axisymmetric system is the fundamental assumption. The validity of axisymmetric assumption is briefly described in next section, and details are available in Ref. [162]. The big advantage of using an axisymmetric model is reduction of the heavy computational cost, especially for CFD calculations. Additionally, it is generally simpler to deal with governing equations of flow, heat, or electromagnetism in 2D rather than in 3D. A schematic representation of the geometry and boundaries are illustrated in Figure 3.1.

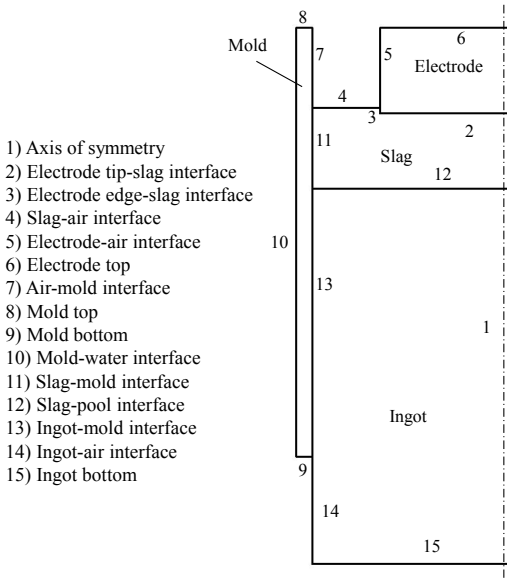

Figure 3.1. Schematic of the geometry and boundaries.

3.2 Validity of axisymmetric modeling

Nearly all proposed CFD models for ESR are in 2D. There are only a very small number of 3D calculations [96, 102]. The limitations of computational resources are constraining us to perform full scale 3D simulations. Herein, a different 3D modeling concept is proposed that focuses on an industrial scale AC electroslag remelting process including solidification of

the ingot (ϕ 750 mm ingot). It is assumed that the slag-pool interface is stationary. Furthermore, the effect of droplets passing through the slag on the global electromagnetic field is ignored. As a result, the electromagnetic field can be obtained independent of the influence of other fields, such as temperature or flow, making the 3D calculation feasible. Therefore, the magnetic field is computed in a 2D axisymmetric domain including an electric conductive mold based on the electromagnetic induction equation. Then, the calculated parameters, such as Lorentz force and Joule heating are interpolated and patched in the azimuthal direction within our 3D domain.

A typical non-axis symmetry flow pattern and temperature field in the slag region, which has been observed in-situ from the slag surface during operation, was demonstrated. A statistical analysis of the turbulent flow in the slag and melt pool is performed to quantitatively characterize the transient behavior of the flow (see [162]). Nevertheless, The mean velocity and mean temperature fields averaged over 30 minutes are shown in Figure 3.2. The flow direction is also drawn. The hot molten slag under the electrode is continuously pushed toward the mold wall. The flow is dominantly driven by buoyancy in the melt pool. The hottest zone in the slag region is observed under the electrode where the current density is the largest. The predicted shape of the melt pool (profile of the solidifying mushy zone of the ingot) is found to be less influenced by the transient 3D flow in the slag region, and it shows good axis symmetry. In addition, the predicted shape of the melt pool is verified against the experimentally measured pool profile [163]. By comparing the 3D calculation with a 2D axis-symmetrical calculation, we find that the predicted melt pool profiles are quite similar, leading to the conclusion that a 2D calculation is sufficient to solve the melt pool profile of the ingot (Figure 3.3). Accordingly, all the presented simulations in this dissertation were performed in a 2D axis symmetrical computational domain.

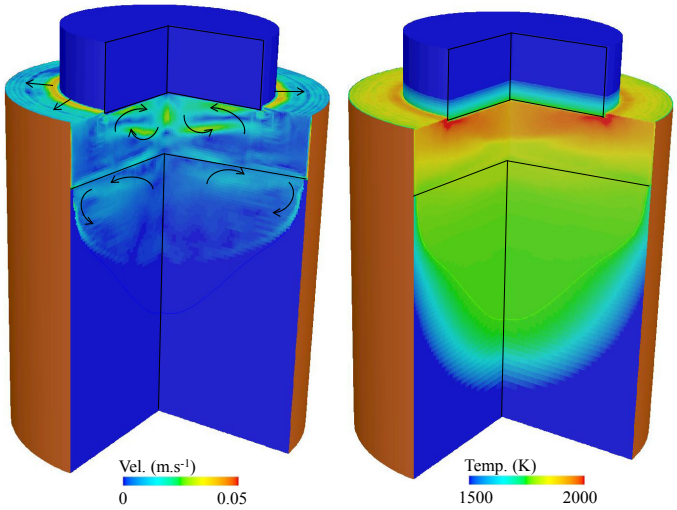

Figure 3.2. (a) Mean velocity field, and (b) mean temperature field averaged over 30 min.

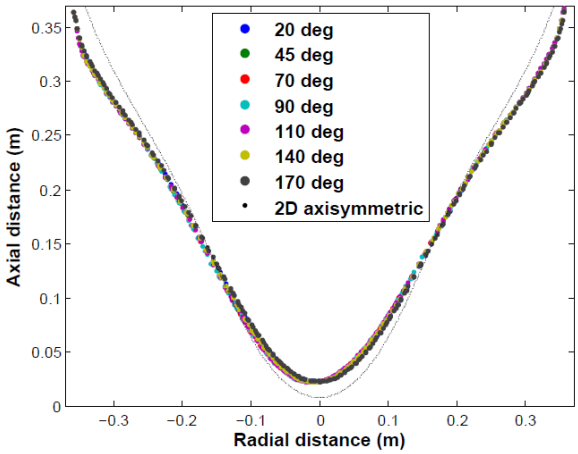

Figure 3.3. Pool profile obtained in various angular vertical sections of 3D simulation compared with a 2D axisymmetric simulation

3.3 Electric current path

The shape of the melt pool is strongly dependent on the conditions of the temperature distribution and flow which are in turn influenced by the current path in the system. Most crucial electrical parameters that influence the current path are the applied AC frequency, electrical conductivity of slag (liquid and solid), slag cap height, and the type of mold (live or isolated). Herein, effects of the aforementioned parameters are analyzed. The following

assumptions are made: The slag-pool, slag-air, and electrode-slag interfaces are assumed to be stationary and flat. Moreover, the immersion depth of the electrode is ignored.

3.3.1 Mold current

The electric conductivity of solidified slag skin layer is not well known. The slag skin layer is assumed to be a perfect electrical insulator in most of simulations found in literature. On the other hand, preliminary trials to produce ESR ingot using the current conductive mold (CCM) technology strongly rejects this assumption [139]. Furthermore, the perfect contact between the mold and baseplate brings the possibility for a portion of current to go directly toward the mold (mold current). In fact, the current selects the less resistive path through either the mold or melt pool to reach the baseplate. The mechanism of current conduction through the solidified slag layer is stated to be ionic [164]. However, the types of faradaic reactions and involved ions are unknown. Nonetheless, the mold current can greatly influence distributions of Lorentz force and Joule heating in the system [105].Therefore, it determines the internal [105] as well as surface quality [109] of the final ingot. Figure 3.4 illustrates the current path for different mold type (live or isolated) at different frequencies (ϕ 750 mm ingot). The skin effect takes place at large AC frequency is clearly visible in the electrode, ingot, and mold. The eddy currents generated within the copper mold can propagate to the steel ingot in the region where full contact is considered between the isolated (short collar) mold and the ingot (Figure 3.4 (c)). The total electrical resistance of the system and consequently the amount of generated power decreases because of the mold current that is further described in [105].

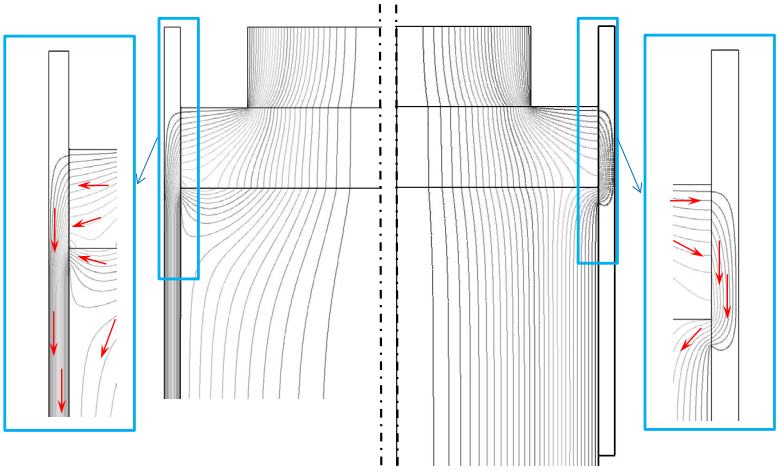

(a) DC current

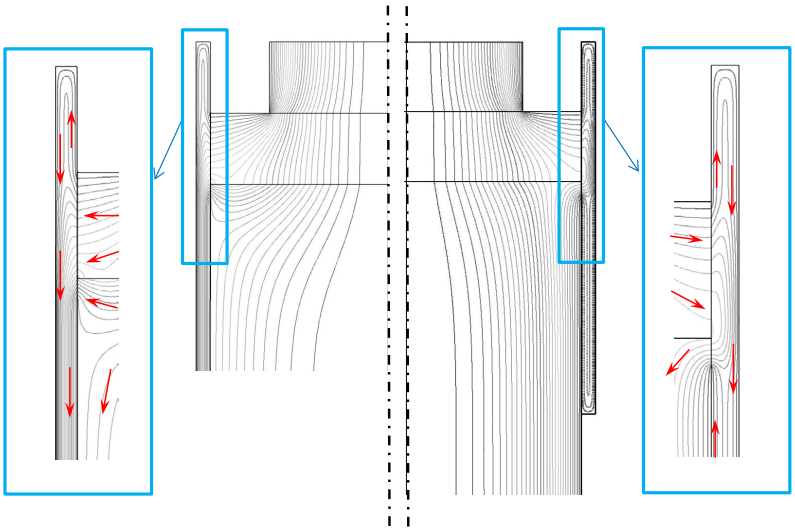

(b) AC current (f=5 Hz)

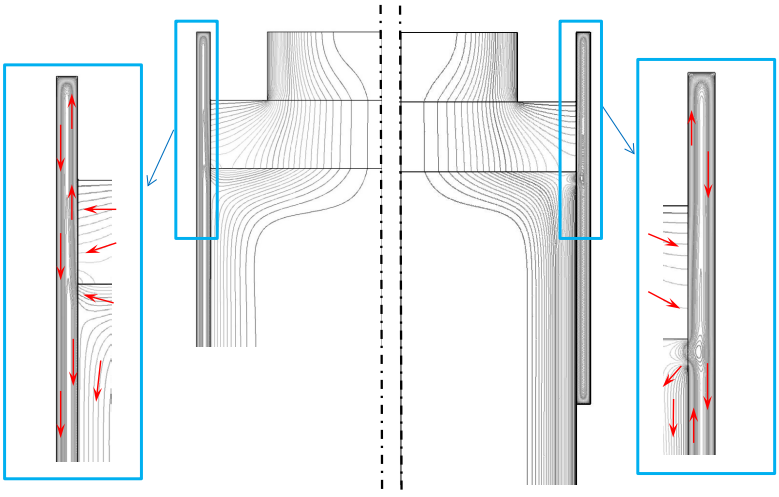

(c) AC current (f=50 Hz)

Figure 3.4. Electric current path in the whole ESR process running at different applied frequencies with different types of mold: live (left), and isolated (right).

3.3.2 Effect of slag cap height

The total resistance of the system is directly related to the height of slag cap. Note that, the electric current selects the less resistive path through either the mold or melt pool to reach the baseplate. Therefore, the portion of mold current dramatically increases by the increase of slag cap height. Figure 3.5 compares the amount of mold current considering different slag cap height for isolated type of mold in the ESR (ϕ 750 mm ingot). All the operational parameters except the slag cap height are similar for both cases. Almost 66% of total current flows through the mold when the height of slag cap is 30 cm. However, there exists only 30% as mold current in the case with slag height of 15 cm. Therefore, the length of slag cap can influence the current path that in turn determines internal and surface quality of the ingot.

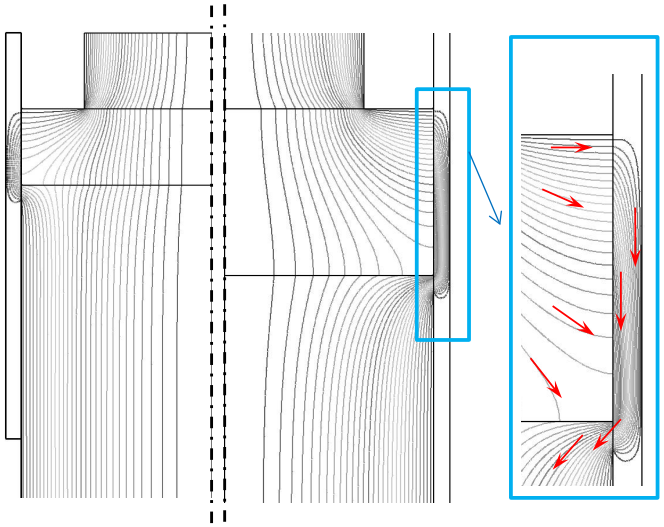

Figure 3.5. Electric current path for two different heights of the slag cap for the ESR running with an isolated (short collar) mold, (a) 15 cm of slag cap, (b) 30 cm of slag cap.

3.3.3 Effect of slag electric conductivity

The electric conductivity of the slag is dependent on the temperature and composition. Uncertainties of the physicochemical properties of slag such as electric conductivity exist due to the difficulty of the measurement at high temperature of the metallurgical processes. The conductivity of a conventional ESR slag made of CaF_2-CaO-Al_2O_3 was reported to vary between 80 and 300 $\Omega^{-1}.m^{-1}$.

In the current study (ϕ 1823 mm ingot), the thickness of solidified slag layer (~ 1 cm) and the amount of generated power in the process (~ 1.8 MW) are known in advance. This provides us helpful information to theoretically analyze the amount and consequences of the mold current in the static mold ESR [165]. Several simulations were performed to compute the electric current path and total power generation considering variable magnitude for electric conductivity of slag and solidified slag skin. For this reason, the conductivity of slag skin layer is tuned to generate the target power in the system. In other words, variation in total power generation as a function of slag skin electric conductivity was calculated whereas the conductivity of liquid slag is kept constant. The aim is to estimate adequate values of electric conductivity for the slag and solidified slag layer. A summary of the results is plotted in Figure 3.6 (a) where each curve is obtained for a constant electric conductivity of the liquid slag. The calculated generated power decreases almost exponentially with the increase of slag skin electric conductivity. The latter indicates that opening the path to the mold strongly decreases the overall resistance of the whole system. Some correlations can be established between the electric conductivities, proportion of mold current, and proportion of total generated power in the solid slag layer. The proportion of generated power in slag skin layer is raised by decrease of electric conductivity as shown in Figure 3.6 (b). The results reveal that significant amount of Joule heating is released in the thin layer of slag skin. For this reason, the skin layer will be definitely remelted, and

assumption of constant thickness is not valid. However, the generated power in the solid slag layer with electric conductivity of 48 $\Omega^{-1}.m^{-1}$ is negligible compared to the total generated power in the system (~ 12% of total power). Accordingly, our primary assumption of constant thickness of the skin layer can be accepted. For the latter, the ratio of current entering into the mold was predicted to be around 92 %. In order to explore the influence of mold current on the formation of solidifying ingot, we continue our study for two extreme cases (one with no mold current and the other with 92% mold current) in which the fundamental assumptions (e.g. constant thickness of slag skin layer, similar total generated power) are valid. The temperature field and pool shape are compared as shown in Figure 3.7. In fact, mold current intensifies flow stirring, which leads to approximately uniform temperature in the slag and melt pool regions. Furthermore, promotion of stirring with mold current enhances the global energy transfer in the process results in deeper pool and thinner mushy zone. Additionally, the distance from the slag-pool interface to the start of solidification at the ingot surface known as standing height (liquid head) is increased. With mold current, the direction of Lorentz force bents downward near the contact region. Consequently, the hot liquid metal is pushed down near the mold wall causes increase of standing height. As discussed in the previous section, presence of mold current can improve the surface quality of the ingot. Mitchell et al [166-167] stated that presence of a finite depth of liquid head is essential to produce ESR ingots with superior surface quality. To achieve this goal, the melting point of slag must be kept higher than the melting point of metal. Therefore, they suggested adding more Al_2O_3 to the slag.

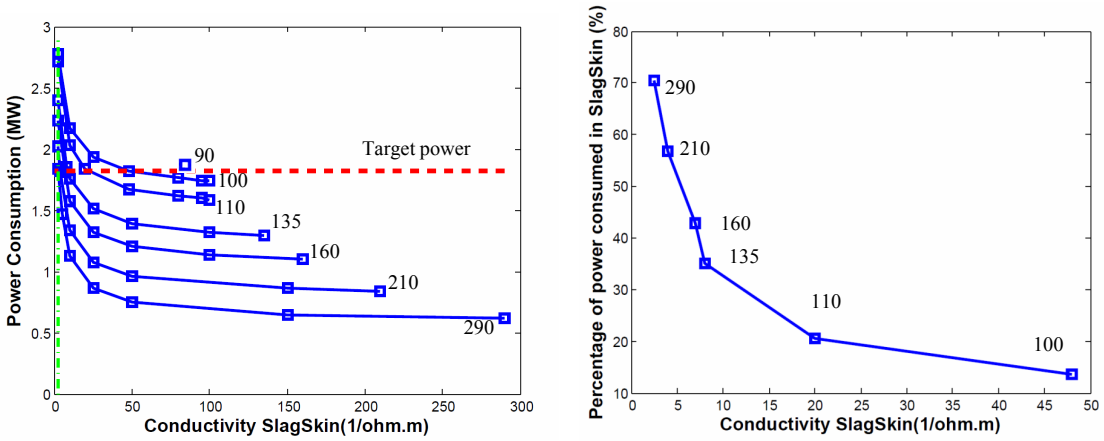

(a) (b)

Figure 3.6. (a) Total generated power in the process versus the electric conductivity of the solidified slag layer (the constant value used to label each curve indicates the conductivity of liquid slag) ; (b) Proportion of total generated power in slag skin at target power (the points are labeled according to the conductivity of liquid slag).

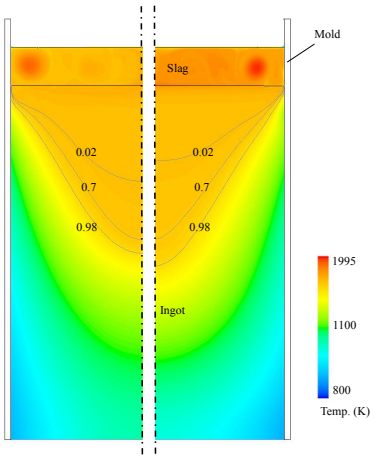

Figure 3.7. Contour of temperature overlaid with isolines of fraction solid (0.02, 0.7, 0.98) to indicate the mushy zone, (left) with mold current, (right) without mold current.

3.3.4 Effect of applied AC frequency

Most conventional electroslag remelting (ESR) processes are operated with AC current. The inductive loss of the power becomes a major problem when the process is operated at the high frequency for large scale ESR. Nowadays, the demand on large scale ingots has driven

the people to think of operating the process with AC current at low frequency (quasi-DC). The effect of applied frequency on the distribution of Lorentz force, Joule heat, temperature, and velocity is extensively discussed in [105]. Up to my knowledge, there is no experimental study on the effect of applied frequency on the melt pool of large scale ESR ingots. As described in the section 3.3.1, the applied frequency significantly influences the current path because of the related skin effect phenomena. Therefore, the velocity, temperature, and solidification fields are influenced. An example of calculation (ϕ 2000 mm ingot) of the aforementioned fields for two different frequencies (0.2 and 50 Hz) is shown in Figure 3.8. Here, no turbulence model is applied. Additionally, the current is not allowed to flow through the mold. Strong mixing of liquid metal is observed at the center of melt pool where electric current is flowing at low AC frequency. A longer liquid head is predicted in the case with higher applied frequency.

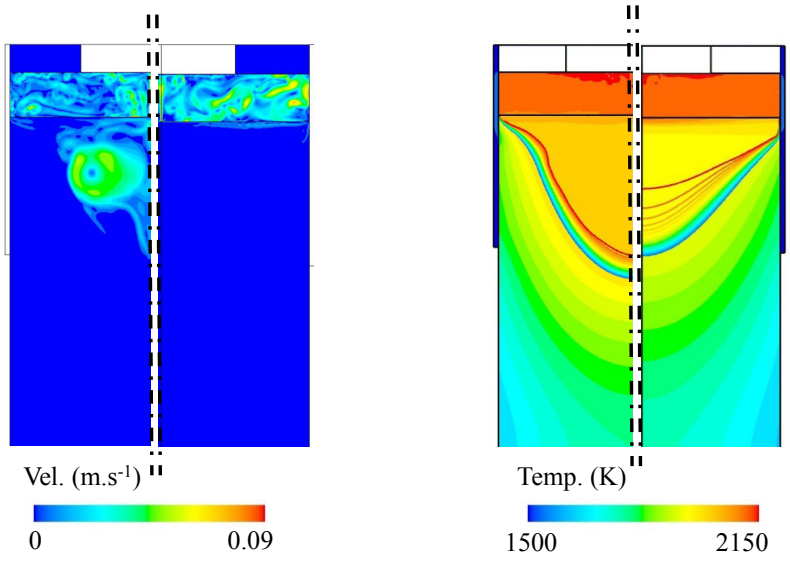

Figure 3.8. (a) Velocity field at low frequency (left), and high frequency (right) ; (b) Temperature field at low frequency (left), and high frequency (right).

3.4 Crystal morphology parameters

The quality of the ingot is strongly dependent on the shape of melt pool, i.e. the depth and thickness of mushy zone, which is in turn influenced by the bulk and interdendritic flow. The dendritic structure is mostly influenced by the cooling rate in the process, temperature gradient ahead of the crystallization front, and the intensity of interdendritic flow. With the increase of cooling rate, the local solidification time (LST) decreases and the mushy zone become thinner. Furthermore, an intensive flow in the melt pool promotes the formation of the freckles and leads to macrosegregation [168]. Here, a numerical study is performed to investigate the effect of crystal morphological parameters such as primary dendrite arm spacing (PDAS) on the solidification of the ESR ingot (ϕ 750 mm ingot). The crystal morphology is dominantly columnar and dendritic, thus a mixture enthalpy-based solidification model is used. Accordingly, the mushy zone is considered as a porous media where the interdendritic flow is calculated based on the permeability. The permeability is determined as function of the liquid fraction and primary dendrite arm spacing according to Heinrich and Poirier [169, 170]. A number of models were presented to estimate the spacing of the dendrites arm according to the cooling rate, casting speed, and solute concentration [171]. Here, we used the model of Jacobi [172]. Figure 3.9 (b) shows the calculated primary dendrite arm spacing. With the increase of the distance from the mold toward the center, the cooling rate decreases and consequently the PDAS increases. As such, the largest PDAS (~ 2.8 mm) is observed in the region near to the ingot axis. The distribution of arm spacing is found to be dominantly parabolic inside the mushy zone. However, dendrites become finer with approximately uniform size in the vicinity of the ingot surface. Unfortunately, the measuring data of dendritic structure is not available for this experimental ingot. Previously, Borodin [173] performed experiments on ESR ingots (ϕ 400-500 mm ingot) of Cr-Mo-V to investigate crystal morphology and segregation of

elements. The PDAS was observed to be in the range between 50 to 3000 μm that is not far from what we predicted. Furthermore, Figure 3.9 (c) compares the predicted pool profile considering constant (~ 300 μm) or variable PDAS. Essentially, the interdendritic flow is controlled by the permeability that strongly depends on the PDAS. Generally, the liquid velocity inside the mushy zone is significantly smaller than the velocity in the melt pool or slag. However, the two cases presented above were predicting different pool profile as a consequence of interdendritic velocity (Figure 3.9 (d)). For this reason, the permeability, PDAS, and interdendritic velocity must be modelled with extreme care to improve the accuracy of results. It must be noted that, the structure of ingot is assumed to be fully columnar in the current study. However, columnar to equiaxed transition (CET) is quite common for ESR ingots of super alloys such as Ni-based alloy [174]. Therefore, it is essential to include CET in future models for large scale ESR process.

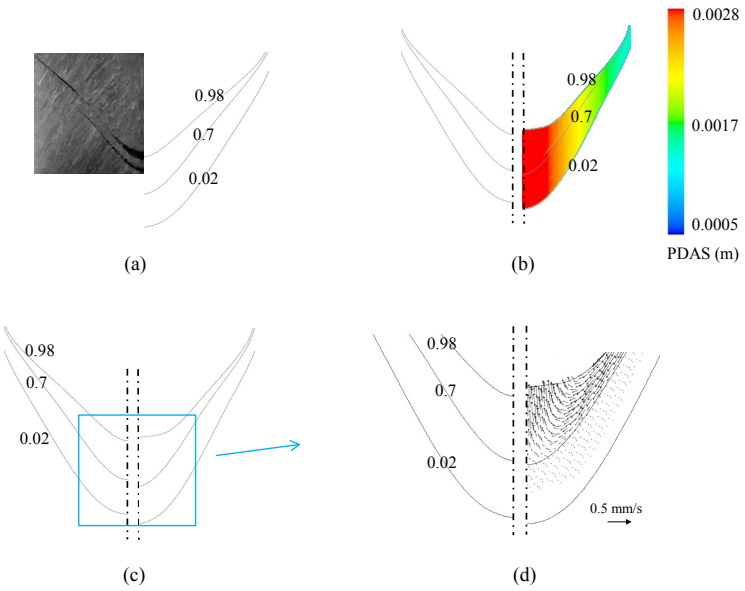

Figure 3.9. (a) Comparison of the experimental (left) result of the shape of the melt pool with the numerical (right) one when PDAS is assumed constant (~ 300 μm), (b) Distribution of the calculated PDAS inside the mushy zone, (c) shapes of melt pool predicted with a constant (left) PDAS vs. variable (right) PDAS, (d) interdendritic melt flow with a constant (left) PDAS vs. variable (right) PDAS.

3.5 Slag-pool interface movement

Here, the influence of movement of slag–pool interface on the electromagnetic field in a large scale ESR (~ ϕ 2000 mm ingot) is discussed. A coupled VOF and magnetohydrodynamics (MHD) model is applied to determine the interaction between interface movement and the flow, temperature, and magnetic fields. The current is allowed to flow through the mold. The amount of generated power in the whole system is tracked during a short period of time (~ 20 s). Here, the conditions are very similar to the start of the process after power interruption where the electric current initially flows. Impacts of movement of interface on the total generated power can be divided to two categories. Initially, the movement is very chaotic (transient) that results in strong variation in the generated power. Then, the interface moves smoothly when the generated power is slightly oscillating over an averaged value (steady) as shown in Figure 3.10.

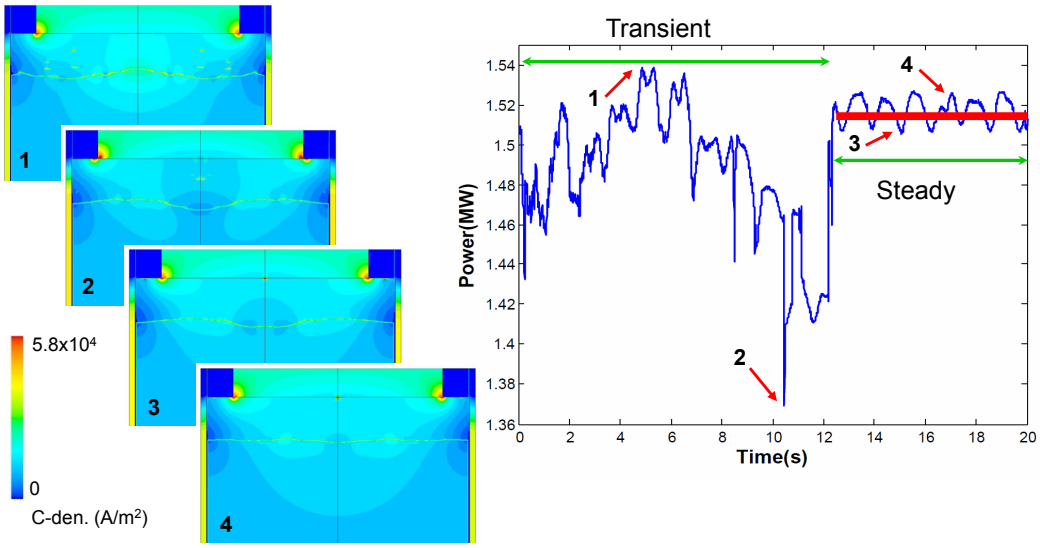

Figure 3.10. (left) Contour of current density at different times : (1) *t*= 5 s, (2) *t*= 11 s, (3) *t*= 15 s, (4) *t*= 17 s; (right) Total generated power is plotted versus time.

Therefore, the shape of the interface strongly influences the total generated power. Consider that, the amount of electrical resistance in the slag is dependent on the height of slag cap as well the cross section area. In other word, a convex shape of interface results in decreasing

the total area and consequently increasing the total resistance and total generated power (snapshot 1). In contrast, a concave shape of interface leads to increasing the total area and consequently decreasing the total resistance and total generated power (snapshot 2). Note that, high frequency power fluctuations observed in the process is due to movement of slag-air interface which is not included in the current simulation.

3.6 Electrode change

The features of electrode change technology were described in section 2.3.1. The technology is used to produce very large heavy ingots in which a number of electrodes are remelted one after another during the ESR process. Preparing the new electrode for remelting requires a certain period of time when the electric current is stopped (power off). Here, CFD simulation is used to study the behavior of a large scale ESR process during the electrode change (power off). First, the process is simulated before electrode change, and temperature, velocity, and electromagnetic fields are obtained (ϕ 1979 mm ingot). Afterwards, the following conditions are imposed on the system during the first step of electrode change (power off). The electric current is stopped flowing through the system, thus the Lorentz force and Joule heating are vanished . The electrode melting is ceased (no droplets), and subsequently the casting velocity is changed to zero. Additionally, the whole slag surface is considered to be exposed to the air.

Sequences of flow, temperature, and solidification during the first step of electrode change (power off) are illustrated in Figure. 3.11. The pool profile is slightly influenced near the mold wall where the cooling rate is large. However, the flow distribution is totally altered. During power interruption, the flow is completely driven by buoyance force results in counter-clock wise rotation of flow (diverging flow) in the slag. Furthermore, the magnitude of velocity decreases in the bulk as the time proceeds whereas the flow is still

strong near the mold wall due to thermal buoyancy. The temperature response is observed to be much slower than flow response to the power interruption. Based on the simulation result, a minor impact on the pool profile is observed during power interruption. Details of analysis are more fully discussed in [132].

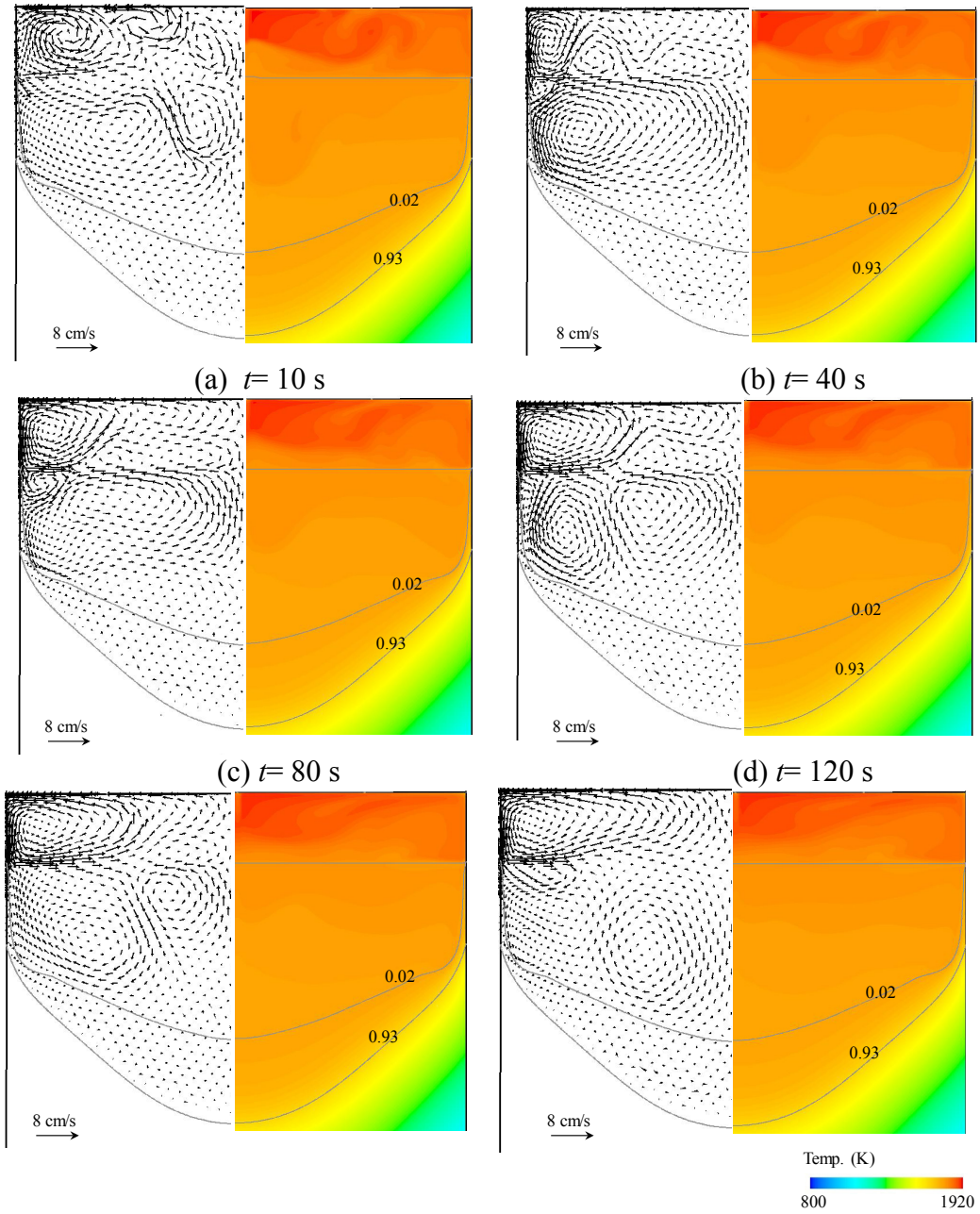

Figure 3.11. Sequences of dynamic change of thermal and velocity fields at different times during power off: (a) t= 10 s, (b) t= 40 s, (c) t= 80 s, (d) t= 120 s, (e) t= 150 s, (f) t= 175 s, Left: vectors of velocity, Right: contour of temperature overlaid with isolines of solid fraction.

3.7 Melting of an ESR electrode

Melting parameters of ESR process such as melt rate and immersion depth of electrode are of great importance. An advanced dynamic mesh based simulation framework was developed to model melt rate and shape of electrode for a laboratory scale ESR process (ϕ 80 mm electrode and ϕ 160 mm mold). The modeling results are validated against an experiment [61]. Details of the modeling approach and assumptions as well as several examples are given in [106, 113]. Transient behavior of melting process considering interactions between flow field, temperature field, electromagnetic field, and shape of electrode was studied. The evolution of electrode shape as well as electric potential, temperature, and velocity fields are illustrated in Figure 3.12. Additionally, the mesh resolution near moving–deforming boundary (electrode tip–slag interface) is shown. The magnitude of voltage drop and subsequently power generation is strongly dependent on immersion depth of electrode (maximum distance between electrode tip and slag–air interface).As a result of higher voltage drop at lower immersion depth, the power generation increases in the system. Consequently, the temperature rises in the slag at low immersion depth as shown in Figure 3.12 (c). Furthermore, the velocity is increased under the shadow of electrode at higher immersion depth as shown in Figures 3.12 (d) through (f). At larger immersion depth, the current density increases under the electrode that intensifies the Lorentz force. Thus, the velocity becomes higher in central region of slag where stirring is promoted and the temperature field is relatively uniform. The evolutions of immersion depth, melt rate, and power generation are plotted in Figure 3.13. The results reveal that variation in power is much gentler than the variation of melt rate. In other words, the melt rate can dramatically change although the power generation remains relatively stable before reaching the steady state (> 900 seconds).

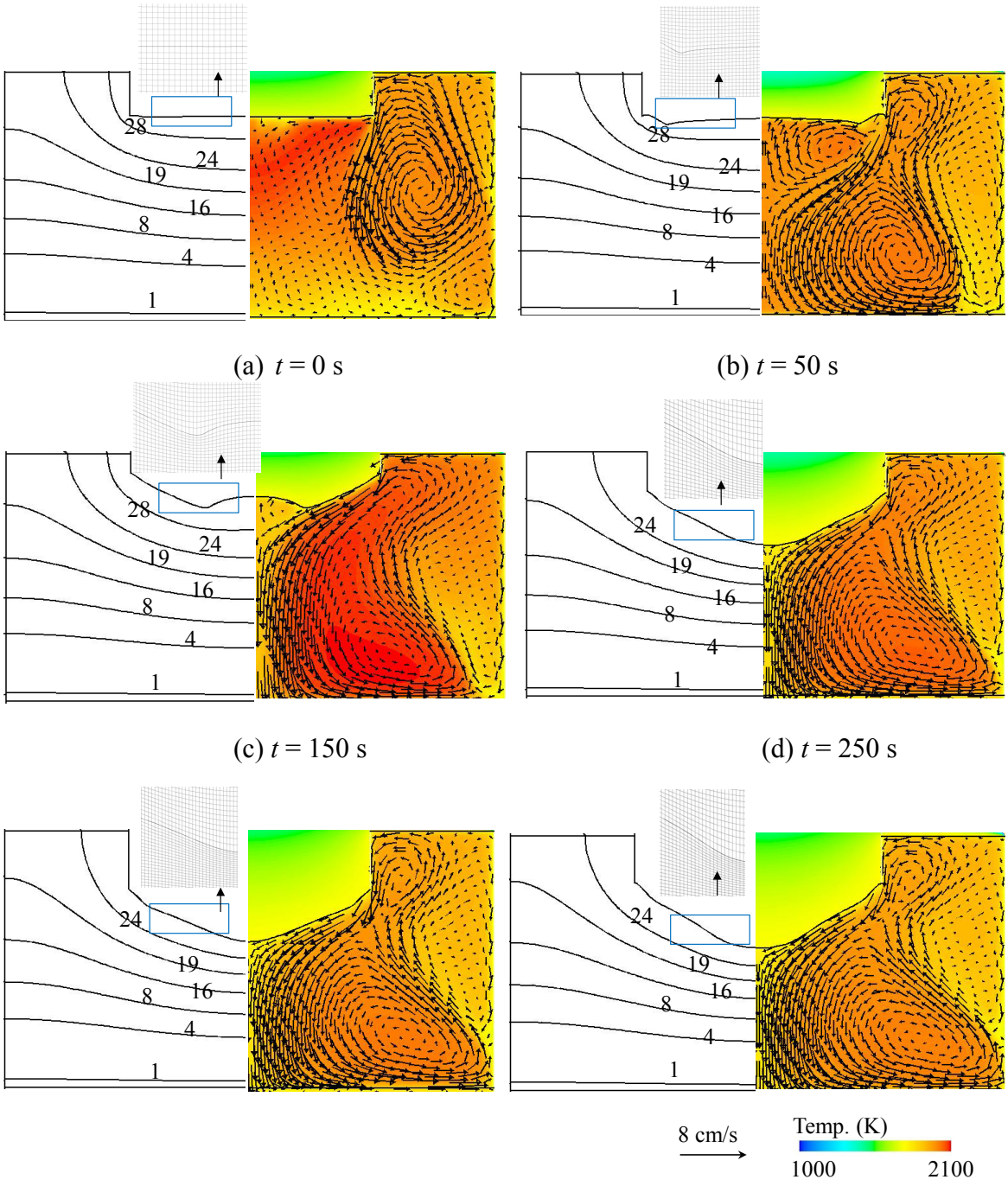

Figure. 3.12. Evolution of shape of electrode tip: (a) t=0, (b) t=50 s, (c) t=150 s, (d) t=250 s, (e) t=650 s, (f) t=1000 s. On left half: isolines of voltage, and the grid node near the moving boundary (electrode tip). On right half: contour of temperature overlaid with the vectors of velocity in the slag region.

Furthermore, the peak is observed in the power generation when the immersion depth becomes very shallow. Essentially, power generation and immersion depth oppose each

other (Figures 3.13). In other words, the power generation is higher at lower immersion depth and vice versa. The physicochemical properties of the slag such as electric conductivity and thermal conductivity can significantly influence the shape of electrode tip, immersion depth and melt rate (see [106]) as shown in Figure 3.14.

The melt rate, immersion depth, and shape of electrode tip are interdependent parameters of the process. Furthermore, the ratio of power generation to melt rate, called power consumption, is an important factor to determine the shape of electrode. It is observed that the shape of electrode remains almost the same when the ratio is kept constant.

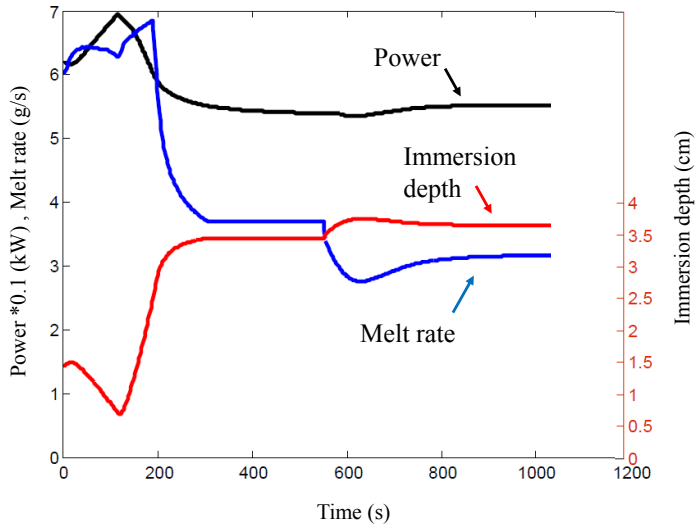

Figure 3.13. Analysis of melting parameters: generated power, melt rate, and immersion depth of electrode.

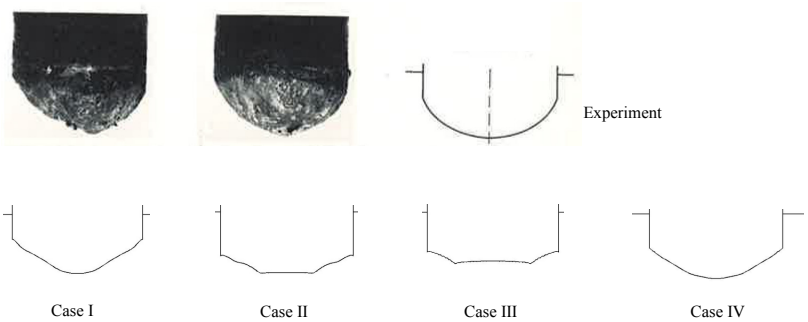

Figure 3.14. Shape of electrode tip observed in experiment conducted (upper row) by Tacke and Schwerdtfeger [61], numerically simulated shapes of electrode tip of different case studies (bottom row).

3.8 Miscellaneous

Some of our studies and modeling results are not presented in this dissertation due to the commercial reasons. It is to be hoped that they will be published in the future.

- The major topic is formation, thickness and composition of the slag skin layer. We developed a one-dimensional model coupled with temperature and flow fields to predict the thickness of slag skin layer along the mold wall. Furthermore, several slag skin samples were experimentally analyzed to study the influence of process operational parameters on the compositions of species, formation and thickness of skin layer.

- The entire electrode change procedure is not only the first step (power off). The procedure also includes heating of the new electrode until reaching melting temperature (second step) and remelting of the electrode until reaching the target melt rate (third step). Generally, those steps take much longer time (~ 30 min) compared to the first step (power off). During second and third steps, operation conditions of process such as input power or melt rate are dynamically changing. The second and third steps of electrode change procedure were also numerically investigated.

- The electroslag rapid remelting process (ESRR) was developed to produce small ingots such as billets at high casting speed. A fully coupled 2D axisymmetric model including calculations of flow, temperature, and electromagnetic fields in the ESRR was established. In addition, simulation results were validated against the experiment.

4 Future prospects

Not only the new technologies such as CCM or ESRR, but also several phenomena involved in the original ESR process require further study.

- The role of droplets in the flow, temperature, and global electromagnetic field is crucial. A number of experimental investigations were published on this topic. Campbell [175] studied the role of droplets in remelting of an aluminum-copper alloy in the ESR using a transparent slag composed of LiCl-KCl eutectic (ratio in %mol. 59:41). The variation of electric potential during formation and departure of one droplet was reported. Makropoulos et al. [176] studied remelting of low melting point metals such as zinc, lead, and aluminum during ESR in presence of an external horizontal magnetic field. It was observed that droplets move toward the mold wall. Kojima et al [177] studied the size and weight of falling droplets made of pure iron or carbon steel in a laboratory scale DC ESR process. Korousic [178] investigated influences of process parameters such as melt rate on droplet formation and frequency of detachment in the ESR process. Recently, Kharicha et al [179] developed a 3D multiphase VOF-MHD coupled model to study the electric signal during formation and departure of one single droplet. The model is computationally extremely expensive which cannot be applied to study large scale systems where multiple droplets form and detach. Therefore, it is required to develop volume-averaged models which can efficiently describe the overall effects of droplets on flow, temperature, and magnetic fields for large scale ESR systems.

- Distribution, type and size of inclusions in the final ingot are of great interest. It is necessary to establish advanced models in which the coupling between behavior of inclusions and MHD phenomena in the slag and melt pool is taken into account. The

future model must enable us to study the influence of operational parameters such as applied AC frequency or the composition of slag on the behavior of inclusions.

- Investigation on the probability of formation of macrosegregation or gas evolution in the ESR [180] requires further attention. The proposed models to calculate macrosegregation in the ESR are rather simple because of using the enthalpy-porosity model of solidification [101, 103]. The interdendritic velocity that dominantly influences the formation of macrosegregation in the ingot cannot be accurately modeled using permeability laws. In the future, applying volume-averaged models such as two-phase, three-phase or five-phase models to predict growth of columnar or equiaxed dendrites can give us valuable insight into segregation phenomena in the ESR [181-183]. Furthermore, the columnar to equiaxed transition (CET) phenomenon that was commonly observed in production of Ni based alloys through ESR needs further investigation.

- The shrinkage of ingot during solidification in the ESR and formation of air gap between ingot and mold have a significant effect on the efficiency of mold cooling system, and consequently on the internal and surface quality of the final product. It is crucial to develop an accurate coupled model considering interactions between flow, temperature, and electric current distributions in the whole process together with shrinkage of the ingot.

- Finally, the proposed species transport models in the past to describe the involved chemical and electrochemical reactions were uncompleted. It is essential to develop species transport models coupled with MHD phenomena to understand the role of operational parameters on the efficiency of purification in the ESR process.

5 Summary

In this dissertation, the ESR model that has been developed by Abdellah Kharicha in Montanuniversität Leoben since 2005 has been extended to improve our knowledge of the impacts of key operational parameters on the ESR process. The transport phenomena including fluid flow, heat transfer and electromagnetism in different size from a laboratory benchmark to very large industrial scale were investigated. A summary of main conclusions are drawn as follow:

1. A full scale 3D numerical model was developed for an industrial ESR process (ϕ 750 mm ingot) to examine the validity of axisymmetric assumption for the ESR process.

   - The flow in the slag and melt pool was found to be completely chaotic and spatially disordered. A statistical analysis of the flow was performed in which the velocity field was decomposed to mean and fluctuation velocities. The fluctuations were observed to be very strong under the electrode, near the mold wall, and near slag-pool interface. However, a relatively axisymmetric pattern of fluctuations was observed.
   - Despite the 3D chaotic flow in the whole process, the shape of melt pool (profile of the solidifying mushy zone of the ingot) was found to be firmly steady and axisymmetric. Therefore, using axisymmetric assumption to model the pool profile of steel ingot at industrial scale is valid.
   - Numerical results were verified by the experiment [163], and a very good agreement was observed between the modeling results and the experiment.

2. The electromagnetic field was solved in the whole process including electrode, slag, ingot, and mold considering a 2D axisymmetric model for an industrial scale ESR process (ϕ 750 mm ingot)

- By applying AC current (0, 5, and 50 Hz), the electromagnetic skin effect in the electrode, ingot, and mold was predicted. Furthermore, the ratio of mold current (electric current crosses the slag skin and flows through the mold) to total current is found to be independent of applied frequency when other parameters of the process were kept invariant (e.g. constant slag skin thickness, constant slag cap height, etc.).
- With the increase of the height of slag cap, the ratio of mold current to total current increased.
- Opening the path to the mold (mold current) causes a noticeable decrease in the overall electrical resistance of the process.
- The ratio of mold current to total current is dependent on the mold type. At similar operational condition, the ratio for an isolated (short collar) mold is smaller than the ratio for a live (static) mold.
- Eddy currents could propagate from the mold to the ingot in the contact region when the process was operated under AC current using an isolated mold.

3. The effects of applied AC frequency and electrical conductivity of slag (solid and liquid) on the current path and consequently flow and temperature fields as well as solidification of the ingot were studied. The flow, temperature, and electromagnetic field were solved in the whole process including electrode, slag, ingot, and mold considering a 2D axisymmetric model for an industrial scale ESR process (ϕ 1823 mm ingot).

- The electric current changes its direction when it passes the slag-pool interface, and so does the Lorenz force. As a consequence, it influences the hydrodynamic behavior of the slag and melt pool near the slag-pool interface.
- Assuming Ohmic conduction in the slag, the distributions of Joule heating and Lorentz force in the slag region are quite independent of the applied frequency.

- A large amount of Joule heating can be released in the slag skin layer. As a consequence, the slag skin partially melts and becomes thinner that is in favor of producing ingots with good surface quality.
- Distribution patterns of the Lorentz force and Joule heating in the slag region are significantly influenced by the mold current, especially near the mold wall.
- Mold current promotes stirring that results in a relatively uniform temperature in the slag region.
- Mold current increases the standing height (liquid head) of the melt pool.

4. The effect of crystal morphological parameters such as permeability and primary dendrite arm space (PDAS) in the solidifying mushy zone were studied. The flow, temperature, and electromagnetic field were solved including a conductive short collar mold for an industrial scale ESR process (ϕ 750 mm ingot).

   - Essentially, the interdendritic flow is controlled by the permeability that strongly depends on the PDAS. Different interdendritic melt flow and different shape of the melt pool were predicted by variation in the PDAS.
   - The pool profile of the ingot is strongly influenced by the velocity of melt inside the mushy zone even though the interdendritic velocity is significantly smaller than the velocity in the melt pool or slag. For this reason, the permeability, PDAS, and interdendritic velocity must be modelled with extreme care to improve the accuracy of modeling results.

5. The effect of movement of slag-pool interface on the total generated power was studied. The flow, temperature, and electromagnetic field were solved including a conductive static mold considering a 2D axisymmetric multiphase model coupled with VOF for an industrial scale ESR process (ϕ 2000 mm ingot).

- The movement of interface can significantly influence the electrical resistance and subsequently generated power. A chaotic movement leads to a strong variation, whereas a smooth movement results in a slight oscillation over an averaged value of generated power.
- The shape of the interface influences the power generation since the resistance in the slag depends on the cross section area where the electric current enters. In other words, a convex shape of interface results in decreasing the total area (increasing generated power), and a concave shape results in increasing the total area (decreasing generated power).

6. The entire electrode change procedure was numerically modeled, but only results of the first step of electrode change (power off) were presented for commercial reasons. The flow, temperature, and electromagnetic fields were solved in the whole process considering a 2D axisymmetric multiphase model coupled with VOF for an industrial scale ESR process (ϕ 1979 mm ingot).

   - The behavior of system during electrode change including flow, and temperature fields were tracked. The flow was completely altered since it was driven only by buoyancy force during the power off step. However, the temperature response was observed to be much slower than the flow response to the power interruption.
   - No significant change in the pool profile of the ingot was observed during the short time of power off (< 5 min).

7. Influences of physicochemical properties of the slag such as thermal and electrical conductivities on the melt rate, shape, and immersion depth of electrode were studied. The flow, temperature, and electromagnetic field were solved in the whole process considering a 2D axisymmetric model coupled with dynamic mesh technique for a laboratory scale ESR process (ϕ 80 mm electrode and ϕ 160 mm ingot).

- The dynamic mesh-based approach was proved to be a successful method to model the electrode shape. The simulation results agree with the experimental fact that with the increase of melt rate, the immersion depth decreases when the magnitude of imposed current is kept constant.
- The ratio of power generation to melt rate, called power consumption, is an important factor to determine the shape of electrode. The shape of electrode remains almost the same when the ratio is kept constant.
- The voltage drop and subsequent power generation in the system are governed by both immersion depth and shape of electrode tip. Similar power generation was observed for systems where the shapes of tip and immersion depth were different. Therefore, the melt rate, immersion depth, and shape of electrode tip are interdependent parameters.
- The electrical conductivity of slag (liquid and solid) mainly influences the electric current path which impacts the velocity and temperature distribution in the process. As a consequence of different electric current paths, the power generation, melt rate, and shape of electrode are significantly influenced.
- The thermal conductivity of slag determines the efficiency of global heat transfer in the process. Increasing thermal conductivity of slag will result in decreasing melt rate.

Aiming at developing well-directed mathematical models for the ESR process, the following topics are of great interest for future research: the behavior of inclusions; the global impact of droplets; solidification aspects such as macrosegregation, CET, and gas evolution; shrinkage of ESR ingot; mass transfer including chemical and electrochemical reactions. Additionally, models should also be adapted for new technologies such as ESRR, CCM, etc.

6 References

[1] N. G. Slavyanov, Electrical metal casting, SPB, 1892.

[2] W. E. Duckworth and G. Hoyle, Electro-slag refining, Chapman and Hall publisher, 1969.

[3] P. A. E. Armstrong, Method of forming alloys, U.S. Patent No. (1,781,490), 1930.

[4] W. A. McKeen, L. G. Joseph, and D. M. Speher, Melting alloys by the Hopkins process, Met. Prog., 1962, vol. 82, p. 86

[5] G. Hoyle, Electroslag Processes, Applied Science Publishers, 1983.

[6] R. H. Nafziger, The electroslag melting process , U.S. Bureau of Mines, 1976.

[7] B. I. Medovar and G.A. Boyko, Electroslag technology, Springer-Verlag publisher, 1991.

[8] G. Hoyle, Surface phenomena in ESR, in: 6th Int. Vac. Metall. Conf. on Special Melting, 1979, San Diego, p. 624

[9] E.J. Pickering, Macrosegregation in Steel Ingots: The Applicability of Modelling and Characterization Techniques, ISIJ Int., 2013, vol. 53, p. 935.

[10] K. O. Yu, J. A. Domingue, G. E. Maurer, H. D. Flanders, Macrosegregation in ESR and VAR process, JOM,1986, vol. 38, p. 46.

[11] S. Kou, Macrosegregation in electroslag remelted ingots, Ph.D. Thesis, MIT, 1978.

[12] Y. M. Shash, T. E. Gammal, M. A. EL Salamoni, and F. A. Denkhaus, Improving solidification pattern of ESR ingots combined with energy saving, Steel Res., 1988, vol. 59 (6), p. 269.

[13] A. Mitchell, Electroslag and vacuum arc remelting processes, AIME, Iron and Steel Society, 1985.

[14] A. Mitchell, R. M. Smailer, Practical aspects of electroslag remelting technology, Int. Met. Rev., 1979, No. 5 and 6, p. 231.

[15] J. M. Sathaye, Aspects of mould design in electroslag casting, M. Sc. Thesis, UBC, 1977.

[16] H. Holzgruber, ESRR-electroslag rapid remelting, a novel technology for the production of high quality near net shaped billets and blooms, PhD thesis, MU Leoben, 2005.

[17] M. E. Peover, Electroslag remelting: a review of electrical and electrochemical aspects, J. Inst. Metals, 1972, vol. 100, p.97.

[18] A. Mitchell, The chemistry of ESR slags, Canadian Metallurgical quarterly, 1981, vol. 20 (1), p. 101.

[19] M. Allibert, H. Gaye, J. Geiseler, D. Janke, B. J. Keene, D. Kirner, M. Kowalski, J. Lehmann, K. C. Mills, D. Neuschütz, R. Parra, C. Saint-Jours, P. J. Spencer, M. Susa, M. Tmar, E Woermann, Slag Atlas, Verlag Stahleisn GmbH, 1995.

[20] W. W. Smeltzer, Z. A. Foroulis, Metal-Slag-Gas reactions and processes, Electrochemical society publisher, 1975.

[21] M. Etienne, The loss of reactive elements during electroslag processing of iron-based alloys, PhD Thesis, UBC, 1971.

[22] G. Patlesky, H. Blele, and H. J. Flelscher, The reactions of titanium and silicon with Al_2O_3-CaO-CaF_2 slags in the ESR process, J. Vac. Sci. Tech. , 1972, vol. 9 (8), p. 1318.

[23] M. Allibert, J. F. Wadier, and A. Mitchell, Use of SiO_2 containing slags in electroslag remelting, Ironmak. steelmak., 1978, No. 5, p. 211.

[24] A. Mitchell, M. Hilborn, E. Samuelsson, and A. Kanagawa, The magnesium problems in superalloys, Superalloy, 1988, p. 407.

[25] C. B. Shi, J. Li, J. W. Cho, F. Jiang, and I. H. Jung, Effect of SiO_2 on the crystallization behaviors and in-mold performance of CaF_2-CaO-Al_2O_3 slags for drawing-ingot.type electroslag remelting, Metall. Mater. Trans. B., 2015, DOI: 10.1007/s11663-015-0402-2.

[26] K.C. Mills and B.J. Keene, Physicochemical properties of molten CaF_2 –based slags, Int. Met. Rev., 1981, vol. 1, p. 21.

[27] Li Zheng Bang Zhu, Electroslag metallurgy theory and practice (in Chinese), publisher unknown, 1991.

[28] J. Korp, R. Rabitsch, R. Schneider, Determination of the specific electrical conductivity of ESR slags containing MgO, in: liquid metal processing and casting (LMPC), 2005, Santa Fe.

[29] J. korp, Einfluss ausgewählter Schlackenkomponenten auf den Energieverbrauch beim Elektroschlacke Umschmelzen (ESU), PhD thesis, MULeoben, 2007.

[30] J. Medved, P. Mrvar, V. Gontarev, F. Kavicka, M. Zdovec, Electrical conductivity of molten slags measured by the new method, in: 11th Int. Metall. Mater. conf. (METAL 2002), 2002, Czech Republic.

[31] M. Hajduk and T.E. Gammal, Schrifttumszusammenstellung von Leitfähigkeitsmessungen an CaF_2-haltigen Schlackenschmelzen, Stahl und Eisen, 1979, vol. 99, p. 113.

[32] T. E. Gammal and M. Hajduk, The electric conductivity of CaF_2-CaO-Al_2O_3 slags, Arch. Eisenhüttenwes, 1978, vol. 49, p. 235.

[33] B. Birol, G. Polat, and M. Saridede, Estimation model for electrical conductivity of molten CaF_2-Al_2O_3-CaO slags based on optical basicity, JOM, 2015, vol. 67 (2), p. 427.

[34] R. Taylor, and K. C. Mills, The thermal conductivity of slags used in electroslag remelting, Arch. Eisenhüttenwes, 1982, vol. 53, p. 55.

[35] A. Mitchell, J. F. Wadier, Some observations on the radiative properties of ESR slags, Canadian metallurgical quarterly, 1981, vol. 20 (4), p. 373.

[36] X. Li, S. Wang, J. Zhao, Y. Cui, and Y. Chen, Changes in physical properties of ANF-6 slag during electroslag remelting process, Adv. Mater. Res., 2011, vol. 239-242, p. 1960.

[37] F. Liu, Z. Jiang, X. Zang, X. Geng, Coupled modeling of electromagnetic, fluid flow, and heat transfer in slag bath during current-conductive mould ESR process, in: liquid metal processing and casting (LMPC), 2009, Santa Fe, p. 213.

[38] K. Wroblewski, B. Dibiaso, J. Fraley, J. Fields, and S. Rudoler, Design of ESR slags according to requested physical properties; part 2: density and viscosity, in: liquid metal processing and casting (LMPC), 2013, Austin, p. 43.

[39] S. Akbari, J. Reitz, B. Friedrich, Thermophysical properties of ESR-electrofluxes (part 1: density), in: liquid metal processing and casting (LMPC), 2009, Santa Fe, p. 243.

[40] A. Mitchell and S. Joshi, The densities of melts in the systems CaF_2-CaO and CaF_2-Al_2O_3, Metall. Trans., 1972, vol. 3, p. 2306.

[41] K. Ogino and S. Hara, Density, surface tension and electrical conductivity of calcium fluoride based fluxes for Electroslag Remelting (in Japanese), 1977, UDC 621.365.3:669.187.26:669.046.587.4

[42] D. Gohil, and K. C. Mills, The heat capacity and enthalpy of fusion of slags used in electroslag remelting , Arch. Eisenhüttenwes, 1981, vol. 52, p. 335.

[43] B. V. Muu, Untersuchung der Grenzflächenspannung zwischen Schlacken des systems CaO- CaF_2-Al_2O_3 und Stahlschmelzen aus 100Cr6 und X85WmoCo6.5.5, Neue Hütte, 1976, Heft 6, p. 335.

[44] B. J. Keene and K. C. Mills, Total normal emissivity of slags used in electroslag remelting, Arch. Eisenhüttenwes, 1981, vol. 52, p. 311.

[45] K.C. Mills, L. Yuan, R.T. Jones, Estimating the physical properties of slags, J. S. Afr. I. Min. Metall., 2011, vol. 111(10), p. 649.

[46] L. Willner, P. Varhegyi, A plant applicable mathematical model of the electroslag refining process, Arch. Eisenhüttenwes. 1976, vol. 47 (4), p. 205.

[47] B. Hernandez-Morales and A. Mitchell, Review of mathematical models of fluid flow, heat transfer, and mass transfer in electroslag remelting process, Ironmak. Steelmak., 1999, vol. 26 (6), p. 423.

[48] M. A. Maulvault, Temperature and heat flow in the electroslag remelting process, PhD thesis, MIT, 1967.

[49] L. F. Carvajal and G. E. Geiger, An analysis of the temperature distribution and the location of the solidus, mushy, and liquidus zones for binary alloys in remelting processes, Metall. Trans.,1971, vol. 2 (8), p. 2087.

[50] A. Mitchell, S. Joshi, and J. Cameron, Electrode temperature gradient in the electroslag process, Metall. Trans., 1971, vol. 2, p. 561.

[51] J. Mendrykowski, J.J. Poveromo, J. Szekely, and A. Mitchell, Heat transfer and the melting process in electroslag remelting: Part I. The behavior of small electrodes, Metall. Trans., 1972, vol. 4, p. 1761.

[52] M. Basaran, R. Mehrabian, T. Z. Kattamis, and M. C. Flemings, A study of the heat and fluid flow in electroslag remelting, Report CTR 74–36, Army Materials and Mechanics Research Center, 1974.

[53] A. H. Dilawari and J. Szekely, A mathematical model of slag and metal flow in the ESR process, Metall. Trans. B, 1977, vol. 8, p. 227.

[54] A. S. Ballantyne and A. Mitchell, Modeling of ingot thermal fields in consumable electrode remelting process, Ironmak. Steelmak.,1977, No. 4, p. 222.

[55] S. D. Ridder, F. C. Reyes, S. Chakravarty, R. Mehrabian, J. D. Nauman, J. H. Chen, and H. J. Klein, Steady state segregation and heat flow in ESR, Metall. Trans. B, 1978, vol. 9, p. 415.

[56] J. Kreyenberg and K. Schwerdtfeger, Stirring velocities and temperature field in the slag during electroslag remelting, Arch. Eisenhüttenwes,1979, vol. 50 (1), p. 1.

[57] M. Choudhary and J. Szekely, The modeling of pool profiles, temperature profiles and velocity fields in ESR systems, Metall. Trans. B, 1980, vol. 11, p. 439.

[58] C. L. Jeanfils, J. H. Chen, H. J. Klein , Modeling of macrosegregation in electroslag remelting of superalloys, Superalloys, 1980, p. 119.

[59] M. Choudhary and J. Szekely, Modeling of fluid flow and heat transfer in industrial-scale ESR system, Ironmak. steelmak., 1981, No. 5, p. 225.

[60] G. Sanchez Sarmiento, E. Vicente, and A. Leyt, in: 2nd Int. Conf. on Numerical methods in thermal problems, 1981, Venice, p. 697.

[61] K.H. Tacke and K. Schwerdtfeger, Melting of ESR electrodes, Arch. Eisenhuüttenwesen, 1981, vol. 52, p. 137.

[62] S. F. Medina and P. de Andres, Electrical field in the resistivity medium (slag) of the ESR process: influence on ingot production and quality, Ironmak. steelmak., 1987, vol. 14, No.3, p. 110.

[63] Y. M. Ferng, C. C. Chieng, and C. Pan, Numerical simulations of electro-slag remelting process, Numer. Heat Trans. A, 1989, vol. 16, p. 429.

[64] A. Jardy, D. Ablitzer, and J. F. Wadier, Magnetohydrodynamics and thermal behavior of electroslag remelting slags, Metall. Trans. B, 1991, vol. 22, p.111.

[65] L. Nastac, S. Sundarraj, and K.-O. Yu, Stochastic modeling of solidification structure in Alloy 718 remelt ingots, Superalloys 718,625,706 and various derivatives, Ed. by E.A. Loria, TMS Publisher, 1997, p. 55-66.

[66] A. Kharicha, A. Ludwig, M. Wu, Shape and stability of the slag/melt interface in a small dc ESR process, Mater. Sci. Eng. A, 2005, vol. 413-414, p. 129.

[67] S. Viswanathan, D. K. Melgaard, A. D. Patel, D. G. Evans, Effect of processing parameters on temperature profiles, fluid Flow, and pool shape in the ESR Process, in: liquid metal processing and casting (LMPC), 2005, Santa Fe.

[68] K. M. Kelkar. and S.V. Patankar, A. Mitchell, Computational modeling of the electroslag remelting (ESR) Process used for the Production of Ingots of High-Performance Alloys, in: liquid metal processing and casting (LMPC), 2005, Santa Fe.

[69] A. D. Patel, An analysis of electromagnetic fields in ESR, in: liquid metal processing and casting (LMPC), 2005, Santa Fe.

[70] W. Yang and J. J. deBarbadillo, Analysis of the thermal stresses in electroslag remelting of large diameter Inconel Alloy 706 ingots, in: liquid metal processing and casting (LMPC), 2005, Santa Fe.

[71] D. Yan-wu, J. Zhou-hua, L. Zheng-bang, Mathematical model for electroslag remelting process, J. of Iron and Steel Res., 2007, vol. 14 (5), p. 7.

[72] A. D. Patel, Effect of electrode pipe and mold current on electromagnetic fields in ESR, in: liquid metal processing and casting (LMPC), 2007, Nancy, p.95.

[73] A. Kharicha, W. Schützenhöfer, A. Ludwig, and R. Tanzer, Multiphase modelling of the slag region in ESR process, in: liquid metal processing and casting (LMPC), 2007, Nancy, p. 107.

[74] A. Kharicha, A. Mackenbrock, A. Ludwig, W. Schützenhöfer, V. Maronnier, M. Wu, O. Köser, R. Tanzer, Selected Numerical Investigations on ESR Process, in: liquid metal processing and casting (LMPC), 2007, Nancy, p. 113.

[75] A. Kharicha, W.Schützenhöfer, A. Ludwig, R. Tanzer, M. Wu, On the importance of electric currents flowing directly into the mold during an esr process, Steel Res. Int., 2008, vol.79, p. 632.

[76] A. Rückert, H. Pfeifer, Mathematical modeling of the flow field, temperature distribution, melting and solidification in the electroslag remelting process, Magnetohydrodynamics, 2009, 45 (4), p. 527.

[77] A. Kharicha, W. Schützenhöfer, A. Ludwig, R. Tanzer, and M. Wu, Reformulation of time averaged Joule heating in presence of temperature fluctuations, Int. J. of Cast Met. Res., 2009, vol. 22(1-4), p. 155.

[78] A. Jardy, and D. Ablitzer, Mathematical modelling of superalloy remelting operations, Mat. Sci. Tech., 2009, vol. 25 (2), p. 163.

[79] V. Weber, A. Jardy, B. Dussoubs, D. Ablitzer, S. Ryberon, V. Schmitt, S. Hans, and H. Poisson, A comprehensive model of the electroslag remelting process: description and validation, Metall. Trans. B, 2009, vol. 40, p. 271.

[80] A.D. Patel, M. Gierula, D. J. Tallman, Bounds on model parameters for computational analysis of the ESR process, in: liquid metal processing and casting (LMPC), 2009, Santa Fe, p. 201.

[81] A. Kharicha, W. Schützenhöfer, A. Ludwig, R. Tanzer, Numerical and experimental investigation on the ESR process of the hot work tool steel H11, in: liquid metal processing and casting (LMPC), 2009, Santa Fe, p. 235.

[82] A. Kharicha, W. Schützenhöfer, A. Ludwig, and G. Reiter, Influence of the slag/pool interface on the solidification in an electroslag remelting process, Mat. Sci. Forum, 2010, vol. 649, p 229.

[83] A. Kharicha, A. Ludwig, M. Wu, 3D simulation of the melting during an electroslag remelting process, in: EPD Congress, 2011, San Diego, p. 771.

[84] A. Kharicha, A. Ludwig, and M. Wu, Thermal state of electrode during the electroslag remeltinng process, in: liquid metal processing and casting (LMPC), 2011, Nancy, p. 73.

[85] A. D. Patel, Electrode immersion depth effects in the ESR process, in: liquid metal processing and casting (LMPC), 2011, Nancy, p. 49.

[86] M. J. M. Krane, M. Fahrmann, J. Yanke, E. Escobar de Obaldia, K. Fezi, and J. Busch, A comparison of predictions of transport phenomena in electroslag remelting to industrial data, in: liquid metal processing and casting (LMPC), 2011, Nancy, p. 65.

[87] A. Kharicha, A. Ludwig, and M.Wu, Droplet formation in small electroslag remelting process, in: liquid metal processing and casting (LMPC), 2011, Nancy, p. 113.

[88] A. Kharicha, M. Wu, A. Ludwig, M. Ramprecht, H. Holzgruber, Influence of the frequency of the applied AC current on the electroslag remelting process, CFD Modeling and Simulation in Materials, Wiley Interscience, 2012, p. 139.

[89] A. Kharicha, J. Korp, M. Wu, A. Ludwig, Investigations on the Origin of Radial Distribution of Non Metallic Inclusions in ESR ingot, in: CLEANSTEEL8, 2012, Budapest, p. 145.

[90] B. Li, F. Wang, and F. Tsukihashi, Current, magnetic Field and Joule heating in electroslag remelting processes, ISIJ Int., 2012, vol. 52 (7), p. 1289.

[91] J. Yanke, K. Fezi, Mike Fahrmann, M. J. M. Krane, Predicting melting behavior of an industrial electroslag remelting ingot, in: liquid metal processing and casting (LMPC), 2013, Austin, p.47.

[92] M. Hugo, B. Dussoubs, A. Jardy, J. Escaffre, H. Poisson, Impact of the solidified slag skin on the current distribution during electroslag remelting, in: liquid metal processing and casting (LMPC), 2013, Austin, p.79.

[93] K. M. Kelkar, S. V. Patankar, S. K. Srivatsa, R. S. Minisandram, D. G. Evans, J. J. deBarbadillo, R. H. Smith, R. C. Helmink, A. Mitchell, H. A. Sizek, Computational modeling of electroslag remelting (ESR) process used for the production of high-performance alloys, in: liquid metal processing and casting (LMPC), 2013, Austin, p.3.

[94] A. Kharicha, M. Wu, and A. Ludwig, Variation of the resistance during the electrode movement in the electroslag remelting process, in: liquid metal processing and casting (LMPC), 2013, Austin, p. 145.

[95] L. Rao, J.-h. Zhao, Z.-x. Zhao, G. Ding, M.-P. Geng, Macro- and Microstructure evolution of 5 CrNiMo Steel ingots during electroslag remelting process, J. Iron Steel Res., 2014, vol. 21 (7), p. 644.

[96] Q. Wang, Z. He, B. LI, and F. Tsukihashi, A General Coupled Mathematical Model of Electromagnetic Phenomena, Two-Phase Flow, and Heat Transfer in Electroslag Remelting Process Including Conducting in the Mold, Metall. Trans. B, 2014, vol. 45, p. 2425.

[97] B. Li, Q. Wang, F. Wang, and M. Chen, A Coupled Cellular Automaton–Finite-Element Mathematical Model for the Multiscale Phenomena of Electroslag Remelting H13 Die Steel Ingot, JOM, 2014, vol. 66 (7), p.1153.

[98] M. Eickhoff, N. Giesselmann, A. Rückert, H. Pfeifer, J. Tewes, J. Klöwer, Introduction an analytic approach on air gap formation during the ESR/VAR process and numerical validation, in: 2nd Int. Conf. on Ingot Casting, Rolling, and Forging, Milan, 2014.

[99] J. Yanke, K. Fezi, R. W. Trice, and M. J. M. Krane, Simulation of slag-skin formation in electroslag remelting using a Volume-Of-Fluid method, Num. Heat Transfer A, (2014), vol. 67 (3), p. 268.

[100] A. Kharicha, M. Wu, and A. Ludwig, On melting of electrodes during electro-slag remelting, ISIJ Int., 2014, vol. 54, p. 1621.

[101] Q. Wang, F. Wang, B. Li, and F. Tsukihashi, A Three-Dimensional Comprehensive Model for Prediction of Macrosegregation in Electroslag Remelting Ingot, ISIJ Int., 2015, vol. 55 (5), p. 1010.

[102] X. Wang and Y. Li, A comprehensive 3D mathematical model of the electroslag remelting process, Metall. Trans. B, 2015, DOI: 10.1007/s11663-015-0342-x.

[103] K. Fezi, J. Yanke, and M. J. M. Krane, Macrosegregation during electroslag remelting of Alloy 625, Metall. Trans. B, 2015, vol. 46, p. 766.

[104] N. Giesselmann, A. Rückert, M. Eickhoff, H. Pfeifer, J. Tewes and J. Klöwer, Coupling of Multiple Numerical Models to Simulate Electroslag Remelting Process for Alloy 718, ISIJ Int., 2015, vol. 55 (7), p. 1408.

[105] E. Karimi-Sibaki, A. Kharicha, M. Wu, A. Ludwig, H. Holzgruber, B. Ofner, M. Ramprecht, A numerical study on the influence of the frequency of the applied AC current on the electroslag remelting process, in: liquid metal processing and casting (LMPC), 2013, Austin, p.13.

[106] E. Karimi-Sibaki, A. Kharicha, J. Bohacek, M. Wu, A. Ludwig, A dynamic mesh-based approach to model melting and shape of an ESR electrode, Metall. Trans. B, 2015, vol. 46, p. 2049.

[107] K. Preis, I Bardi, O. Biro, C. Magele, W. Renhart, K. R. Richter, G. Vrisk, Numerical analysis of 3D magnetostatic fields, IEEE Trans. on Magnetics, 1991, vol. 27, p. 3798.

[108] H. Song and N. Ida, An eddy current constraint formulation for 3D electromagnetic field calculation, IEEE Trans. on Magnetics, 1991, vol. 27, p. 4012.

[109] A. Kharicha, E. Karimi-Sibaki, M. Wu, A. Ludwig, Contribution of the mould current to the ingot surface quality in the electroslag remelting process, in: Liquid metal processing and casting conference (LMPC), 2013, Austin, p. 95.

[110] A. S. Ballantyne, Heat flow in consumable electrode remelted ingots, PhD thesis, 1978, UBC.

[111] R. Mehrabian, M. Keane, and M. C. Flemings, Interdendritic fluid flow and macrosegregation; influence of gravity, Metall. Trans. B, 1970, vol. 1. p. 1209.

[112] W. Kurz, B. Giovanola, and R. Trivedi, Theory of microstructure development during rapid Solidification, Acta. Metall., 1986, vol.34, p. 823.

[113] A. Kharicha, E. Karimi-Sibaki, J. Bohacek, M. Wu, A. Ludwig, Transient melting of an ESR electrode, ín: Liquid metal processing and casting conference (LMPC), 2015, Leoben, p. 111.

[114] A. Mitchell, Oxide inclusion behavior during consumable electrode remelting, Ironmak. Steelmak., 1974, No. 3, p. 172.

[115] D. A. R. Kay and R. J. Pomfret, Removal of oxide inclusions during AC electroslag remelting, J. Iron Steel Inst., 1971, p. 962.

[116] N. Q. Minh and T. B. King, The contribution of electrochemical reactions to sulfur transfer from electrode to slag in electroslag remelting, 1979, Metall. Trans. B, pp. 623-629.

[117] M. Kato, K. Hasegawa, S. Nomura, M. Inouye, Transfer of oxygen and sulfur during direct current electroslag remelting, Trans. ISIJ, 1983, vol. 23, p. 618.

[118] M. Kawakami, T. Takenaka, and M. Ishikawa, Electrode reactions in dc electroslag remelting of steel rod, Ironmak. Steelmak., 2002, vol. 29 (4), p. 287.

[119] M. Kawakami , K. Nagata , M. Yamamura , N. Sakata, Y. Miyashita, and K. S. Goto, Profiles of temperature, voltage and local heat generation in slag phase and metal pool of ESR unit under operation, Testsu-to-Hagane,1977, vol. 63, p. 220.

[120] A. Mitchell and G. Beynon, Electrode polarization in the DC electroslag melting of pure iron, Metall. Trans., 1971, vol. 2, p.3333.

[121] A. Mitchell and J. Cameron, The electrical conductivity of some liquids in the system CaF_2+CaO+Al_2O_3, Metall. Trans., 1971, vol. 2, p.3361.

[122] M. Etienne, The loss of reactive elements during electroslag processing of iron-base alloys, PhD Thesis, UBC, 1970.

[123] N. Nowack, K. Schwerdtfeger, and D. Krause, Some observations on current transfer at iron/calcium fluoride electrodes. Model experiments for current transfer in the ESR process, Arch. Eisenhüttenwes. 1982, vol. 53 (12), p. 463.

[124] R. Prange, K. Heusler, and K. Schwerdtfeger, Charge transfer at Fe/FeO (CaF_2) electrodes at 1450 °C: Exchange current density, electrode capacitance, diffusivity. Metall. Trans. B, 1984, vol. 15, p. 281.

[125] K. Schwerdtfeger, W. Wepner, and G. Pateisky, Modeling of chemical reactions occuring during electroslag remelting: oxidation of titanium in stainless steel, Ironmak. steelmak., 1978, No. 3, p. 135.

[126] M. E. Fraser and A. Mitchell, Mass transfer in the electroslag process: Part 1: mass transfer model, Ironmak. steelmak., 1976, No. 5, p. 279.

[127] M. E. Fraser and A. Mitchell, Mass transfer in the electroslag process: Part 2: mass transfer coefficients, Ironmak. steelmak., 1976, No. 5, p. 288.

[128] E. Karimi-Sibaki, A. Kharicha, M. Wu, A. Ludwig, A numerical study on electrochemical transport of ions in calcium fluoride slag, in: Liquid metal processing and casting conference (LMPC), 2015, Leoben, p.163.

[129] W. Holzgruber, C. Kubisch, and H. H. Jaeger, Einfluss der Umschmelzbedingungen auf die Makro – und Mikrostruktur elektroschlacke umgeschmolzener Blöcke unter besonderer Berücksichtigung der Verhältnisse beim Elektrodenwechsel, Neue Hütte, 1971, vol. 16, p. 606.

[130] L. I. Matushkina, M. Klyuver, L.A Dedushev, L. L. kosyrev, S.E. Volkov, and A. A. Sharapov, S.b. Tr. Tsent. Nauch-Issted. Inst Chern. Met. , in Russian, 1970, vol. 75, p. 167.

[131] R.O. Jackson, A. Mitchell, and J. Luchok, An examination of electrode-change practice in electroslag remelting, J. Vac. Sci. Tech., 1972, vol. 9 (6), p. 1301.

[132] E. Karimi-Sibaki, A. Kharicha, M. Wu, A. Ludwig, H. Holzgruber, B. Ofner, A. Scheriau, M. Kubin, M. Ramprecht, An attempt to model electrode change during the ESR process, in: Liquid metal processing and casting conference (LMPC), 2015, Leoben, p.61.

[133] B. Li, B. Wang, and F. Tsukihashi, Modeling of electromagnetic field and liquid metal pool shape in an electroslag remelting process with two series-connected electrodes, Metall. Trans B, , 2014, vol. 45, p. 1122.

[134] Y. Dong, Z. Jiang, H. Liu, R. Chen, and Z. SONG, Simulation of multi-electrode ESR process for manufacturing large ingot, ISIJ Int., 2014, vol. 52 (12), p. 2226.

[135] D. Alghisi, M. Milano, L. Pazienza, From ESR to continuous CC-ESRR process: development in remelting technology toward better products and productivity, in: 2nd Int. Conf. on New Develop. in Metall. Proc. Tech., 2005, Riva del garda.

[136] M. Kubin, A. Scheriau, M. Knabl, and H. Holzgruber, Electroslag rapid remelting (ESRR), a novel technology for the production of high quality, near net shaped billets and blooms, in: AISTech, 2014, Indianapolis.

[137] C. Deville-Cavellin, and A. Scheriau, Simulation and testing of a modified mould, on UGITECH's ESRR™, in: liquid metal processing and casting (LMPC), 2015, Leoben, p. 79.

[138] F.S. Suarez, J.E. Roberts, and L.D Schley, Ingot size optimization in a superalloy Inconel Alloy 706, in: 5th Int. Symp. Electroslag and Other Special Melting Techn.,1974, Pittsburgh, p. 126.

[139] H. Holzgruber, W. Holzgruber, A. Scheriau, M. Knabl, M. Kubin, J. Korp, R. Pierer, Investigation of the implications of the current conductive mold technology with respect to the internal and surface quality of ESR ingots, in: liquid metal processing and casting (LMPC), 2011, Nancy, p. 57.

[140] L.B. Medovar, V.L. Petrenko, A.K. Tsykoulenko, V. Ya. Saenko, B.B. Fedorovsky, ESR with Two Power Sources and Process Control, in: liquid metal processing and casting (LMPC), 2005, Santa Fe.

[141] F. Liu, X. Zang, Z. Jiang, X. Geng, M. Yao, Comprehensive model for a slag bath in electroslag remelting process with a current-conductive mould, Int. J. of Min. Metall. Mater., 2012, vol. 19, p. 303.

[142] B. Hernandez-Morales, Electromagnetic stirring with alternating current during electroslag remelting, M.Sc. Thesis, UBC, 1988.

[143] Q. Wang, H. Yan, F. Wang, and B. Li, Impact of electromagnetic stirring on grain structure of electroslag remelting ingot, JOM, 2015, vol. 67 (8), p. 1821.

[144] G. Brückmann, G. Sick, K. Schwedtfeger, Slag movement in ESR of steel, Metall. Trans. B, 1983, vol. 14, p. 761.

[145] Q. Wang, L. Gosselin, and B. Li, Effect of rotating electrode on magneto hydrodynamic flow and heat transfer in electroslag remelting process, ISIJ Int., 2014, vol. 54 (12), p. 2821.

[146] A.D. Patel, J. Reitz, J. H. Magee, R. Smith, G. Maurer, B. Friedrich, On nitrogen pick-up during Pressure-ESR of austenitic steels in: liquid metal processing and casting (LMPC), 2009, Santa Fe, p. 253.

[147] S. Yamamoto, Y. Momoi, K. Kajikawa, Nitrogen addition using a gas blow in an ESR process, in: liquid metal processing and casting (LMPC), 2015, Leoben, p. 53.

[148] L. Medovar, G. Stovpchenko, G. Dudka, A. Kozminskiy, B. Fedorovskii, V. Lebid, I. Gusiev, Evolution of ESR technology and equipment for long hollow ingots manufacture, in: liquid metal processing and casting (LMPC), 2013, Austin, p.137.

[149] F. B. Liu, Z. H. Jiang, H. B. Li, X. Geng, X. Chen, H. Feng and X. M. Zang, Mathematical modelling of electroslag remelting P91 hollow ingots process with multi-electrodes, Ironmak. steelmak., 2014, vol. 41(10), p. 791.

[150] X. Chen, F. Liu, Z. Jiang, H. Li, X. Zang, X. Deng, Mathematical modeling of ESR process for hollow ingot with current supplying mould, J. Iron Steel Res., 2015, vol. 22(3), p. 192.

[151] H. Versteeg, W. Malalasekera, An introduction to computational fluid dynamics: the Finite Volume Method, Prentice Hall, 2007.

[152] M. C. Schneider and C. Beckermann, A numerical study of the combined effects of micro segregation, mushy zone permeability and flow, caused by volume contraction

and thermosolutal convection on macrosegregation and eutectic formation in binary alloy solidification, Int. J. Heat Mass Transfer, 1995, vol. 38(18), p. 3455.

[153] F. R. Menter, Two-equation eddy-Viscosity turbulence models for engineering applications, AIAA Journal, 1994, vol. 32 (8), p. 1598.

[154] F.R. Menter, M. Kuntz, and R. Langtry, Ten years of industrial experience with the SST turbulence model, Turb. Heat Mass Transfer, 2003, vol. 4, p. 625.

[155] F.R. Menter and Y. Egorov, A scale-adaptive simulation model using two-equation models, in: AIAA paper 2005-1095, 2005, Nevada.

[156] E. Karimi-Sibaki, A. Kharicha, J. Korp, M. Wu, A. Ludwig, Influence of crystal morphological parameters on the solidification of ESR ingot, Mater. Sci. Forum, 2014, vol. 790-791, p. 396.

[157] V. R. Voller, C. Prakash, A fixed grid numerical modelling methodology for convection-diffusion mushy region phase-change problems, Int. J. Heat Mass Transfer, 1987, vol. 30 (8), p. 1709.

[158] T.W. Clyne, W. Kurz, Solute redistribution during solidification with rapid solid state diffusion, Metall. Trans. A, 1981, vol. l2 (6), p. 965.

[159] C.W. Hirt and B.D. Nichols, Volume of fluid (VOF) method for the dynamics of free boundaries. J. of Comp. Physics, 1981, vol. 39 (1), p. 201.

[160] Fluent 14.5 User's Guide, Fluent Inc., 2012.

[161] A. Menendez Blanco and J.M. Fernandez Oro, Unsteady numerical simulation of an air-operated piston pump for lubricating grease using dynamic meshes, Computers Fluids, 2012, vol. 57, p. 138.

[162] E. Karimi-Sibaki, A. Kharicha, J. Bohacek, M. Wu, A. Ludwig, On validity of axisymmetric assumption for modeling an industrial scale electroslag remelting process, Adv. Eng. Mater., 2015, DOI: 10.1002/adem.201500391.

[163] J. C. Korp, M. Kubin, Influence of melting rate on properties of non-metallic inclusions during electroslag remelting under protective gas, INTECO Remelting and Forging Symposium, 2010, Shanghai.

[164] A. Mitchell, Electrochemical aspects of the ESR process, in: liquid metal processing and casting (LMPC), 2015, Leoben, p. 13.

[165] E. Karimi-Sibaki, A. Kharicha, M. Wu, A. Ludwig, H. Holzgruber, B. Ofner, M. Ramprecht, A parameter study on the effect of slag electric conductivity on the solidification of a large scale ESR ingot, in: 2nd Int. conference on ingot casting rolling and forging (ICRF), 2014, Milan.

[166] M. Bell, A. Mitchell, Some observations on the surface quality of electroslag ingots, J. Iron and Steel Inst., 1971, p. 658.

[167] J. Cameron, M. Etienne, A. Mitchell, Some electrical characteristics of a DC electroslag unit, Metall. Trans., 1970, vol. 1 (7), p. 1839.

[168] K. O. Yu, J. A. Domingue, G.E. Maurer and H.D. Flanders, Macrosegregation in ESR and VAR processes, J. of Met., 1986, vol. 38 (1), p. 46.

[169] D. R. Poirier, Permeability for flow of interdendritic liquid in columnar-dendritic alloys, Metall. Trans. B, 1987, vol. 18, p. 245.

[170] J. C. Heinrich and D. R. Poirier, Convection modeling in directional solidification, Comptes Rendus Mecanique, 2004, vol. 332 (5-6), p. 429.

[171] E. J. Pickering, Macrosegregation in steel ingots: the applicability of modeling and characterization techniques, ISIJ Int., 2013, vol. 53 (6), p. 935.

[172] H. Jacobi and K. Schwerdtfeger, Dendritic morphology of steady state unidirectionally solidified steel, Metall. Trans. A, 1976, vol. 7, p. 811.

[173] I. P. Borodin, V. A. Goryainov, V. S. Koshman, L. A. Zaitseva, and L. L. Tsapaeva, Influence of solidification conditions on dendritic structure and segregation of elements in electroslag remelted ingots, Steel in the USSR, 1985, Vol. 15, p. 533.

[174] M. Wang, X. Zha, M. Gao, Y. Ma, K. Liu, Y. Li, Structure, microsegregation, and precipitates of an alloy 690 ESR ingot in industrial scale, Metall. Trans. A, 2015, vol. 46, p. 5217.

[175] J. Campbell, Fluid flow and droplet formation in the electroslag remelting process. J. Met., 1970, vol. 20 (7), p. 23.

[176] K. Makropoulos and H. Winterhager, Influence of electromagnetic fields on drop formation in the electroslag remelting process, Arch. Eisenhüttenwesen, 1976, vol. 47, p. 211.

[177] Y. Kojima, M. Kato, T. Toyoda, and M. Inouye, On the droplet formation at the tip of electrode by DC ESR with small scale unit, Trans. ISIJ, 1975, vol. 15, p. 397.

[178] B. Korousic, Drop formation in the electroslag remelting process, Arch. Eisenhüttenwesen, 1976, vol. 47, p. 283.

[179] A. Kharicha, M. Wu, A. Ludwig, E. Karimi-Sibaki, Simulation of the electric signal during the formation and departure of droplets in the Electroslag Remelting Process, Metall. Trans. B, in press.

[180] A. Mitchell, Freckles and gas evolution in ESR and VAR ingots, Ironmak. steelmak., 1975, No. 3, p. 198.

[181] M. Wu, J. Domitner, A. Ludwig, Using a two-phase columnar solidification model to study the principle of mechanical soft reduction in slab casting, Metall. Trans. A,

2012, vol. 43, p. 945.

[182] M. Wu, A. Ludwig, Using a three-phase deterministic model for columnar to equiaxed transition, Metall. Trans. A, 2007, vol. 38, p. 1465.

[183] M. Ahmadein, M. Wu, A. Ludwig, Analysis of macrosegregation formation and columnar to equiaxed transition during solidification of Al-4wt.%Cu ingot using a 5-phase model, J. Crystal Growth, 2015, vol. 417, p. 65.

7 Publications

I. A numerical study on the influence of the frequency of the applied AC current on the electroslag remelting process

E. Karimi-Sibaki, A. Kharicha, M. Wu, A. Ludwig, H. Holzgruber, B. Ofner, M. Ramprecht

In: Liquid metal processing and casting conference (LMPC), 2013, Austin, Ed. by: M. Krane, A. Jardy, R. Williamson, J. Beaman, TMS Publications, John Wiley and sons, pp. 13-19.

II. Contribution of the mould current to the ingot surface quality in the electroslag remelting process

A. Kharicha, E. Karimi-Sibaki, M. Wu, A. Ludwig

In: Liquid metal processing and casting conference (LMPC), 2013, Austin, Ed. by: M. Krane, A. Jardy, R. Williamson, J. Beaman, TMS Publications, John Wiley and sons, pp. 95-99.

III. Influence of crystal morphological parameters on the solidification of ESR ingot

E. Karimi-Sibaki, A. Kharicha, J. Korp, M. Wu, A. Ludwig

Mater. Sci. Forum 790-791 (2014) 396-401.

IV. A parameter study on the effect of slag electric conductivity on the solidification of a large scale ESR ingot

E. Karimi-Sibaki, A. Kharicha, M. Wu, A. Ludwig, H. Holzgruber, B. Ofner, M. Ramprecht

In: 2nd Int. conference on ingot casting rolling and forging (ICRF), 2014, Milan.

V. A dynamic mesh-based approach to model melting and shape of an ESR electrode

E. Karimi-Sibaki, A. Kharicha, J. Bohacek, M. Wu, A. Ludwig

Metall. Mater. Trans. B 46 (2015) 2049-2061.

VI. On validity of axisymmetric assumption for modeling an industrial scale electroslag remelting process

E. Karimi-Sibaki, A. Kharicha, J. Bohacek, M. Wu, A. Ludwig

Adv. Eng. Mater. In press, 2015, Online available
DOI: 10.1002/adem.201500391

VII. Transient melting of an ESR electrode

A. Kharicha, E. Karimi-Sibaki, J. Bohacek, M. Wu, A. Ludwig

In: Liquid metal processing and casting conference (LMPC), 2015, Leoben, Ed. by: A. Kharicha, R. Mark Ward, H. Holzgruber, M. Wu, IOP Conf. Series: Materials Science and Engineering, In Press.

VIII. An attempt to model electrode change during the ESR process

E. Karimi-Sibaki, A. Kharicha, M. Wu, A. Ludwig, H. Holzgruber, B. Ofner, A. Scheriau, M. Kubin, M. Ramprecht

In: Liquid metal processing and casting conference (LMPC), 2015, Leoben, Ed. by: A. Kharicha, R. Mark Ward, H. Holzgruber, M. Wu, IOP Conf. Series: Materials Science and Engineering, In Press.

IX. A numerical study on electrochemical transport of ions in calcium fluoride slag

E. Karimi-Sibaki, A. Kharicha, M. Wu, A. Ludwig

In: Liquid metal processing and casting conference (LMPC), 2015, Leoben, Ed. by: A. Kharicha, R. Mark Ward, H. Holzgruber, M. Wu, IOP Conf. Series: Materials Science and Engineering, In Press.

Publication I

A numerical study on the influence of the frequency of the applied AC current on the electroslag remelting process

E. Karimi-Sibaki, A. Kharicha, M. Wu, A. Ludwig, H. Holzgruber, B. Ofner, M. Ramprecht

In: Liquid metal processing and casting conference (LMPC), 2013, Austin, Ed. by: M. Krane, A. Jardy, R. Williamson, J. Beaman, TMS Publications, John Wiley and sons, pp. 13-19.

A NUMERICAL STUDY ON THE INFLUENCE OF THE FREQUENCY OF THE APPLIED AC CURRENT ON THE ELECTROSLAG REMELTING PROCESS

E. Karimi Sibaki [1], A. Kharicha [1,2], M. Wu [1,2], A. Ludwig [2], H. Holzgruber [3]

B. Ofner [3], M. Ramprecht [3]

[1] Christian Doppler Laboratory for Advanced Process Simulation of Solidification and Melting, Univ. of Leoben, Austria

[2] Chair of Simulation and Modeling of Metallurgical Processes, Univ. of Leoben, Austria

[3] INTECO Special Melting Technologies GmbH, 8600 Bruck/Mur, Austria

Correspondent author: abdellah.kharicha@unileoben.ac.at

Keywords: Electroslag Remelting (ESR), Magnetohydrodynamics (MHD), Solidification, AC Current.

Abstract

Most conventional electroslag remelting (ESR) processes are operated with AC current, but the inductive loss of the power becomes a major problem when the process is operated at the high frequency for large scale ESR. Nowadays, the demand on large scale ingots has driven the people to think of operating the process with AC current at low frequency. Here the influence of the applied frequency of AC current on the large scale ESR process is numerically investigated. For this purpose, simulations with two operating AC frequencies (0.2 and 50 Hz) are performed. The main goal is to achieve some fundamental understanding of the two-phase flow and the formation of melt pool of the solidifying ingot under the influence of AC frequency. As we also know that the mold current (portion of electric current entering through solid slag skin into the mold) plays an important role in the process, calculations considering different current paths are also analyzed.

1 Introduction

The aim of the electroslag remelting (ESR) process is purifying and refining steel and other alloys such as Ni-based super alloys. Thermal energy is supplied to the process through the Joule heating that results in remelting the electrode and formation of droplets. The droplets then pass through the slag and reach the liquid pool. The melt pool solidifies directionally and builds the high-grade ingot in a water-cooled mold [1].

In the ESR process the electromagnetic field drives the flow of the molten slag and liquid melt pool, thus the electrical parameters of the process have a significant effect on the quality of the final product. Currently, the ESR process is mostly operating with AC current (50 - 60 Hz) in order to minimize the negative impacts of the electrochemical reactions occurring in the slag.

Comprehensive reviews of electrochemical reactions in the ESR process were presented by Peover and Mitchel [2-3]. In fact, the electric current is conducted by ions in the slag region [4]. Oxidation loss of elements such as Ti, Si, and Al is addressed as a big issue during DC remelting of the electrode in the ESR process [5-7]. The composition fluctuation of elements can significantly reduce the yield strength of the alloys. For instance, a major loss of Ti element (40-80 %) is reported by Etienne in a DC electrode remelting process [5]. Furthermore, the degree of sulphur removal by an ESR process operated with AC current is higher than by an ESR process operated with DC current [8]. Previously, Chang studied experimentally the effect of low frequency AC power supply on qualities of alloy steel [9]. It is generally recognized that the aforementioned alloying phenomena are due to electrochemical reactions taking place at the slag-metal interface when the process is operating with DC or quasi-DC current.

On the other hand, the inductive losses of the power for large scale ESR are the main disadvantage of operating the process at large frequencies. The demand on large scale

ingots (diameter > 1 m) has been increased since the last decade. Unfortunately, the inductive losses become more significant as the ingot size increases which are the major drawbacks of applying large frequency for large scale ESR process. Therefore, the industry intends to operate the process at low frequency (0.1 - 5 Hz).

Over the last decades, some efforts were done to model ESR process using CFD [10-12]. Additionally, attempts have been made to investigate the effect of frequency of the applied AC current on the ESR process using numerical simulation. Kharicha studied the effect of the AC electromagnetic field on the flow and slag-pool interfaces [13]. In addition, Liang studied the quality of the ingot for producing GH4169 under different current frequency for a small scale ESR process [14]. Furthermore, Li developed a 3D finite element model (FEM) considering current frequency to simulate the current density, magnetic field, electromagnetic force and Joule heating for the process [15].

In the current work, the influence of the applied frequency of AC power supply for a large scale ESR process using a static mold is investigated. The main goal is to achieve some fundamental understanding of the two-phase flow and the formation of melt pool of the solidifying ingot under the influence of AC frequency.

2 Numerical model

In the present study, the Finite Volume Method (FVM) is used for simulation of the fluid flow, heat transfer, and electromagnetic field in the process. The buoyancy and Lorentz forces as well as Joule heating due to the electrical resistance in the whole system are taken into account. The temperature field is obtained by solving the enthalpy conservation equation where Joule heating is added as a source term [16]. The momentum equation is solved to determine the velocity field. The drag resistance of the solidifying dendrites to the

flow in the two-phase mushy zone is modeled according to the Black-Kozeny model [17]. Additionally, Lorentz force is added as a source to the momentum equation.

The origin of the Lorentz force is the interaction between the electric current and the self-induced magnetic field in the system. For the sinusoidal AC field, the magnetic field can be expressed using the phasor notation ($B_\theta = \tilde{B}_\theta e^{i\omega t}$) where $\tilde{B}_\theta$ is a function of position. The magnetic field has only azimuthal direction since there is no external magnetic field and the process conditions are axisymmetric. The equation for magnetic field that is derived from the Maxwell's system of equations must be solved in cylindrical coordinate [18]. The equation is given as:

$$\frac{\partial B_\theta}{\partial t} + \left[\frac{\partial}{\partial z}\left(\frac{1}{\sigma\mu_0}\frac{\partial B_\theta}{\partial z} \right) + \frac{\partial}{\partial r}\left(\frac{1}{r\sigma\mu_0}\frac{\partial (rB_\theta)}{\partial r} \right) \right] = 0 \tag{1}$$

Where μ_0 and σ denote the magnetic permeability and electric conductivity respectively.

After computing the real and imaginary components of the magnetic field, the electric current in the whole system can be obtained using the Ampere's law that is expressed as:

$$\tilde{\vec{j}} = \frac{1}{\mu_0}(\vec{\nabla} \times \tilde{B}_\theta) \tag{2}$$

Finally, the time average Lorentz force and Joule heating can be computed:

$$\vec{F}_L = \mathrm{Re}\left(\frac{1}{2}\vec{j} \times \tilde{B}_{\theta\ Conjugate}\right) \tag{3}$$

$$q_{Joule} = \mathrm{Re}\left(\frac{1}{2\sigma}\tilde{\vec{j}} \times \tilde{\vec{j}}_{\theta\ Conjugate}\right) \tag{4}$$

Configuration of the computational domain and boundaries are schematically shown in Figure 1. The computational domain includes the slag and ingot. A 2D axisymmetric

calculation is performed. The slag-pool, electrode-slag, and slag-air interfaces are assumed to be flat. The electrode immersion depth is ignored.

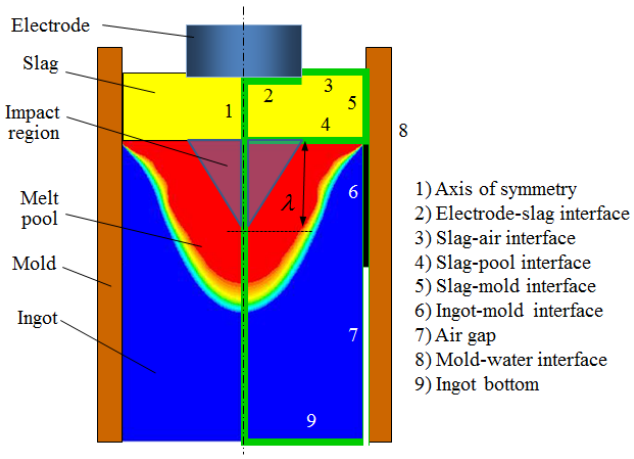

Figure 1: Schematic representation of the computational domain for the ESR process.

The classical way to consider the impact of falling droplets is to use a mass flux of liquid metal at the slag-pool interface [19-20]. Another way of modeling the droplets is prescribing a Gaussian distribution of velocity profile at the interface between the slag and melt pool [18]. In fact, the impact of droplets is not limited only at the surface but deeply inside the melt pool. Therefore, we modify the model considering the impact of droplets by introducing the parameter called impact depth of droplets (λ). With this approach, the droplets are considered to be as the mass, energy, and momentum source carriers which deeply penetrate into the melt pool. The amounts of the sources are assumed to be linearly decreased from the slag-pool interface till the impact depth. The impact depth can be obtained by experiment or direct numerical simulation of droplet–liquid surface splash phenomenon. For our simulations, we assumed that the droplet size is 1 cm and the corresponding impact depth is 15 cm. Furthermore, it is assumed that the droplets enter the pool under the shadow of the electrode.

Non-slip boundary condition is applied for the flow at the electrode-slag interface and at the mold wall, whereas at the slag-pool interface the condition is free-slip. The heat is transferred by convection and radiation between electrode and air, and at the slag-air interface. A value of 0.8 is applied for the emissivity for the mentioned boundaries. The heat is conducted to the mold passing through the slag skin layer from the slag and ingot. In addition, the air gap between the slag skin layer and mold due to shrinkage of solidified ingot is taken into account. The gap alters the thermal boundary condition from the conduction condition to a combined radiation-convection condition. The tip of the electrode (slag-electrode interface) where the droplets form takes the liquidus temperature of the alloy.

In addition, the boundary conditions for the magnetic flux, Eq.(1), are obtained using the Ampere's law. The magnetic induction is prescribed at the slag-air and mould-water interfaces. The continuity of the magnetic induction is applied at the following interfaces: electrode-slag, slag-pool, slag-mold, and ingot-mold. Furthermore, an induction flux of zero is used for the ingot bottom.

Details about the geometry and the average physical properties of the slag and steel are described in Table 1.Several calculations under different operating conditions were performed using the commercial software FLUENT. Table 2 lists the operating conditions for the case studies.

Table 1. Parameters used in the simulations.

Steel	
Density ($kg \cdot m^{-3}$)	7100
Viscosity ($Kg \cdot m^{-1} \cdot s^{-1}$)	0.006
Liquidus Temp. (K)	1779
Solidus Temp. (K)	1719
Specific heat, liquid ($J \cdot Kg^{-1} \cdot K^{-1}$)	800
Latent heat of fusion ($J \cdot Kg^{-1}$)	268000
Thermal Conductivity, liquid($W \cdot m^{-1} \cdot K^{-1}$)	40
Electric Conductivity, liquid($ohm^{-1} \cdot m^{-1}$)	880000
Slag	
Density ($kg \cdot m^{-3}$)	2800
Viscosity ($Kg \cdot m^{-1} \cdot s^{-1}$)	0.002
Specific heat, liquid ($J \cdot Kg^{-1} \cdot K^{-1}$)	1250
Thermal Conductivity, liquid($W \cdot m^{-1} \cdot K^{-1}$)	10
Electric Conductivity, liquid($ohm^{-1} \cdot m^{-1}$)	100
Geometry (Static mold)	
Mold radius (m)	0.9115
Electrode radius (m)	0.725
Slag height (m)	0.265

Table 2. Operating conditions of the parameter studies

	RMS current (KA)	Frequency (Hz)	Mold current
Case I	36.5	0.2	No
Case II	36.5	50	No
Case III	36.5	50	Yes

3 Results

Case I

In Case I a low frequency (0.2 Hz) AC current is applied, and no current enters into mold. Figure 2 (a) shows the temperature field in the whole system and the isolines of solid fraction in the ingot region. The hottest area in the whole system is under the shadow of the slag-air interface.

In fact, an intense vortex forms under the edge of the electrode due to the Lorentz force and buoyancy force. The recirculation of the flow captures the released Joule heat in the slag

region. The relative velocity between the melt and the ingot is illustrated in Figure 2 (b). The flow recirculation in the slag region corresponds to the maximum velocity in the whole system. The velocity is predicted to be much smaller in the melt pool than in the slag region. One point needs to be kept in mind is that the slag-pool interface is assumed to be stationary. This assumption would cause underestimation of the flow velocity in the melt pool especially in the vicinity of the slag.

The Lorentz force in the slag and melt pool is shown in Figure 2 (c). It is observed that the Lorentz force is quite homogeneously distributed. Exceptionally, the magnitude of the Lorentz force becomes large near the edge of the electrode. In fact, the variation in the Lorentz force and Joule heating in the slag region is consistent with the current density. Figure 2 (d) shows distributions of the current lines and Joule heating in the process. The maximum amount of Joule heating is released near the edge of the electrode where the current lines are denser. As a matter of fact, the amount of Joule heating is negligible in the electrode and ingot due to low electrical resistance of steel.

Case II

Figure 3 shows the contour of temperature, velocity, Lorentz force, and electric current together with Joule heating when the process is run under the frequency of 50 Hz. Again no current enters into mold since the skin layer is assumed to be an insulator. The region where the flow recirculates matches the hottest area in the slag zone as shown in Figure 3 (a). In the slag region, the Lorentz force is quite homogeneously distributed excluding the edge of the electrode where the force is the strongest. For this case, the force gradually increases from the bulk to the region near the mold wall in the melt pool as shown in Figure 3(c).This is due to change of electric current distribution once they enter the melt pool, as shown in Figure 3(d). The electric current flows radially towards the ingot surface as it passes the

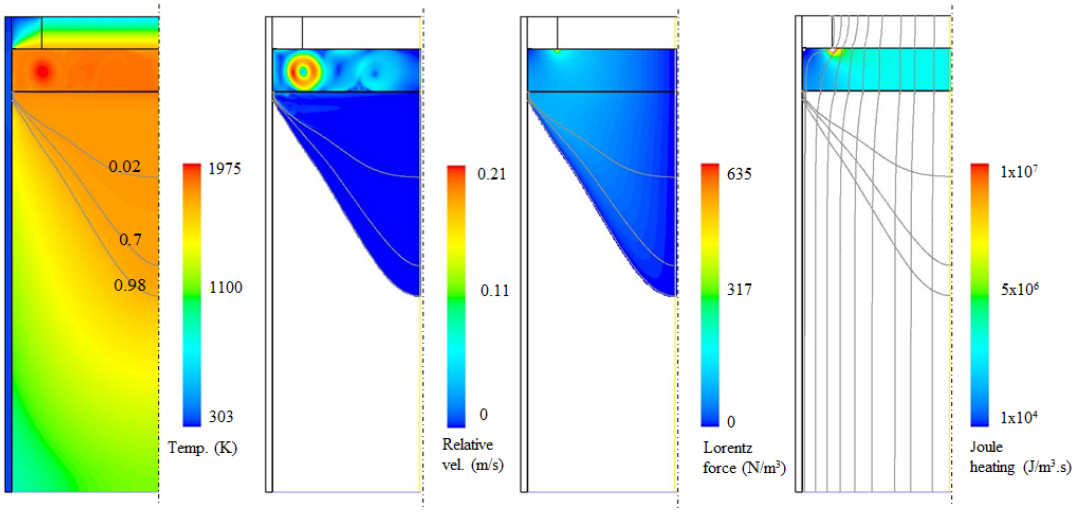

(a) (b) (c) (d)

Figure 2. Contours of (a) the temperature field (b) magnitude of the relative velocity (c) Lorentz force and (d) Joule heating overlaid with the path of electric current for Case I. Isolines of fraction solid (0.02, 0.7 and 0.98) are plotted to indicate the mushy zone.

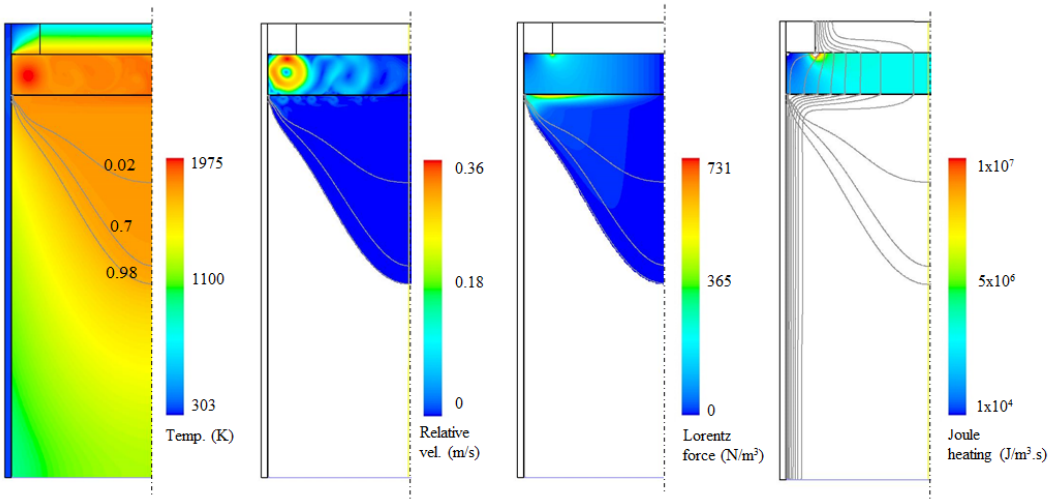

(a) (b) (c) (d)

Figure 3. Contours of (a) the temperature field (b) magnitude of the relative velocity (c) Lorentz force and (d) Joule heating overlaid with the path of electric current for Case II. Isolines of fraction solid (0.02, 0.7 and 0.98) are plotted to indicate the mushy zone.

slag-pool interface. In fact, the electric current tends to flow along the ingot surface because of skin effect.

Case III

Figure 4 shows the modeling results of Case III. This case is same as Case II (50 Hz), but the electric current is allowed to cross the slag skin and enter into the mold.

The thickness of the slag skin layer is assumed to be 1 cm, and the contact length where the current can enter into the mold is 5 cm. Electric conductivities of the liquid slag and the solid slag skin are 100 and 48 respectively. In this case, around 90 % of total current is predicted to pass across the skin layer, as shown in Figure 4 (d). However, only 10 % of the total power is consumed in the skin layer. Due to the special current distribution in this case, strong Lorenz force is predicted in the region near the outer radius region of the slag layer and ingot, and only a very week Lorenz force acting in the bulk of the melt pool, as illustrated in Figure 4 (c).

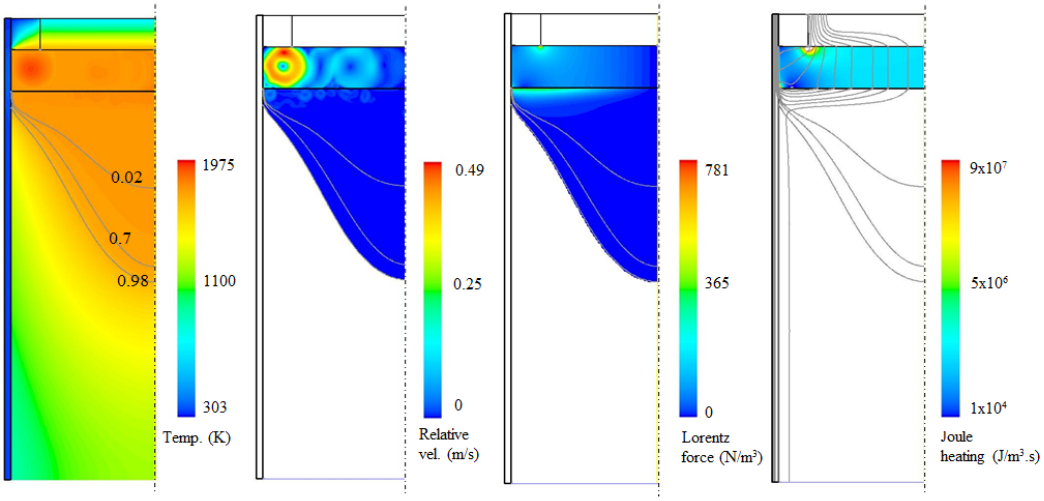

(a) (b) (c) (d)

Figure 4. Contours of (a) the temperature field (b) magnitude of the relative velocity (c) Lorentz force and (d) Joule heating overlaid with the path of electric current for Case III. Isolines of fraction solid (0.02, 0.7 and 0.98) are plotted to indicate the mushy zone.

4 Discussion

The shape of melt pool is an important indicator for the ESR process, and it determines the quality of the as-cast ingot. Parameters of the melt pool (depth, mush zone, standing height) are mainly governed by the global transport phenomena, which are in turn related to the flow intensity of different fluid regions. Intensity of the flow is evaluated by the time-averaged kinetic energy. Influence of the process operating parameters (Case I, II, III) on the average kinetic energy is analyzed (Table 3).

Table 3. Summary of the computed average kinetic energy in different fluid regions.

	Average kinetic energy in slag (J)	Average kinetic energy in melt pool (J)
Case I	6.83	0.03
Case II	23.69	0.096
Case III	56.06	0.186

Effect of frequency

A comparison is made between Case I and Case II to analyze the effect of frequency of AC current as shown in Figure 5. The aver-age kinetic energy in the slag for Case II is larger than that for Case I, see Table 3. It means that the present ESR process run with high frequency has a more severe mixing in the slag region than the process run with low frequency. The more severe the mixing in slag region, the larger the amount of energy being transport into the melt pool. Therefore, with the increase of the current frequency, the pool depth (distance between the slag-pool interface and the isoline of 0.02 solid fraction) is slightly increased. However, the isoline of 0.98 solid fraction moves down that results in thicker mushy zone for Case I than for Case II.

Additionally, the frequency of the AC current can affect the dis-tribution of the Lorentz force at the region near to the slag-melt interface. As shown in Figure 5 (b), the electric current lines have similar distribution at the slag region independent of the applied frequency. Thus, the Lorentz force direction is identical for both cases, that is towards the axis of symmetry. However, at the slag-pool interface the direction is altered for Case II with 50 Hz frequency. It is horizontal and downward, as shown in Figure 6.

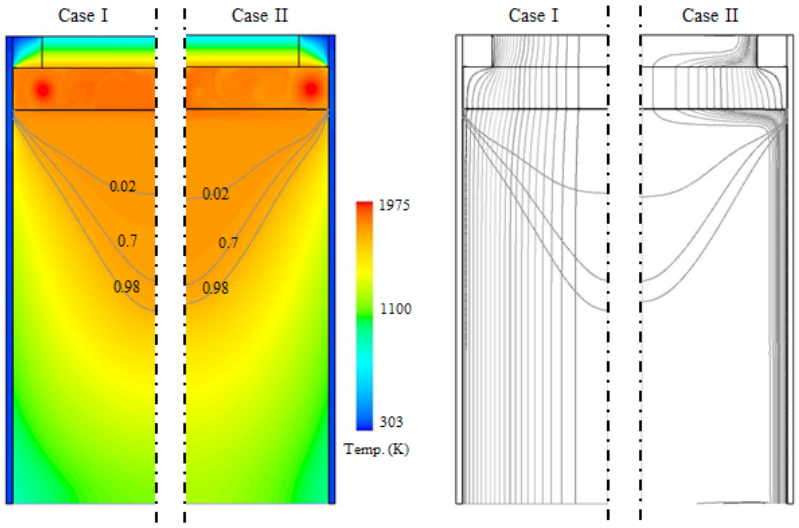

(a) (b)

Figure 5: Influence of the AC current frequency on (a) the temperature field and mushy zone (b) electric current distribution. Two cases are compared: Case I with frequency of 0.2 Hz: Case II with frequency of 50 Hz.

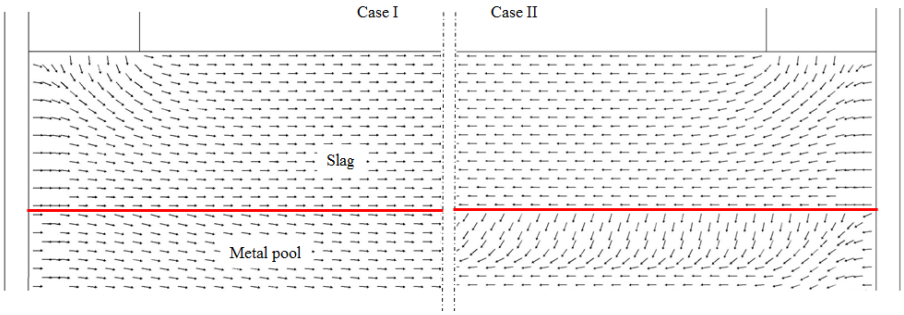

Figure 6: Influence of the AC current frequency on the direction of the Lorentz force, Two cases are compared: Case I with frequency of 0.2 Hz: Case II with frequency of 50 Hz.

Effect of mold current

Here, Case II and Case III are compered to study the influence of mold current on the pool shape, as illustrated in Figure 7. The average kinetic energy in the slag and melt pool is much larger for Case III than for Case II. Accordingly, the bulk of the slag is severely mixed in Case III with mold current. This mixing promotes the transfer of heat from slag to melt pool, hence leads to a raise of the melt pool temperature and a deeper pool.

The electric current lines are shown in Figure7 (b). For Case III a huge amount (92%) of the current enters into the mold in the region close to slag-pool interface where there is still contact between the metal and mold. This changes the pattern of the flow in this region, and results in larger standing height of the melt pool than for Case II without mold current. In addition, the skin effect in the copper mold is significant. Inside the mold the electric current only flows near the mold surfaces, as shown in Figure 7(b).

At high frequency, the current density and consequently the Lorentz force is week in the bulk of the melt pool where the flow is mainly driven by buoyancy. The direction of the Lorentz force is compared to study the effect of the mold current on the flow, as indicated in Figure 8. The direction of the Lorentz force is similar in the slag region and slag-pool interface in the central part of the system. However, for Case III with the mold current, the direction of the Lorentz force bents downwards near the mold wall both in the slag and melt pool regions. The Lorentz force and buoyancy act in the same direction and the flow is pushed downwards. The downward flow near the mold wall increases the standing height of the melt pool. The standing height is defined as the distance from the slag-pool interface to the start of solidification at the ingot surface (as shown in Figure 7a).

Joule heat is uniformly released under the electrode for both cases as shown in Figure 9. However, for Case II inhomogeneous distribution of Joule heat is released along the slag-mold interface. The minimum heat source is noticed near the slag-air interface for Case II

where the slag skin layer acts as an electric insulator. In contrast, the magnitude of Joule heat source is significantly large at this region for Case III with mold current. Since this area is closer to the edge of the electrode, the electric resistance drops and more current flows through it. In the vicinity of the slag-pool interface Joule heating is pretty large for case III. This region is the most favorable path for the electric current to flow.

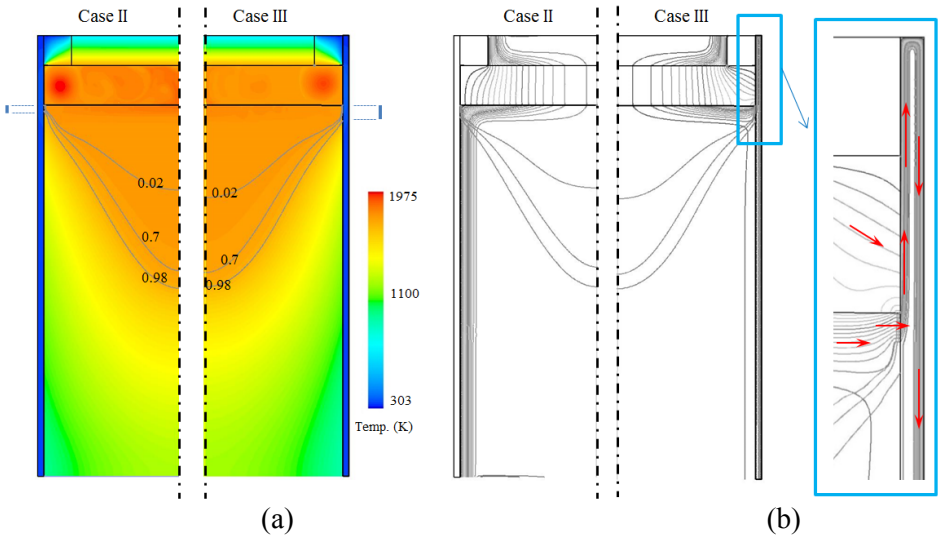

Figure 7: Influence of the mold current (frequency of 50 Hz) on (a) the temperature field and mushy zone (distance between dotted lines indicates the standing height) (b) electric current path (red arrows indicate the direction of electric current). Two cases are compared: Case II without mold current: Case III with mold current.

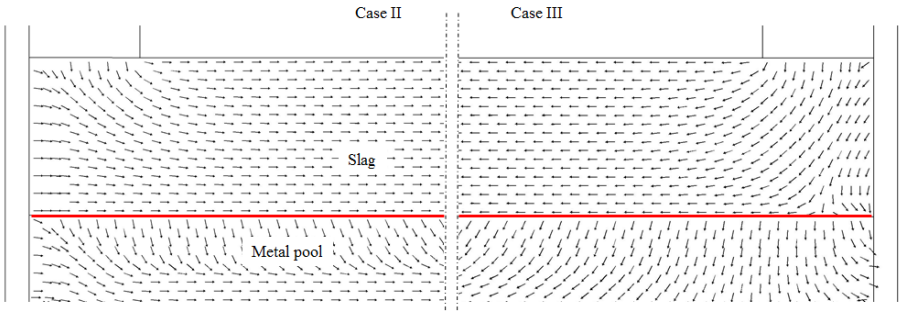

Figure 8: Influence of the mold current (frequency of 50 Hz) on the direction of the Lorentz force. Two cases are compared: Case II without mold current: Case III with mold current.

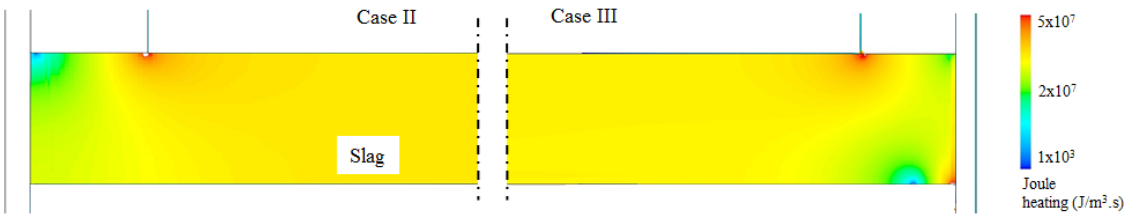

Figure 9: Influence of the Mold current (frequency of 50 Hz) on the distribution of the Joule heating, Two cases are compared: Case II without mold current: Case III with mold current.

Validity of the modeling result

A 2D axisymmetric model is used to solve the governing equations of electromagnetic field, heat transfer, and flow of the ESR process. The model is robust and computationally efficient to study the influence of electrical parameters on the solidification of the ingot. It is observed that the electrical parameters such as electric conductivity and frequency of the applied AC current have a huge influence on the shape of the melt pool. The electric conductivities of the slag (liquid and solid) are the main properties determining the electric current path, hence influencing other quantities of the process. As such properties are assumed, the current study is considered to be preliminary and qualitative. Some other factors influencing the quantitative accuracy of the modeling results should be kept in mind for improving the future model: the forming metal droplets under the electrode would adapt the electromagnetic field to a certain extend [21]; the motion of the slag-pool interface can affect the flow, temperature and electromagnetic fields of the system [22]; the nature of the flow in the real process is in 3D, but the current calculation can only be performed in 2D; the turbulence of the flow which is ignored would enhance the global energy transfer as well. In spite of the model simplifications, which are necessary at the current stage, the performed parameter studies in this paper can provide valuable information about the qualitative influence of the process parameters on some key solidification quantities of the ingot, such as the shape and depth of the melt pool, standing height, mushy zone, etc.

5 Summary

The influence of the applied frequency of AC current on the large scale ESR process with static mold has been numerically investigated. Main findings are summarized as follows.

The melt pool shape of the solidifying ingot is slightly influenced by the applied frequency.

In the case of high AC frequency, due to the skin effect, the current path changes its direction when the current passes the slag-pool interface, and so does the Lorenz force. As a consequence, it influences the hydrodynamic behavior of the slag and melt pool near the slag-pool interface.

The distribution patterns of Joule heating and Lorentz force in the slag region are quite independent of the applied frequency in the slag region.

Additionally, the effect of the mold current (allow current entering into mold) is also considered. We found:

Distribution patterns of the Lorentz force and Joule heating in the slag region are significantly influenced by the mold current, especially near the mold wall.

Mold current promotes stirring in the slag region.

Mold current increases the standing height of the melt pool.

Acknowledgements

The authors acknowledge the financial support by the Austrian Federal Ministry of Economy, Family and Youth and the National Foundation for Research, Technology and Development.

References

1. G. Hoyle, *Electroslag Processes* (London, Applied Science Publishers, 1983).
2. M.E. Peover, "Electroslag remelting, a review of electrical and electrochemical aspects*," J. Inst. Metals,* 100 (1972), 97-106.
3. A. Mitchell and G. Beynon, "Electrode polarization in the DC electroslag melting of pure iron," *Met. Trans B*, 10 (1971), 3333-3345.
4. Y. Kojima, M. Kato, T. Toyoda, and M. Inouye, "The formation of liquid droplet and behavior of oxygen in direct current electroslag remelting process," *ISIJ*, 15 (1975), 397-406.
5. M. Etienne, "The loss of reactive elements during electroslag processing of iron-base alloys," (Ph.D. Thesis, University of British Columbia, 1970).
6. G.K. Bhat and A. Mitchell, *Proc. Sec. Symp. On ESR technology*, Part I (1969).
7. B.I. Medovar, *Electroslag remelting* (Moscow, House of Literature on Ferrous and Nonferrous Metallurgy, 1963).
8. D.A. Whittaker, (Ph.D. Thesis, McMaster University, 1968).
9. L. Chang, X. Shi, H. Yang, Z. Li, "Effect of low-frequency AC power supply during electroslag remelting on qualities of alloy steel," *J. of Iron and Steel Research*, 16 (4) (2009), 7-11.
10. V. Weber, A. Jardy, B. Dussoubs, D. Ablitzer, S. Ryberon, V. Schmitt, S. Hans, H. Poisson, "A comprehensive model of the electroslag remelting process: description and validation," *Proc. of LMPC,* Nancy, 2007, 83-88.
11. Z. Jiang and Y. Dong, "Solidification model for electroslag remelting process," *Proc. of LMPC,* Nancy, 2007, 89-94.
12. Matthew J. M. Krane, Michael Fahrmann, Jeff Yanke, Enrique Escobar de Obaldia, Kyle Fezi, and Jonathan Busch, "A comparison of predictions of transport phenomena in electroslag remelting to industrial data," *Proc. of LMPC,* Nancy, 2011, 65-72.

13. A. Kharicha, M. Wu, A. Ludwig, B. Ofner, and H. Holzgruber*, CFD Modeling and simulation in materials processing* (US, Wiley publication, 2012), 139.

14. Q. Liang, X. Chen, H. Ren, C. Shi, and H. Guo, "Numerical simulation of electroslag remelting process for producing GH4169 under different current frequency," *Adv. Materials Research*, (482-484)(2012), 1556-1565.

15. B. Li, F. Wang, and F. Tsukihashi, "Current, magnetic field and joule heating in electroslag remelting processes," *ISIJ Int*., 52 (7) (2012), 1289-1295.

16. A. Kharicha, W. Schützenhöfer, A. Ludwig, and R. Tanzer, "Numerical and experimental investigations on the ESR process of the hot work tool steel H11," *Proc. of LMPC,* Santa Fe, 2009, 235-242.

17. V. R. Voller, and C. Prakash, "A fixed grid numerical modeling methodology for convection-diffusion mushy region phase-change problems," *Int. J. Heat Mass Transfer*, 30(8) (1987), 1709-1719.

18. A. Kharicha, W. Schützenhöfer, A. Ludwig, and R. Tanzer, "Selected numerical investigations on ESR process," *Proc. of LMPC,* Nancy, 2007, 113-119.

19. A. H. Dilawari, and J. Szekely,"Heat transfer and fluid flow phenomena in electroslag refining," *Metall. Trans. B*, 9B (1) (1975), 77-87.

20. M. Choudhary, and J. Szekely, "Modeling of fluid flow and heat transfer in industrial-scale ESR system," *Ironmaking Steelmaking*, 8(5) (1981), 225-239.

21. A. Kharicha, A. Ludwig, M. Wu, "Droplet formation in small electroslag remelting processes," *Proc. of LMPC,* Nancy, 2011, 113-119.

22. A. Kharicha, A. Ludwig, M. Wu, "3D simulation of the melting during an industrial scale electro-slag remelting process," *Proc. of LMPC,* Nancy, 2011, 41-48.

Publication II

Contribution of the mould current to the ingot surface quality in the electroslag remelting process

A. Kharicha, E. Karimi-Sibaki, M. Wu, A. Ludwig

In: Liquid metal processing and casting conference (LMPC), 2013, Austin, Ed. by: M. Krane, A. Jardy, R. Williamson, J. Beaman, TMS Publications, John Wiley and sons, pp. 95-99.

CONTRIBUTION OF THE MOULD CURRENT TO THE INGOT SURFACE QUALITY IN THE ELECTROSLAG REMELTING PROCESS

A. Kharicha [1,2] , E. Karimi Sibaki [1], M. Wu [1,2], A. Ludwig [2]

[1] Christian Doppler Laboratory for Advanced Process Simulation of Solidification and Melting, Univ. of Leoben, Austria

[2] Chair of Simulation and Modeling of Metallurgical Processes, Univ. of Leoben, Austria

Correspondent author: abdellah.kharicha@unileoben.ac.at

Keywords: electroslag remelting (ESR), slag skin, mould current, slag electrical conductivity

Abstract

Thickness, uniformity and mechanical properties of slag skin are main factors controlling the surface quality of the electroslag remelting (ESR) ingot. Thin and homogeneous slag skin is a key to obtain a nice ingot surface quality. It is classically believed that surface quality is mainly influenced by the slag temperature at the vicinity of the mould. In the present paper considers the effect of the Joule heating on the slag skin energy balance. The slag skin between ingot and mould is expected to have a significantly different electrical resistivity than the bulk slag, complicating the electrical boundary conditions at the ingot/mould interface. The amount of electric current crossing the skin towards the mould depends on the electric slag skin conductivity. It is shown that the magnitude of Joule heating generated within the skin can control its thickness. Thus, it is suggested that the known sensibility of the ingot quality on the melt rate, the electrode immersion depth, fill

ratio and the resistivity of the slag can be reduced to its dependence on the electric current path and intensity.

1 Introduction

The surface treatment of ingots produced by the ESR process is expensive. The optimum slag would enable the production of ingots with smooth surfaces, thus reducing the need for surface treatment prior to forming. Mitchel et al. [1] explain the mechanism of slag skin formation by using the phase diagrams of the corresponding phase. A slag skin is formed by the selective solidification of one or more phases on the water cooled copper wall [1]. Its formation plays an important role in controlling the heat transfer to the mould. The phases which solidify and their order of solidification are determined by the composition of the liquid slag and the governing phase relationships. Mitchell [2] has pointed out that the phases present in the slag skin have a direct influence on ingot surface quality. However Korousic and Osterc [3] performed mineralogical analysis of several sample of slag skin, and found that the crystallisation did not follow the path given by the phase diagram.

It has been observed that good quality surface is associated with the presence of a finite depth (few cm) of liquid-metal contact on the slag skin [4] also known as “liquid head” or “standing height”. To achieve these requirements, the melting point of the slag must be higher than that of the metal. For this reason it was stated that a slag with higher Al_2O_3 content than the eutectic will produce good surfaces, while those with lower will not[2]. It was found that two slags with 25 and 10 wt-% gave uniform smooth slag skin. The slag with 1 wt-% Al_2O_3 was embedded within the ingot surface. The resistivity of the slag was also mentioned as an important parameter since it controls the heat generated within the slag [2]. Slags with lower fluoride contents (higher electric resistivity) are known to be operationally more efficient in achieving good ingot surface quality [5]. A resistive slag is believed to be able to sustain a sufficiently high temperature at the slag/pool interface to

sustain the existence of a sufficiently thick depth of liquid metal against the slag skin. However it can be argued that the temperature in a process is primarily determined by the targeted melt rate. A resistive slag needs a smaller amount of imposed current to reach the same melt condition than a more conductive slag. So the temperature might not be the only reason. In addition the explanations given, melting point of the slag versus electric resistivity, are clearly overlapping since slags with higher (Al_2O_3) content have generally higher electric resistivity and simultaneously higher melting point.

It was suggested by industry to run the process with warmed mould may encourage the formation of smooth skin [6]. But in most common industrial practice, the problem with poor surface has been dealt with increasing the power input (and so the melt rate), and by using the highest stable fill-ratio. An explanation based on slag temperature can again be given, a large fill ratios decreases the heat losses at the exposed slag surface, and thus increases the slag temperature near the mould. The thickness of the slag skin is also largely affected by immersion volume of the electrode. Immersing a large volume of electrode into the slag layer increases the amount of heat extracted by the electrode and by the mould, which lowers the temperature of the slag cap and thus increases the thickness of the slag skin. Therefore it is highly recommended to keep the immersion volume of the electrode as small as possible.

The slag viscosity was also mentioned as a parameter that can control the slag skin thickness. Due to similar molecular mechanism of the viscosity with the electric resistivity (ions movement), electrically resistive slags are more viscous than conducting ones. By using a slag with high viscosity the slag flow velocities are lower. Kusamichi et al.[7] reported larger radial temperature gradient in slags with low fluoride content than for larger one. The hottest region was located near the electrode, and the coldest near mould. Low fluoride slags are usually used together with lower applied electric current intensities, which together with a higher viscosity level mean lower magnitude of the electromagnetic forces,

which in turn generate less stirring in the slag region. The fact that colder temperatures were found near the slag skin for low fluoride slags is an indication that the slag temperature is not the proper mechanism to explain why resistive slags are more efficient in producing thin slag skins.

In previous numerical works it was shown that the electric current flowing directly towards the mould has a considerable effect on the slag skin thickness [8-9]. For better prediction, the Joule heating generated by the electric current must be added to the heat balance of the slag skin. To our knowledge, Medina et al. [10] were the first to notice experimentally a possible relation between the electric current and slag skin thickness: "..a considerable increase in slag skin weight may be produced when remelting shows wide oscillation in current". This average conductivity must also take into account the existence of a contact resistance at the slag skin/mould interface [11-12]. Just as for the heat transfer, this contact resistance might depend on the slag composition but also on the temperature. For some compositions or/and at high temperatures the slag skin possesses a "plasticity" which promotes a very good contact with the mould [12]. According to our own estimations, by taken into account the slag/mould contact resistance, the effective solid slag conductivity lies in the range of 0.1-50 Ω/m.

In the case of "mould isolated" from the baseplate, J.Cameron et al. [13] estimated the amount of mould current to be less than 5% of the total current. However, the processes studied were small ESR units (moulds ~2.5-8 cm mould and 2.5-3 cm electrodes diameters) which in normal condition operate with deep electrode immersion depth. The shape of the electrodes tip in such small size ESR are conical, the current path is thus mostly oriented towards the liquid pool. If the electrode tip would have been deepen close to the slag surface the amount of mould current would have probably reached 20 to 40 % of the total current (according to our own calculations). For other ESR scales the amount of mould current can reach up to 90% of the total applied current [8-9].

We propose the hypothesis that the current flowing through the slag/mould and the ingot/mould interfaces is a major key parameter to explain the empirical correlations gathered by industry on the quality of the ingot surface. After having presented some generalities about electric current path, the effect of mould current on the slag skin thickness is investigated.

2 Electric current path in ESR system

To correctly predict the electric current path, a numerical model based on the potential formulation A-ϕ of the electromagnetic field has been used. The mould and the electrode diameter are 0.75 and 0.5 m respectively. The slag height is 0.15 m, the liquid and solid slag conductivities are taken equal to 140 and 5 $\Omega^{-1}m^{-1}$. The slag skin thickness is assumed constant along the height $\delta = 1\ mm$. The ingot is assumed to be in perfect electric contact over 3 cm under the slag/metal interface. An rms current of 14200 A is applied from the top electrode. The results of calculations show that different electric current paths can exist in the ESR process (Figures 1-2). The possible paths depend on whether the mould is connected or not to the baseplate.

In the case of a “live mould” the possible electric current circuits are:

a: Electrode->Slag->Mould

b: Electrode->Ingot->Mould

c: Electrode->Ingot ->Baseplate->Mould

In the case of “insulated mould”:

d: Electrode->Slag->Mould->Ingot->Baseplate

e: Electrode->Ingot-> Baseplate

The magnitude of the current flowing in each circuit depends on the electric resistances of each path. In the isolated concept the current in the circuit (d) has to cross two times the skin. Thus if the slag skin covers the entire ingot, less current flows within the mould in the "isolated" than in the "live mould". However a distinction must be drawn between the current entering (or leaving) the mould at the slag and at the ingot level. At the slag level, for the present configuration, a small difference exists between the live and insulated mould concept. However at the mould level it can be seen that for the live concept, the slag skin has only a very limited power of insulation since almost 30% the current enters the mould. At 50 Hz for the insulated mould, eddy currents generated within the copper media propagate inside the steel media (Figure 2). In the case of live mould, the model predicts that a small amount of current is flowing from the ingot to the mould trough the liquid slag. If the slag skin is totally remelted at the liquid metal level, a good contact metal against the copper mould can increase considerably the amount of mould current. In the present configuration the mould and the ingot are assumed to be in contact over a height of 3 cm, in reality this height can be much larger especially in the presence of a "liquid head". So from a process to another this contact height can be very different, so the magnitude of current that can potentially flow through this boundary cannot be clearly defined. In opposite the amount of current flowing from the liquid slag to the mould, topic of the next section is much more universal.

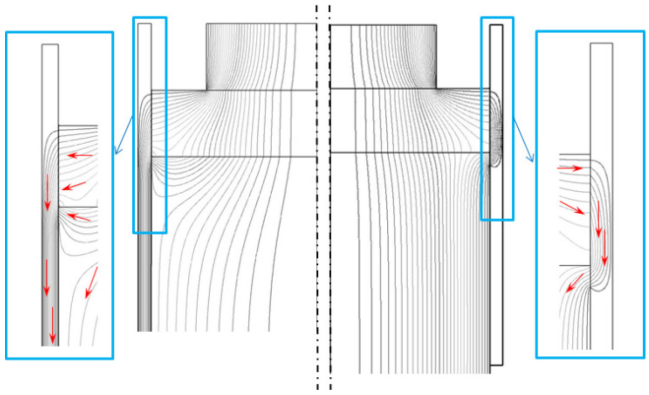

(a) Live Mould (b) Insulated Mould

Figure 1: Electric current path for a low frequency current (DC or < 5Hz)

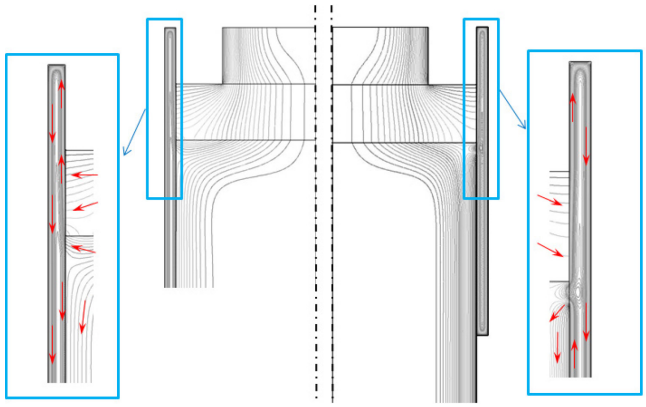

(a) Live Mould (b) Insulated Mould

Figure 2: Electric current path for a 50Hz frequency AC current

Effect of a finite slag skin conductivity on power generated

To illustrate the effect of the slag skin electric conductivity on the power generated a parametric study were performed on the case of a "live mould" ESR process. The slag skin thickness is still assumed to be constant along the height $\delta = 1\ mm$. Figures 3 shows the evolution of the total power generated in the slag (P_t) with the slag skin conductivity.

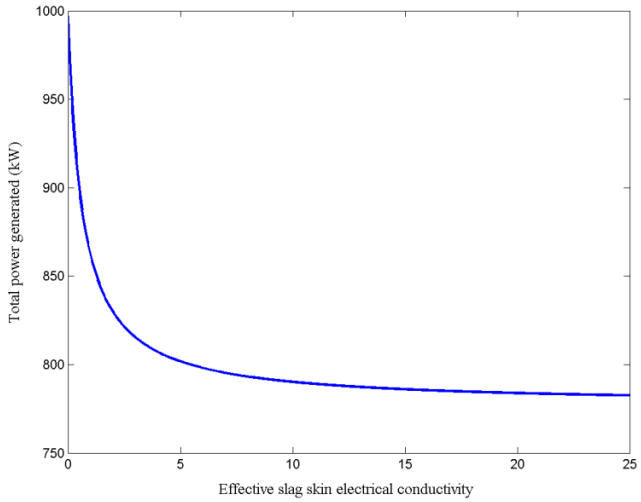

Figure 3: Total power generated versus slag skin electrical conductivity

The power decreases almost exponentially with the slag skin electric conductivity, which means that opening the path to the mould decreases the overall resistance. The power reaches 1000 kW for the case of perfectly insulating slag skin, for conductivities larger than 15 Ω/m the power almost reached its asymptotic level (~775kW).

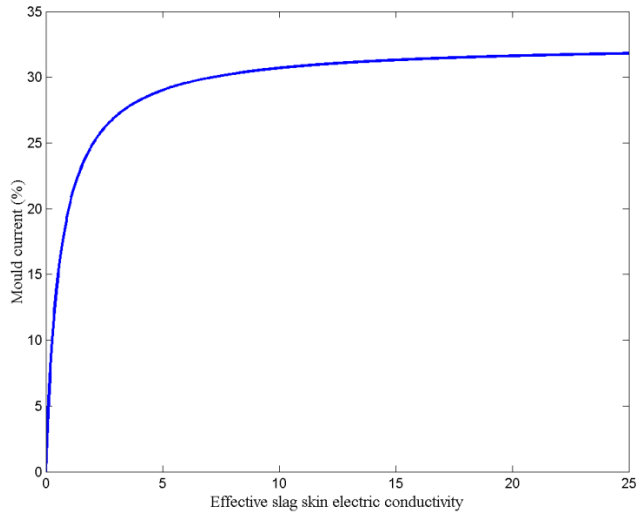

Figure 4: Proportion of electric current entering the mould at the slag level

The proportion of mould current I_m/I_t increases strongly for conductivities smaller than 3, for $\sigma > 15$ the proportion increases asymptotically towards a maximum of about 32 %(Figure4).

The proportion of power generated within the slag skin reaches a maximum of 27 % for slag skin electric conductivities $\sigma \sim 1-2$ Ω/m (Figure 5). The existence of a maximum can be explained by the fact that j_m^2 increases while $1/\sigma$ decreases with σ. Due to the lack of knowledge of the actual slag skin electric conductivity it is difficult to determine the actual state of the process. However in the real ESR plant the experimental power was found to fluctuate from 790 to 830 kW. This indicates that the actual slag skin conductivity might be around 2 to 3 Ω/m. If uncertainty about actual liquid slag conductivity is taken into account ($\sigma_l \sim 120-180$ Ω/m), the slag skin conductivity can be assumed to be within the range of 1 to 5 Ω/m.

Within this range the power generated within the slag skin (Ps) is high 80-220 kW, it represents 10 to 27 % of the total power. This power must be compared with the heat lost through the mould, which is in the order of 350 kW (assuming 10^6 Watt/m^2). Even in the largest case the Joule heating generated in the slag skin contributes for 2/3 of the heat received by the mould. So it can be stated that having 27% of the total power generated within the slag skin cannot be considered as unphysical. However this large amount of power generated in a so thin volume will definitively modify the actual skin thickness.

Effect of slag height and fill ratio on the mould current

The larger is the slag height, the higher is the resistance of the electrode/liquid pool path. For the case of slag skin conductivity of about $\sigma = 15$ and slag height of about 30 cm, 66% of the current flows to the mould in the live mould concept, and 50% in the insulated mould concept (Figure 6). Similarly the fill ratio controls the ratio between the electrode/mould and the electrode/pool distances. Smaller is the electrode radius, less current flows into the mould.

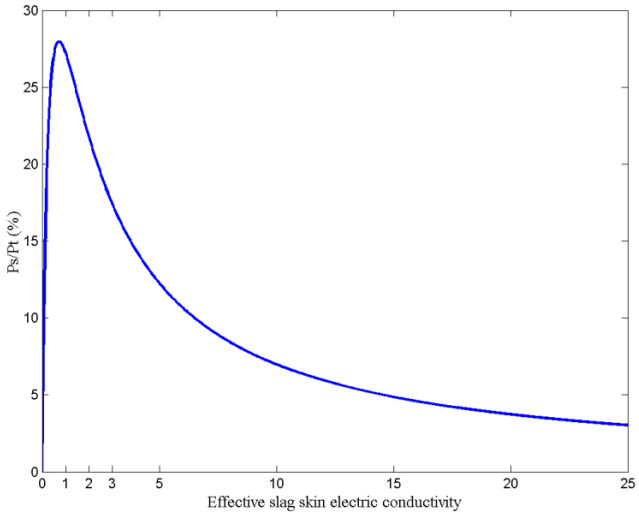

Figure 5: Proportion of the total power generated within the slag skin

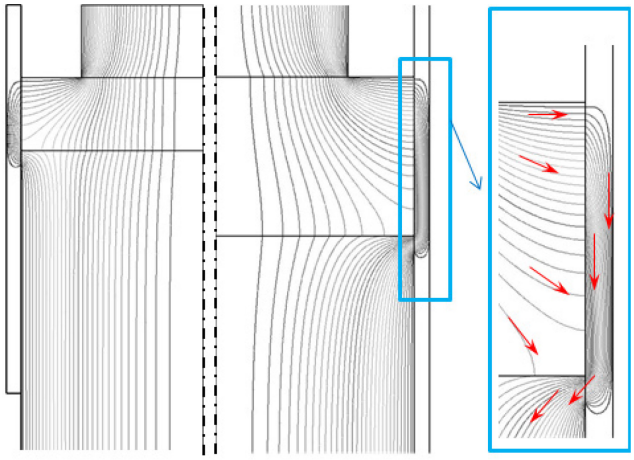

(a) 15 cm slag cap (b) 30 cm slag cap

Figure 6: Electric current path for two slag heights for the case of mould insulated from the baseplate. On the right the electric current vectors are shown in a the region near the mould.

Effect of the mould current on the slag skin thickness

Let us consider the energy balance within the slag skin. The warmer liquid slag (or liquid metal) provides a heat flux Q_{Slag} wich enters the slag skin. At equilibrium the heat entering the mould Q_{Mould} consists in the sum of Q_{Slag} and the heat generated by the Joule heating within the slag skin Q_{Joule} :

$$Q_{Slag} + Q_{Joule} = Q_{Mould} \quad (1)$$

The thin attribute of the slag skin allows us to rewrite it in the following form:

$$\delta^2 \frac{j^2}{\sigma} + \delta Q_{Slag} - k_s \Delta T = 0 \quad (2)$$

Where j is the electric current crossing the skin, δ is the skin thickness, σ is the effective slag skin electric conductivity, and $\Delta T = T_{liq} - T_{mould}$ is the drop in temperature across the slag skin. In the present analysis consider the hot side of the skin to be the slag liquidus temperature. k_s is an average heat conductivity of the solid slag . The magnitude of the temperature drop across the slag skin depends on the quality of the heat contact with the copper mould. In the case of a perfect contact, $\Delta T \sim 1650 - 500 \sim 1000\ K$. In real process a jump in temperature exists at the interface with the mould, so the temperature drop across the skin is probably smaller $\Delta T \sim 400 - 900\ K$.

Without mould current (j=0) the thickness is simply inversely proportional to the heat flux:

$$\delta_0 = \frac{k_s \Delta T}{Q_{Slag}} \quad (3)$$

In the presence of mould current the solution is:

$$\delta(j) = Q_{Slag} \frac{\sqrt{1 + \frac{j^2}{j_c^2}} - 1}{2\frac{j^2}{\sigma}} \quad (4)$$

with j_c defined as:

$$j_c^2 = \frac{\sigma Q_{Slag}^2}{4 k_s \Delta T} = \frac{\sigma}{4\delta_0^2} k_s \Delta T \quad (5)$$

When $j \ll j_c$, the slag skin thickness decreases quadratically with the intensity of mould current :

$$\delta(j) \approx \quad \delta_0\left(1 - \frac{j^2}{2j_c^2}\right) \tag{6}$$

For very large electric current density $j \gg j_c$, the thickness decreases with the inverse of the electric current density :

$$\delta(j) = Q_{Slag}\frac{\sqrt[2]{1+\frac{j^2}{j_c^2}}-1}{2\frac{j^2}{\sigma}} \approx \quad \frac{\sigma Q_{Slag}}{2j_c\, j} \tag{7}$$

In the ESR process the current j is function of the difference in electric potential across the skin thickness is not independent of δ :

$$\mathrm{j} \sim \sigma\frac{\varphi_{liq} - \varphi_{Mould}}{\delta} = \sigma\frac{\Delta\varphi}{\delta} \tag{8}$$

For the sake of simplicity we assume that the mould is connected with the baseplate, in this case we can assume φ_{Mould} constant and equal to zero. The solution of equation (Eq. 2) simplifies into:

$$\delta \quad = \frac{k_s\Delta T - \sigma\Delta\varphi^2}{Q_{Slag}} \tag{9}$$

The slag skin thickness decreases linearly with σ and quadratically with the jump in potential acros the skin. The maximum possible difference between the liquid slag and the mould electric potential is:

$$\Delta\varphi_{max} = \sqrt{\frac{k_s \Delta T}{\sigma}} \qquad (10)$$

This represents a physical limit for the Joule heat released over which the skin layer cannot sustain its solid nature ($\delta > 0$). As example by using $k_s = 0.5$, $\sigma = 1$, we obtain $\Delta\varphi_{max}$~22 Volt. The maximum difference in potential $\Delta\varphi$ is reached at the gas/slag interface. The question is whether the limit (Eq. 10) can be reached or not during the process. In both live and insulated mould cases, the potential of the mould φ_{Mould} can be considered as constant. The magnitude of $\Delta\varphi$ varies with the axial position along the mould and reaches its maximum at the top slag/gas interface. This maximum depends directly on the fill ratio and must be compared with$\Delta\varphi_{max}$. By increasing the size of the electrode, $\Delta\varphi$ becomes closer to the operating voltage of the process (typically 30-70 Volts). Therefore depending on the properties and the height of the slag, there exists a maximum fill ratio so that $\Delta\varphi < \Delta\varphi_{max}$. It is clear that more resistive is the slag skin, larger can be the fill/ratio. We believe that relation (Eq. 10) explains also why ESR processes are successfully run with large fill ratio only if the slag height is not too high.

Correlation between Electric current distribution and Ingot surface quality

The slag skin is first formed at the slag level, and then it enters the liquid metal pool where it can either keep its size or melt. Good ingot surface quality is believed to be achieved if the slag skin melts completely or at least partly. For each empirically known correlation, a conventional explanation related to heat transferred to the slag skin (Q_{Slag} in Eq.1.) exists.

The proposed explanation based on the Joule heat released within the slag skin Q_{Joule} is related to the magnitude I_m or proportion of the mould current (I_m/I_t). A summary of concurrent explanations is presented in table1.

The two cases (B-C) are highly related and cannot be separated, higher melt rate are only reached by increasing the magnitude of the applied current and so the power. The cases D and C decrease the heat losses by decreasing the area in contact with the electrode, the air and the mould. However these two cases, as mentioned in previous sections, are related to the geometrical characteristics which control the amount of mould current. The case A is better related to the electric explanation by the fact that if similar melt rates are obtained with two different slags, resistive slags although using lower electric intensity gives usually better surface quality.

Table 1. Factors influencing the ingot surface quality and possible explanation

Cases	Empirical correlation towards better ingot surface quality	Explanation based on slag temperature	Explanation based on mould current
A	Higher slag resistance ↑	Higher slag temperature ↑	I_m/I_t ↑
B	Melt rate ↑	Higher slag temperature Stronger liquid pool stirring	I_m ↑
C	Power, applied current ↑	Higher slag temperature Stronger stirring in the slag and metal	I_m ↑
D	Fill ratio (Re/Rm) ↑	Heat lost at the exposed slag surface ↓	I_m/I_t ↑
E	Electrode penetration depth ↓	Slag/mould surface ↓ heat lost ↓	I_m/I_t↑

3 Summary

Despite its very small electric conductivity, the solid slag skin can largely conduct a large amount of electric current. The proportion of electric current entering the mould is function

of the slag electrical conductivity, the slag height, electrode penetration depth and the fill ratio. These parameters are also known to influence the ingot surface quality. We suggest the hypothesis that the Joule heating generated within the slag skin contributes largely to the ingot surface quality. Results of simulations show that a large amount of Joule heating is generated within the slag skin volume. The electric current that crosses skin at the liquid metal level can easily reach high electric current density. Depending on the heat balance, this additional heat contributes certainly to the melting of the slag skin volume.

Acknowledgements

The authors acknowledge the financial support by the Austrian Federal Ministry of Economy, Family and Youth and the National Foundation for Research, Technology and Development.

References

1. A. Mitchell, M. Etienne, "The solidification of Electroslag fluxes," *Transactions of The Metallurgical Society of AIME,* 242 (1968), 1462-1464

2. M. Bell, A. Mitchell, "Some observations on the surface quality of Electroslag ingots," *Journal of the Iron and Steel Institute,* 209 (8) (1971), 658-670.

3. B. Korousic, V. Osterc, *Radex-Rundschau* (Österreichisch,Österreichisch Amerikanische Magnesit A.G., 1976), 803-813.

4. J. Cameron, M. Etienne, A. Mitchell, "Some electrical characteristics of a DC electroslag unit," *Metallurgical Transactions*,1 (7) (1970), 1839 – 1844.

5. J.D.W. Rawson, G. Jeszensky, A.W. Bryant, "Novel slags for ESR," *Proc. of 6th Int. Vac. Met. Conf. on Special Melting*, San Diego, 1979, 848-863.

6. P.O. Mellberg, "Temperature distributions in slag and metal during Electroslag remelting of ball-bearing steel," *ISIJ Proc. of 4th Int. Symp. on ESR Processes*, Tokyo, 1973, 13-25.

7. T.Kusamach, T.Ishii, T. Onoye, K. Narita, “Effects of composition of slags on heat transfer characteristics in electroslag remelting process,” *Tetsu-to-Hagane*, 12 (1980), 1640-1649.

8. A. *Kharicha ,* W. *Schützenhöfer*, A. Ludwig , G. Reiter, “Reformulation of the Joule heating in presence of turbulent fluctuation,” *Int. J. Cast Metals Research*, 22 (2009), 155-159.

9. A. *Kharicha ,* W. *Schützenhöfer*, A. Ludwig , G. Reiter, M. Wu, “On the importance of electric currents flowing directly into the mould during an ESR process*,” Steel Research Int.*, 79 (2008) 632-36.

10. S.F. Medina and M.P. de Andres, “Electrical field in the resistivity medium (slag) of the ESR process: influence on ingot production and quality,” *Institute of Metals,* 2 (1987), 110-121.

11. A.Mitchell and S.Joshi, “The thermal characteristics of the electroslag process,” *Met. Trans.*, 4 (1973), 631-642.

12. A. Mitchell and S. Joshi, “Some observations on the electrical and thermal properties of the slag-skin region in the Eletroslag remelting process,” *Met. Trans.,* 2 (1971), 449–455.

13. A. Mitchell and J. Cameron, “The electrical conductivity of some liquids in the system CaF_2+ CaO + Al_2O_3,” *Met. Trans.,* 2 (1971), 3361-3366.

Publication III

Influence of crystal morphological parameters on the solidification of ESR ingot

E. Karimi-Sibaki, A. Kharicha, J. Korp, M. Wu, A. Ludwig

Mater. Sci. Forum 790-791 (2014) 396-401

Influence of Crystal Morphological Parameters on the Solidification of ESR Ingot

E. Karimi-Sibaki[1,a], A. Kharicha[1,2,b], J. Korp[3,c], M. Wu[1,2,d] and A. Ludwig[2,e]

[1] Christian Doppler Laboratory for Advanced Process Simulation of Solidification and Melting,

[2] Chair of Simulation and Modeling of Metallurgical Processes, Univ. of Leoben, Austria

[3] Schmiedetechnik Breitenfeld GmbH, 8662 Mitterdorf im Mürztal, Austria

[a] ebrahim.karimi-sibaki@unileoben.ac.at, [b] abdellah.kharicha@unileoben.ac.at,

[c] Joerg.korp@breitenfeld.at, [d] menghuai.wu@unileoben.ac.at, [e] ludwig@unileoben.ac.at

Keywords: Electroslag remelting, AC frequency, Dendrite arm spacing, Permeability.

Abstract

Electroslag remelting (ESR) is an advanced process to produce high quality steel. During the ESR process, the steel electrode is melted and then solidified directionally in a water-cooled mold. The quality of the ingot is strongly dependent on the shape of melt pool, i.e. the depth and thickness of mushy zone, which is in turn influenced by the bulk and interdendritic flow. Here, we perform a numerical study to investigate the effect of crystal morphological parameter such as primary dendrite arm spacing on the solidification of the ESR ingot (ϕ 750 mm). The crystal morphology is dominantly columnar and dendritic, thus a mixture enthalpy-based solidification model is used. Accordingly the mushy zone is considered as a porous media where the interdendritic flow is calculated based on the permeability. The permeability is determined as function of the liquid fraction and primary dendrite arm spacing according to Heinrich and Poirier [Comptes Rendus Mecanique, 2004, pp. 429-445]. The modeling results were verified against experimental results.

1 Introduction

Electroslag remelting (ESR) process is known for production of homogenous ingot with minimal defects such as macrosegregation, accumulation of non-metallic inclusions, and microporosity [1]. Within the process, the melt pool is solidified directionally that results in uniform and relatively fine dendritic structure [2]. The dendritic structure is mostly influenced by the cooling rate in the process, temperature gradient ahead of the crystallization front, and the intensity of interdendritic flow. With the increase of cooling rate, the local solidification time decreases and the mushy zone becomes thinner. Furthermore, an intensive flow in the melt pool promotes the formation of the freckles and leads to macrosegregation [3]. Slow and laminar interdendritic flow is desirable to achieve a finer structure for the final ingot. Principally, the flow is driven by the induced magnetic field that strongly depends on the operating conditions of the process. Over the last decades, attempts have been made to predict the melt pool shape of an ESR ingot using CFD models [4-6]. Most often, the decay of liquid movement in mushy zone has been modeled using the isotropic drag law of Carman-Kozeny [7] in which the dependency of permeability on the direction of solidification is ignored. In the meanwhile, some efforts were done to calculate the dendrite arm space based on local solidification time for ESR process [8-9]. In the current study, the effect of the direction of solidification on the interdendritic flow is considered using an anisotropic model for permeability. For this purpose, the distribution of dendrite arm space is calculated for the ESR ingot. Then, the effect of local variation in arm space on the directional permeability is taken into account. Additionally, the importance of dendrite arm space on the predicted melt pool shape is investigated by performing another simulation in which the parameter is kept homogenously constant in the mushy zone. The goal is to achieve some fundamental understanding of the formation of melt pool of

solidifying ESR ingot considering the influence of crystal morphology and interdendritic velocity.

2 The Numerical model

The Finite Volume Method (FVM) is applied to simulate the fluid flow, electromagnetic field, heat transfer and solidification during the ESR process. The required modeling equations are implemented in the commercial CFD software, FLUENT-ANSYS v.14.5, using User-Defined Functions (UDF). The computational domain and boundaries are schematically illustrated in Fig. 1. The induced magnetic field has only azimuthal direction, and thus the conditions are axisymmetric in the process. The latter is expressed using the phasor notation ($B_\theta = \widetilde{B}_\theta e^{i\Omega t}$) in which Ω is the angular frequency.

After computing the magnetic field (Eq. 1), the electric current ($\widetilde{\vec{j}}$) can be obtained through Ampere's law (Eq. 2):

$$\frac{\partial B_\theta}{\partial t} + \left[\frac{\partial}{\partial z}\left(\frac{1}{\sigma\mu_0}\frac{\partial B_\theta}{\partial z} \right) + \frac{\partial}{\partial r}\left(\frac{1}{r\sigma\mu_0}\frac{\partial (rB_\theta)}{\partial r} \right) \right] = 0. \tag{1}$$

$$\widetilde{\vec{j}} = \frac{1}{\mu_0}(\vec{\nabla} \times \widetilde{B}_\theta). \tag{2}$$

Finally, the Lorentz force ($\vec{F}_L$) and Joule heating (Q) are computed, and added as the source terms to the momentum and energy equations respectively [10-11].

$$\vec{F}_L = \mathrm{Re}(\frac{1}{2}\vec{j} \times \widetilde{B}_{\theta\ Conjugate}). \tag{3}$$

$$Q = \mathrm{Re}(\frac{1}{2\sigma}\widetilde{\vec{j}} \times \widetilde{\vec{j}}_{\theta\ Conjugate}). \tag{4}$$

An enthalpy conservation equation is solved to model the solidification of the ingot:

$$\frac{\partial}{\partial t}(\rho h)+\nabla\cdot\left(\rho\vec{u}h\right)=\nabla\cdot(\lambda\nabla T)+Q+S. \tag{5}$$

Where λ is thermal conductivity of the alloy, and S is the source term of solidification latent heat. The treatment of solidification latent heat includes two parts:

$$S=-\frac{\partial}{\partial t}(\rho fL)-\rho L\vec{u}_{\mathrm{s}}\nabla f \tag{6}$$

Eq. (6) ρ and L are density and latent heat of fusion, u_{s} is the casting velocity and f denotes the liquid fraction. The unsteady term in the right hand side of the Eq. (6) can be omitted when the process approaches steady state. We treat the steel as an effective binary Fe-C alloy system, and the alloy element C is very diffusive in both liquid and solid. Thus, lever rule [12] is chosen to calculate the liquid fraction as a function of temperature. The equation is expressed as:

$$f=\begin{cases}1 & T>T_{liquidus}\\ 1-\left[(T_{liquidus}-T)/\left((T_f-T)(1-k_p)\right)\right] & T_{solidus}<T\le T_{liquidus}\\ 0 & T\le T_{solidus}\end{cases} \tag{7}$$

Where T_{f} is the melting point of solvent (1811 K) and k_{p} is the partition coefficient (k_{p} =0.35).

The turbulence in the slag and liquid melt pool is modeled using SST-k-ω approach [13]. It is assumed that the turbulence kinetic energy is damping inside the mushy zone. For this purpose, a sink term for turbulence kinetic energy (k) is considered according to: $-10^6 k(1-f)$. Similarly, a sink term for the turbulence specific dissipation rate (ω) is used: $-10^6\omega(1-f)$. It is beyond the scope of the present study to model the macrosegregation and solutal buoyancy driven flow. However, thermal buoyancy (Boussinesq approximation) and Lorentz force are taken into account as source terms for

momentum equation. The drag resistance of the dendrites to the flow in the mushy region is estimated according to the permeability [14]. For the latter, the anisotropic model of Heinrich and Poirier is used [15].

$$K_{Parallel} = \begin{cases} 3.75\times10^{-4} f^2 {d_1}^2 & 0 < f \le 0.65 \\ 2.05\times10^{-7}\left[\dfrac{f}{1-f}\right]^{10.739} {d_1}^2 & 0.65 \le f \le 0.75 \\ 0.074\left(\ln(1-f)^{-1} - 1.49 + 2(1-f) - 0.5(1-f)^2\right) {d_1}^2 & 0.75 \le f < 1.0 \end{cases} \tag{8a}$$

$$K_{Perpendicular} = \begin{cases} 1.09\times10^{-3} f^{3.32} {d_1}^2 & 0 < f \le 0.65 \\ 4.04\times10^{-6}\left[\dfrac{f}{1-f}\right]^{6.7336} {d_1}^2 & 0.65 \le f \le 0.75 \\ \left[-6.49\times10^{-2} + 5.43\times10^{-2}\left[\dfrac{f}{1-f}\right]^{0.25}\right] {d_1}^2 & 0.75 \le f < 1.0 \end{cases} \tag{8b}$$

where d_1 refers to the spacing of the primary dendrite arm, K_{Parallel} and $K_{\text{Perpendicular}}$ are the directional permeabilities. A number of models were presented to estimate the spacing of the dendrites arm according to the cooling rate and solute concentration [16]. Here, we used a model of Jacobi [17] where the size of the dendrites (expressed in μm) are computed according to the cooling rate, $\dot{T} = \vec{\nabla} T \cdot \vec{u}_s$, ahead of the crystallization front.

$$d_1 = 283\dot{T}^{-0.49} \tag{9}$$

The rate of cooling is considered to be very fast adjacent to the mold wall where the primary dendrite arm spacing is assumed constant (d_1 =50 μm). The heat radiation at air gap, slag-air, and ingot-air interfaces is considered using a value of 0.8 for the emissivity. The tip of the electrode takes the liquidus temperature of the steel. The free-slip boundary

condition is applied for the flow at slag-pool interface, whereas the condition is no-slip at electrode-slag interface and at the mold wall. The boundary conditions for magnetic induction (Eq. 1) are obtained using ampere's law. In addition, the continuity of magnetic flux is applied at slag-pool, and electrode-slag interfaces [18].

The solidification of a conventional steel ingot (X12CrNiMoV) with the size (diameter: 750 mm, height: 1875 mm) was simulated. Diameter of the electrode is 500 mm. The industrial measurements of material properties of slag and steel that are temperature dependent are used for our simulations. Details about the operating conditions of the process and the average physical properties of the slag and alloy are described in Table 1. Transient calculation was made, but only the final steady state results are analyzed.

Table 1. Averaged material properties and process parameters.

Slag	
Density ($kg \cdot m^{-3}$)	2650
Viscosity ($kg \cdot m^{-1} \cdot s^{-1}$)	0.002
Specific heat, liquid ($J \cdot kg^{-1} \cdot K^{-1}$)	1250
Thermal Conductivity, liquid ($W \cdot m^{-1} \cdot K^{-1}$)	10
Electric Conductivity, liquid ($ohm^{-1} \cdot m^{-1}$)	120
Electric Conductivity, solid ($ohm^{-1} \cdot m^{-1}$)	15
Steel	
Density ($kg \cdot m^{-3}$)	7100
Viscosity ($kg \cdot m^{-1} \cdot s^{-1}$)	0.006
Liquidus Temp. (K)	1760
Solidus Temp. (K)	1670
Thermal expan. Coefficient (K^{-1})	$9x10^{-5}$
Latent heat of fusion ($J \cdot kg^{-1}$)	260000
Thermal Conductivity, liquid($W \cdot m^{-1} \cdot K^{-1}$)	40
Electric Conductivity, liquid($ohm^{-1} \cdot m^{-1}$)	$8.8x10^{5}$
Operating condition	
RMS current (kA)	14.1
AC frequency (Hz)	50
Slag height (m)	0.15

The simulation results were verified against experimental ingot (Fig. 2(c)). The pool profile was marked using solid tungsten granulate. The sizes of markers are in the range between 1 to 2 mm. Two lines are visible on the macrograph where the lower line is obtained by

addition of tungsten to the process from a blind hole in the electrode. The upper line indicates the pool profile that was marked manually during remelting. Details about the conditions of the experiment were presented by Holzgruber [19].

3 Results and Discussions

The process is run under the frequency of 50 Hz and the electric current is allowed to cross the slag skin layer and flow through the mold as shown in Fig. 2(a). The skin effect, tendency of the electric current to flow near the surface, can be observed in the electrode, ingot, and mold.

The current re-enters to the steel ingot from the contact region (assumed to be 3 cm) between the solidified ingot and mold. Additionally, eddy currents generated in the copper mold can propagate inside the steel ingot. As indicated in Fig. 2(b), the temperature is relatively uniform in the slag region due to rigorous stirring of the flow. The well-known flow recirculation under the edge of the electrode captures significant amount of heat released in the slag [18, 20]. Consequently, the hottest zone is under the shadow of the electrode where the flow is swirling. A relatively good agreement in the shape of melt pool is obtained between the simulation and experimental results, as shown in Fig. 2(c). Fig. 2(d) illustrates the distribution of primary dendrite arm spacing (PDAS).

With the increase of the distance from the mold wall toward the center, the cooling rate decreases and consequently the PDAS increase as well. As such, the largest PDAS (~ 2.8 mm) is observed in the region near to the ingot axis. The distribution of arm spacing is found to be dominantly parabolic inside the mushy zone. However, dendrites become finer with approximately uniform size in the vicinity of the ingot surface. The measuring data of dendritic structure is not available for this experimental ingot. Previously, Borodin [21] performed experiments on ESR ingots (ϕ 400 mm and ϕ 500 mm) of Cr-Mo-V to

investigate crystal morphology and segregation of elements. The PDAS is observed to be in the range between 50 to 3000 µm which is not far from what we predicted by using Eq. (9).

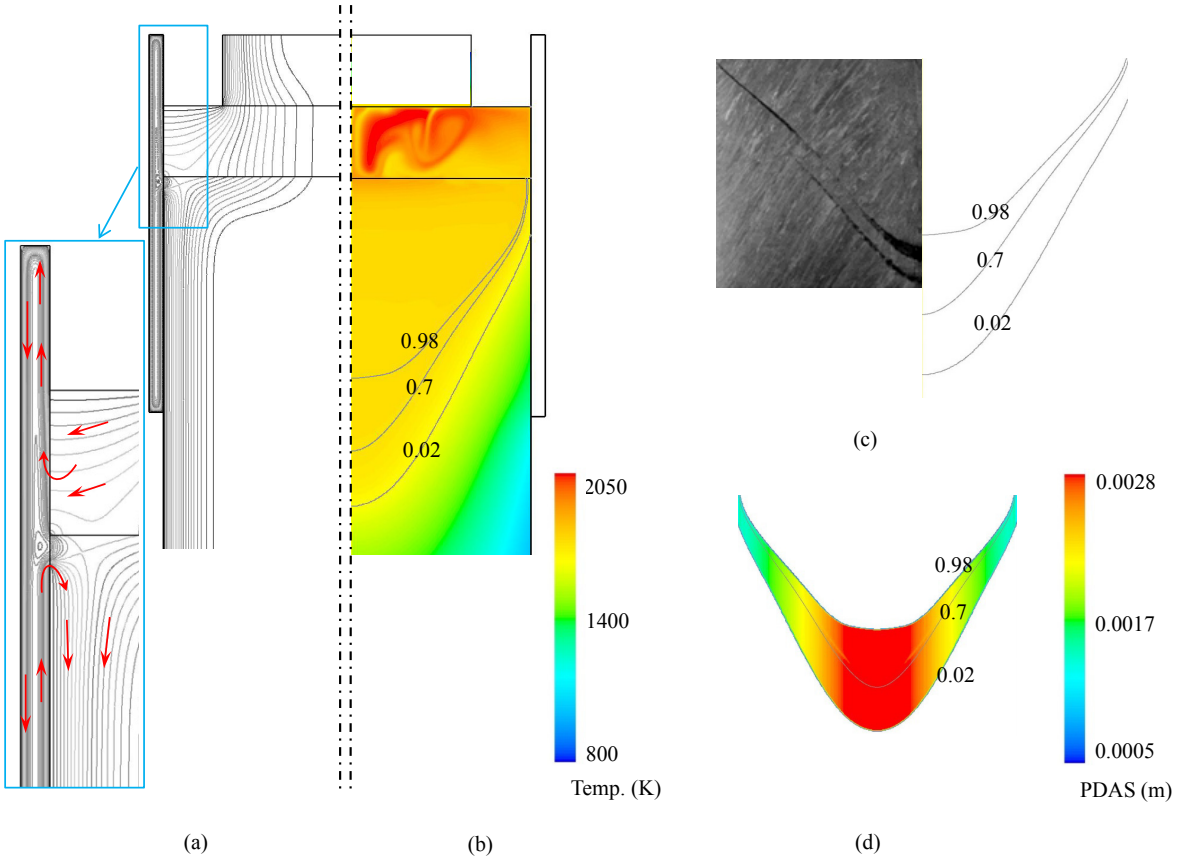

Fig. 2. (a) Electric current path (red arrows show the direction of electric current); (b) contour of temperature overlaid with isolines of fraction liquid (0.02, 0.7, 0.98) to indicate the mushy zone ; (c) Comparison of the experimental (left) with the numerical (right) results of the shape of the melt pool; (d) distribution of the calculated PDAS in the mushy zone.

The influence of the interdendritic flow on the pool shape is studied by performing an additional simulation in which the PDAS is kept to be constant (d_1 =300 µm) inside the mushy zone. For the latter, it is observed that the V-shaped pool profile is relatively deep without flattening at the center as shown in Fig. 3(a). However, flattening of the pool profile is predicted when the PDAS is computed using Eq. (9). In addition, the interdendritic melt flow is illustrated in Fig. 3(c). The relative velocity of interdendritic flow and casting

velocity is zero for the case with constant arm space. Thus, the velocity of the melt inside the mushy zone is equal to the casting velocity. In contrast, the interdendritic flow is quite intensive for the case when the PDAS is computed using Eq. (9). It is found that melt can flow in any direction inside the mushy zone especially at large liquid fraction ($f > 0.7$).

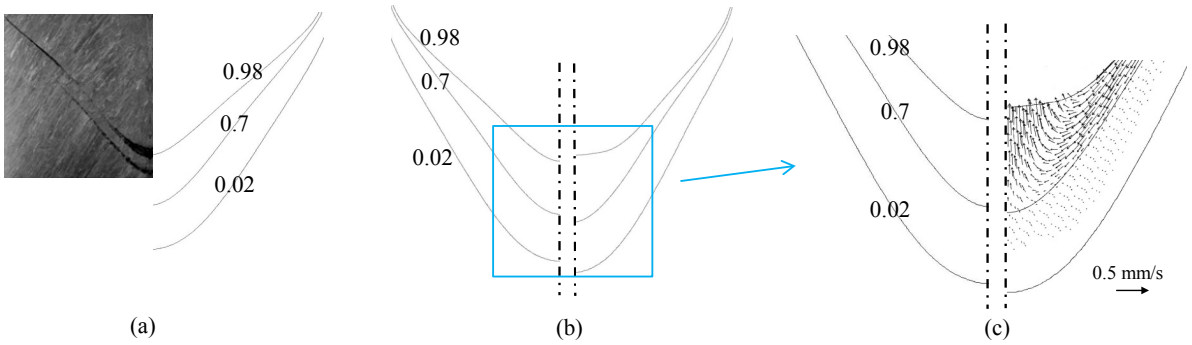

Fig. 3. (a) comparison of the experimental (left) result of the shape of the melt pool with the numerical (right) one when PDAS is assumed constant (d_1=300 μm); (b) shapes of melt pool predicted with a constant (left) PDAS vs. variable (right) PDAS; (c) interdendritic melt flow with a constant (left) PDAS vs. variable (right) PDAS.

4 Summary

A numerical study was performed to investigate the influence of crystal morphological parameters such as the primary dendrite arm spacing (PDAS) on the shape of the melt pool for an ESR ingot (ϕ 750 mm). The ESR process is operated under alternating electric current (50 Hz), and the electric current can cross the slag skin and enter into the mold. The shape of the melt pool was also measured experimentally in a plant trial. The distribution of PDAS is calculated as a function of the local cooling rate. Then, the computed PDAS is applied to estimate the directional permeability inside the mushy zone. Finally, the predicted pool profile is validated against the experiment. In addition, the effect of interdendritic flow is investigated by performing another simulation with an assumption of

constant and homogenously distributed PDAS (d_1 = 300 μm) in the mushy zone. Different interdendritic melt flow and different shape of the melt pool were predicted in the two simulations. Essentially, the interdendritic flow is controlled by the permeability that strongly depends on the PDAS. Generally, the liquid velocity inside the mushy zone is significantly smaller than the velocity in the melt pool or slag. However, the two cases presented above were predicting different pool profile as a consequence of interdendritic velocity. For this reason, the permeability, PDAS, and interdendritic velocity must be modelled with extreme care to improve the accuracy of results.

Acknowledgements

The authors acknowledge the financial support by INTECO GmbH and the Austrian Federal Ministry of Economy, Family and Youth and the National Foundation for Research, Technology and Development within the framework of the Christian Doppler Laboratory for Advanced Process Simulation of Solidification and Melting.

References

[1] G. Hoyle, Electroslag Processes, Applied Science Publishers, London, 1983.

[2] E. Plöckinger, Electroslag remelting – A modern tool in metallurgy, J. of the Iron and Steel Institute, (1973) 533-541.

[3] K. O. Yu, J. A. Domingue, G.E. Maurer and H.D. Flanders, Macrosegregation in ESR and VAR processes, J. of Metals, (1986) 46-50.

[4] V. Weber, A. Jardy, B. Dussoubs, et al., A comprehensive model of the electroslag remelting process: description and validation, Metall. Trans. B, 40B (2009), 271-280.

[5] A.D Patel, M. Gierulal, D.J. Tallman, Bounds on model parameters for computational analysis of the ESR process, Proc. of LMPC, USA (2009), 201-211.

[6] M.J.M. Krane, M. Fahrmann, Jeff Yanke, et al., A comparison of predictions of transport phenomena in electroslag remelting to industrial data, Proc. of LMPC, France (2011), 65-72.

[7] P.C. Carman, Flow of gases through porous media, Butterworths Publisher, London, 1956.

[8] W. Schutzenhofer, G.Reiter, R. Tanzer, et al., Experimental investigations for the validation of a numerical PESR-model, Proc. of LMPC, France (2007), 49-54.

[9] Z. Jiang and Y. Dong, Solidification model for electroslag remelting process, Proc. of LMPC, France (2007), 89-94.

[10] A. Kharicha, M. Wu, A. Ludwig, B. Ofner, H. Holzgruber, CFD Modeling and simulation in materials processing, Wiley publication, USA, 2012, pp. 139-148.

[11] A. Kharicha, W. Schützenhöfer, A. Ludwig and R. Tanzer, Numerical and experimental investigations on the ESR process of the hot work tool steel H11, Proc. of LMPC, USA (2009) 235-242.

[12] T.W. Clyne, W. Kurz, Solute redistribution during solidification with rapid solid state diffusion, Metall. Trans., 12A (1981), 965-971.

[13] F. R. Menter, Two-equation eddy-Viscosity turbulence models for engineering applications, AIAA Journal, 32 (8) (1994) 1598-1605.

[14] M. C. Schneider and C. Beckermann, A numerical study of the combined effects of micro segregation, mushy zone permeability and flow, caused by volume contraction and thermosolutal convection, on macrosegregation and eutectic formation in binary alloy solidification, Int. J. Heat Mass Transfer, 38(18) (1995) 3455-3473.

[15] J. C. Heinrich and D. R. Poirier, Convection modeling in directional solidification, Comptes Rendus Mecanique, 332 (5-6) (2004), 429-445.

[16] E. J. Pickering, Macrosegregation in steel ingots: the applicability of modeling and characterization techniques, ISIJ Int., 53 (6) (2013) 935-949.

[17] H. Jacobi and K. Schwerdtfeger, Dendritic morphology of steady state unidirectionally solidified steel, Metall. Trans. A, 7A (1976) 811-819.

[18] E. Karimi Sibaki, A. Kharicha, M. Wu, A. Ludwig, H. Holzgruber, B. Ofner, M. Ramprecht, A numerical study on the influence of the frequency of the applied AC current on the electroslag remelting process, Proc. of LMPC, USA (2013), 13-19.

[19] H. Holzgruber, W. Holzgruber, A. Scheriau, et al, Investigation of the implications of the current conductive mold technology with respect to the internal and surface quality of ESR ingots, Proc. of LMPC, France (2011) 57-64.

[20] A. H. Dilawari, and J. Szekely, Heat transfer and fluid flow phenomena in electroslag refining, Metall. Trans. B, 9B (1975) 77-87.

[21] I. P. Borodin, V. A. Goryainov, V. S. Koshman, et al., Influence of solidification conditions on dendritic structure and segregation of elements in electroslag remelted ingots, Steel in the USSR (15) (1985) 533-537.

Publication IV

A parameter study on the effect of slag electric conductivity on the solidification of a large scale ESR ingot

E. Karimi-Sibaki, A. Kharicha, M. Wu, A. Ludwig, H. Holzgruber, B. Ofner, M. Ramprecht

In: 2nd Int. conference on ingot casting rolling and forging (ICRF), 2014, Milan

A parameter study on the effect of slag electric conductivity on the solidification of a large scale ESR ingot

E. Karimi-Sibaki[1], A. Kharicha[1,2], M. Wu[1,2], A. Ludwig[2] , H. Holzgruber [3]

B. Ofner [3], M. Ramprecht [3]

[1] Christian Doppler Laboratory for Advanced Process Simulation of Solidification and Melting,

[2] Chair of Simulation and Modeling of Metallurgical Processes, Univ. of Leoben, Austria

[3] INTECO Special Melting Technologies GmbH, 8600 Bruck/Mur, Austria

KEYWORDS: Electroslag remelting (ESR), Magnetohydrodynamics (MHD), Solidification, Electric conductivity, Current path, Mold current, Melt pool shape.

ABSTRACT

During the electroslag remelting process (ESR), the steel electrode is melted and re-solidified directionally in a water-cooled mold to build the high grade ingot. The quality of the ingot is governed by the solidification which is characterized by the shape of the melt pool i.e. the depth, thickness of mushy zone, and etc. The shape of the melt pool is strongly dependent on the conditions of the temperature distribution and flow which are in turn influenced by the electrical parameters such as the electric conductivity of the slag (solid and liquid). The latter dominantly controls the electric current path in the process. Here, we perform a numerical study to investigate the effect of the electric conductivity of the slag on the pool shape of a large scale ESR ingot (ϕ 1823 mm). For this purpose, simulations considering different current paths (with or without mold current) are performed. Some details will be analyzed in the paper.

INTRODUCTION

The goal of the electroslag remelting (ESR) process is purifying steel or other alloys such as Ni-based super alloys. The supplied thermal energy through the Joule heating released in the slag causes formation of droplets at the tip of the remelting electrode. The droplets then pass through the slag and reach the liquid melt pool. The melt pool solidifies directionally in a water-cooled mold to manufacture the high quality ingot [1].

Most conventional ESR slags contain CaF_2-CaO-Al_2O_3 in which the electric current is conducted by ions [2-3]. A number of oxides such as SiO_2, MgO, and TiO2 may be added to modify the electric conductivity or chemical reactivity of the slag [4]. A high degree of desulphurization and deoxidation is a desirable characteristic of the slag [5]. Additionally, the electrical conductivity of slag must be decreased to generate sufficient heat through the Joule heating.

In fact, the flow of the molten slag and liquid melt pool is strongly influenced by the electromagnetic field in the ESR process. Consequently, the electrical parameters such as the AC frequency and electric conductivity of the slag have a significant effect on the quality of the final ingot. Principally, the current path is strongly dependent on the electric conductivity of slag (liquid and solid). In spite of low electric conductivity of the solid slag skin, considerable amount of current can cross the solid slag skin (mold current) entering into the mold [6-8]. In the current work, the influence of the electric conductivity of the slag on the pool shape of a large scale ESR ingot is numerically investigated.

A BREIF DESCRIPTION OF MODEL

The electromagnetic field, fluid flow, heat transfer, and solidification during the ESR process are modeled using the Finite Volume Method (FVM). The equations are

implemented in the commercial CFD software, FLUENT-ANSYS v.14.5, using User-defined functions (UDF). An axisymmetric computational domain is considered for our simulations as illustrated in Fig. 1. The crystal morphology is assumed to be mainly columnar and dendritic, thus the mushy zone is considered as a porous media. The interdendritic flow in the mushy zone is modelled based on the permeability law of Black-Kozeny [9].

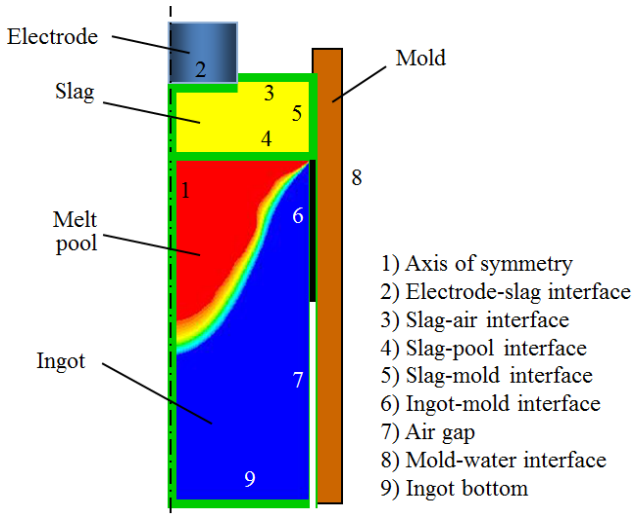

Fig. 1. Schematic representation of the boundaries and computational domain.

The Phasor notation can be used to express the sinusoidal AC magnetic field in the process ($B_\theta = \tilde{B}_\theta e^{i\omega t}$) where ω is the angular frequency. The equation to be solved is given as:

$$\frac{\partial B_\theta}{\partial t} + \left[\frac{\partial}{\partial z}\left(\frac{1}{\sigma\mu_0} \frac{\partial B_\theta}{\partial z} \right) + \frac{\partial}{\partial r}\left(\frac{1}{r\sigma\mu_0} \frac{\partial (rB_\theta)}{\partial r} \right) \right] = 0 \qquad (1)$$

Where μ_0 and σ are magnetic permeability and electric conductivity of the materials. The boundary conditions for Eq. (1) are obtained using the Ampere's law. The magnitude of magnetic flux is prescribed at mold-water and slag-air interfaces. In addition, the continuity of magnetic induction is applied at slag-pool, slag-mold and ingot-mold interfaces. After computing the magnetic field, the electric current can be obtained through: $\tilde{\vec{j}} = \frac{1}{\mu_0}(\vec{\nabla} \times \tilde{B}_\theta)$.

Finally, the time averaged Lorentz force ($\vec{F}_L$) and Joule heating (q_{Joule}) can be calculated:

$$\vec{F}_L = \mathrm{Re}(\frac{1}{2}\vec{j} \times \tilde{B}_{\theta\ Conjugate}) \tag{2}$$

$$q_{Joule} = \mathrm{Re}(\frac{1}{2\sigma}\tilde{\vec{j}} \times \tilde{\vec{j}}_{\theta\ Conjugate}) \tag{3}$$

The Lorentz force and Joule heating are added as source terms to momentum and energy equations respectively. More details about the solution of induction equation and the required boundary conditions for ESR process were presented by Kharicha [10].

The slag-pool, slag-air, and electrode-slag interfaces are assumed to be stationary and flat. Moreover, the immersion depth of the electrode is ignored in this study. The flow and thermal boundary conditions refer to the previous publication [11]. The thickness of solidified slag layer is estimated based on plant observation to be 1 cm. The slag skin layer is not in full contact with the mold surface due to shrinkage of the solidified ingot and subsequent formation of an air gap. As such, a value of 5 cm is estimated for the length of the contact region between the ingot and mold. The average physical properties of the steel and slag, operation conditions, and process geometry are listed in Table 1.

The slag system designed for this process has approximately the following composition (CaF_2: 30-40%, CaO: 30-40%, Al_2O_3: 30-40%). The electric conductivity of this slag in liquid phase was reported [12] to be between 80-300 $\Omega^{-1}.m^{-1}$. However, the parameter is unknown for the slag in solid phase. The slag skin layer is assumed to be a perfect electrical insulator in most of simulations found in literature. On the other hand, preliminary trials to produce ESR ingot using the current conductive mold (CCM) technology strongly rejects this assumption [13]. Furthermore, the perfect contact between the mold and baseplate brings the possibility for a portion of current to go directly toward the mold.

Table 1. Parameters used for our simulations.

Slag	
Density ($kg \cdot m^{-3}$)	2800
Viscosity ($Kg \cdot m^{-1} \cdot s^{-1}$)	0.002
Specific heat, liquid ($J \cdot Kg^{-1} \cdot K^{-1}$)	1250
Thermal Conductivity, liquid($W \cdot m^{-1} \cdot K^{-1}$)	10
Steel	
Density ($kg \cdot m^{-3}$)	7100
Viscosity ($Kg \cdot m^{-1} \cdot s^{-1}$)	0.006
Liquidus Temp. (K)	1779
Solidus Temp. (K)	1719
Specific heat, liquid ($J \cdot Kg^{-1} \cdot K^{-1}$)	800
Latent heat of fusion ($J \cdot Kg^{-1}$)	268000
Thermal Conductivity, liquid($W \cdot m^{-1} \cdot K^{-1}$)	40
Electric Conductivity, liquid($ohm^{-1} \cdot m^{-1}$)	880000
Operation conditions	
RMS current (kA)	36.5
AC frequency (Hz)	0.2
Power (MW)	1.8
Geometry (Static mold)	
Mold radius (m)	0.9115
Electrode radius (m)	0.725
Slag height (m)	0.265

In fact, the current selects the less resistive path through either the mold or melt pool to reach the baseplate. In the current study, the amount of power generated in the process is known in advance. This provides us helpful information to theoretically analyze the amount and consequences of mold current in the ESR process.

RESULTS AND DISCUSSIONS

A number of simulations were performed to compute the electric current path and total power consumption in the process considering variable magnitude for electric conductivity of slag and solidified slag skin. The target power of the process is known and given in Table 1. For this reason, the conductivity of slag skin layer is tuned to generate the target power in the system. In other words, variation in total power consumption as a function of slag skin electric conductivity was calculated whereas the conductivity of liquid slag is kept constant. The aim is to estimate adequate values of electric conductivity for the slag and solidified

slag layer. As indicated in Fig. 2, a summary of the results is plotted where each curve is obtained for a constant electric conductivity of liquid slag. The calculated power decreases almost exponentially with the increase of slag skin electric conductivity. The latter indicates that opening the path to the mold decreases the overall resistance of the whole system.

Since the target power is known, some correlations can be established between the electric conductivities of slag (liquid and solid), proportion of mold current, and proportion of total power consumed in solid slag layer. For the adequate conductivities, the amount of mold current and fraction of total power consumed in the slag skin were computed. The analyses were plotted against the conductivity of solid slag skin as shown in Fig. 3. The proportion of generated power in slag skin layer is raised by decrease of electric conductivity as indicated in Fig. 3 (a). The results reveal that significant amount of Joule heating is released in the thin layer of slag skin. For this reason, the skin layer will be definitely remelted and assumption of constant thickness is not valid. However, the generated power in solid slag layer with electric conductivity of 48 is negligible compared to the total consumed power in the system (~ 12% of total power). Accordingly, our primary assumption of constant thickness of the skin layer can be accepted for this case. For the latter, the ratio of current entering into the mold was predicted to be around 92 % as shown in Fig. 3 (b).

In order to explore the influence of mold current on the formation of solidifying ingot, we continue our study for two extreme cases in which the fundamental assumptions (e.g. constant thickness of slag skin layer) are valid. The operation conditions of the case studies are listed in Table 2.

Table 2. Operation conditions of the case studies.

	Electric conductivity of liquid slag ($ohm^{-1}\cdot m^{-1}$)	Electric conductivity of solid slag skin ($ohm^{-1}\cdot m^{-1}$)	Mold current
Case I	100	48	YES
Case II	90	Perfect insulator	NO

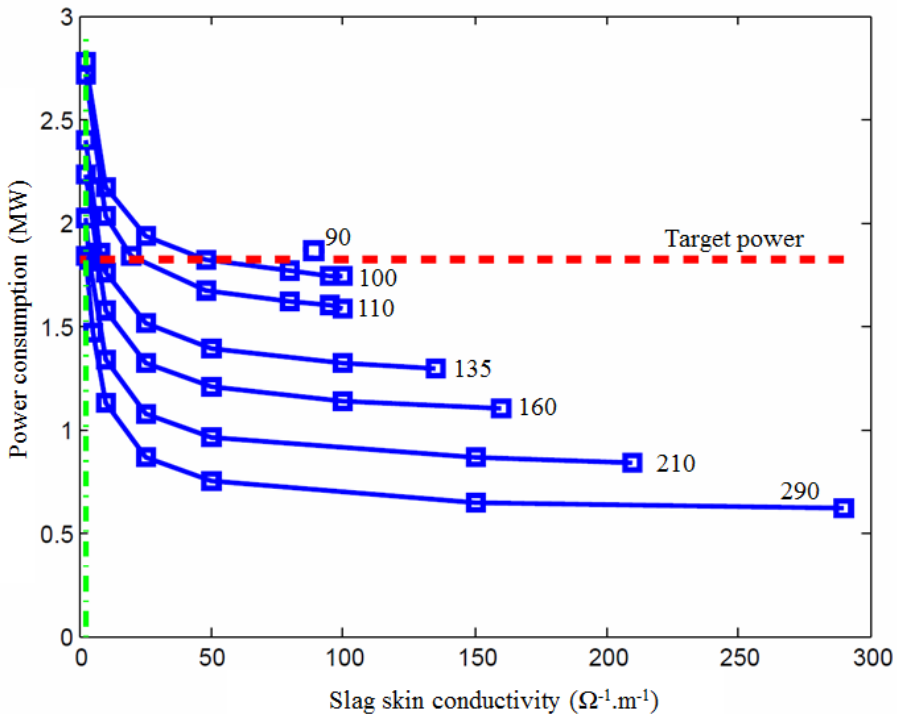

Fig. 2. Total power consumed in the process versus the electric conductivity of solidified slag layer (the constant value used to label each curve indicates the conductivity of liquid slag.)

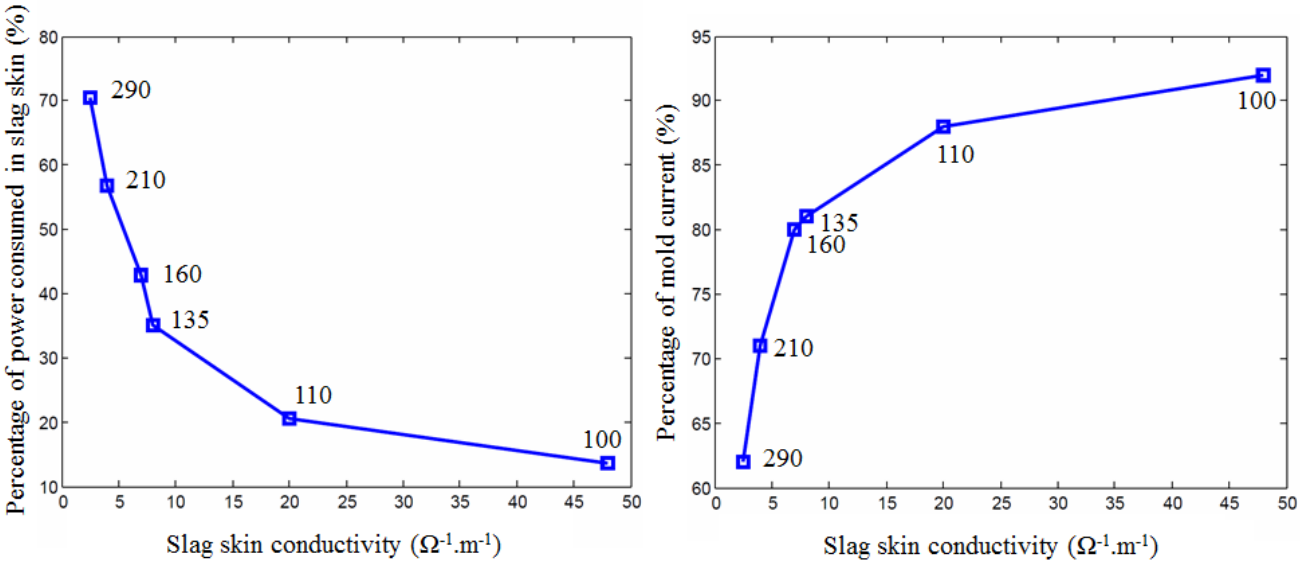

(a) (b)

Fig. 3. Proportion of (a) total power consumed in slag skin, (b) electric current entering into the mold, at target power, (the points are labeled according to the conductivity of liquid slag).

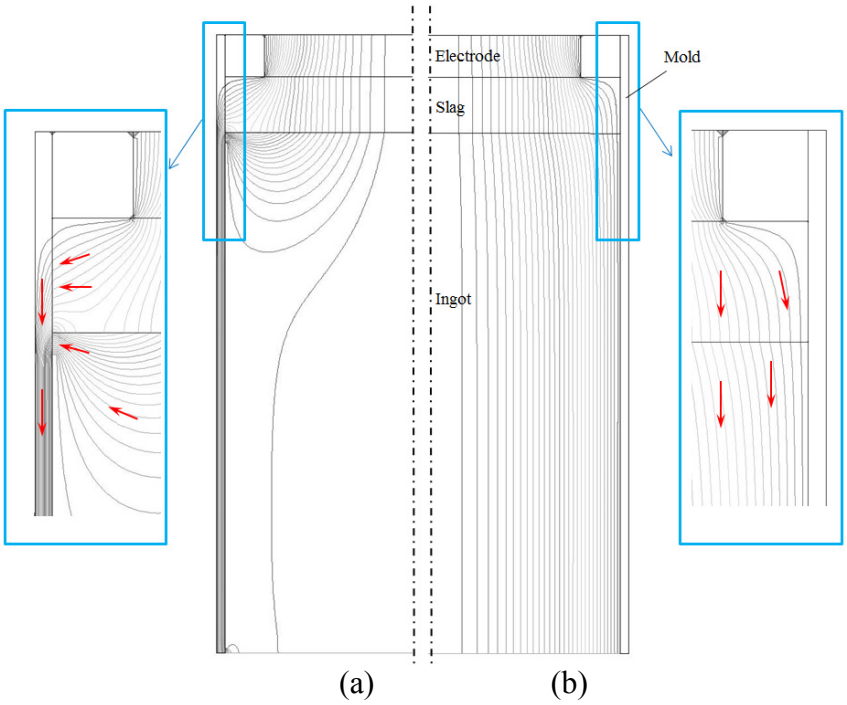

Fig. 4. Comparison of electric current paths (red arrows show the direction of current path) between the cases of (a) conducting slag skin, and (b) insulating slag skin.

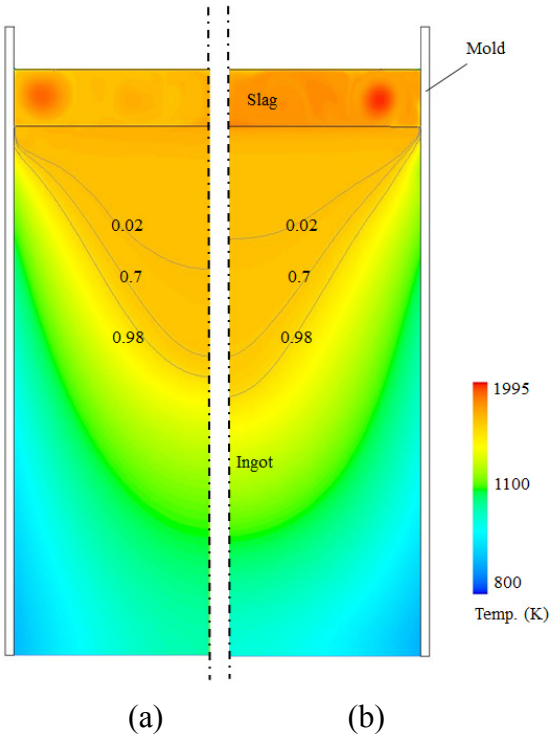

Fig. 5. Contour of temperature overlaid with isolines of fraction solid (0.02, 0.7, 0.98) to indicate the mushy zone, (a) with mold current, (b) without mold current.

The current paths in the whole system are compared for the two cases (with and without mold current) as shown in Fig. 4. In the case with mold current, a significant portion of

current enters to the mold from the contact region where noticed to be the most favorable path with minimum electrical resistance. In addition, the temperature field and pool shape are compared as shown in Fig. 5. In fact, mold current intensifies stirring leads to approximately uniform temperature in slag and melt pool regions. In the case with mold current, the depth of melt pool (the distance between the slag-pool interface and the isoline of 0.02 solid fraction) is increased. As a matter of fact, promotion of stirring with mold current enhances the global energy transfer in the process results in deeper pool and thinner mushy zone. Additionally, the distance from the slag-pool interface to the start of solidification at the ingot surface known as standing height (liquid cap) is increased. With mold current, the direction of Lorentz force bents downward near the contact region. Consequently, the hot liquid metal is pushed down near the mold wall causes increase of standing height.

SUMMARY

A numerical study was performed to investigate the influence of electric conductivity of slag (liquid and solid) on the shape of the melt pool for a large scale ESR ingot (ϕ 1823 mm). The electric current path lines were computed in the whole system considering variable electric conductivity for liquid slag and solidified slag layer. Some correlations between the conductivities are established according to the total power generated in slag and solidified slag skin. It is found that a significant amount of current can flow through the mold (mold current) despite low electric conductivity of slag skin layer. Furthermore, the fraction of mold current is increased exponentially by the decrease of electric conductivity of liquid slag. Additionally, two extreme cases are compared (with and without mold current) concerning the effect of mold current on the pool shape. Essentially, the mold current can significantly influence the standing height (liquid cap) and the melt pool shape

by promoting stirring in the process. The standing height is increased and the melt pool becomes deeper in the case with mold current.

ACKNOWLEDGEMENTS

The authors acknowledge the financial support by INTECO GmbH and the Austrian Federal Ministry of Economy, Family and Youth and the National Foundation for Research, Technology and Development within the framework of the Christian Doppler Laboratory for Advanced Process Simulation of Solidification and Melting.

REFERENCES

[1] G. Hoyle, Electroslag Processes, Applied Science Publishers, London (1983).

[2] A. Mitchell and G. Beynon, Met. Trans B. 10, (1971), p.3333.

[3] M.E. Peover, J. Inst. Metals. 100, (1972), p.97.

[4] K. Wroblewski, J. Fraley, J. Fields, R. Ewerner, S. Rudoler, Proc. of LMPC, Nancy (2011), p.121.

[5] J.J. Debarbadilo , Met. Trans A. 14, (1983), p.329.

[6] A. Kharicha, E. Karimi Sibaki, M. Wu, A. Ludwig, Proc. of LMPC, Texas (2013), p.95.

[7] M. Kawakami, K. Nagata, M. Yamamura, N. Sakata, Y. Miyashita, and K.S. Goto, Testsu- to-Hagane, 63 (1977), p. 220.

[8] S.F. Medina and M.P. de Andres, Ironmaking and steelmaking, 14 (3) (1987), p.110-121.

[9] V. R. Voller, and C. Prakash, Int. J. Heat Mass Transfer, 30(8), (1987), p.1709.

[10] A. Kharicha, W. Schützenhöfer, A. Ludwig, and R. Tanzer, Proc. of LMPC, Nancy (2011), p.113.

[11] E. Karimi-Sibaki, A. Kharicha, M. Wu, A. Ludwig, et al., Proc. of LMPC, Texas (2013), p.13.

[12] M.hajduk and T.E. Gammal, Stahl Eisen, 99 , (1979), p.113.

[13] H. Holzgruber, W. Holzgruber, A. Scheriau, et al., Proc. of LMPC, Nancy (2011), p.57.

Publication V

A dynamic mesh-based approach to model melting and shape of an ESR electrode

E. Karimi-Sibaki, A. Kharicha, J. Bohacek, M. Wu, A. Ludwig

Metall. Mater. Trans. B 46 (2015) 2049-2061

A Dynamic Mesh Based Approach to Model Melting and Shape of an ESR Electrode

E. Karimi-Sibaki[1], A. Kharicha[1,2*], J. Bohacek[2], M. Wu[1,2], and A. Ludwig[2]

[1] Christian Doppler Laboratory for Advanced Process Simulation of Solidification and Melting,

[2] Chair of Simulation and Modeling of Metallurgical Processes, Univ. of Leoben, Austria

*abdellah.kharicha@unileoben.ac.at

KEYWORDS: Melting, Joule heating, electroslag remelting (ESR), dynamic mesh, melt rate, shape of electrode tip, immersion depth, electric conductivity, thermal conductivity, electric current path, magneto hydrodynamics (MHD).

ABSTRACT

This paper presents a numerical method to investigate the shape of tip and melt rate of an electrode during electroslag remelting process. The interactions between flow, temperature, and electromagnetic fields are taken into account. A dynamic mesh based approach is employed to model the dynamic formation of the shape of electrode tip. The effect of slag properties such as thermal and electrical conductivities on the melt rate and electrode immersion depth is discussed. The thermal conductivity of slag has a dominant influence on the heat transfer in the system; hence on melt rate of electrode. The melt rate decreases with increasing thermal conductivity of slag. The electrical conductivity of slag governs the electric current path that in turn influences flow and temperature fields. The melting of electrode is a quite unstable process due to the complex interaction between the melt rate, immersion depth and shape of electrode tip. Therefore, a numerical adaptation of electrode position in the slag has been implemented in order to achieve steady state melting. In fact, the melt rate, immersion depth and shape of electrode tip are interdependent parameters of

process. The generated power in the system is found to be dependent on both immersion depth and shape of electrode tip. In other words, the same amount of power was generated for the systems where the shapes of tip and immersion depth were different. Furthermore, it was observed that the shape of electrode tip is very similar for the systems running with the same ratio of power generation to melt rate. Comparison between simulations and experimental results were made to verify the numerical model.

1 INTRODUCTION

The electroslag remelting (ESR) process is used for manufacture of premium-grade steel and super alloys such as Ni-based or titanium alloys. The Joule heating released within the molten slag layer is used to melt a consumable electrode. The departed melt droplets from the tip of electrode pass through the slag and reach the liquid melt pool. The melt pool solidifies finally in a water-cooled mold to build the high-grade, with minimum defect and segregation ingot [1]. Generally, the quality of the ingot is characterized by the surface and internal quality, which depends highly on the shape of melt pool, i.e. the depth and thickness of mushy zone. The desired outcome of the ESR process is a shallow melt pool that promotes unidirectional (upwards) solidification of the ingot and subsequent formation of segregation-minimal alloy [2]. In addition, ingots with good surface quality can be directly forged after the ESR process. The expensive process of surface machining is not required for ESR ingots with smooth surfaces [3].

The remelting parameters of the ESR process such as melt rate and immersion depth can significantly influence the quality of the final ingot. The influence of melt rate of the electrode on the melt pool depth was investigated by Holzgruber [4]. It was found that the melt pool becomes deeper with the increase of melt rate. In addition, Mitchell [5] studied the effect of melt rate on the pool profile and the thickness of mushy zone for an ESR ingot. The depth of melt pool and thickness of the mushy zone were found to increase when the

process was run with higher melt rate. On the other hand, a relatively smooth ingot surface can be obtained with higher melting rate as reported by Suarez [6]. Furthermore, it is believed that maintaining a constant shallow immersion depth of the electrode leads to producing superior quality ingots [7]. As stated by Kharicha [8], the surface quality of ingot is significantly influenced by distribution of mold current in the process that in turn depends on the electrode immersion depth.

As a consequence, the improper control of immersion depth can severely influence the compositional homogeneity and grain structure of the solidified ingot. Currently, there is no system or method for the direct measurement of the melt rate and immersion depth of electrode. Practically, the immersion depth is controlled based on the variation of impedance or voltage (voltage swing) during the process [9-12]. In this way, the increase of impedance swing is quantitatively related to the immersion depth. However, fluctuations of immersion depth are observed over the standard swing controller in many instances during the process. Therefore, the measurement precision of the actual immersion depth is questionable.

During the ESR process a massive amount of heat generated in the slag is lost through radiation and mold cooling. Only a small portion of power is supplied to melt the electrode. Over the last decades, attempts have been made to investigate the temperature profile, immersion depth, melt rate, and the shape of electrode. The effect of input power and electrode polarity on the melt rate and shape of the electrode tip were experimentally investigated by Maulvault [13]. It is reported that increasing the input power leads to higher melting speed and subsequently to a flattening of electrode tip. Mitchell et al. [14] proposed a two-dimensional model to study the heat balance across the electrode. The immersion depth is taken into account to compute the steady state temperature profile of the electrode. In addition, the electrode temperature gradient was experimentally measured for a laboratory scale ESR process. The model agreed successfully with the experimental results.

A one-dimensional analytical model was developed by Mendrykowski et al. [15] to study the heat transfer above and below the slag level. Their computed results suggest that thermal radiation is negligible in comparison to the heat conduction along the electrode. A good agreement is observed between the calculated and measured temperature profile within the electrode. Kishida et al. [16] reported the relationship between the immersion depth, shape of the electrode tip and voltage drop for a small scale ESR process. They found that with the increase of voltage, the immersion depth decreases and the shape of the electrode tip becomes flatter. Tacke et al. [17] used a two-dimensional numerical model to compute the temperature, pool profile, and immersion depth for a laboratory scale ESR electrode. An approximation formula for the immersion depth was proposed and validated against experiments.

Jardy et al. [18] modeled the ESR process to evaluate the thermal fluxes through boundaries. Their model predicted the highest melt rate for the case where the buoyance force is stronger than electromagnetic force. Yanke et al. [19] predicted melting behavior of an industrial electroslag remelting process using an effective heat transfer coefficient between electrode and slag. The results were fairly similar to measured data.

Recently, Kharicha et al. [20] directly simulated the melting of electrode using the multiphase Volume of Fluid (VOF) method considering complex interactions between flow, temperature, and magnetic fields. It is found that the coupling between the Joule heat release and melting rate is very unstable. Furthermore, it is shown that the stability in simulation can be achieved only by including a numerical adaptation on immersion depth and feeding velocity of electrode. Within the framework of the multiphase model, details of process conditions such as temperature, velocity and magnetic force can be captured. However, the method used in this investigation is computationally expensive.

It is generally recognized that the electric current is conducted by ions in the slag region [21]. The melt rate was reported to be dependent on electrode polarity. During DC ESR

process, smaller current is required for electrode positive in comparison to electrode negative to achieve the same melt rate, even though the voltage is kept unchanged [22]. The highest specific melt rate is obtained using positive polarity for electrodes containing high oxide concentrations (> 10 wt.%) due to the increase of electrochemical polarization overpotential at electrode tip-slag interface [21]. There are other phenomena that can influence the amount of supplied heat to electrode tip and consequently melt rate. For instance, a thin liquid film is formed related to formation and departure of droplets at electrode tip during remelting. Furthermore, droplets drip through the slag and they intensify turbulence under the electrode tip. As a consequence of strong turbulence, reaction rate and heat transfer between the remelting electrode and slag is enhanced [23-24].

The present model is an extension of electromagnetic model developed by Kharicha for ESR process [12, 20]. Here, a dynamic mesh based approach is used to predict the shape and melt rate of the electrode. The method is robust and computationally efficient. The effects of electrochemical polarization overpotential, formation of liquid film near the electrode tip, and dripping of droplets in slag bath are not included in the current model. Solidification of liquid metal in melt pool is ignored. Simulations considering different electric current path (with and without mold current) are performed and compared. Furthermore, the influence of electric conductivity and molecular thermal conductivity of slag on the melt rate and shape of electrode tip are investigated. Experimental results of Tacke et al. [17] are used to evaluate the current model.

2 MODELING

The commercial CFD software, FLUENT-ANSYS v.14.5, is used with a finite volume approach to simulate the fluid flow, heat transfer, and electromagnetic fields. The software includes a dynamic mesh technique for the simulation of displacements of boundaries. The required modeling equations for boundaries (stationary and moving) and fields (e.g.

electromagnetic field) are implemented using User-Defined Functions (UDF). Transient calculation is made to predict the evolution of shape of electrode tip. The induced magnetic field is dominantly azimuthal and the process conditions are assumed to be mainly axisymmetric [25], thus a 2D axisymmetric computational domain is considered. Configuration of the computational domain and boundaries are schematically illustrated in Fig. 1(a).

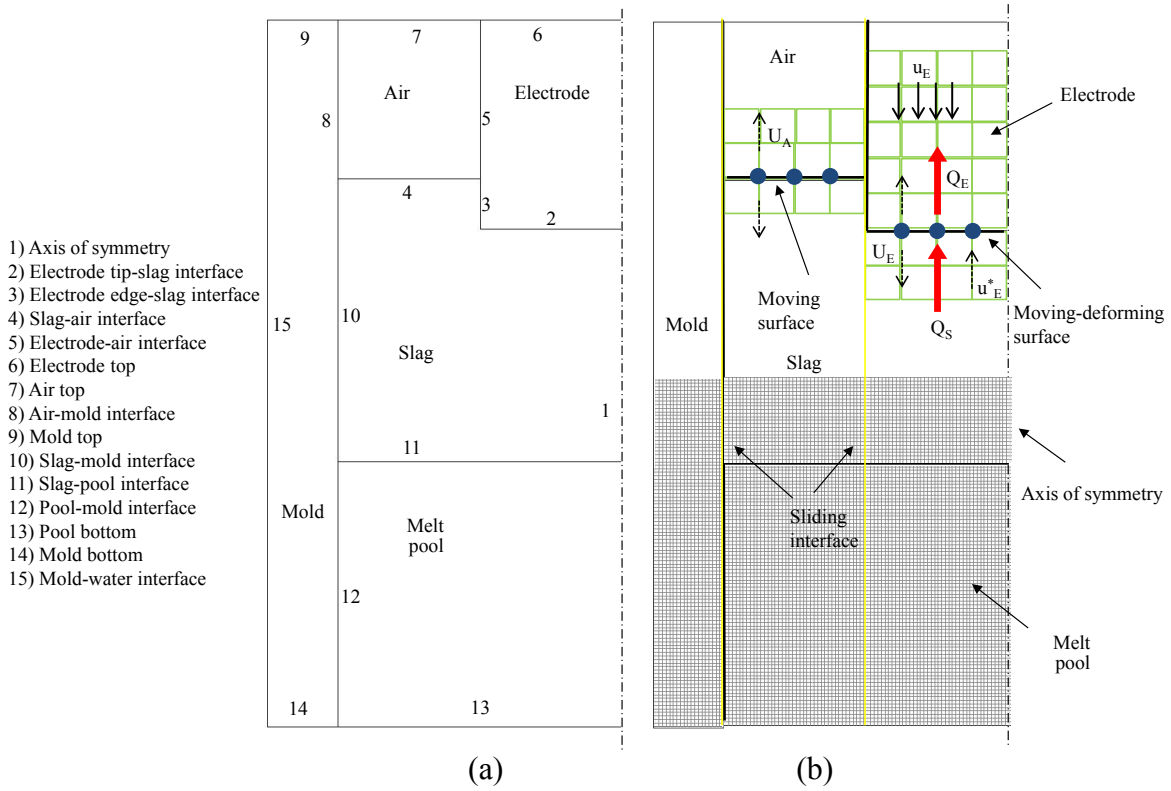

Fig. 1. (a) Schematic representation of computational domain and boundaries,

(b) Conceptual illustration of heat balances across the electrode tip and velocity of grid nodes at electrode tip-slag and slag-air interfaces. The mesh resolution is very high with equisized cells in the whole domain as shown partly in mold, slag, and melt pool. Note that the mesh resolution is shown exaggeratedly coarse near the electrode tip-slag interface (moving-deforming surface) and slag-air interface (moving surface) for illustrative purpose.

2.1 Governing equations

The computational domain includes zones of air, electrode, slag, melt pool and mold. Each zone is treated separately. However, the transport phenomena at interfaces such as momentum or heat transfer are taken into account. The interface between zones can be rigid, deforming, moving or stationary. The governing equations and the boundary conditions are introduced in the following sections. A summary of thermal and electrical boundary conditions is given in Table 1.

Air top: $T = 300K$ (27 °C), $\frac{\partial \phi}{\partial z} = 0, \frac{\partial A_z}{\partial z} = \frac{\partial A_r}{\partial z} = 0$.
Electrode top: $T = 900K$ (627 °C), $-\sigma \frac{\partial \phi}{\partial z} = \frac{I_0}{\pi R_e^2}, \frac{\partial A_z}{\partial z} = \frac{\partial A_r}{\partial z} = 0$
Slag-air interface: $\varepsilon_r = 0.8, H = 50\ W \cdot m^{-2} \cdot K^{-1}$. Slag-mold interface (slag side): $T = 1725K$ (1452 °C) Slag-mold interface (mold side): $H = 500\ W \cdot m^{-2} \cdot K^{-1}$
Pool-mold interface (pool side): $T = 1725K$ (1452 °C) Pool-mold interface (mold side): $H = 500\ W \cdot m^{-2} \cdot K^{-1}$ Pool bottom: $T = 1725K$ (1452 °C), $\phi = 0, \frac{\partial A_z}{\partial z} = \frac{\partial A_r}{\partial z} = 0$.
Mold-water interface (with mold current): $H = 7000\ W \cdot m^{-2} \cdot K^{-1}, \frac{\partial \phi}{\partial z} = 0, \frac{\partial A_z}{\partial z} = \frac{I_0}{2\pi R_m}, A_r = 0,$ Mold Top: $\frac{\partial \phi}{\partial z} = 0, \frac{\partial A_z}{\partial z} = \frac{\partial A_r}{\partial z} = 0$. Mold bottom: $\phi = 0, \frac{\partial A_z}{\partial z} = \frac{\partial A_r}{\partial z} = 0$.

Table 1. Thermal and electrical boundary conditions.

2.1.1 Electromagnetic field

The A-ϕ formulation is used to calculate the electromagnetic field [20], where ϕ denotes the electric scalar potential and $\vec{A}$ is the magnetic vector potential. The method is computationally more expensive in comparison to the common approach based on electromagnetic induction equation (B_θ), but the A-ϕ formulation is very robust and accurate for solving electromagnetic field in presence of moving boundaries. In addition, it can effectively model the current path including mold current and eddy current. The electric scalar potential is obtained by solving the conservation equation of electric current:

$$\nabla \cdot \vec{j} = 0 \tag{1}$$

The treatment of current density ($\vec{j}$) includes two parts:

$$\vec{j} = -\sigma \nabla \varphi - \sigma \frac{\partial \vec{A}}{\partial t} \tag{2}$$

First, the imposed current is computed as a function of electric conductivity of material (σ) and electric scalar potential. The second term includes the effect of eddy currents generated in the process. Note that, the unsteady term in the right hand side of Eq. (2) can be omitted when the process approaches steady state when a direct current (DC) is applied.

The magnetic field ($\vec{B}$) is calculated by solving the equation of magnetic vector potential that is expressed as:

$$\nabla \times \left(\frac{1}{\mu_0} \nabla \times \vec{A} \right) = \vec{j} \tag{3}$$

$$\nabla \times \vec{A} = \vec{B} \tag{4}$$

Note that, to obtain a unique solution for Eq. (3), the Coulomb gauge ($\nabla \cdot \vec{A} = 0$) is used [26]. Additionally, the displacement currents are ignored and the magnetic permeability (μ_0) is assumed to be constant ($4\pi \times 10^{-7}\ J \cdot m^{-1} \cdot A^{-2}$). Finally, the Joule heating (Q) and Lorentz force ($\vec{F}_L$) are computed and added as source terms to the energy and momentum conservation equations respectively.

$$Q = \frac{\left|\vec{j}\right|^2}{\sigma} \tag{5}$$

$$\vec{F}_L = \vec{j} \times \vec{B} \tag{6}$$

The required boundary conditions for electric scalar potential and magnetic vector potential (axial and radial components) are obtained from Eq. (2) and Eq. (4). A magnetic induction flux of zero is used at the bottom boundaries (mold and pool) and top boundaries (air, mold, and electrode). Additionally, a value of zero is applied for electric scalar potential at the bottom boundaries. However, an electric potential flux of zero is used at top boundaries (air and mold) except electrode top where the flux of electric potential is prescribed. The electric scalar potential is treated similar to the mold top boundary at mold-water interface where axial component of magnetic induction flux is prescribed. The latter takes the value zero for the radial component of magnetic vector potential. Furthermore, continuity of electric and magnetic potentials is applied at the following interfaces: electrode tip-slag, electrode edge-slag, electrode-air, air-mold, slag-air, slag-mold, slag-pool, and pool-mold. It

should be stated that the electric current is allowed to cross the slag skin entering into the mold (mold current). In the case of insulating mold (without mold current), the slag-mold, air-mold, and pool-mold interfaces take similar boundary conditions as mold-water interface.

2.1.2 Temperature field

The temperature field is obtained by solving an enthalpy (h) conservation equation:

$$\frac{\partial}{\partial t}(\rho h) + \nabla \cdot (\rho \vec{u} h) = \nabla \cdot (\lambda \nabla T) + Q - S_{LH} \tag{7}$$

where ρ is the density, $\vec{u}$ the velocity, and λ the effective thermal conductivity including the effect of turbulence. S_{LH} denotes the energy sink required to melt the electrode in the vicinity of electrode tip, and it is further described in section 2.3.

A combined radiation-convection condition is applied to model the heat transfer between electrode and air, and between slag and air, where a value of 0.8 is used for emissivity. At the top boundaries the temperature is fixed: 300 K (27 °C) at mold and air top, and 900 K (627 °C) at electrode top. The latter is calculated based on the electrode feeding velocity and distance from the electrode tip [20]. In addition, temperature is fixed at the slag liquidus temperature that is 1725K (1452 °C) at the following interfaces: slag-mold (slag side), and pool-mold (melt pool side). Assuming a constant thickness of solidified slag skin layer (1 mm), the heat conduction through the slag skin at slag-mold (mold side), and pool-mold (mold side) interfaces is taken into account. The cooling condition at mold-water interface is modeled using a constant convective heat transfer coefficient (7000 W/m^{2}K). The restricted maximum allowable temperature at electrode tip-slag and electrode edge-slag interfaces is the melting temperature of the alloy. In addition, the two sides of the wall at slag-pool interface are thermally coupled.

2.1.3 Turbulent flow field

The continuity and momentum equations are solved:

$$\frac{\partial \rho}{\partial t} + \nabla \cdot (\rho \vec{u}) = 0 \tag{8}$$

$$\frac{\partial}{\partial t}(\rho \vec{u}) + \nabla \cdot (\rho \vec{u}\vec{u}) = -\nabla p + \nabla \cdot (\mu(\nabla \vec{u} + \nabla \vec{u}^{T})) + \rho_0 \vec{g}\beta(T - T_0) + \vec{F}_L \tag{9}$$

where p is the pressure, μ the dynamic viscosity, $\vec{g}$ the gravity, β the thermal expansion coefficient, ρ_0 and T_0 are reference density and reference temperature, respectively. Boussinesq approximation is considered for the thermal convection in the slag region.

Non-slip boundary condition is applied at electrode edge-slag, electrode tip-slag, and slag-pool interfaces. Additionally, a free-slip condition is applied for the interfaces of slag-air, slag-mold, and pool-mold. No flow calculation is made in the air zone. Treatment of velocity inside the electrode will be discussed in section 2.4.

The turbulence is considered using the shear stress transport model (SST). The model is known to effectively blend the precision and robustness of $k-\omega$ model in the near wall region with the bulk liquid $k-\varepsilon$ modeling in far field. One of the essential features of SST model is an accurate and effective near wall treatment. The model is insensitive to the grid spacing of the near wall cells [27]. In fact, the model automatically shifts from low-Re formulation to wall functions based on the near wall grid resolution. A comprehensive description of the model was given by Menter et al. [28-29].

2.2 Dynamic mesh

Displacement of domain boundaries can be modeled using dynamic and deformable meshes in which the mesh nodes are adjusted to new locations. In order to apply this technique, all governing conservation equations must be modified according to the velocity of the grid boundaries ($\vec{u}_g$) [30]. The integral form of the general conservation equation for an arbitrary variable (ξ) with respect to the dynamic meshes is expressed as:

$$\frac{\partial}{\partial t}\int_V \rho\xi dV + \int_\Omega \rho\xi(\vec{u}-\vec{u}_g)\cdot d\vec{S} = \int_\Omega \Gamma\,\nabla\xi\cdot d\vec{S} + \int_V S_\xi dV \tag{10}$$

where Ω represents the boundary of the control volume (V), $\vec{S}$ is the area vector, Γ denotes the diffusion coefficient, and S_ξ is the source term.

The unsteady term in Eq. (10) must take into account the variation of cell sizes during the simulation of moving boundaries [31]. It can also be computed using the grid velocity:

$$\frac{\partial V}{\partial t} = \int_\Omega \vec{u}_g \cdot d\vec{S} = \sum_j^{n_f} \vec{u}_{g,j}\cdot\vec{S}_j \tag{11}$$

where n_f is the number of faces on the control volume, $\vec{u}_{g,j}$ is the velocity and $\vec{S}_j$ is the area vector of j face.

A number of dynamic mesh schemes are available to handle the boundary motion that categorize into layering, re-meshing, and smoothing techniques. In the present study, layering and smoothing techniques are employed to simulate the motion of the boundaries. Essentially, layering technique involves creation and destruction of cell rows in the vicinity of a moving boundary. Layers of cells are added or removed based on a prescribed cell

height (h_{ideal}) that is in the same order of magnitude as the cell size. The layer of cell near to the moving boundary is allowed to expand or compress if the following condition is fulfilled: $(1+\alpha_s)h_{ideal} < h_{\min}$ for expansion and $h_{\min} < \alpha_c h_{ideal}$ for compression. Here, $h_{\min}$ is the minimum cell height of the neighboring layer, α_s and α_c are the user defined split and collapse factors respectively. The method can be applied only for structured grid when the motion is purely linear like the motion of a piston in a cylinder.

On the other hand, the smoothing technique is not restricted to structured mesh. The nodes can be repositioned but the connectivity remains unchanged. Additionally, they are considered as a network of interconnected springs in which positions of interior nodes are updated based on displacements of boundary nodes. The diffusion-based smoothing method to model the mesh motion is governed by the following equation:

$$\nabla \cdot (\frac{1}{d^{\alpha}} \nabla \vec{u}_g) = 0 \tag{12}$$

where d stands for a normalized boundary distance and α is a positive arbitrary input parameter. Note that, quality of the mesh can be better preserved by increasing the diffusivity coefficient ($1/d^{\alpha}$). Thus, a value of zero is recommended for α to reduce the mesh motion away from the moving boundary [30].

The configuration of the dynamic mesh boundaries is illustrated in Fig. 1 (b). In our computational domain, the mesh has two dynamic boundaries: slag-air (moving), and electrode tip-slag (moving-deforming). The moving boundaries are interior faces, thus sliding interfaces are required to allow the relative motion between adjacent grids [30]. Geometrical data of dynamic mesh parameters are listed in Table 2.

Mesh	
Domain size (mm^2)	100 x 200
Number of computational cell	20,000
cell size (mm)	1
Dynamic mesh parameters	
Ideal cell height (mm)	1
Split factor (α_s)	0.4
Collapse factor (α_c)	0.2
Diffusion parameter (α)	0

Table 2. Geometrical data of mesh and dynamic mesh parameter

2.3 Melting of electrode tip

Both the temperature field of electrode and velocity of melting electrode tip are unknown. Generally, an alloy solidifies and develops a dendritic mushy zone. However, no dendrites were observed during melting. Thus, the liquid-solid interface is assumed to remain smooth during melting. Therefore, the melting of the electrode is considered as a Stefan problem where a phase boundary can move with time [32-33]. Here, a dynamic mesh-based approach is proposed to capture the shape of the electrode tip. A set of balance equations are solved to compute the velocity of grid nodes at the electrode tip. As shown in Fig. 1(b), the heat balance across the electrode tip determines the velocity of the grid nodes (U_E). The following equations and conditions describe the melting velocity of electrode tip:

$$Q_S - Q_E = \rho_{metal} \Delta H u_E^* \tag{13}$$

$$\begin{cases} u_E^* \geq 0 & (Q_s > Q_E) \\ u_E^* < 0 & (Q_s < Q_E) \end{cases} \tag{14}$$

$$U_E = u_E + u_E^* \tag{15}$$

According to Eq. (15), the time dependent grid node velocity of the electrode tip is the sum of melting velocity (u_E^*) and the electrode feeding velocity (u_E). The origin of x-referential is fixed at the bottom of computational domain. Consequently, the sign (positive or negative)

of melting velocity depends on the balance of the heat fluxes at the electrode tip, Eq. (14). According to Eq. (13), the melting velocity is dependent on the heat flux provided to electrode (Q_S), heat flux diffused into the electrode (Q_E), density of metal (ρ_{metal}), and latent heat of fusion (ΔH). Note that the right hand side of Eq. (13) describes the energy sink term (S_{LH}) provided to melt the electrode. The following equation expresses the volumetric source of latent heat that is absorbed in the vicinity of electrode tip.

$$S_{LH} = \rho_{metal} u_E^* \Delta H \left(\frac{S_{cell-electrode}}{V_{cell-electrode}}\right) \tag{16}$$

where $S_{cell-electrode}$ is the face area of a cell which belongs to the electrode tip and $V_{cell-electrode}$ is the cell volume.

2.4 Electrode immersion depth

Ideally, the electrode feeding velocity is constant during operation of the ESR process. However, the feeding velocity must be adapted in the simulation due to melting instabilities so that the electrode tip neither reaches the melt pool nor the slag free surface [20]. The electrode feeding velocity is adapted based on the initial feeding velocity (u_E^0), and immersion depth (l) as given by Eq. (17).

$$u_E = u_E^0 \min\left[1, \frac{l_{\max} - l}{l_{\max} - l_{\min}}\right] \tag{17}$$

The immersion depth is bounded between $l_{\min}$ and $l_{\max}$, and both are input parameters. As such, the electrode penetration depth is limited to $l_{\max}$. Note that, the uniform velocity field

inside the electrode zone is specified that has the magnitude equal to the electrode feeding velocity (u_E).

Transient simulation is performed until a steady state is reached when the velocity of the grid nodes (U_E) becomes zero. The melt rate ($\dot{m} \geq 0$) of the electrode can be estimated as:

$$\dot{m} = -\rho_{metal} \iint_{S_{electrode}} \vec{u}_E^* \cdot d\vec{S} \tag{18}$$

where $S_{electrode}$ is the tip area of electrode.

With the increase of electrode immersion depth, the slag level rises since the total mass of slag must be conserved. The latter is modeled by considering a constant velocity for the grid nodes at slag-air interface. The velocity of slag-air interface (U_A) is computed as:

$$U_A = \frac{m_0 - m}{\rho_{slag} \Delta t \left(S_{mold} - S_{electrode} \right)} \tag{19}$$

where m_0 is the initial mass of slag, m is the computed mass, ρ_{slag} is density of slag, Δt is time step size and S_{mold} denotes the cross-sectional area of mold. Note that, the grid node velocity (U_E) weakly fluctuates around zero once the process reaches the steady state.

2.5 Simulation setup

The physical properties of the materials are listed in Table 3. The shape of electrode tip is mainly governed by the thermal field and flow in the slag region, hence the electrical and thermal properties of slag play an important role. The slag has the following composition: 40% CaF_2, 30% CaO, 30% Al_2O_3 [17].The electric or thermal conductivities of the slag are

temperature dependent [34], but due to the difficulty of the measurement, a large uncertainty of the properties exists. The electric conductivity of conventional slags in liquid state was reported to vary between 80-300 $\Omega^{-1}.m^{-1}$ [35]. The electric conductivity of the slag in solid state is even unknown. The solidified slag skin layer formed on the mold wall is assumed to be a perfectly electrical insulator in most of simulations found in literature [25, 36-37]. On the other hand, it is observed that considerable amount of current can cross the solid slag skin (mold current) entering into the mold despite low electric conductivity of the layer [22, 38-45].

Slag	
Density ($kg{\cdot}m^{-3}$)	2700
Viscosity ($kg{\cdot}m^{-1}{\cdot}s^{-1}$)	0.0025
Specific heat ($J{\cdot}kg^{-1}{\cdot}K^{-1}$)	1500
Thermal exp. coefficient (K^{-1})	$9x10^{-5}$
Thermal conductivity, liquid($W{\cdot}m^{-1}{\cdot}K^{-1}$)	Variable [Table 4]
Electric conductivity, liquid($ohm^{-1}{\cdot}m^{-1}$)	Variable [Table 4]
Steel	
Density ($kg{\cdot}m^{-3}$)	7100
Viscosity ($kg{\cdot}m^{-1}{\cdot}s^{-1}$)	0.006
Specific heat, liquid ($J{\cdot}kg^{-1}{\cdot}K^{-1}$)	800
Thermal exp. coefficient (K^{-1})	0.0001
Latent heat of fusion ($J{\cdot}kg^{-1}$)	260000
Thermal conductivity ($W{\cdot}m^{-1}{\cdot}K^{-1}$)	40
Electric conductivity ($ohm^{-1}{\cdot}m^{-1}$)	880000
Air	
Density ($kg{\cdot}m^{-3}$)	1.2
Viscosity ($kg{\cdot}m^{-1}{\cdot}s^{-1}$)	$1.7x10^{-5}$
Specific heat ($J{\cdot}kg^{-1}{\cdot}K^{-1}$)	1000
Thermal conductivity ($W{\cdot}m^{-1}{\cdot}K^{-1}$)	0.02
Electric conductivity ($ohm^{-1}{\cdot}m^{-1}$)	10^{-10}
Copper	
Density ($kg{\cdot}m^{-3}$)	8500
Specific heat ($J{\cdot}kg^{-1}{\cdot}K^{-1}$)	381
Thermal conductivity ($W{\cdot}m^{-1}{\cdot}K^{-1}$)	300
Electric conductivity ($ohm^{-1}{\cdot}m^{-1}$)	$4x10^{7}$

Table 3. Physical properties of materials.

Simulations considering different current paths are performed and details of analyses are given in next section. The rate of heat transfer between molten slag and mold, air, or electrode is governed by thermal conductivity. The latter significantly influences the temperature field in the process. Approximate values for thermal conductivity of CaF_2-based slags at elevated temperatures are reported to be between 0.5 and 5 $W.m^{-1}.K^{-1}$[46]. Therefore, parameter studies by varying the thermal conductivity of slag are also made. Table 4 describes conditions for parameter studies.

	Slag electric conductivity, liquid($ohm^{-1}\cdot m^{-1}$)	Slag thermal conductivity, liquid($W\cdot m^{-1}\cdot K^{-1}$)	Mold current
Case I	250	5	No
Case II	250	5	Yes
Case III	170	1.5	Yes
Case IV	170	5	Yes

Table 4. Conditions of parameter studies.

Tacke and Schwerdtfeger conducted a series of experiments to investigate the influence of operation parameters on the shape of electrode tip for a laboratory scale ESR process [17]. Here, we use the identical geometry for the simulations, and compare the simulation results with one of their experiments (Table 5).

3 RESULTS

3.1 Transient melting of electrode

Here, the capability of model to capture the shape of electrode during remelting is demonstrated. Transient behavior of process for one case study (Case I) is discussed in details considering interactions between flow field, temperature field, electromagnetic field, and shape of electrode. The evolution of electrode shape as well as electric potential, temperature, and velocity fields are illustrated in Fig. 2.

	Experiment [17]	Case I	Case II	Case III	Case IV
Electric current mode	DC	DC	DC	DC	DC
Electric current (kA)	1.9	1.9	1.9	1.9	1.9
Mold current	Unknown	No	Yes	Yes	Yes
Electrode radius (cm)	4	4	4	4	4
Mold radius (cm)	8	8	8	8	8
Slag weight (kg)	4.0	4.1	4.1	4.1	4.1
Slag e-cond. ($ohm^{-1}.m^{-1}$)	Unknown	250	250	170	170
Slag ther. cond.($W.m^{-1}.K^{-1}$)	Unknown	5	5	1.5	5
Voltage (V)	29	28	15	23	22
Power generation (kW)	55	55	28	43	40
Initial feeding vel. (cm/s)	Unknown	0.0153	0.0153	0.0153	0.0153
Steady feeding vel. (cm/s)	0.0153	0.007	0.0063	0.0116	0.0045
Melt rate (g/s)	5.5	3.1	2.2	4.1	1.7
Immersion depth (cm)	3.8	3.6	3.5	2.9	4.0
Power consumption ($kJ.g^{-1}$)	10	18	12.7	10.5	23
L_{min} (cm)	Unknown	2.5	2.5	2.5	2.5
L_{max} (cm)	Unknown	4.5	4.5	4.5	4.5

Table 5. Operation conditions and results of a laboratory scale ESR process [17], and comparison with the simulations (steady state).

Additionally, the mesh resolution near moving-deforming boundary (electrode tip-slag interface) is shown. The magnitude of voltage drop and subsequently power generation is strongly dependent on immersion depth of electrode (maximum distance between electrode tip and slag-air interface). As a result of higher voltage drop at lower immersion depth, the power generation increases in the system. Consequently, the temperature rises in the slag at low immersion depth as shown in Fig. 2(c). Furthermore, the velocity is increased under the shadow of electrode at higher immersion depth as shown in Fig. 2(d)-(f). The current density increases at larger immersion depth under the electrode that intensifies the Lorentz force. Thus, the velocity becomes higher in central region of slag where stirring is promoted and the temperature field is relatively uniform.

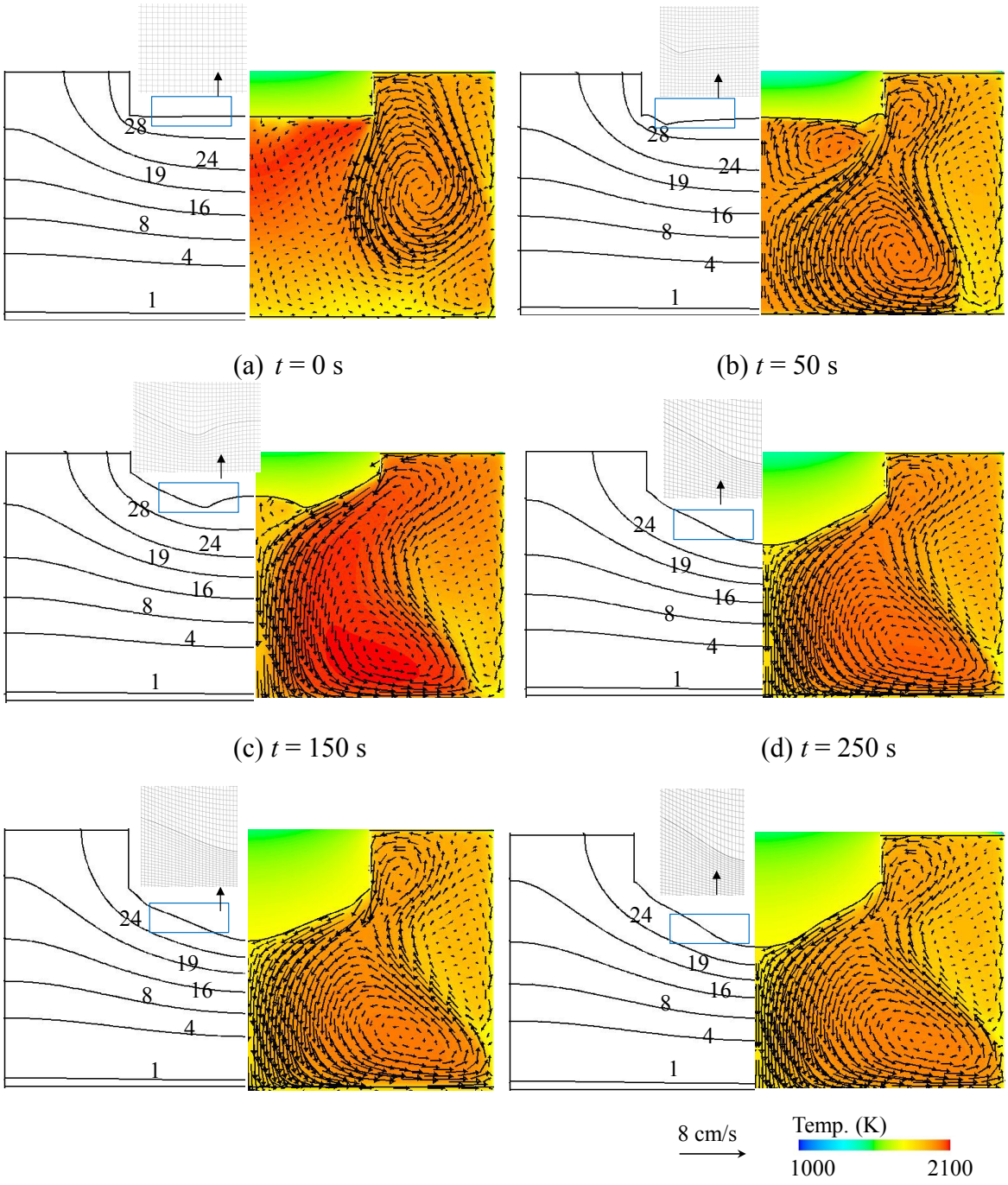

Fig. 2. Modeling result of evolution of shape of electrode tip for Case I: (a) t = 0, (b) t = 50 s, (c) t = 150 s, (d) t = 250 s, (e) t = 650 s, (f) t = 1000 s. On left half: Isolines of voltage and the grid near the moving-deforming boundary (electrode tip-slag interface), On right half: Contour of temperature overlaid with vectors of velocity in the slag region.

We have previously found that the coupling between melt rate and power generation due to Joule heating is very unstable [20]. This fact is verified in this study again. As shown in Fig. 3 (d), the ratio of the power generation to melt rate, called power consumption, changes during the whole remelting process. In addition to that the immersion depth, melt rate and power generation are also plotted in Fig. 3 (a)-(c).

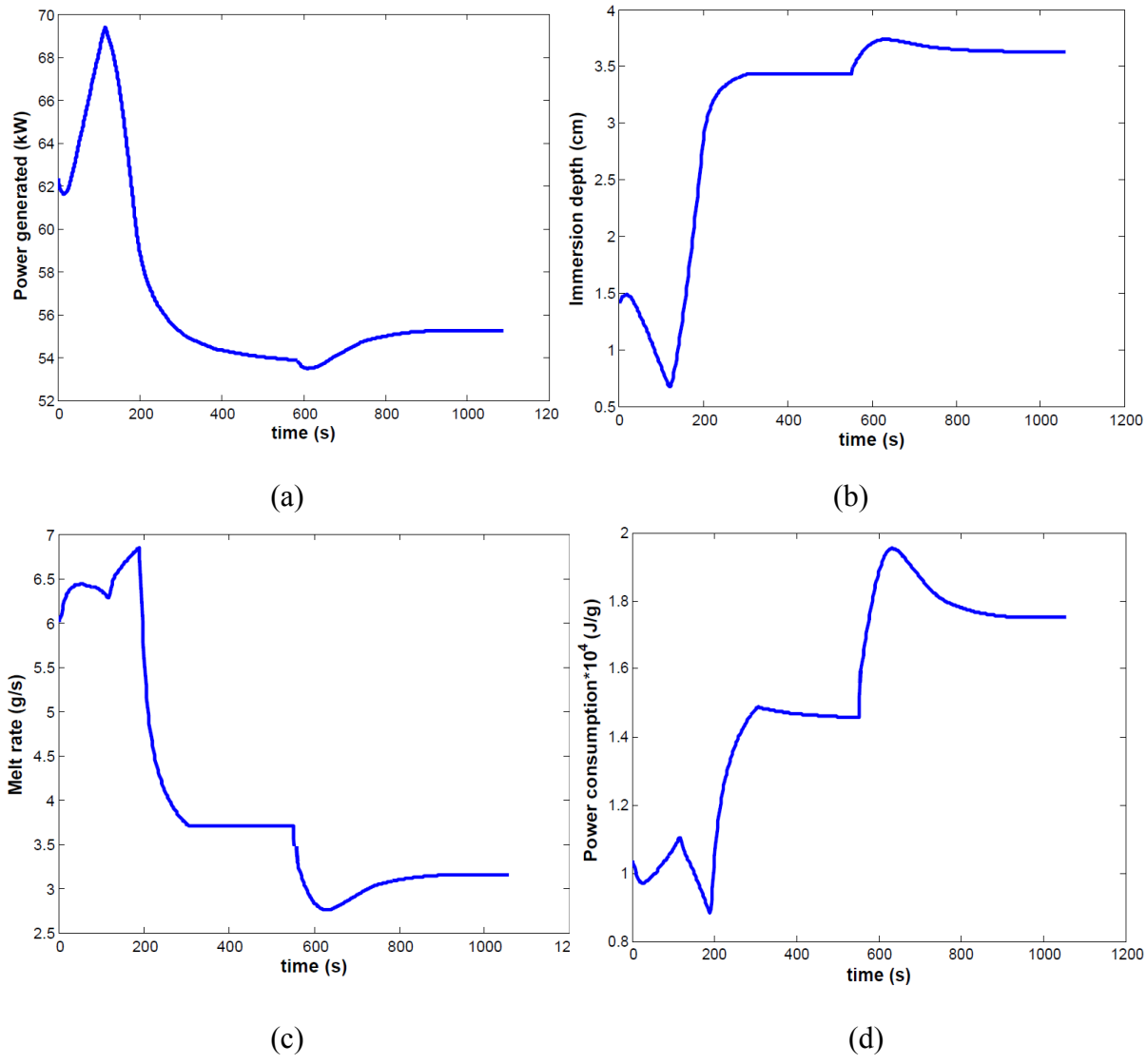

Fig. 3. Analysis of melting parameters for Case I: (a) Power generation, (b) Immersion depth, (c) Melt rate, (c) Power consumption (ratio of power generation to melt rate).

The results reveal that variation in power is much gentler than the variation of melt rate. In other words, the melt rate can change dramatically although the power generation remains relatively stable before reaching the steady state (> 900 s). Furthermore, the peak is

observed in the power generation when the immersion depth becomes very shallow, Fig. 3 (a). Essentially, power generation and immersion depth oppose each other as shown in Fig. 3 (a)-(b). In other words, the power generation is higher at lower immersion depth and vice versa.

In summary, the model enables us to study the dynamic interactions between velocity field, temperature field, electromagnetic field, and shape of electrode tip during remelting. Additionally, melting parameters such as melt rate, immersion depth, power generation, and power consumption can be directly computed.

3.2 Parameter studies

Four cases are simulated (Table 4). Following the experiment [17] a DC current is imposed and kept constant. The initial feeding velocity of the electrode (not reported for the experiment) is assumed and kept unchanged for all simulation cases. Note that two extreme cases might occur when an improper feeding velocity is applied. One is that the electrode tip might totally leave out of the slag during operation when a very low feeding velocity is applied for a case with large melt rate. The another extreme case is that the electrode tip might touch the slag-pool interface when very high feeding velocity is applied for a case of low melt rate, which leads to an electrical shortcut between the electrode tip and molten metal pool. Therefore, the feeding velocity of the electrode must be adjusted according to Eq. (17) to avoid the aforementioned undesirable extreme cases. In the operation, the initial feeding velocity is unknown, but the feeding velocity at steady state is known. The steady state feeding velocity was extracted from the simulations for the case studies. In addition, the melt rate is calculated using Eq. (18). The amplitude of voltage and power depends on the current density and shape of the tip that are reported at the steady state. A summary of

case studies at the initial and steady states are shown in Fig. 4 and Fig. 5. In addition, temperature, velocity, voltage, and current density fields including the submerged part of electrode in slag zone are provided.

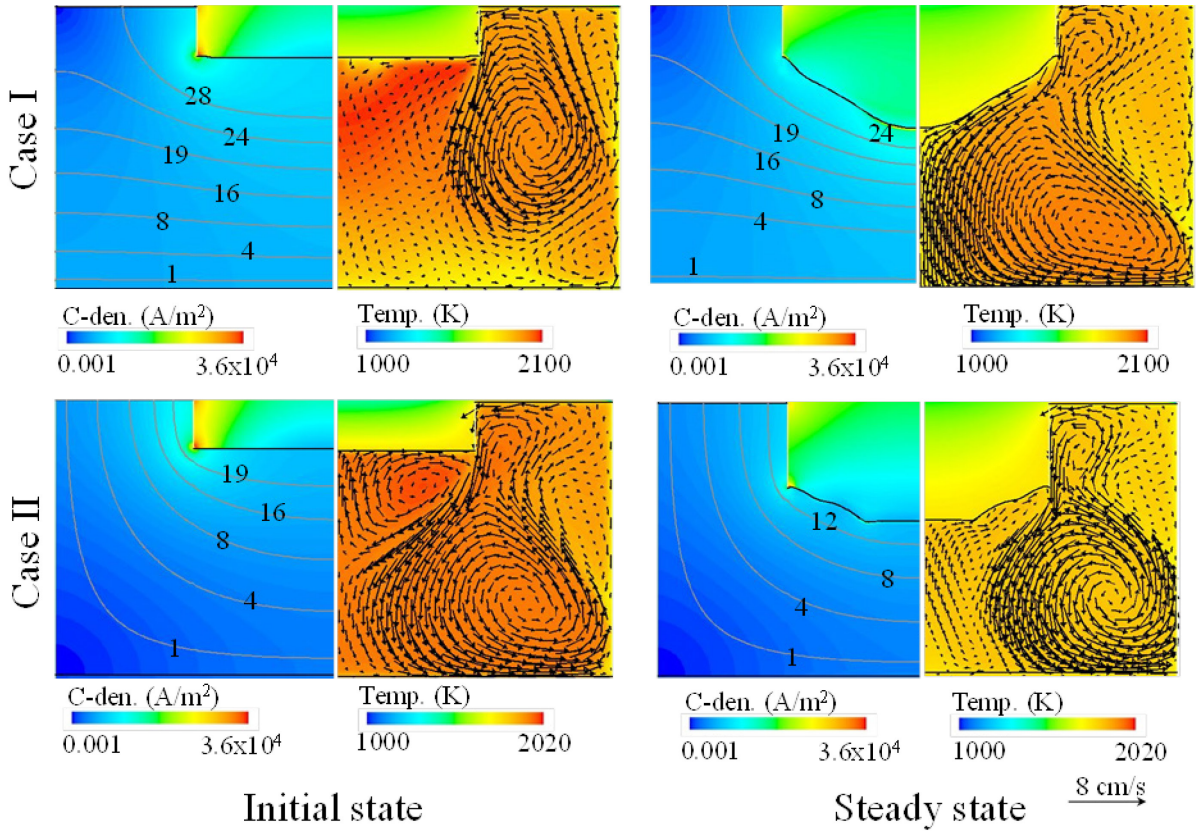

Fig. 4. Contour of current density overlaid with isolines of voltage (left half), contour of temperature overlaid with vectors of velocity (right half) for Case I (upper row) and Case II (bottom row).

3.2.1 Case I

The melting of electrode for this case was previously discussed in details in section 3.1. A high electrical conductivity and high thermal conductivity of the liquid slag are assumed (Table 4). The solidified slag layer near the mold wall is assumed to be an electrical insulator and no current enters into mold. The isolines of voltage in the beginning of simulation and final steady state are compared as shown in Fig. 4 (Case I). With the increase of immersion depth, the isolines of voltage are shifted and the voltage of system is reduced. In addition, the maximum amount of current density is initially observed near the

edge of electrode. However, the amplitude of current density is increased in the slag zone under the shadow of electrode for the deeply submerged electrode. As a consequence, the Lorentz force becomes stronger that results in promotion of stirring and intensification of velocity under the electrode. The amount of generated power due to Joule heating is significant (Table 5) leading to a high temperature in the slag zone. In addition, the electrode tip deforms to a parabolic shape.

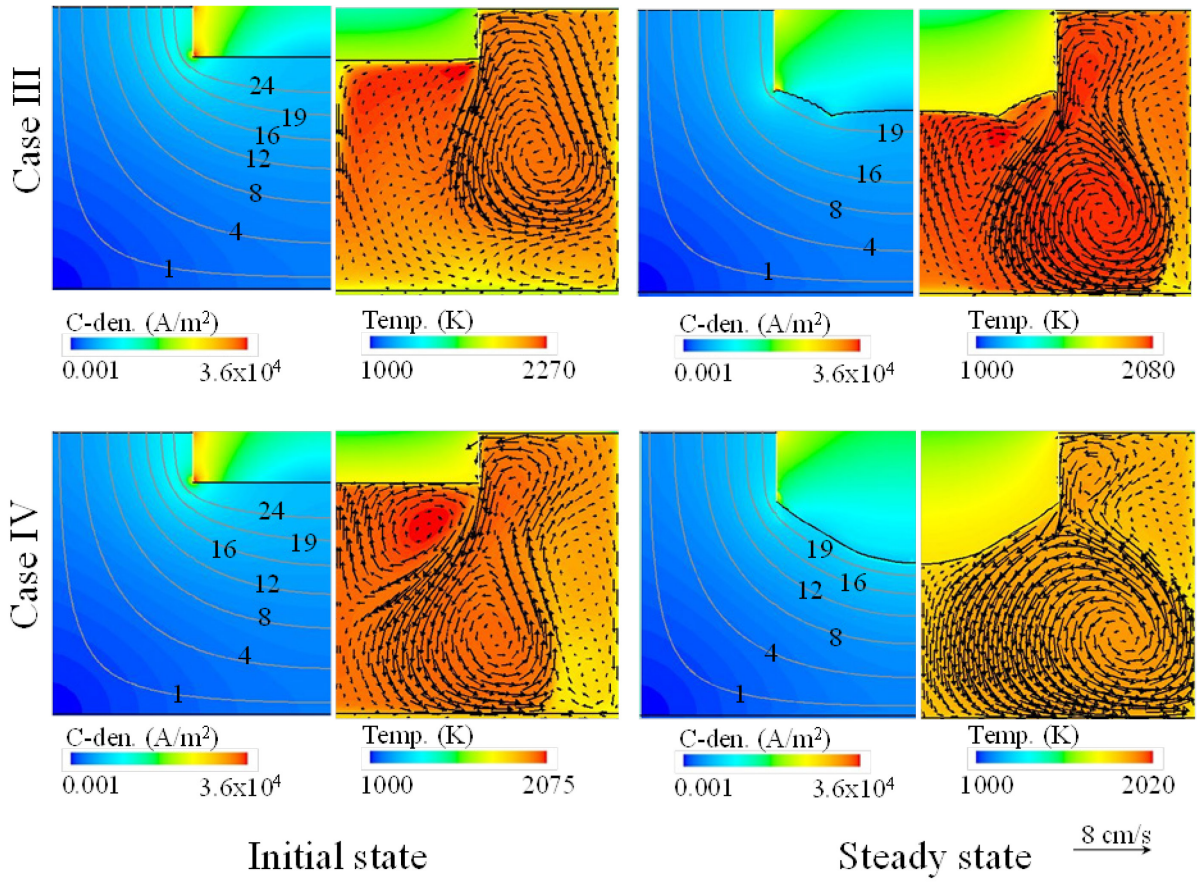

Fig. 5. Contour of current density overlaid with isolines of voltage (left half), contour of temperature overlaid with vectors of velocity (right half) for Case III (upper row) and Case IV (bottom row).

3.2.2 Case II

A high electrical conductivity and high thermal conductivity of the liquid slag are assumed, as same as Case I, but the current is allowed to cross the slag skin flowing through the mold.

As stated by Kharicha [8], opening the path to the mold causes reduction in the overall resistance of the ESR system. Consequently, a significant reduction of voltage is observed for Case II as demonstrated by isolines of voltage in Fig. 4 (Case II). Similar to Case I, the current density becomes larger in the bulk of slag with increasing the submerged volume of electrode. In addition, the molten slag becomes colder due to high thermal conductivity of melt and low magnitude of power generated in the process. In Case II, the electrode tip develops a parabolic shape from the extremities leaving a flat tip at the center. This unique shape of electrode has been previously observed in both simulation [20] and real process [13].

3.2.3 Case III

A lower electrical conductivity and lower thermal conductivity of the slag are assumed, and the current is allowed to cross the slag skin flowing through the mold. The lower electric conductivity of slag results in higher generated power in the system. Significant amount of Joule heating is released under the shadow of electrode where the current density is fairly large .With the increase of immersion depth, the reduction in total voltage is observed as shown using isolines of voltage for initial and final steady states. Note that, the global energy transfer is weak due to low thermal conductivity of molten slag. As a consequence, the bulk of molten slag becomes very hot as shown in Fig. 5 (Case III). The immersion depth is shallow, and the electrode tip develops a relatively flat concave shape.

3.2.4 Case IV

The molten slag in Case IV is considered thermally a better conductor compared to former cases. Consequently the heat transfer is efficient in the slag zone results in colder slag

compared to Case III as indicated in Fig. 5 (Case IV). The current density is intensified in the bulk of slag with the increase of electrode immersion depth. Thus, the Lorentz force becomes dominant resulting in promotion of stirring in slag zone. The electrode is deeply immersed into the slag zone at the steady state. Therefore, a significant reduction of the voltage is observed comparing the initial and final steady states for Case IV. In addition, the amount of released Joule heating is notably decreased during the process for this case. Finally, electrode tip develops a parabolic shape.

4 DISCUSSIONS

The melting rate and shape of electrode tip are important indicators of the ESR process, and they determine the efficiency of system. The predicted shape of electrode tip is compared with the experimentally observed one (Fig. 6). A fairly good agreement with the experiment is obtained for Case I and Case IV. Additionally, the power generation predicted by Case I and Case IV agrees with the experiment as well (Table 5). The heat can efficiently transfer to the electrode due to large thermal conductivity of the slag (~5 $W.m^{-1}.K^{-1}$). In fact, the turbulent flow in the bulk of slag zone can dramatically increase the effective thermal conductivity of the slag (~ 84-973 $W.m^{-1}.K^{-1}$) as described by Choudhary [47].

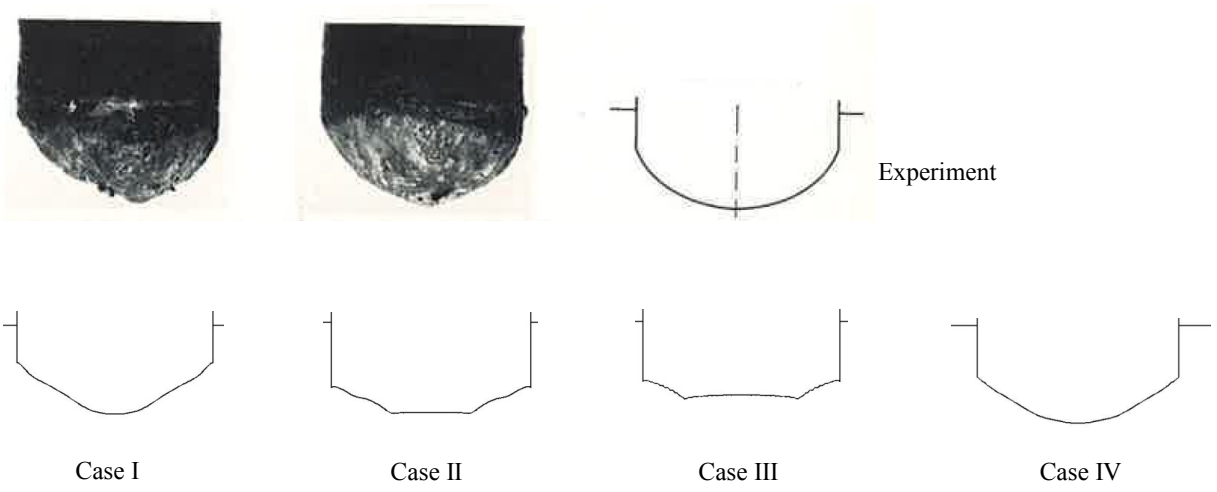

Fig.6. Shape of electrode tip observed in experiment conducted (upper row) by Tacke et. al [17], numerically simulated shapes of electrode tip of 4 Cases (bottom row).

As illustrated in Fig. 7, the effective thermal conductivity is significantly increased by the turbulence, and it leads to a strong enhancement of heat transfer in the bulk slag.

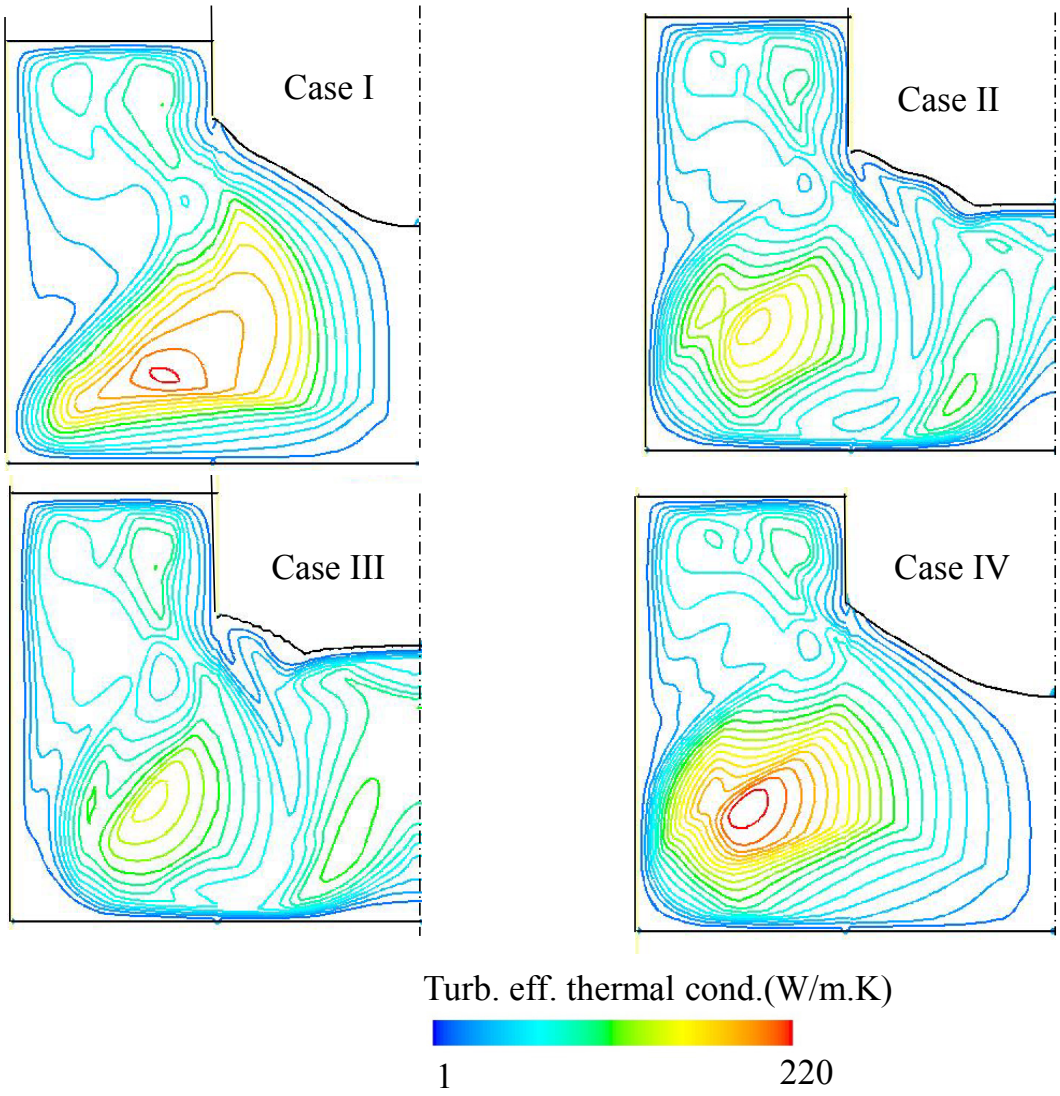

Fig. 7. Isolines of effective thermal conductivity due to turbulence for simulation cases.

Thus, the temperature remains relatively uniform in the bulk as shown in Fig. 5 and Fig. 6. On the other hand, the effective turbulence thermal conductivity gradually decreases from the bulk to the region near walls where it has the same order of magnitude as molecular thermal conductivity due to damping of turbulence near walls [27-29]. The main difference

between Case III and Case IV is the molecular thermal conductivity of slag. The heat transfers to the boundaries such as mold, air, or electrode are minimized for Case III leading to high temperature in the slag zone. As a consequence, the melt rate becomes large and the immersion depth decreases. In other words, increasing thermal conductivity of slag will lead to a decrease of melt rate. It must be noted that significant differences are observed regarding to the shape of electrode tip and the immersion depth between Case III and Case IV despite similar power generation. Thus, the voltage drop and subsequently power generation depend on both immersion depth and shape of electrode tip. A comparison is made between Case I and Case II to explore the effect of current path (without and with mold current). The amount of power generation and temperature are larger and higher for Case I (without mold current) that causes higher melt rate as described in Table 5. The shape of tip for Case II is quite similar to Case III although the thermal and electrical conductivities are noticeably different. The immersion depth is approximately the same for all cases except Case III which has the highest melting rate and lowest immersion depth. For the latter, the highest temperature in slag zone is observed among all cases due to low molecular thermal conductivity and inefficient heat transfer through the walls.

In a real ESR process, the stability is achieved by including a control system on electrode immersion depth to avoid undesirable extreme cases happening (the electrode tip touches melt pool). Therefore, it is necessary to apply a numerical adaptation of electrode immersion depth as described in Eq. (17). It should also be stated that the choice of $l_{\min}$ and $l_{\max}$ in Eq. (17) might influence the feeding velocity of electrode (u_E) and consequently the melt rate and shape of electrode tip of steady state. For that further investigations are demanded. According to Table 5, approximately equivalent ratios (power generation to melt rate) are obtained for Case I and Case IV at steady state in which the shape of electrode tip is fairly similar. Additionally, Case II and Case III are following the same behavior due to

insignificant difference in the ratio calculated at steady state. In conclusion, the shape of electrode tip at steady state is much similar for ESR processes running with the same ratio of power generation to melt rate.

The predicted melt rate for all cases is always lower than the value reported from the experiment (Table 5). This indicates that the amount of heat provided to electrode is underestimated by simulations. The current model does not take into account electrochemical polarization overpotential, enhancement of turbulence in the slag bulk due to droplet dripping, and formation of liquid film under the electrode. Departure of droplets from the electrode can generate stronger turbulence in the slag bulk that certainly enhances the global energy transfer and melt rate [23-24]. In order to improve the quantitative accuracy of the numerical result, the aforementioned factors must be included in the future model.

5 SUMMARY

A 2D axisymmetric numerical model was applied to simulate the electrode melting during ESR process. The submerging and remelting of electrode is modeled using a dynamic mesh based approach. The shape of electrode tip at the steady state validated against an experiment. The following conclusions were made:

1) The dynamic mesh based approach is proved to be a successful method to model the electrode shape. The simulation results agree with the experimental fact that with the increase of melt rate, the immersion depth decreases when the magnitude of imposed current is kept constant. Furthermore, the ratio of power generation to melt rate, called power consumption, is an important factor to determine the shape of electrode: it is observed that the shape of electrode remains almost the same when the ratio is kept constant.

2) The voltage drop and subsequent power generation in the system are governed by both immersion depth and shape of electrode tip. In other words, similar power generation is observed for systems where the shapes of tip and immersion depth were different. Therefore, the melt rate, immersion depth and shape of electrode tip are interdependent parameters.

The total power generation and the efficiency of global heat transfer in the system are highly dependent on the molten slag physicochemical properties such as electrical and thermal conductivities. Due to difficulty of measurements of properties, a large uncertainty of the properties exists. Therefore, parameter studies by varying the electrical and thermal conductivities of slag are made. It is found that:

3) The electrical conductivity of slag (liquid and solid) mainly influences the electric current path which impacts the velocity and temperature distribution in the process. As a consequence of different electric current path, the power generation, melt rate and shape of electrode are significantly influenced.

4) The thermal conductivity of slag determines the efficiency of global heat transfer in the process. Increasing thermal conductivity of slag will result in decreasing melt rate.

To improve the quantitative accuracy of the modeling results, the following phenomena must be included to the current model. Firstly, it is essential to incorporate the effect of droplets dripping through the slag into the model. Secondly, it is necessary to include the influence of electrochemical polarization overpotential since the electric current is conducted by ions in the slag.

ACKNOWLEDGEMENTS

The authors acknowledge the financial support by the Austrian Federal Ministry of Economy, Family and Youth and the National Foundation for Research, Technology and Development within the framework of the Christian Doppler Laboratory for Advanced Process Simulation of Solidification and Melting.

REFERENCES

1. G. Hoyle: Electroslag Processes, Applied Science Publishers, London, 1983.
2. E. J. Pickering: ISIJ Int., 2013, vol. 53, pp. 935-949.
3. G. Hoyle: 6th Int. Vacuum Meta. Conf. on Special Melting, San Diego, USA, 1979, pp. 624-640.
4. W. Holzgruber: 5th Int. Symposium on Electroslag and Other Special Melting Technologies, Pittsburgh, USA, 1974, pp. 70-91.
5. A. Mitchell: Perspective in Metallurgical Development Conference, Sheffield, England, 1984, pp. 89-98.
6. F.S. Suarez, J.E. Roberts, and L.D Schley: 5th Int. Symposium on Electroslag and Other Special Melting Technologies , Pittsburgh, USA, 1974, pp. 126-145.
7. A. Mitchell: Electric furnace steelmaking Conference, Warrendale, PA: ISS, USA, 1985, p. 212.
8. A. Kharicha, E. Karimi-Sibaki, M. Wu and A. Ludwig: Int. Symposium on Liquid Metal Processing and Casting, Austin, USA, 2013, pp. 95-99.
9. D.K. Melgaard, J.J. Beaman and G.J. Shelmidine: U.S. Patent 7,180,931 B1, 2007.
10. D.K. Melgaard, G.J. Shelmidine and B.K. Damkroger: U.S. Patent 6,496,530 B2, 2002.

11. D.K. Melgaard, R.L. Williamson and J.J. Beaman: JOM, March 1998, pp. 13-17.

12. A. Kharicha, M. Wu and A. Ludwig: Int. Symposium on Liquid Metal Processing and Casting, Austin, USA, 2013, pp. 145-150.

13. M. A. Maulvault: PhD thesis, MIT, 1967, pp. 80-85.

14. A. Mitchell, S. Joshi and J. Cameron: Metall. Trans., 1971, vol. 2, pp. 561-567.

15. J. Mendrykowski, J.J. Poveromo, J. Szekely and A. Mitchell: Metall. Trans., 1972, vol. 4, pp. 1761-1768.

16. T. Kishida, K. Yamaguchi, T. Tomioka, and T. Ichihara: Electrical Steel, 1974, vol. 45, pp. 219-227.

17. K. H. Tacke and K. Schwerdtfeger: Arch. Eisenhüttenwesen,1981, vol. 52, pp. 137-142.

18. A. Jardy, D. Ablitzer and J.F. Wadier: Met. Trans. B, 1991, vol. 22, pp. 111-120.

19. J. Yanke, K. Fezi, M. Fahrmann and M. J.M. krane: Int. Symposium on Liquid Metal Processing and Casting, Austin, USA, 2013, pp. 47-55.

20. A. Kharicha, M. Wu and A. Ludwig: ISIJ, 2014, vol. 54, pp. 1621-1628.

21. A. Mitchell, G. Beynon: Met. Trans., 1971, vol. 2, pp. 3333-3345.

22. M. Kawakami, K. Nagata, M. Yamamura, N. Sakata, Y. Miyashita and K.S. Goto, Testsu- to-Hagane,1977, vol. 63, p. 220.

23. A. Kharicha, A. Ludwig, and M. Wu: EPD congress, San Diego, USA, 2011, pp. 771-778.

24. A. Kharicha, M. Wu, A. Ludwig, M. Ramprecht, H. Holzgruber: CFD modeling and simulation in materials, Florida, USA, 2012, pp.139-146.

25. V. Weber, A. Jardy, B. Dussoubs, D. Ablitzer, S. Ryberon, V. Schmitt, S. Hans and H. Poisson: Metall. Mater. Trans. B, 2009, vol. 40, pp. 271-280.

26. H. Song and N. Ida: IEEE Trans. on Magnetics, 1991, vol. 27, pp. 4012-4015.

27. T. Esch and F. R. Menter: Turbulence Heat and Mass Transfer Conference, Antalya, Turkey, 2003.

28. F. R. Menter: AIAA Journal, 1994, vol. 32, pp. 1598-1605.

29. F. R. Menter, M. Kuntz and R. Langtry: Turbulence Heat and Mass Transfer, 2003, vol. 4, pp. 625-632.

30. Fluent 14.5 User's Guide, Fluent Inc.; 2012.

31. A. Menendez Blanco and J. M. Fernandez Oro: Computers and Fluids, 2012, vol. 57, pp.138-150.

32. G. Lame and B.P. Clapeyron: Ann. Chem. Phys., 1831, vol. 47, pp. 250-256.

33. L.I. Rubinstein: The Stefan Problem, American mathematical society, USA, 1971.

34. K.C. Mills and B.J. Keene: Int. Metals Rev., 1981, vol. 1, pp. 21-69.

35. M. Hajduk and T.E. Gammal: Stahl Eisen, 1979, vol. 99, p. 113.

36. K.M. Kelkar, S. V. Patankar, et. al: Int. Symposium on Liquid Metal Processing and Casting, Austin, USA, 2013, pp. 3-12.

37. A.D. Patel : Int. Symposium on Liquid Metal Processing and Casting, Nancy, France, 2011, pp. 49-56.

38. S.F. Medina and M.P. de Andres: Ironmaking and Steelmaking, 1987, vol. 14, pp.110-121.

39. E. Karimi-Sibaki, A. Kharicha, M. Wu and A. Ludwig: Int. Symposium on Liquid Metal Processing and Casting, Austin, USA, 2013, pp. 13-19.

40. E. Karimi-Sibaki, A. Kharicha, M. Wu and A. Ludwig: Ingot Casting Rolling Forging conference, Milan, Italy, 2014.

41. H. Holzgruber, W. Holzgruber, A. Scheriau, et. al: Int. Symposium on Liquid Metal Processing and Casting, Nancy, France, 2011, pp. 57-64.

42. M. Hugo, B. Dussoubs, A. Jardy, J. Escaffre and H. Poisson: Int. Symposium on Liquid Metal Processing and Casting, Austin, USA, 2013, pp. 79-85.

43. A. Kharicha, A. Ludwig and M. Wu: Mater. Sci. Eng. A, 2005, vol. 413-414, pp. 129-134.

44. E. Karimi-Sibaki, A. Kharicha, J. Korp, M. Wu and A. Ludwig: Met. Trans. Forum, vol. 790, p.396.

45. A. Kharicha, W. Schützenhöfer, A. Ludwig, R. Tanzer and M. Wu: Steel Res. Int., 2008, vol. 79, pp. 632-636.

46. R. Taylor and K.C. Mills: Arch. Eisenhüttenwesen, 1982, vol. 53, pp. 55-63.

47. M. Choudhary and J. Szekely: Ironmaking and steelmaking, 1981, vol. 5, pp. 225-232.

Publication VI

On validity of axisymmetric assumption for modeling an industrial scale electroslag remelting process

E. Karimi-Sibaki, A. Kharicha, J. Bohacek, M. Wu, A. Ludwig

Adv. Eng. Mater. Published online 5 Oct. 2015
DOI: 10.1002/adem.201500391

On validity of axisymmetric assumption for modeling an industrial scale electroslag remelting process[**]

By *E. Karimi-Sibaki*, *A. Kharicha*, *J. Bohacek*, *M. Wu*[*], *A. Ludwig*

[*] *M.Sc. E. Karimi-Sibaki, Dr. A. Kharicha, Prof. M. Wu*
Christian Doppler Laboratory for Advanced Process Simulation of Solidification and Melting, Dept. of Metallurgy, Uni. of Leoben, Franz-Josef-Str. 18, A-8700, Leoben, Austria
Email: menghuai.wu@unileoben.ac.at
Dr. A. Kharicha, Dr. J. Bohacek, Prof. M. Wu, Prof. A. Ludwig
Chair of Simulation and Modeling of Metallurgical Processes
Dept. of Metallurgy, Uni. of Leoben, Franz-Josef-Str. 18, A-8700, Leoben, Austria

[**] *The authors acknowledge financial support from the Austrian Federal Ministry of Economy, Family, and Youth and the National Foundation for Research, Technology, and Development within the framework of the Christian Doppler Laboratory for Advanced Process Simulation of Solidification and Melting.*

A full 3D simulation of an industrial scale electroslag remelting (ESR) process (ϕ 750 mm ingot) is performed. The electromagnetic field, its interaction with the turbulent flow in the molten slag and melt pool regions, the thermal field of the entire ESR system (including electrode, molten slag, ingot and mold), and the solidification of the ingot are calculated. A typical non-axis symmetry flow pattern and temperature field in the slag region, which have been observed *in-situ* from the slag surface during operation, are demonstrated. A statistical analysis of the turbulent flow in the slag and melt pool is performed to quantitatively characterize the transient behavior of the flow. The predicted shape of the melt pool (profile of the solidifying mushy zone of the ingot) is found to be less influenced by the transient 3D flow in the slag region, and it shows good axis symmetry. By comparing the 3D calculation with a 2D axis-symmetrical calculation, we find that the predicted melt pool profiles are quite similar, leading to the conclusion that a 2D calculation is sufficient to solve the melt pool profile of the ingot. The predicted shape of the melt pool profile is verified by comparison with the experimentally measured pool profile.

Over past decades, a number of studies have been performed to model the ESR process containing the complex interaction between turbulent flow, heat, and electromagnetic fields [1]. Choudhary et al. [2] used the vorticity transport equation to calculate the velocity field only in the slag. Nevertheless, they calculated the temperature field both in the slag and ingot, focusing on the effect of ingot size (ϕ 100 or 660 mm). They found that the temperature field in the slag appeared to be more uniform in large-scale units. Jardy et al. [3] studied the flow and temperature fields only in the slag zone for an industrial scale ESR (ϕ 500 mm ingot). Their model predicted that a higher melt rate could be achieved when the buoyancy force is stronger than the Lorentz force in the slag region. Kelkar et al. [4] proposed a coupled model for flow, temperature, and electromagnetic fields in the slag and ingot (ϕ 470 mm) at steady state conditions. Patel [5] presented results based on an analytical model for electromagnetic distribution in ESR (ϕ 430 mm). A parabolic variation between the voltage drop across the slag and electrode diameter was predicted. Kharicha et al. developed a series of models with different focuses to investigate, for example, the shape and stability of the slag-pool interface [6], the effect of applied frequency [7], the importance of electric current flowing through the mold [8], the interaction between released Joule heating and temperature fluctuation in the slag [9], and the effect of slag-pool interface movement on solidification of the ingot [10]. Weber et al. [11] studied the effect of electrode fill ratio on the melt rate of the electrode and the liquid pool volume (ϕ 500 mm ingot). They reported a higher melt rate and larger liquid pool volume in the case with a lower electrode fill ratio. Eickhoff et al. [12] studied air gap formation due to shrinkage of a solidifying ESR ingot (ϕ 100 mm). Using a prescribed parabolic temperature distribution, radial contraction was calculated in the fully solidified ingot. Fezi et al. [13] proposed a numerical model to investigate the effects of process parameters, such as ingot diameter (ϕ

508 to 762 mm ingots) and the initial composition of the alloy, on macrosegregation of alloy 625.

All of the above mentioned calculations were performed in a 2D axisymmetric domain because of the limitation of the computational resources. Generally speaking, dealing with the governing equations of flow, heat transfer, or electromagnetism in 2D is simple, whereas only limited work has been attempted in 3D. One example shown by Kharicha et al. [14] modeled the effects of slag-pool interface movement, formation, departure, and dripping of droplets through the slag for an industrial scale (ϕ 600 mm ingot) ESR process. The interaction between flow and electromagnetic field was found to generate a strong 3D flow, which could not be predicted by typical 2D models. Recently, Wang et al. [15] established a 3D model to investigate a laboratory scale ESR process (ϕ 120 mm ingot). The multiphase Volume of Fluid (VOF) approach was used to model the melting of electrodes with the formation of droplets as well as slag pool interface movement. This type of calculation is computationally costly. For instance, the calculation performed by Kharicha et al. [14] took six months using a multi-CPU cluster (24 cores, parallel computing) for only five seconds of process even without including the solidification of the ingot. Therefore, it is not computationally feasible to include all of these phenomena, such as interface movement and droplet formation, in the industry process in 3D.

Herein, a different 3D modeling concept is proposed that focuses on an industrial scale AC electroslag remelting process by including solidification of the ingot. The governing equations are solved using the commercial CFD software FLUENT-ANSYS v.14.5, which is based on the Finite Volume Method (FVM). The modeling equations and corresponding boundary conditions are implemented using User-Defined Functions (UDF). Table 1 describes all of the governing equations regarding fluid flow, heat transfer, and electromagnetism. The thermal and electrical boundary conditions are summarized in Table 2.

Governing equations	**Symbols**
1. Electromagnetic field $\frac{\partial B_\theta}{\partial t}+\left[\frac{\partial}{\partial z}\left(\frac{1}{\sigma\mu_0}\frac{\partial B_\theta}{\partial z}\right)+\frac{\partial}{\partial r}\left(\frac{1}{r\sigma\mu_0}\frac{\partial(rB_\theta)}{\partial r}\right)\right]=0.$ $\tilde{\tilde{j}}=\frac{1}{\mu_0}(\vec{\nabla}\times\tilde{B}_\theta)$	Magnetic induction (B_θ), Mag. Perm. constant (μ_0), Elec. Cond. (σ), Radial distance (r), Axial distance (z), Time (t), Current density (j)
2. Flow field $\frac{\partial\rho}{\partial t}+\nabla\cdot(\rho\vec{u})=0$ $\frac{\partial}{\partial t}(\rho\vec{u})+\nabla\cdot(\rho\vec{u}\vec{u})=-\nabla p+\nabla\cdot(\mu_{eff}(\nabla\vec{u}+\nabla\vec{u}^T))+\rho_0\vec{g}\beta(T-T_0)+\vec{F}_P+\vec{F}_L$ $\vec{F}_L=\mathrm{Re}(\frac{1}{2}\vec{j}\times\tilde{B}_{\theta\ Conjugate}).$ $\vec{u}_m=f\vec{u}_l+(1-f)\vec{u}_s$ $\vec{u}_r=(\vec{u}_m-\vec{u}_s)$ $F_{\parallel}=-\frac{\mu}{K_{\parallel}}(\vec{u}_r\cdot\vec{n}_{\parallel})$ $F_{\perp}=-\frac{\mu}{K_{\perp}}(\vec{u}_r\cdot\vec{n}_{\perp})$ $\vec{F}_p=(F_{\perp})\vec{n}_{\perp}+(F_{\parallel})\vec{n}_{\parallel}$ $K_{\parallel}=\begin{cases}3.75\times10^{-4}f^2d_1^2 & 0<f\le0.65\\ 2.05\times10^{-7}\left[\frac{f}{1-f}\right]^{10.739}d_1^2 & 0.65\le f\le0.75\\ 0.074\left(\ln(1-f)^{-1}-1.49+2(1-f)-0.5(1-f)^2\right)d_1^2 & 0.75\le f<1.0\end{cases}$ $K_{\perp}=\begin{cases}1.09\times10^{-3}f^{3.32}d_1^2 & 0<f\le0.65\\ 4.04\times10^{-6}\left[\frac{f}{1-f}\right]^{6.7336}d_1^2 & 0.65\le f\le0.75\\ \left[-6.49\times10^{-2}+5.43\times10^{-2}\left[\frac{f}{1-f}\right]^{0.25}\right]d_1^2 & 0.75\le f<1.0\end{cases}$ Turbulence: Scale-Adaptive Simulation (SAS) model [19].	Velocity (u), Density (ρ), Pressure (P), Effective viscosity (μ_{eff}), Gravity (g), Therm. expan. coeff. (β), Temperature (T), Lorentz force (F_L), Casting velocity (u_s), Liquid velocity (u_l), Mixture liquid-solid velocity (u_m), Relative velocity (u_r), Parallel drag force ($F_{\parallel}$), Perpendicular drag force ($F_{\perp}$), Parallel unit vector ($n_{\parallel}$), Perpendicular unit vector ($n_{\perp}$), Mushy zone drag force (F_P), Liquid fraction (f), Primary dendrite arm space (d_1), Parallel perm. ($K_{\parallel}$), Perpendicular perm. ($K_{\perp}$),
3. Temperature field and solidification $\frac{\partial}{\partial t}(\rho h)+\nabla\cdot(\rho\vec{u}h)=\nabla\cdot(\lambda_{eff}\nabla T)+Q+S_{LH}$ $Q=\mathrm{Re}(\frac{1}{2\sigma}\tilde{\tilde{j}}\times\tilde{\tilde{j}}_{\theta\ Conjugate}).$ $S_{LH}=-\frac{\partial}{\partial t}(\rho fL)-\rho L\vec{u}_s\nabla f$ $f=\begin{cases}1 & T>T_{liquidus}\\ 1-\left[(T_{liquidus}-T)/((T_f-T)(1-k_p))\right] & T_{solidus}<T\le T_{liquidus}\\ 0 & T\le T_{solidus}\end{cases}$	Enthalpy (h), Effective therm. cond. (λ_{eff}), Joule heating (Q), Latent heat (S_{LH}), Enthalpy of fusion (L), Partition coeff. (k_p), Liquidus temp. ($T_{liquidus}$), Solidus temp. ($T_{solidus}$), Melting temp. of solvent (T_f),

Table 1. Governing equations of flow, electromagnetic, and temperature fields.

Boundaries (labelled in Figure (1a))	**Electromagnetic**	**Thermal**
1. Electrode tip-slag	Coupled	$T = T_{liquidus}$
2. Electrode edge-slag	Coupled	$T = T_{liquidus}$
3. Slag-air	$B_\theta = \frac{\mu_0 I_0}{2\pi r}$	$\varepsilon = 0.8, H = 50\ W \cdot m^{-2} \cdot K^{-1}$
4. Electrode-air	$B_\theta = \frac{\mu_0 I_0}{2\pi r}$	Zero flux
5. Electrode top	Zero flux	$T = 900K$
6. Mold-air	$B_\theta = \frac{\mu_0 I_0}{2\pi r}$	Zero flux
7. Mold top	$B_\theta = \frac{\mu_0 I_0}{2\pi r}$	Zero flux
8. Mold bottom	$B_\theta = \frac{\mu_0 I_0}{2\pi r}$	Zero flux
9. Mold-water	$B_\theta = \frac{\mu_0 I_0}{2\pi r}$	$H = 7000\ W \cdot m^{-2} \cdot K^{-1}$
10. Slag-mold	Coupled	$H = 500\ W \cdot m^{-2} \cdot K^{-1}$
11. Slag-pool	Coupled	Coupled
12. Ingot-mold	Coupled	$H = 500\ W \cdot m^{-2} \cdot K^{-1}$
13. Air gap	$B_\theta = \frac{\mu_0 I_0}{2\pi r}$	$\varepsilon = 0.8, H = 30\ W \cdot m^{-2} \cdot K^{-1}$
14. Ingot air	$B_\theta = \frac{\mu_0 I_0}{2\pi r}$	$\varepsilon = 0.8, H = 50\ W \cdot m^{-2} \cdot K^{-1}$
15. Ingot bottom	Zero flux	$T = 800K$

Table 2. Electromagnetic and thermal boundary conditions.

Note that, industrial measurements of material properties that are temperature dependent are used for our simulations. Table 3 lists the averaged material properties of the slag and steel as well as process parameters. The slag-pool interface is assumed to be stationary. The effect of droplets passing through the slag on the global electromagnetic field is ignored. As a result, the electromagnetic field can be obtained independent of the influence of other fields, such as temperature or flow, making the 3D calculation feasible.

Material properties	Slag	Steel
Density ($kg.m^{-3}$)	2650	7000
Viscosity (Pa.s)	0.002	0.0062
Specific heat ($J.kg^{-1}$)	1250	800
Liquid thermal conductivity ($W.m^{-1}.k^{-1}$)	4	40
Solid thermal conductivity ($W.m^{-1}.k^{-1}$)	0.5	25
Thermal expansion coefficient (K^{-1})	$9x10^{-5}$	0.0001
Liquidus temp. (K)	1685	1760
Solidus temp. (K)	1598	1670
Enthalpy of fusion ($J.kg^{-1}$)	475000	260000
Liquid electric conductivity ($ohm^{-1}.m^{-1}$)	120	$8.8x10^{5}$
Solid electric conductivity ($ohm^{-1}.m^{-1}$)	15	$8.8x10^{5}$
Mag. Perm. ($J.m^{-1}.A^{-1}$)	$4\pi x10^{-7}$	$4\pi x10^{-7}$
d_l (μm)	-	300
k_p	-	0.35
T_f (K)	-	1811
Operation parameters		
Ingot diameter (m)	0.75	
Electrode diameter (m)	0.5	
Slag height (m)	0.15	
Melt rate ($kg.hr^{-1}$)	750	
RMS current (kA)	14.1	
AC frequency (Hz)	50	
Power (MW)	0.75	

Table 3. Averaged material properties and operation parameters of the ESR process.

As shown in Figure 1(b), the magnetic field is computed in a 2D axisymmetric domain including an electric conductive mold based on the electromagnetic induction equation (B_θ). Then, the calculated parameters, such as Lorentz force and Joule heating, are interpolated and patched in the azimuthal direction within our 3D domain. Furthermore, the 2D axisymmetric computational domain and boundaries, which were also used in our previous study, [16] are shown in Figure 1(a). Note that the boundary conditions of the 2D axisymmetric and 3D domains are the same. A total number of 1.85 million mesh elements is used for the 3D calculation. The calculation requires three weeks using a multi-CPU cluster (24 cores, parallel computing).

Following the industrial process, an alternating current (AC) with a frequency of 50 Hz was applied. According to plant observations, a relatively uniform layer of slag skin (~ 1 mm)

developed between the solidified shell of the ingot and the mold. Electrical and thermal effects of the slag skin layer are included in the model. A portion of the electric current (~ 30 %) crosses the slag skin layer, entering the mold. The electric current tends to flow along the surface because of the electric skin effect. This behavior of electric current is demonstrated in the electrode, ingot, and mold (Figure 1(b)). As the electric current passes through the slag-pool interface, the current lines bend toward the mold. Furthermore, a strong skin effect is observed in the mold as a result of the large electrical conductivity of the copper mold (~ 4 x 10^7 $ohm^{-1}.m^{-1}$). The eddy currents generated within the copper mold can propagate to the steel ingot in the region where full contact (~3 cm) is assumed between the mold and the ingot [17].

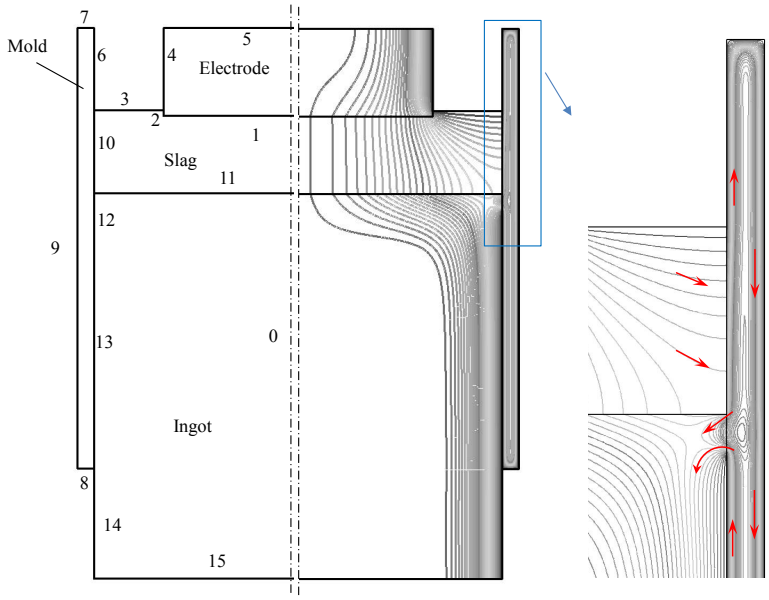

(a) (b)

Figure 1. (a) Computational domain and labelled boundaries. (b) Electric current path (red arrows indicate the direction of electric current).

The governing equations for the flow are solved in 3D within the slag and melt pool, including the ingot mushy zone. The thermal buoyancy is modeled with the Boussinesq approximation. The interdendritc flow in the mushy zone is modeled based on Darcy's law. The anisotropic permeability of the mushy zone according to Heinrich and Poirier [18] is

applied to account for the drag resistance of the mushy zone to the interdendritic melt flow. It is considered that primary dendrites grow in the direction of the temperature gradient inside the mushy zone, thus the unit vector ($\vec{n}_{\parallel} = \frac{\vec{\nabla} T}{\left\| \vec{\nabla} T \right\|}$) determines the parallel direction relative to the primary dendrites. The velocity ($\vec{u}_r$) of the interdendritic melt relative to dendrites can be expressed as the sum of parallel and perpendicular velocities ($\vec{u}_r = \vec{u}_{\perp} + \vec{u}_{\parallel}$). After calculating the parallel velocity using the parallel unit vector ($\vec{u}_{\parallel} = (\vec{u}_r \cdot \vec{n}_{\parallel})\vec{n}_{\parallel}$), one can simply obtain the perpendicular velocity relative to dendrites ($\vec{u}_{\perp} = \vec{u}_r - \vec{u}_{\parallel}$). Similarly, the unit vector in perpendicular direction can be obtained: $\vec{n}_{\perp} = \frac{\vec{u}_{\perp}}{\left\| \vec{u}_{\perp} \right\|}$. Eventually, the calculated unit vectors are used to determine the drag resistance force (Table 1).

The turbulence is modeled using the Scale-Adaptive Simulation (SAS) approach [19], which is an improved version of the shear stress transport (SST-K-ω) turbulent model [20]. The accuracy of the results using the SAS model is comparable to that using the LES model with the advantage of lower computational cost [19]. The effects of droplets are considered as momentum, energy, and mass carries that impact both the slag and liquid melt pool [21]. The temperature fields in the slag, mold, and ingot are determined by solving an enthalpy conservation equation considering the source of Joule heating and solidification latent heat [16]. We treat the steel as an effective binary Fe-C alloy in which the alloy element C is very diffusive in both liquid and solid states. Thus, the Lever rule is applied to compute the liquid fraction as a function of temperature.

A transient simulation is made, and a quasi-steady state can be achieved. Snapshots of the 3D temperature field on the slag surface within a period of fifty seconds are shown in Figure 2.

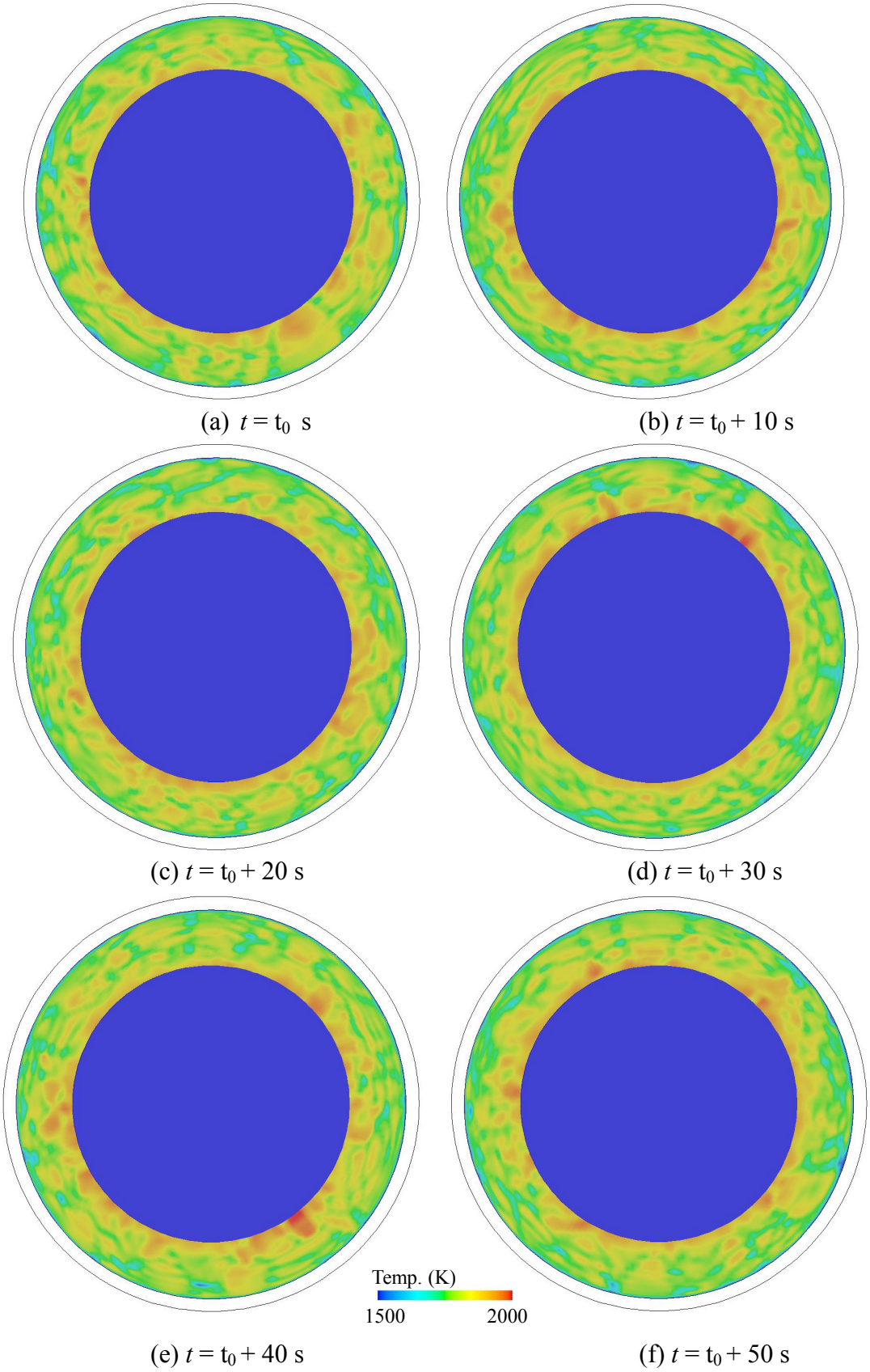

Figure 2. Snapshots of temperature distribution on the slag free surface.

The flow is very chaotic and spatially disordered. The instantaneous velocity components (u_i, $i = r, \theta, z$) in radial (r), axial (z), and tangential (θ) directions can be decomposed to mean ($\overline{u}_i$, $i = r, \theta, z$) and fluctuating (u_i', $i = r, \theta, z$) values aimed at characterizing the turbulent flow in the slag and melt pool. Then, distributions of the fluctuations of velocity components about the mean values are analyzed. For the latter, variances of velocity components ($\frac{1}{N}\sum_{n=1}^{N}(u_i - \overline{u}_i)^2$, $i = r, \theta, z$) are calculated over a long period of time (~ 30 min) until statistical invariance is achieved. Note that N is the total number of samples (~ 18000), which were obtained every 0.1 seconds over a total of 30 min. As shown in Figure 3, distributions of all of the components show considerable fluctuations in the same area under the electrode and near the interfaces (slag-pool or slag-air). However, the flow is almost statistically invariant near the mold wall and deep into the melt pool. Nevertheless, fluctuations are observed to be fairly axisymmetric as shown in different sections (Cut I and Cut II) in Figure 3 (c)-(d). This result implies that a 2D axisymmetric model might be able to predict the flow behavior.

The mean velocity and mean temperature fields averaged over 30 minutes are also shown in Figure 4. The flow direction is drawn under the shadow of the electrode in the slag zone. It is found that the hot melt in the melt pool under the electrode is continuously pushed toward the mold wall. The flow is dominantly driven by buoyancy in the melt pool. The hottest zone in the slag zone is observed under the electrode where the current density is the largest. The turbulence in the slag is strong under the electrode region where the flow is swirling. The effective thermal conductivity in the slag bulk is dramatically increased (~ 80 $W^{-1}.m^{-1}.K$) because of the turbulence [2]. Furthermore, strong turbulence is observed in the melt pool where the effective thermal conductivity is predicted to be as large as 150 $W^{-1}.m^{-1}.K$.

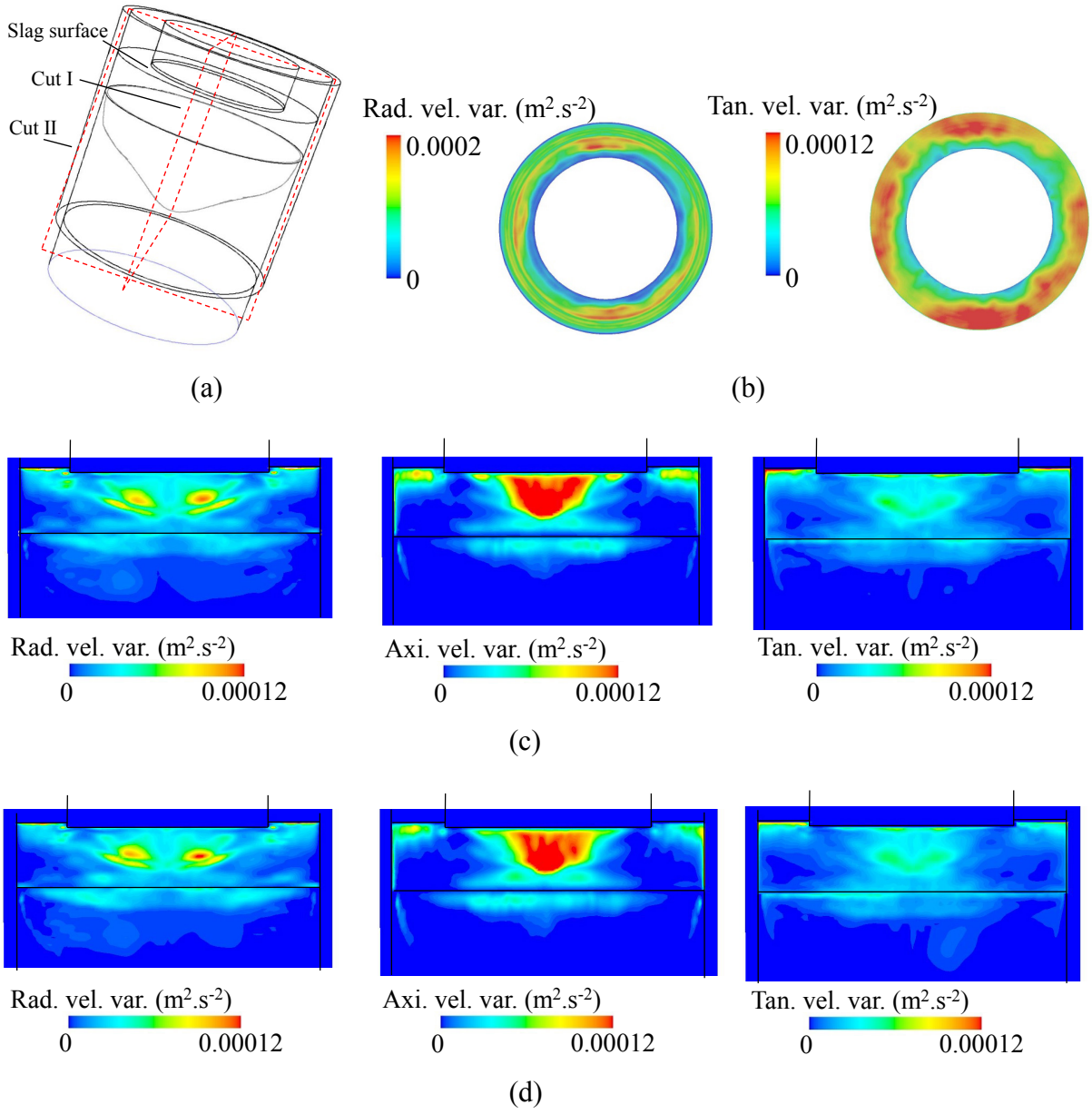

Figure 3. (a) Demonstration of cross sectional cuts in the 3D computational domain; (b) distribution of variance of velocity components (radial and tangential) on slag surface; (c) distribution of variance of velocity components (radial, axial, and tangential) on Cut I; (d) distribution of variance of velocity components (radial, axial, and tangential) on Cut II.

Therefore, the heat transfer is mainly governed by turbulent diffusion rather than mean flow convection in the melt pool. Essentially, the heat transfer is very efficient in the melt pool.

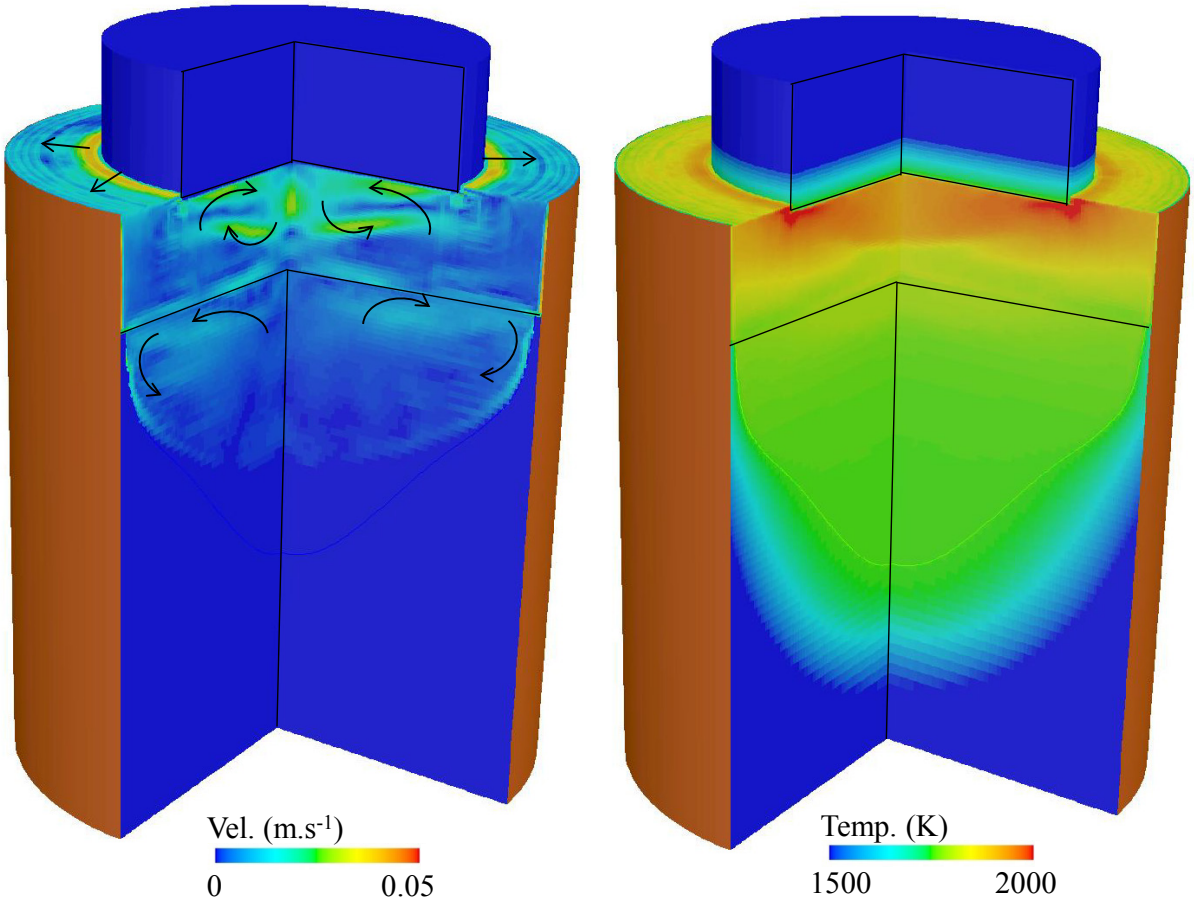

Figure 4. (a) Mean velocity field, and (b) mean temperature field averaged over 30 min.

Despite the transient 3D flow, the pool profile is firmly steady. The kinetic energy of the melt pool ($\sim \iiint \frac{1}{2}\rho f_l \|\vec{u}\|^2$) is continuously tracked. Eventually, a weak oscillation around the average value (~ 0.08 J) is observed, demonstrating that the system reaches a quasi-steady state. It must be considered that the kinetic energy in the system might be underestimated because the interface movement is not included in the current simulation [8].

For comparison, a 2D axis symmetrical calculation with the same numerical model was performed [16]. The pool profile predicted by the 2D calculation is compared with that predicted by the 3D calculation (Fig 5(a)), in which an insignificant difference is observed.

However, a better agreement in the shape of the melt pool is observed between the 3D simulation and the experimental results as shown in Fig 5(b). In the experiment, the pool profile of the ingot defined by $f \approx 0.98$ was marked using solid tungsten granulate markers (Fig 5(b)). The conditions of the experiment were presented in detail by Korp et al. [22]. No markers were found in the region close to the mold wall where liquid metal is in direct contact with the mold, known as the standing height or liquid cap. The length of the standing height (typically ~ 1 to 10 cm) depends on many factors, such as the amount of mold current, contact length, and slag-pool interface movement [7-8].

In summary, a 3D simulation is performed to analyze the transient flow behavior of an industrial scale ESR process. The numerical model includes the calculation of the electromagnetic field; the thermal field in the electrode, molten slag, ingot, and mold; the flow in the molten slag and melt pool regions; and the solidification of the ingot. The velocity field is very chaotic and turbulent; therefore, the heat transfer as a result of the turbulent eddy diffusion is very efficient, and the temperature distribution tends to become uniform in the melt pool. As a consequence, the melt pool profile is predicted to be axis symmetric, which indicates and verifies that a 2D axis symmetrical calculation is sufficient to model the melt pool profile. The results are validated against the experiment.

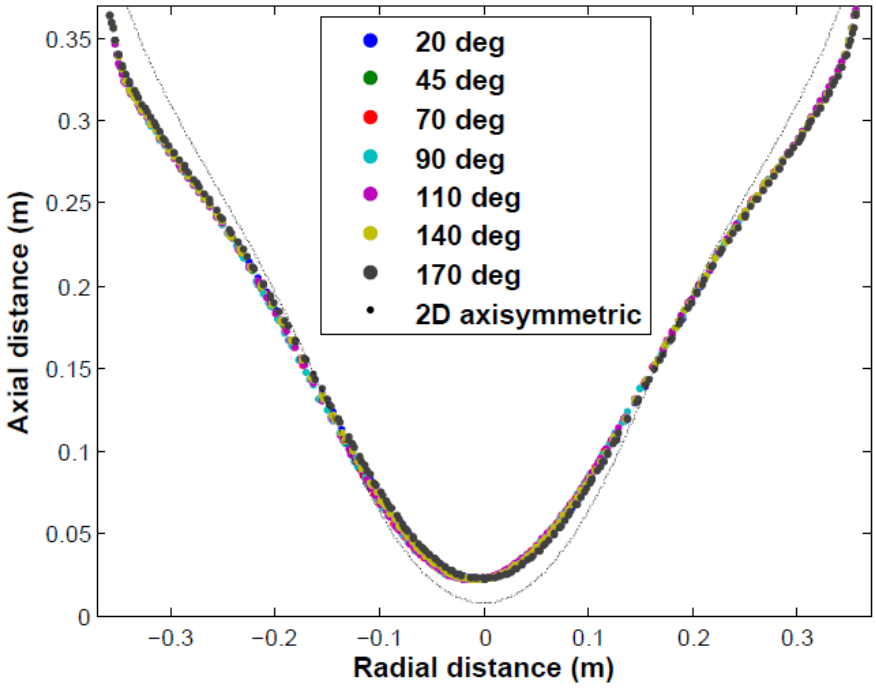

(a)

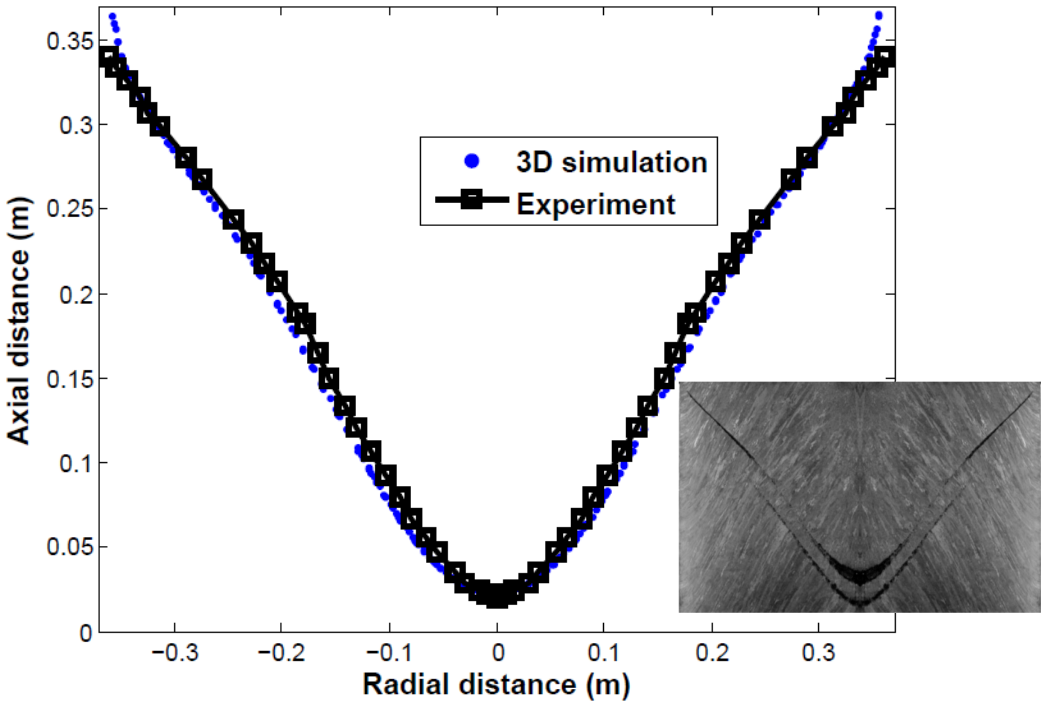

(b)

Figure 5. (a) Pool profile obtained in various angular vertical sections of 3D simulation compared with 2D axisymmetric simulation. (b) Comparison between the simulation (3D) and experimental pool profile.

References

[1] B. Hernandez-Morales, A. Mitchell, *Ironmak. and Steelmak.* **1999**, 26, 423.

[2] M. Choudhary, J. Szekely, *Ironmak. and Steelmak.* **1981**, 5, 225.

[3] A. Jardy, D. Ablitzer, J. F. Wadier, *Metall. Trans.* **1991**, 22, 111.

[4] K.M. Kelkar, J. Mok, S.V. Patankar, A. Mitchell, *Phys. IV France* **2004**, 120, 421.

[5] A. Patel, in *Proc. of Liquid Metal Processing and Casting,* Nancy **2007**, p. 95.

[6] A. Kharicha, A. Ludwig, M. Wu, *Mater. Sci. Eng. A* **2005**, 413, 129.

[7] A. Kharicha, W. Schützenhöfer, A. Ludwig, R. Tanzer, M. Wu, *Steel Res. Int.* **2008**, 79, 632.

[8] A. Kharicha, M. Wu, A. Ludwig, M. Ramprecht, H. Holzgruber, in *CFD Modeling and Simulation in Materials Processing* (Eds: L. Nastac, L. Zhang, B. G. Thomas, A. Sabau, N. El-Kaddah, A. C. Powell, H. Combeau), Wiley, New jersey **2012**, p. 139.

[9] A. Kharicha, W. Schützenhöfer, A. Ludwig, R. Tanzer, M. Wu, *Int. J. Cast Metals Res.* **2009**, 22, 155.

[10] A. Kharicha, A. Ludwig, R. Tanzer, W. Schützenhöfer, *Mater. Sci. Forum* **2010**, 649, 229.

[11] V.Weber, A. Jardy, B. Dussoubs, D. Ablitzer, S. Ryberon, V. Schmitt, S. Hans, and H. Poisson, *Metall. Trans. B* **2009**, 40, 271.

[12] M. Eickhoff, N. Giesselmann, A. Rückert, H. Pfeifer, J. Tewes, J. Klöwer, in *2nd Int. Conf. on Ingot Casting, Rolling, and Forging*, Milan **2014**.

[13] K. Fezi, J. Yanke, M. J. M. Krane, *Metall. Trans. B* **2014**, 46, 766.

[14] A. Kharicha, A. Ludwig, M. Wu, in *Proc. of EPD Congress*, San Diego **2011**, p. 771.

[15] Q. Wang, Z. He, B. Li, F. Tsukihashi, *Metall. Trans. B* **2014**, 45, 2425.

[16] E. Karimi-Sibaki, A. Kharicha, J. Korp, M. Wu, A. Ludwig, *Mater. Sci. Forum* **2014**, 790, 396.

[17] A. Kharicha, E. Karimi-Sibaki, M. Wu and A. Ludwig, in *Proc. of Liquid Metal Processing and Casting*, Austin **2013**, p. 95.

[18] J. C. Heinrich and D. R. Poirier, *Comptes Rendus Mecanique* **2004**, 332, 429.

[19] F.R. Menter and Y. Egorov, in *AIAA paper 2005-1095*, Nevada **2005**.

[20] F. R. Menter, *AIAA Journal* **1994**, 32, 1598.

[21] E. Karimi-Sibaki, A.Kharicha, M. Wu and A. Ludwig, H. Holzgruber, B. Ofner, M. Ramprecht, in *Proc. of Liquid Metal Processing and Casting*, Austin **2013**, p. 13.

[22] J.C. Korp, M. Kubin, in *INTECO Remelting and Forging Symposium*, Shanghai **2010**.

Publication VII

Transient melting of an ESR electrode

E. Karimi-Sibaki, A. Kharicha, J. Bohacek, M. Wu, A. Ludwig

In: Liquid metal processing and casting conference (LMPC), 2015, Leoben, Ed. by: A. Kharicha, R. Mark Ward, H. Holzgruber, M. Wu, IOP Conf. Series: Materials Science and Engineering, In Press

Transient melting of an ESR electrode

A Kharicha[a,b] , E Karimi-Sibaki [a] , J Bohacek[b], M Wu[a,b], and A Ludwig[b]
[a]Christian-Doppler Lab for Adv. Process Simulation of Solidification & Melting,
[b]Chair of Simulation and Modeling of Metallurgical Processes,
University of Leoben, Franz-Josef-Str. 18, A-8700 Leoben, Austria

E-mail: abdellah.kharicha@unileoben.ac.at

Abstract

Melting parameters of ESR process such as melt rate and immersion depth of electrode are of great importance. In this paper, a dynamic mesh based simulation framework is proposed to model melt rate and shape of electrode during the ESR process. Coupling interactions between turbulent flow, temperature, and electromagnetic fields are fully considered. The model is computationally efficient, and enables us to directly calculate melting parameters. Furthermore, dynamic change of electrode shape by melting can be captured. It is necessary to control the feeding velocity of electrode due to melting instabilities in the ESR process. As such, a numerical control is implemented based on the immersion depth of electrode to achieve the steady state in the simulation. Furthermore, the modeling result is evaluated against an experiment.

Introduction

The electroslag remelting (ESR) process is used for manufacture of superior quality steel and super alloys such as titanium alloys. Within the process, a consumable electrode melts through an electrically resistive slag layer through Joule heating. Then, droplets from the electrode pass through the slag and reach the liquid melt pool. Finally, the melt pool solidifies in a water-cooled mold to build the high-grade ingot. The internal quality of ingot is characterized according to the shape of melt pool especially depth and thickness of mushy zone. A shallow melt pool is favorable to achieve unidirectional solidification. Furthermore, producing an ingot with a defect-free surface is desirable. The electrode melt rate is a key parameter, affecting internal and surface quality of ingot. The influence of melt rate on the pool shape of an ESR ingot was investigated by Mitchell [1]. The depth of melt pool and thickness of the mushy zone were found to increase when the process was operated with higher melt rate. However, Suarez [2] reported that with the increase of melt rate a relatively smooth ingot surface can be obtained.

As reported by Kishida et al. [3], the melt rate, shape and immersion depth of electrode are interdependent parameters that are significantly influenced by the amount of power generated in the process. With the increase of voltage (generated power) in the process, the following melting behaviors were observed: the melt rate increases, the immersion depth decreases, and the shape of electrode tip becomes flatter. Over the last decades, a number of studies were carried out on this topic. For instance, Mitchell et al. modeled the temperature field in the electrode for a laboratory scale ESR process [4]. Their calculated temperature profile agreed with the experimental result. Mendrykowski et al, found that thermal radiation on the surface is ignorable compared to heat conduction along the electrode [5]. Tacke et al. [6] conducted a series of experiments to investigate melting behavior of a

laboratory scale ESR electrode. Furthermore, they proposed an approximate formula for the immersion depth which was validated against experiments. By evaluation of thermal fluxes through boundaries, Jardy et al. predicted higher melt rate when buoyancy force is stronger than electromagnetic force [7]. Yanke et al. applied an effective heat transfer coefficient to study the melting behavior of an industrial scale ESR process [8]. Recently, Kharicha et al [9] modeled electrode melting within the framework of multiphase Volume of Fluid (VOF) method. It was stated that the coupling between melt rate and Joule heat is very unstable. Details of flow, temperature, and magnetic field during electrode melting were described. However, the proposed VOF based method is computationally expensive.

In this paper, a dynamic mesh-based simulation framework is proposed to model melting and shape of electrode tip. The proposed method is robust and computationally efficient. Complex interactions between flow, temperature, and electromagnetic fields are considered. In ESR process, it is necessary to continuously track and control immersion depth of electrode due to melting instability. In order to achieve stability in the simulation, a numerical control of immersion depth is implemented. Details of flow, temperature, and electromagnetic fields during remelting are demonstrated. Furthermore, the model is evaluated against experimental results [6].

A brief description of the model

Previously, the governing equations of flow, heat, and electromagnetic fields together with related boundary conditions as well as simulation parameters such as material properties and operation conditions were presented in details [10]. Here, a short description of the model is given. An axisymmetric computational domain is considered including electrode, slag, air, mold, and liquid zones as shown in Figure 1 (a). The Finite Volume Method (FVM) is used to simulate fluid flow, heat transfer, and electromagnetic fields. The

commercial CFD software, FLUENT-ANSYS v.14.5, is the solver that includes a dynamic mesh technique for the simulation of displacements of boundaries. The modeling equations for fields such as electromagnetic field or boundaries (stationary and moving) are implemented using User-Defined Functions (UDF).

The well-known A-ϕ formulation is used to compute the electromagnetic field where ϕ is the electric scalar potential and A denotes the magnetic vector potential. After calculating the magnetic field and subsequently electric current density distribution, the Lorentz force as well as Joule heating are obtained and added as source terms to momentum and energy equations respectively. Applying A-ϕ formulation to calculate electromagnetic field was extensively described by Kharicha [9].

The turbulent flow field in slag and melt pool is calculated considering the effect of Lorentz force and thermal buoyancy (Boussinesq approximation). The turbulence in the system is modeled using SST-k-ω approach. The essential feature of SST model is an accurate and effective near wall treatment due to insensitivity of the model to grid spacing of near wall cells [11-12]. The enthalpy conservation equation is solved to determine the temperature field taking into accounts Joule heating and latent heat sink (S_{LH}) required to melt the electrode [10, 13]. The latter will be described after introducing equations regarding to displacement of boundaries (electrode tip-slag and slag-air interfaces).

Displacements of domain boundaries are modeled using dynamic and deformable meshes in which the mesh nodes can be relocated. The following dynamic mesh schemes are used to handle boundary movement in the system. Firstly, layering scheme is used that involves creation and destruction of cell rows in the vicinity of a moving boundary. Secondly, smoothing scheme is applied in which the grid nodes are considered as a network of interconnected springs. The connectivity between grid nodes remains unchanged, but they can reposition [14]. In the computational domain, slag-air interface (moving) and electrode tip (moving-deforming) boundaries are allowed to move as shown in Figure 1(b).

A high resolution mesh with equisized cells is used in the whole domain with the total number of 20000 cell elements (the mesh resolution is shown in melt pool).

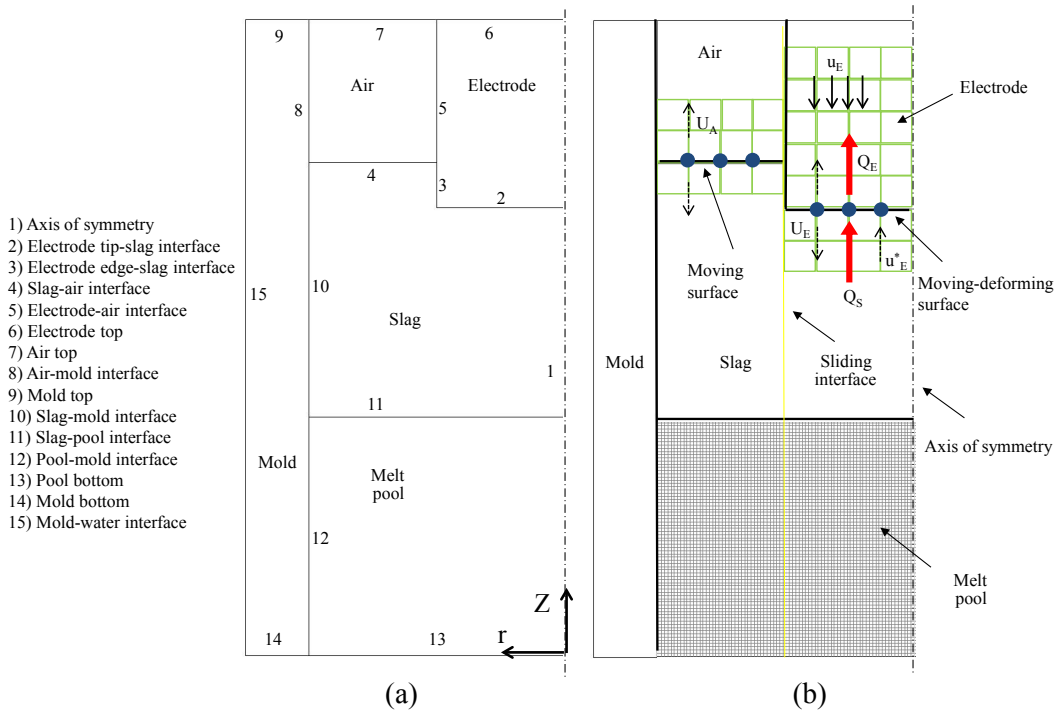

Figure 1. (a) Configuration of computational domain and boundaries, (b) Conceptual demonstration of heat balances across the electrode tip, melting velocity, feeding velocity, total velocity, and slag-air interface velocity (Note that the mesh resolution is very fine with equisized cells in the whole domain that is shown in melt pool, however the mesh is exaggeratedly shown to be coarse near the electrode for illustrative purpose)

Note that, both temperature field of electrode and velocity of melting at electrode tip are unknown. Physically, no dendritic mushy zone was observed during melting process, and the liquid-solid interface remained smooth. As such, melting of electrode can be considered as a Stefan problem where a phase boundary moves with time. The velocity of grid nodes at moving boundaries are computed using a set of balances equations. The velocity of dynamically deforming electrode tip is determined according to the amount of heat provided to the electrode through the slag.

$$U_E = u_E^* - u_E \tag{1}$$

$$Q_S - Q_E = \rho_{metal} \Delta H u_E^* \tag{2}$$

$$\begin{cases} u_E^* \geq 0 \quad (Q_s > Q_E) \\ u_E^* < 0 \quad (Q_s < Q_E) \end{cases} \tag{3}$$

According to Eq. (1), the grid node velocity of the electrode tip (U_E) is the sum of melting velocity (u_E^*) and the electrode feeding velocity (u_E). Based on Eq. (2), the melting velocity is dependent on the heat flux provided to the electrode (Q_S), heat flux diffused into the electrode (Q_E), density of metal ($\rho_{metal} \sim 7100$ kg.m^{-3}), and the latent heat of fusion ($\Delta H \sim 260$ kJ.kg^{-1}). The origin of z-referential is set at the bottom of computational domain. Therefore, the sign (positive or negative) of melting velocity depends on the balance of heat fluxes at the electrode tip as expressed in Eq. (3). Consider that, the right hand side of Eq. (2) describes the amount of latent heat provided to melt the electrode. Therefore, the volumetric source of latent heat (S_{LH}) that is absorbed adjacent to electrode tip is given by

$$S_{LH} = \rho_{metal}\ u_E^* \Delta H \left(\frac{S_{cell-electrode}}{V_{cell-electrode}}\right) \tag{4}$$

where ($S_{cell\text{-}electrode}$) denotes the face area of a cell that belongs to the electrode tip and ($V_{cell\text{-}electrode}$) is the cell volume.

With the increase of electrode immersion depth, the slag level rises to conserve the total mass of slag. Therefore, the slag-air interface is also modeled as a moving boundary. The velocity of grid nodes (U_A) of the slag-air moving boundary is computed as:

$$U_A = \frac{m_0 - m}{\rho_{slag} \Delta t \pi \left(R^2_{mold} - R^2_{electrode}\right)} \tag{5}$$

where (m_0) denotes the slag initial mass, (m) is the computed mass, ($\rho_{slag} \sim 2700$ kg.m^{-3}) is density of slag, ($\Delta t \sim 0.1$ s) is time step size, and (R_{mold}) and ($R_{electrode}$) are the radius of the mold and electrode respectively.

The electrode feeding velocity is preferred to be kept constant during industrial operation of an ESR process. It is necessary to adapt feeding velocity (u_E) according to the immersion depth to stabilize the electrode position so that the electrode tip neither reaches the melt pool nor the slag free surface [9]. The following restriction is imposed on the feeding velocity of electrode:

$$u_E = u_E^0 \min\left[1, \frac{l_{\max} - l}{l_{\max} - l_{\min}}\right] \tag{6}$$

(l_{min}) and (l_{max}) are minimum and maximum allowable immersion depth of electrode, and (u_E^0) is initial feeding velocity which are the input parameters of the process. Furthermore, a uniform velocity field inside the electrode zone is specified which has similar magnitude as the electrode feeding velocity (u_E).

The simulation is executed in transient where the immersion depth and shape of electrode tip is continuously tracked. The steady state is achieved once the velocity of grid nodes (U_E) converges to zero. The melt rate ($\dot{m} \geq 0$) of electrode can be directly computed as follow:

$$\dot{m} = -\rho_{metal} \iint_{S_{electrode}} \vec{u}_E^* \cdot d\vec{S} \tag{7}$$

Following the experiment of Tacke [6] on a laboratory scale ESR process, we used an identical geometry and operating parameters. Table 1 lists the parameters used in the experiment [6] and our simulation. Furthermore, the steady state melting parameters of simulation such as computed immersion depth are listed.

Table 1. Operation conditions and results of a laboratory scale ESR process [6], a comparison is also made with the simulation results (steady state).

	Experiment [6]	**Simulation**
Electric current mode	DC	DC
Electric current (kA)	1.9	1.9
Mold current	Unknown	Yes
Electrode radius (cm)	4	4
Mold radius (cm)	8	8
Slag weight (kg)	4.0	4.1
Slag electric cond. ($ohm^{-1}.m^{-1}$)	Unknown	150
Slag thermal cond.($W.m^{-1}.K^{-1}$)	Unknown	4
Slag therm. exp. coeff. (K^{-1})	Unknown	$9x10^{-5}$
Voltage (V)	29	28
Power (kW)	55	57
Initial feeding vel. ($cm.s^{-1}$)	Unknown	0.0153
Steady feeding vel. ($cm.s^{-1}$)	0.0153	0.0076
Melt rate ($g.s^{-1}$)	5.5	3.7
Immersion depth (cm)	3.8	3.56
L_{min} (cm)	Unknown	2.5
L_{max} (cm)	Unknown	4.5

It must be noted that the following phenomena are not considered in our model. As generally recognized, the electric current is conducted by ions in the slag region. Consequently, difference in melt rate is observed based on the polarity of electrode (positive or negative) due to polarization overpotential [15]. Formation of a liquid film under the electrode and dripping of droplets through the slag are also not included [16-17]. Solidification of liquid pool is also ignored.

Results and discussions

A constant magnitude of DC current is imposed in the process. Additionally, it is assumed that the current can cross the slag skin flowing through the mold [15, 18-19]. The initial feeding velocity is not reported for the experiment, but the steady feeding velocity is known. Furthermore, the feeding velocity is adjusted adapted by Eq. 6 in the simulation. Figure 2 illustrates the evolution of electrode shape including electric potential, velocity, and temperature fields in slag and submerged part of the electrode. The amplitude of

voltage drop and power generated in the system depends on immersion depth (indicated by the distance between electrode tip and isolines of voltage drop). Decreasing immersion depth leads to significant voltage drop and power generation in the system as shown in Figure 2 (c). Therefore, the temperature notably elevates in the bulk of slag. With the increase of immersion depth, the isolines of voltage are shifted and the total voltage in the system decreases. However, the current density increases in the central region of slag and subsequently the Lorentz force become stronger. The latter intensifies the velocity under the shadow of electrode which results in promotion of stirring in the slag zone that is shown in Figure 2 (e). Here, the global energy transport is efficient due to strong turbulence which causes relatively uniform slag temperature. Finally, electrode develops a conical shape at steady state (t = 350 s). The mesh resolution near moving-deforming boundary (electrode tip) is also shown in Figure 2. Accordingly, the quality of mesh is very well preserved.

The variation in melt rate and generated power as well as feeding velocity and immersion depth are plotted during deformation of electrode tip until reaching the steady state which is shown in Figure 3. The results show that variation in generated power is much smoother than melt rate. The peak observed in generated power indicates the situation where the immersion depth is very shallow.

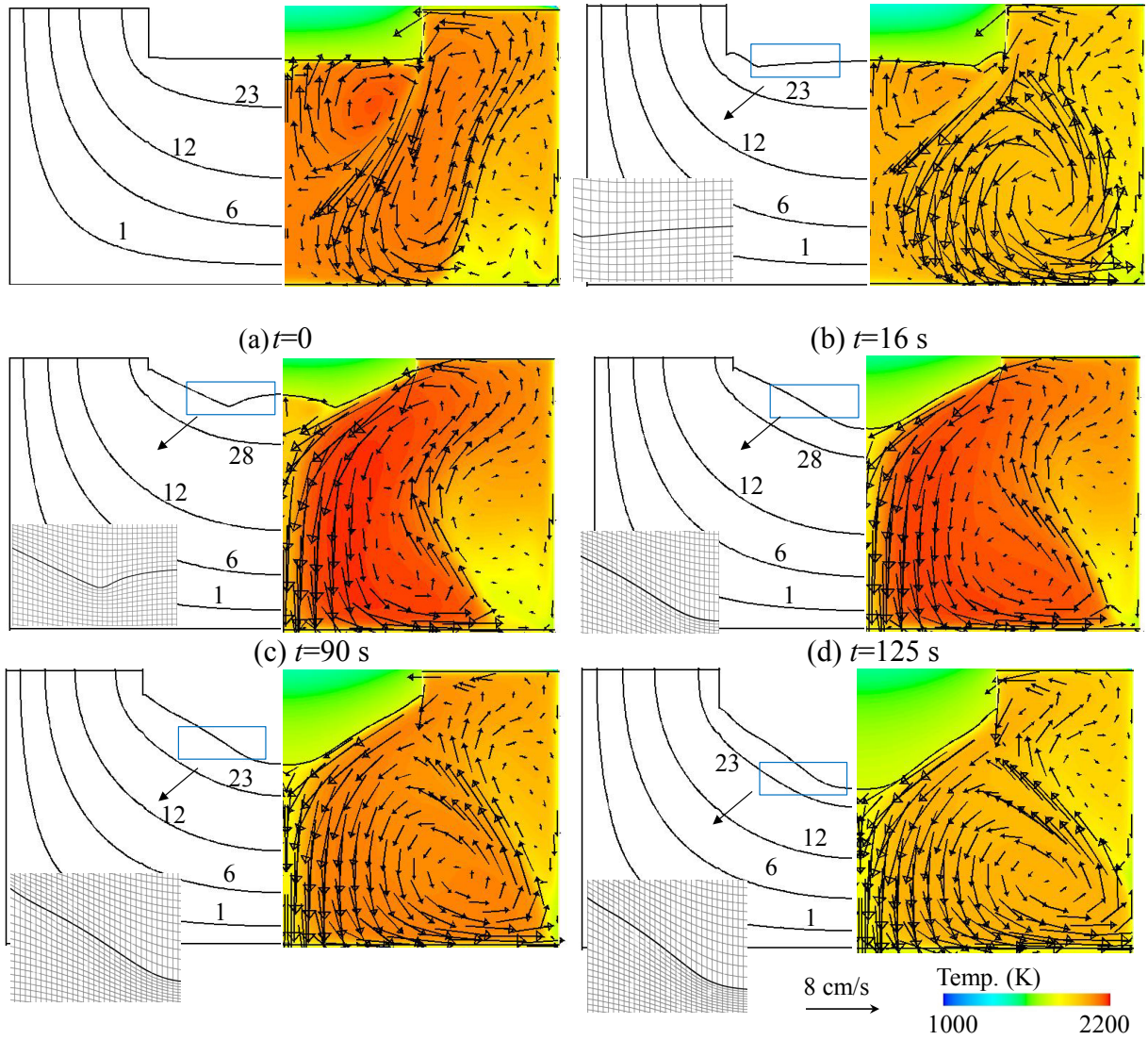

Figure. 2. Evolution of shape of electrode tip: (a) t=0, (b) t=16 s, (c) t=90 s, (d) t=125 s, (e) t=260 s, (f) t=350 s. On left half: isolines of voltage, and the grid node near the moving boundary (electrode tip). On right half: contour of temperature overlaid with the vectors of velocity in the slag region.

Despite gentle variation in generated power, the melt rate can dramatically increase or decrease before reaching the steady state. In fact, the melt rate is governed by the amount of heat provided to the electrode which is highly influenced by complex interactions between flow, temperature, and electromagnetic fields. For example, with decrease of immersion depth, Figure 3 (d), the generated power increases, Figure 3 (a) that leads to hotter slag and increase of melt rate as shown in Figure 2 (c). Furthermore, the constraint imposed on the immersion depth based on Eq. 6 can certainly affect the feeding velocity as well as melt rate

of electrode. Further investigation is required to explore the effect of immersion depth control on melting behavior of electrode that is beyond the scope of the current work. Figure 4 compares the experimentally observed shape of electrode with the predicted shape in the simulation at steady state where a relatively good agreement is obtained. In any case, the shape of electrode tip is mainly influenced by temperature and flow distribution which are highly dependent on slag properties. The slag properties are temperature dependent, so a large uncertainty on the reported values exists due to difficulty of measurements at high temperature. For instance, the thermal conductivity of slag was reported to vary between 1 to 5 $W.m^{-1}.K^{-1}$, whereas the electrical conductivity was measured to be between 80 to 300 $ohm^{-1}.m^{-1}$ [20-21].

It must be reported that we ran many simulations to perform a parameter study to investigate the effect of slag physicochemical properties such as electrical and thermal conductivity on the melt rate and shape of electrode. Our investigations were published with details in the previous paper [10]. It must be stated that the predicted melt rate by the simulation is lower than the value reported in experiment [Table 1]. The current model does not take into account effects of electrochemical reactions, formation of liquid film at electrode tip and dripping of droplets through slag. In fact departure and dripping of droplets can create stronger turbulence which enhance global energy transfer and melt rate of electrode [16-17]. The aforementioned phenomena must be included in the future model to improve quantitative accuracy of the model.

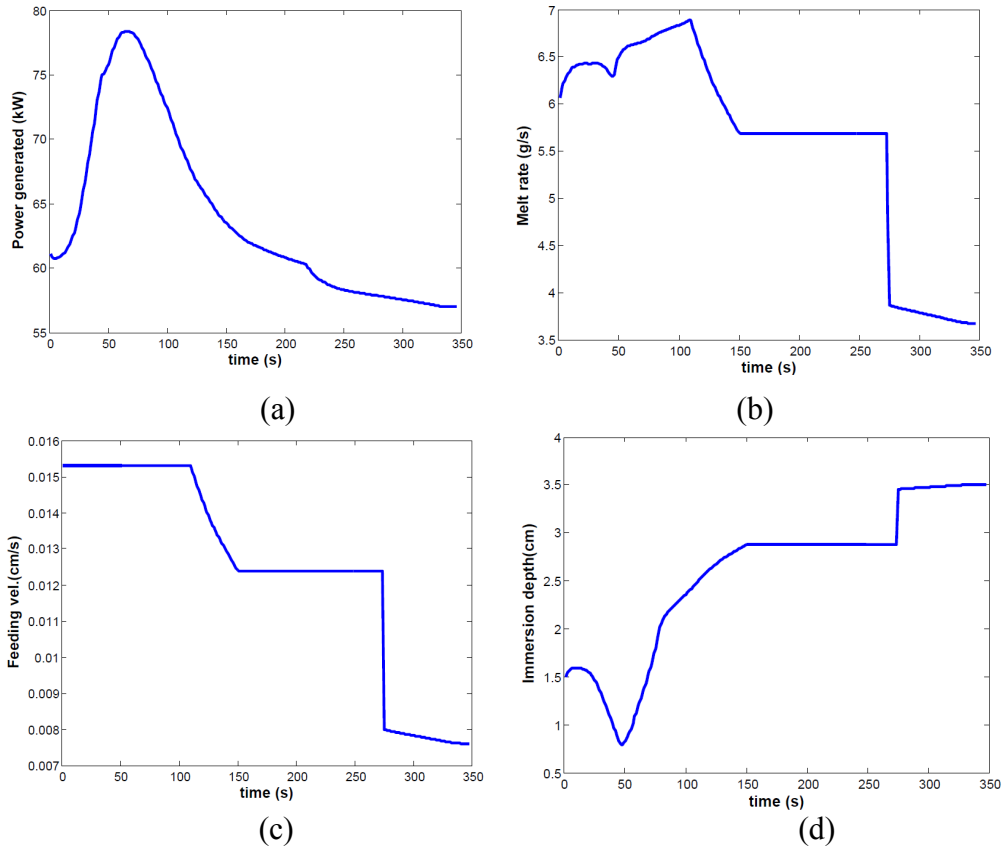

Figure 3. Analysis of melting parameters: (a) generated power, (b) melt rate of electrode, (c) feeding velocity, (d) immersion depth.

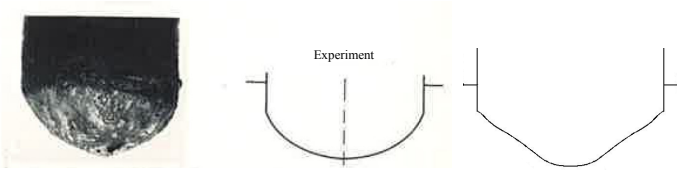

Figure 4. A comparison of (a) the shape of electrode tip as observed in the experiment [6] with (b) the calculated shape of electrode from simulation.

Summary

A dynamic mesh based approach is used to model submerging and remelting of electrode in electroslag remelting (ESR) process. The computational domain is 2D axisymmetric where interactions between turbulent flow, temperature, and electromagnetic fields are fully taken into account. It is shown that the model is capable of predicting the evolution of electrode shape during remelting. In order to achieve steady state, the immersion depth of electrode is continuously tracked and controlled. For the latter, a numerical control of feeding velocity is implemented dependent on the immersion depth. The model is computationally robust that enables us to directly compute melt rate without using any further assumption (e.g. heat transfer coefficient between electrode-slag). The shape of electrode is also validated against the experiment. Melt rate and shape of electrode are highly dependent on physicochemical properties of slag such as thermal and electrical conductivities. The effect of slag properties on melting behavior of electrode is extensively discussed in other paper [10].

Acknowledgement

The authors acknowledge the financial support by the Austrian Federal Ministry of Economy, Family and Youth and the National Foundation for Research, Technology and Development within the framework of the Christian Doppler Laboratory for Advanced Process Simulation of Solidification and Melting.

References

[1] Mitchell A 1984 *Conf. on Perspective in Metallurgical Development* (Sheffield) p 89

[2] Suarez F S, Roberts J E, and Schley L.D 1974 *5th Int. Symp. on Electroslag and Other Special Melting Technologies* (Pittsburgh) p 126

[3] Kishida T, Yamaguchi T, Tomioka T, and Ichihara T 1974 *Elect. steel* **45** 219

[4] Mitchell A, Joshi S, and Cameron J 1971 *Metall. Trans.* **2** 561

[5] Mendrykowski J, Poveromo J, Szekely J, and Mitchell A 1972 *Metall. Trans.* **4** 1761

[6] Tacke K H and Schwerdtfeger K 1981 *Arch. Eisenhüttenwesen* **52** 137

[7] Jardy A, Ablitzer D, Wadier J F 1991 *Metall. Trans.* **22** 111

[8] Yanke J, Fezi K, Fahrmann M, and Krane M J M 2013 *Proc. Of LMPC* (New York: Wiley–Interscience)

[9] Kharicha A, Wu M, and Ludwig A 2014 *ISIJ* **54** 1621

[10] Karimi-Sibaki E, Kharicha A, Bohacek J, Wu M, and Ludwig A, *Metall. Mater. Trans. B,* DOI 10.1007/s11663-015-0384-0

[11] Menter F R 1994 *AIAA Journal* **32** 1598

[12] Menter F R, Kuntz M, and Langtry R 2003 *Turb. Heat and Mass Trans.* **4** 625

[13] Karimi-Sibaki E, Kharicha A, Korp J, Wu M, Ludwig A 2014 *Mater. Sci. Forum* **790** 396

[14] Fluent 14.5 user's guide 2012 (Austin: Fluent Inc.)

[15] Kawakami M, Nagata K, Yamamura M, Sakata N, Miyashita Y, and Goto K S 1977 *Testsu-to-Hagane* **63** 220

[16] Kharicha A, Ludwig A, and Wu M 2011 *EPD congress* (San Diego) p 771

[17] Kharicha A, Wu M, Ludwig A, Ramprecht M, Holzgruber H 2012 *CFD modeling and simulation in materials* (New York: Wiley–Interscience) p 139

[18] Kharicha A, Ludwig A, and Wu M. 2005 *Mater Sci. Eng. A* **413** 129

[19] Kharicha A, Schutzenhofer W, Ludwig A, Tanzer R, and Wu M 2008 *Steel Res. Int.* **79** 632

[20] Taylor R, Mills K C 1982 *Arch. Eisenhüttenwesen* **53** 55

[21] Hajduk M and Gammal T E 1979 *Stahl Eisen* **99** 113

Publication VIII

An attempt to model electrode change during the ESR process

E. Karimi-Sibaki, A. Kharicha, M. Wu, A. Ludwig, H. Holzgruber, B. Ofner, A. Scheriau, M. Kubin, M. Ramprecht

In: Liquid metal processing and casting conference (LMPC), 2015, Leoben, Ed. by: A. Kharicha, R. Mark Ward, H. Holzgruber, M. Wu, IOP Conf. Series: Materials Science and Engineering, In Press

An attempt to model electrode change during the ESR process

E Karimi-Sibaki [a], A Kharicha[a,b], M Wu[a,b], A Ludwig[b], H Holzgruber[c], B Ofner[c], A Scheriau[c], M Kubin[c], and M Ramprecht[c]

[a]Christian-Doppler Lab for Adv. Process Simulation of Solidification & Melting,
[b]Chair of Simulation and Modeling of Metallurgical Processes,
University of Leoben, Franz-Josef-Str. 18, 8700 Leoben, Austria
[c]INTECO Special Melting Technologies GmbH, 8600 Bruck/Mur, Austria

E-mail: abdellah.kharicha@unileoben.ac.at

Abstract

The electrode change technology is used to produce very large heavy ingots in which a number of electrodes are remelted one after another during the ESR process. Preparing the new electrode for remelting requires a certain period of time when the electric current is stopped (power off). Here, CFD simulation is used to study the behavior of a large scale ESR process during the electrode change (power off). Firstly, the electromagnetic, temperature, and turbulent flow fields in the process before electrode change are modelled. Mold current and thermal effect due to shrinkage of ingot is considered in the model. Then, a transient simulation is performed and the response of the system to the power off is continuously tracked. It is observed that the pool profile of ingot is preserved before and after electrode change. Details of the flow and temperature distributions during electrode change are presented in the paper.

Introduction

Nowadays, the demand for very large heavy ingots (> 100 tons) through ESR process is increased especially in chemical, oil and gas industry. Producing a large ingot by ESR process is quite a long process that might take several days. Manufacturing a large ingot requires electrode change technology in which several smaller electrodes are remelted to produce one big ingot. Special care must be taken to avoid internal and surface defects during electrode change due to power interruption in the system.

The entire electrode change procedure is divided to three steps. Firstly, within a very short time (< 5 min), the electric power is turned off, and a new preheated electrode is prepared to replace the remelted last one. Secondly, the electric power is again turned on. Consequently, the temperature of the new electrode rises to reach the melting temperature. Finally, the melt rate increases until reaching the target melt rate. As stated by Holzgruber [1], no traceable change in ingot internal composition was observed during the power interruption. However, Matushkina [2] reported slight defects of surface during electrode change. Jackson [3] monitored thermal field in mold using thermocouples to analyze heat balances across the ingot during power interruption. It was observed that solidification occurred much more rapidly at the pool periphery rather than in the ingot center. It was also found that gross changes in structure and composition of ingot are not expected unless power interruption lasts for too long.

There are only few reports available on this topic. As such, further investigation is required to clarify the influence of power interruption on the process. It is a very first attempt to model electrode change based on CFD simulation. Here, a numerical study is conducted in which the interaction between the turbulent flow, heat, and electromagnetism are taken into account. The model includes the effect of interface motion between molten slag and melt pool. A short collar mold ESR process is studied in which the system

behavior is continuously tracked. Formation of surface defects is not explicitly modeled. The thickness of slag skin is kept constant during the whole simulation. This assumption is based on the industrial measurement of skin thickness in plant trial for our case study where a uniformly thin layer is observed along the whole ingot.

Here only results including details of velocity and temperature fields regarding to the first step of electrode change procedure (power off) is presented. The melt pool profile is used as an indicator of the internal quality of ingot. Furthermore, variations in heat fluxes through boundaries are discussed.

Model

A 2D axisymmetric computational domain with a short collar mold is considered [4]. The computational domain includes electrode, mold, slag, and ingot. The Finite Volume Method (FVM) is used to model turbulent flow, temperature, and electromagnetic fields. The A-ϕ formulation is applied to compute the electromagnetic field in the whole domain where ϕ is the electric scalar potential and A denotes the magnetic vector potential ($\nabla \times \vec{A} = \vec{B}$). Details of A-ϕ method applied to solve the electromagnetic field for ESR process were described by Kharicha [5]. Note that, the electric current is allowed to cross the slag skin layer entering into the mold before electrode change (power off) [6-9].

After computing the magnetic field (B), the Lorentz force and Joule heating are calculated and added as source terms to momentum and energy equations.

The flow field in slag and melt pool is calculated. The drag resistance of the dendritic mushy zone to the flow is taken into account using the well-known Blake-Kozeny permeability model [10]. Using the previously described model for droplets as mass, momentum, and energy carriers, the impacts of falling droplets are taken into account [11]. Furthermore, the model includes the movement of slag and melt pool interface.

The turbulence is modeled using Scale-Adaptive Simulation (SAS) approach. The advantage of model is the resolution of turbulent spectrum in unstable flow conditions such as interface movement [12].

The temperature field is modeled by solving an enthalpy (h) conservation equation:

$$\frac{\partial}{\partial t}(\rho h) + \nabla \cdot (\rho \vec{u} h) = \nabla \cdot (\lambda \nabla T) + Q + S_{LH} \tag{1}$$

Where (λ) is thermal conductivity, (ρ) is density, (u) is velocity, (T) is temperature, (Q) is Joule heating, and (S_{LH}) is the source term for treating latent heat released by solidification of the ingot:

$$S_{LH} = -\frac{\partial}{\partial t}(\rho f L) - \rho L \vec{u}_{\mathrm{s}} \nabla f \tag{2}$$

In Eq. 2, (L) is latent heat of fusion, (u_{s}) denotes the casting velocity and (f) is the liquid fraction. A constant thickness of slag skin (~ 5 mm) is assumed for the whole simulation. A combined convection-radiation condition is considered for slag free surface where the emissivity coefficient is 0.8. Furthermore, formation of air gap between slag skin layer and mold due to shrinkage of ingot is modeled. For the latter, the contact between slag kin and mold wall is empirically assumed to be lost once the temperature at mold wall becomes 100 K lower than alloy solidus temperature. At the contact region the heat is conducted through slag skin to the mold. Otherwise, a combined radiation- convection condition is used to model heat transfer through the air gap. Therefore, a fully coupled simulation is performed including the effect of mold current and the thermal effect of solidifying ingot shrinkage. A summary of parameters used in the simulation is described in Table 1.

Table 1. A summary of parameters used in the simulation.

Mater. properties	Slag	Steel	Operation parameters	
Density ($kg.m^{-3}$)	2440	7000	Ingot diam. (m)	1.979
Viscosity (Pa.s)	0.01	0.0062	Elec. diam. (m)	1.1
Specific heat ($J.kg^{-1}$)	1255	500-800	Ingot length (m)	1.245
Liq. therm. cond. ($W.m^{-1}.k^{-1}$)	1.5-5	25-40	Slag height (m)	0.307
Sol. ther. cond. ($W.m^{-1}.k^{-1}$)	0.5	16	Melt rate ($kg.hr^{-1}$)	2200
Ther. exp. Coeff. (K^{-1})	0.0001	0.00011	RMS current (kA)	46
Liquidus temp. (K)	1715	1773	Freq. (Hz)	0.2
Solidus temp. (K)	1598	1668	Power (MW)	2.407
Liq. e. cond. ($ohm^{-1}.m^{-1}$)	180	$8.8x10^5$	Elec. change time (s)	175
Sol. e. cond. ($ohm^{-1}.m^{-1}$)	15	$8.8x10^5$		

First, the process is simulated before electrode change, and temperature, velocity, and electromagnetic fields are obtained. Afterwards, the following conditions are imposed on the system during the first step of electrode change (power off). The electric current is stopped flowing through the system, thus the Lorentz force and Joule heating are vanished. The electrode melting is ceased (no droplets), and subsequently the casting velocity is changed to zero. Additionally, the whole slag surface is considered to be exposed to the air.

Results and discussions

Figure 1 shows the modeling results of process before electrode change (power interruption) including magnetic flux density, current density, velocity, temperature, turbulence kinetic energy, and turbulence effective thermal conductivity. The generated power in the process is slightly oscillating around the average value (~ 2.4 MW) due to interface movement. As shown in Figure 1(a), a portion of electric current (~ 5%) enters to the mold in slag zone then returns to ingot through the contact region (mold and melt pool). The standing height (liquid metal in direct contact to mold) is influenced by the mold current [11, 13]. The flow and temperature distributions are shown in Figure 1(b). The flow is rotating clock-wisely (converging flow) under the edge of electrode in the slag zone that

indicates the Lorentz force is dominant. However, the flow is governed by thermal buoyancy and droplets impact in the bulk of liquid melt pool. Stronger flow under the shadow of electrode is due to the effect of droplets that bring momentum and thermal energy to melt pool. Furthermore, the movement of slag-melt pool interface certainly intensifies the flow in the liquid melt pool [14]. The maximum elevation of interface is observed to be around 7 mm in the simulation. Kharicha [15] reported a maximum elevation of 30 mm for a smaller scale ESR system (Diam. ~ 0.6 m). Nevertheless, with the increase of system size, the current density which is proportional to the inverse of square of diameter decreases in the domain. As such, a smoother movement of interface is expected. Additionally, the temperature distribution and isolines of solid fraction (indicating pool profile) are shown in Figure 1(b). The temperature field is relatively uniform in the melt pool and slag indicating rigorous mixing in the system. The slag is very hot under the shadow of electrode where the current density and subsequently released Joule heating is high. The distributions of turbulence kinetic energy and turbulence effective thermal conductivity are shown in Figure 1 (c). The turbulence kinetic energy is as notably strong in melt pool as in the slag region. Strong turbulence in liquid melt pool has been also reported by Kharicha [16-17] after simulation of the electrode melting in a fully coupled 3D simulation. It must be noted that a region of intense turbulence is created at upper part of melt pool because of interface movement. As shown in Figure 1 (c), the effective thermal conductivity of slag can dramatically increase (~ 150 $W.m^{-1}.K^{-1}$) in the bulk due to strong turbulence. Therefore, the energy transfer is efficiently increased, and it leads to relatively uniform temperature in the slag. However, the turbulence is damped near the walls and slag-melt pool interface where the effective thermal conductivity of slag is in the same magnitude of the molecular thermal conductivity (~ 5 $W.m^{-1}.K^{-1}$).

Snapshots of flow, temperature, and solidification during the first step of electrode change (power off) are illustrated in Figure. 2. The pool profile is slightly influenced near the mold

wall where the cooling rate is large. However, the flow distribution is totally altered. The clock-wise rotating vortex under the edge of electrode (converging flow) disappears in slag zone. During power interruption, the flow is completely driven by buoyance force results in counter-clock wise rotation of flow (diverging flow) in the slag. Furthermore, the magnitude of velocity decreases in the bulk as the time proceeds whereas the flow is still strong near the mold wall due to thermal buoyancy. The temperature response is observed to be much slower than flow response to the power interruption. Based on the simulation result, a minor impact on the pool profile is observed during power interruption.

The heat loss through the slag free surface and mold normalized by their magnitudes before power interruption is plotted against time as shown in Figure. 3. The amount of heat loss through the mold (~ 0.9 MW) remains almost constant since the thickness of slag skin is invariable. However, the heat loss through slag free surface (slag-air interface) during electrode change is notably larger compared to the value before power interruption (~ 0.8 MW). The heat loss through slag free surface is intensified at the beginning of power interruption due to increase in contact area between slag and air. As time proceeds, the temperature of slag at free surface decreases. Consequently, the convective-radiative heat loss at slag free surface is decreasing. Afterwards, increase in heat loss through slag-air interface is observed once again. Because of thermal buoyancy, the colder liquid slag on the slag-air interface sinks whereas hot liquid slag moves toward the free surface. This behavior of flow is clearly demonstrated in Figure 2(e-f).

According to our investigation, it is even possible to solidify slag at the free surface. Nevertheless, it is highly unlikely that solidified slag layers float on the surface because of having higher density compared to the liquid slag. Most probably, the floating solidified slag pieces sink into the hot slag bath where they remelt once again.

Note that the entire electrode change procedure is not only the first step (power off). The procedure also includes heating of the new electrode until reaching melting temperature

(second step) and remelting of the electrode until reaching the target melt rate (third step). Generally, those steps take much longer time (~ 30 min) compared to the first step (power off). During second and third steps, operation conditions of process such as input power or melt rate are dynamically changing. Further investigations are required to explore the behavior of the process during second and third steps.

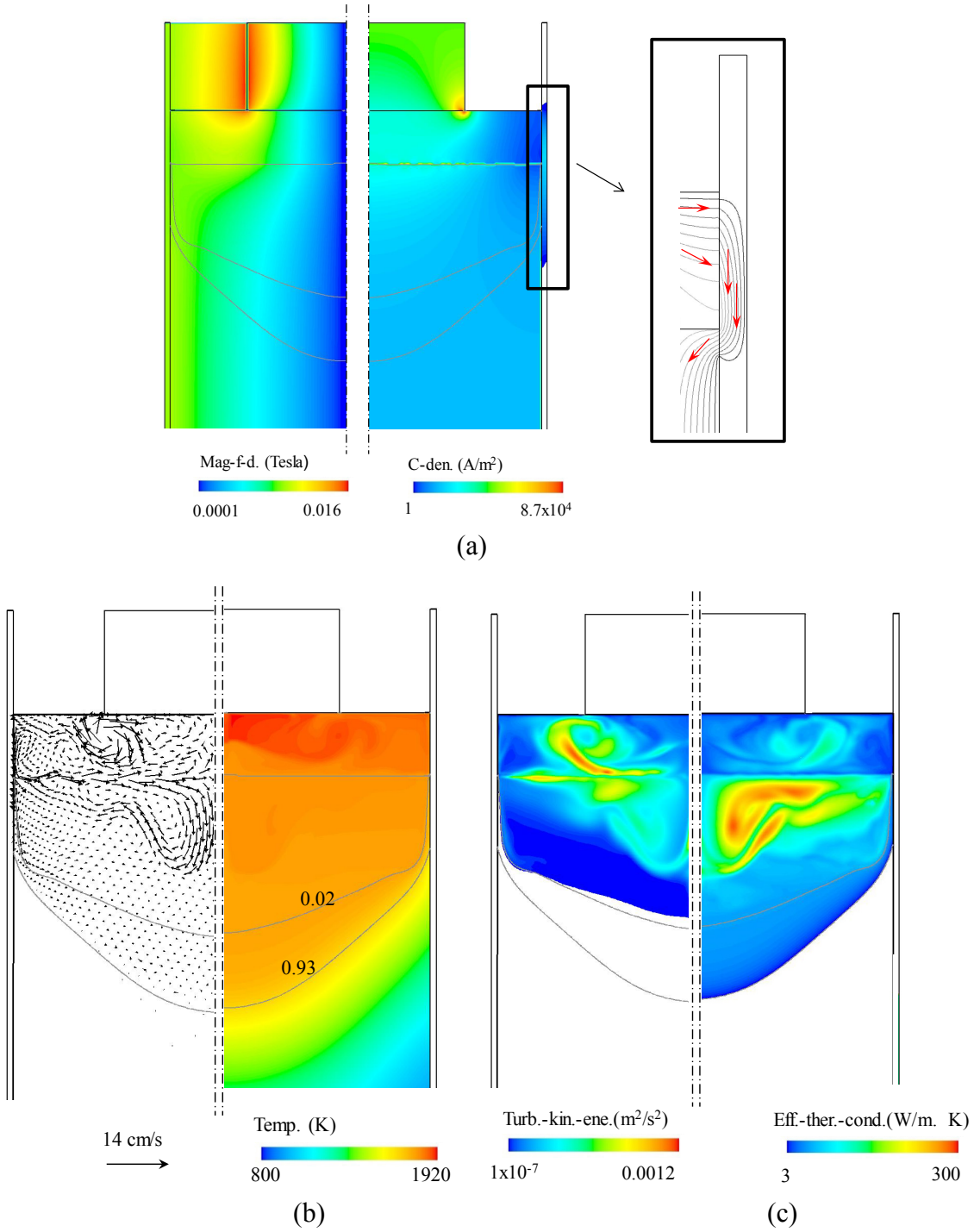

Figure 1. (a) Left: contour of magnetic flux density, Right: contour of electric current density (red arrows show direction of electric current), (b) Left: vectors of velocity, Right: contour of temperature overlaid with isolines of solid fraction, (c) Left: contour of turbulence kinetic energy, Right: contour of turbulence effective thermal conductivity in slag and melt pool.

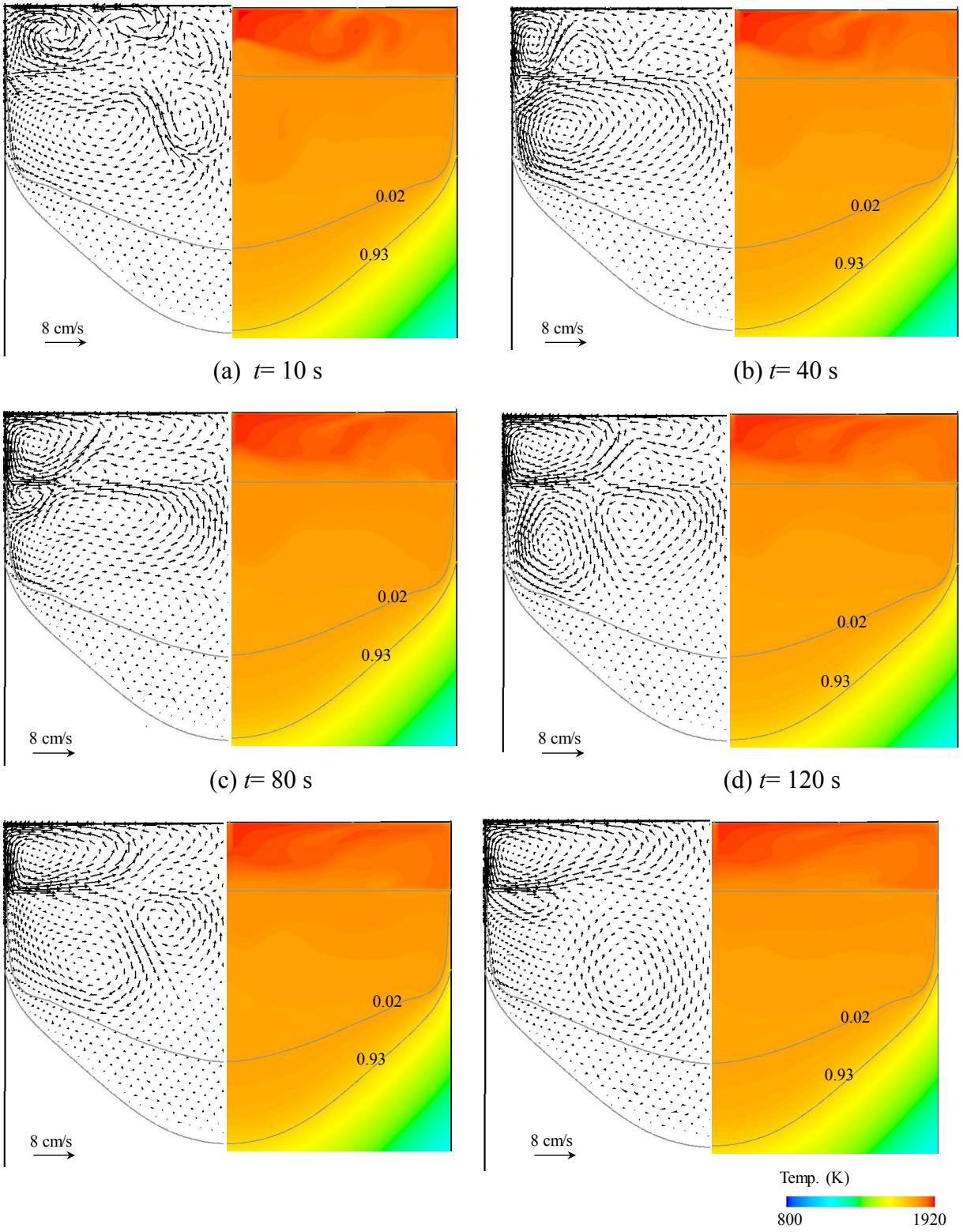

Figure 2. Snapshots of dynamic change of thermal and velocity fields at different times during power off: (a) t= 10 s, (b) t= 40 s, (c) t= 80 s, (d) t= 120 s, (e) t= 150 s, (f) t= 175 s, Left: vectors of velocity, Right: contour of temperature overlaid with isolines of solid fraction.

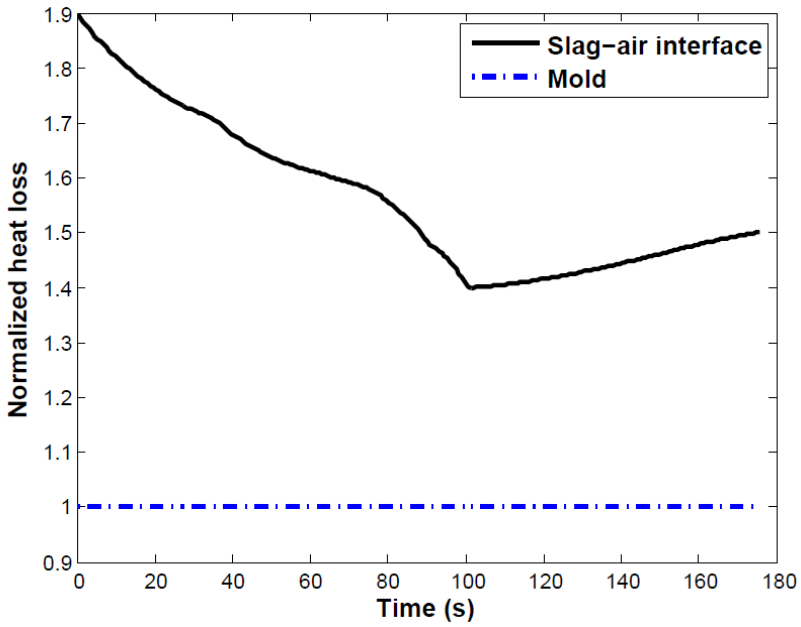

Figure 3. Normalized heat loss through slag-air interface and mold wall is plotted versus time during the first step of electrode change (power off).

Summary

Producing a large ingot by ESR process requires electrode change technology in which a number of smaller electrodes are remelted one after another. The electrode change procedure is divided into three steps. Firstly, the electric power is turned off (power off), and the end of remelted electrode is replaced by a new preheated electrode. Secondly, the electric power is turned on again, and the new electrode is heated to its melting temperature. Finally, the new electrode is continuously remelted until reaching target melt rate. Here, the influence of power interruption on a large scale ESR process during the first step of electrode change (power off) is studied using CFD simulation tool. A 2D axisymmetric computational domain is considered where the slag-melt pool interface is allowed to move. The interactions between turbulent flow, electromagnetic, and temperature fields are considered. The current is allowed to flow through the short collar mold used in the process. Additionally, the thermal effect of shrinkage of ingot is taken into account in the model. The behavior of system during electrode change including details of flow, and temperature

distributions as well as heat loss through boundaries are discussed. Generally, the pool profile is used as an indication of ingot internal quality. Therefore, preserving the original pool profile before and after power interruption is a symptom of maintaining ingot quality. According to simulation results, changes in pool profile of ingot are insignificant during the short period of electrode change (power off). The current study included only the first step of electrode change procedure. Further investigations are required to explore the behavior of process during second and third step of electrode change procedure.

Acknowledgement

The authors acknowledge the financial support by INTECO GmbH and the Austrian Federal Ministry of Economy, Family and Youth and the National Foundation for Research, Technology and Development within the framework of the Christian Doppler Laboratory for Advanced Process Simulation of Solidification and Melting.

References

[1] Holzgruber W, Kubisch C, and Jaeger H H 1971 *Neue Hutte* **16** 606

[2] Matushkina L I, Klyuver M, Dedushev L A, Kosyrev L L, Volkov S E, and Sharapov A, 1970 *Sb. Tr. Tsent. Nauch. Issted. Inst Chern. Met.* **75** 167

[3] Jackson R O, Mitchell A, and Luchok J 1972 *J. Vac. Sci. Tech.* **9** 1301

[4] Karimi-Sibaki E, Kharicha A, Korp J, Wu M, Ludwig A 2014 *Mater. Sci. Forum* **790** 396

[5] Kharicha A, Wu M, and Ludwig A 2014 *ISIJ Int.* **54** 1621

[6] Kharicha A, Karimi-Sibaki E, Wu M, and Ludwig A 2013 *Proc. Of LMPC* (New York: Wiley–Interscience) p 95

[7] Karimi-Sibaki E, Kharicha A, Wu M, Ludwig A, Holzgruber H, Ofner B, Ramprecht M 2014 *Proc. of ICRF* (Milan) on data storage device

[8] Kawakami M, Nagata K, Yamamura M, Sakata N, Miyashita Y, and Goto K S 1977 *Testsu-to-Hagane* **63** 220

[9] Holzgruber H, Holzgruber W, Scheriau A, Knabl M, Kubin M, Korp J, Pierer R 2011 *Proc. of LMPC* (Nancy) p 57

[10] Voller V R, and Prakash C 1978 *Int. J. Heat Mass Trans.* **30** 1709

[11] Karimi-Sibaki E, Kharicha A, Wu M, Ludwig A, Holzgruber H, Ofner B, Ramprecht M 2013 *Proc. of LMPC* (New York: Wiley–Interscience) p 13

[12] Menter F R and Egorov Y 2005 *AIAA paper 2005-1095, Reno/NV*

[13] Kharicha A, Schutzenhofer W, Ludwig A, Tanzer R, Wu M 2007 *Proc. of STEEL SIM* (Graz) p 105

[14] Kharicha A, Ludwig A, Wu M 2005 *Mater. Sci. Eng. A* **413-414** 129

[15] Kharicha A, Ludwig A, Wu M 2011 *Proc. of LMPC* (Nancy) p 41

[16] Kharich A, Ludwig A, and Wu M 2011 *EPD congress* (San Diego) p 771

[17] Kharicha A, Wu M, Ludwig A, Ramprecht M, Holzgruber H 2012 *CFD modelling and simulation in materials* (New York: Wiley–Interscience) p 139

Publication IX

A numerical study on electrochemical transport of ions in calcium fluoride slag

E. Karimi-Sibaki, A. Kharicha, M. Wu, A. Ludwig

In: Liquid metal processing and casting conference (LMPC), 2015, Leoben, Ed. by: A. Kharicha, R. Mark Ward, H. Holzgruber, M. Wu, IOP Conf. Series: Materials Science and Engineering, In Press

A numerical study on electrochemical transport of ions in calcium fluoride slag

E Karimi-Sibaki [a], A Kharicha[a,b], M Wu[a,b], and A Ludwig[b]
[a]Christian-Doppler Lab for Adv. Process Simulation of Solidification & Melting,
[b]Chair of Simulation and Modeling of Metallurgical Processes,
University of Leoben, Franz-Josef-Str. 18, A-8700 Leoben, Austria

E-mail: abdellah.kharicha@unileoben.ac.at

Abstract

Electrically resistive CaF_2-based slags are widely used in electroslag remelting (ESR) process to generate Joule heat for the melting of electrode. The electric current is conducted by ions (electrolyte) such as Ca^{+2} or F^-, thus it is necessary to establish electrochemical models to study electrical behavior of slag. This paper presents a numerical model on electrochemical transport of ions in an arbitrary symmetrical (ZZ) and non-symmetrical (CaF_2) stagnant electrolytes blocked by two parallel, planar electrodes. The dimensionless Poisson-Nernst-Planck (PNP) equations are solved to model electro-migration and diffusion of ions. The ions are considered to be inert that no Faradic reactions occur. Spatial variations of concentrations of ions, charge density and electric potential across the electrolyte are analyzed. It is shown that the applied potential has significant influence on the system response. At high applied voltage, the anodic potential drop near the electrode is significantly larger than cathodic potential drop in fully dissociated CaF_2 electrolyte.

Introduction

In many metallurgical processes such as electroslag remelting (ESR), the slag is core compound served to clean the metal by removing sulfur and non-metallic inclusions. In general, CaF_2-based slags are used since they have high degree of chemical reactivity and low electrical conductivity. The heat required to supply into the process is obtained by passing electric current through the resistive slag layer. The mode of current conduction in the slag is either ionic or a mixed ionic/electronic process [1]. Mitchell et al used a galvanostatic pulsing technique to measure magnitudes of overpotentials resulting from concentration polarization at the interface between iron and CaF_2-based slags in an electrolytic cell [2]. They found that potentials observed on the ESR electrode agreed with the results from the electrolytic cell. Furthermore, addition of a relatively small amount of Al_2O_3 to CaF_2 substantially decreases electric conductivity of liquid slag [3]. As a consequence of formation of complex ions such as $AlOF^-_2$, the mobility of F^- reduces [3]. Kojima studied the effect of mode of current (DC or AC) on electrochemical behavior of oxygen in a small scale ESR unit [4]. The distribution of oxygen in ingot was influenced by mode of current and electrode polarity. Kharicha et al [5] addressed possible effects of electrochemical reactions on formation of droplets at an ESR electrode. Metallic droplets which are surrounded by resistive slag can conduct an electric current when the potential drop at their extremities exceeds the sum of anodic and cathodic overpotential. As a consequence of ionic conduction of slag, dependences of melt rate of electrode and ingot composition on the electrode polarity were observed in DC operation of the ESR process [4]. Kawakami et al reported that electrode with positive polarity has higher melt rate compared to electrode with negative polarity [6]. The roles of electrochemical reactions occur in the slag-metal interface are well known. Loss of alloy elements such as Ti and Al

by oxidation is reported as a significant issue during DC operation of ESR process [7-8]. Furthermore, the efficiency of sulphur removal in ESR process was reported to be dependent on the condition of applied electric current (AC or DC) [9]. In fact, the aforementioned phenomena are as a result of the ionic character of slag. As such, it is essential to develop an electrochemical model to investigate the electrical behavior of slag. The model must take into account ions response to the applied electric field.

In the current study, a typical electrochemical cell is considered including two parallel, planar electrodes and a completely dissociated electrolyte. The Finite Volume Method (FVM) is used to model the ions transfer under the applied electric potential. No Faradaic reaction is modeled. Mass conservations of inert ions are automatically satisfied that is the advantage of using FVM method. First, an arbitrary binary symmetric electrolyte (Z^+Z^-) is investigated in which diffusion coefficients and concentrations of Z^+ and Z^- ions are equal. Then, CaF_2 is considered as a fully dissociated electrolyte consisted of Ca^{2+} and F^- ions where the diffusion coefficients and concentrations are different. The effect of applied potential and electrolyte properties such as concentrations of ions on the system response is discussed. The goal is to achieve some fundamental understanding of electrochemical behavior of CaF_2 slag under the influence of applied electric field.

Transport of ions

For an electrolyte subjected to an electric field, the Poisson-Nernst-Planck (PNP) equations describe the flux of ions through the electrolyte.

$$-\nabla \cdot (\varepsilon_s \nabla \phi) = F \sum z_i c_i = \rho \tag{1}$$

$$\frac{\partial c_i}{\partial t} = -\nabla \cdot \vec{N}_i \tag{2}$$

$$\vec{N}_i = \vec{u} c_i - D_i \nabla c_i - \frac{F z_i D_i \nabla \phi}{RT} c_i \tag{3}$$

The net flux of ions (N_i) including convection, diffusion, and electro-migration must be conserved as described in Eq. (2) where (c_i) is the concentration of *i*-th ion. According to Eq. (3), the convection and diffusion fluxes are dependent on velocity (u) and diffusion respectively where (D_i) is diffusion coefficient of *i*-th ion. Furthermore, the electro-migration flux of ions is included in Eq. (3) where (z_i) is the charge number of *i*-th ion, (F) is Faraday constant, (R) is the universal gas constant, (T) is temperature, and (ϕ) is electric potential. The Poisson equation, Eq. (1), relates the electric potential to the charge density (ρ) of system where (ε_s) is the electric permittivity constant of the electrolyte.

The steady state solution of the PNP equations for a symmetrical binary electrolyte was given in terms of Jacobi elliptic functions by Golovnev [10]. It was shown that the net charge density exists in a very thin boundary layer (diffuse charge layer) near the electrode (~ 1-100 nm). The length of diffuse charge layer is called Debye screening length (λ_D) in electrochemical systems.

$$\lambda_D = \sqrt{\frac{\varepsilon_s RT}{2z^2 F^2 C_0}} \tag{4}$$

where (C_0) is the bulk concentration of electrolyte.

The specific interfacial region formed near the electrode where the charge is separated is called electric double layer. As illustrated in Fig. 1, the double layer is composed of a diffusion layer, diffuse charge layer, and the compact stern layer (~ 0.5 nm) where ions are attracted to the surface. The diffuse charge layer is not electrically neutral as it has a net charge. However, the diffusion layer is electrically neutral where a non-uniform concentration of electrolyte may exist [11]. The definition of thickness of diffusion layer is arbitrary because the concentration reaches asymptotically to the bulk concentration [12].

For instance in cyclic voltammetry, the thickness is considered as: $(D_i t)^{0.5}$ where $(1/t)$ is the scan rate. As such, the thickness can be large (order of micrometer) at slow scan rate or small (order of nanometer) at fast scan rate [12].

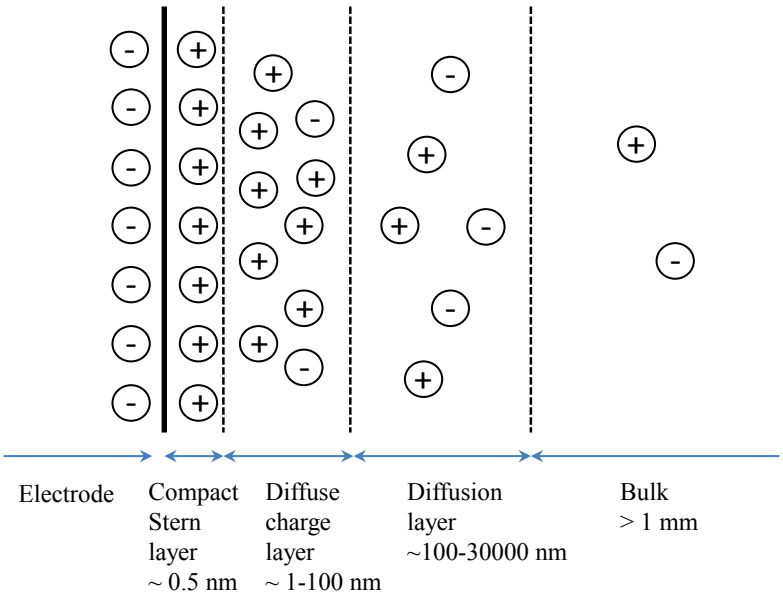

Fig.1. Structure of electric double layer.

Modeling

Configuration of the computational domain including liquid electrolyte blocked by electrodes (anode and cathode) is illustrated in Fig 2. A variable sized mesh is used applying a very fine mesh near the electrodes to resolve the boundary layer where the gradient is large. The mesh element size is gradually increased away from boundaries. The domain size is 1 mm and the total number of mesh elements is 1000. The simulation is performed with the commercial CFD software FLUENT-ANSYS v.14.5. The required transport equations are specified using User-Defined Scalars (UDS).

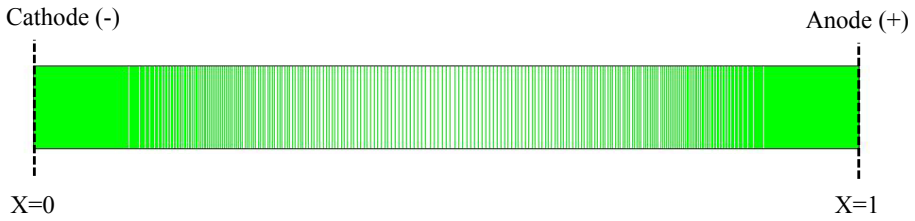

Fig.2. Configuration of computational domain and the mesh.

Applying numerical methods to model the problem requires extremely fine mesh to resolve the boundary layer adjacent to the electrode. As stated by Bazant [13], the investigation of electrochemical systems is significantly simplified using dimensionless formulations of PNP equations. This is the main step to study the asymptotic behavior of an electrochemical system in order to get physical insight into the problem.

Here, a one dimensional model is considered in which the parameter variation is only in one direction across the electrolyte. Furthermore, the electrolyte is assumed to be stagnant (*u=0*). Resultantly, the dimensionless form of PNP equations for the binary electrolyte is expressed as:

$$-\nabla\cdot(\xi^2\,\nabla\phi^*) = z_+C_+ + z_-C_- \tag{5}$$

$$\frac{\partial C_+}{\partial t} = \nabla\cdot(D_+\nabla C_+ + z_+D_+\nabla\phi^*C_+) \tag{6}$$

$$\frac{\partial C_-}{\partial t} = \nabla\cdot(D_-\nabla C_- + z_-D_-\nabla\phi^*C_-) \tag{7}$$

The basic variables in PNP equations are scaled as follow:

$$\phi^* = \frac{F\phi}{RT}, C_\pm = \frac{c_\pm}{C_{ref}}, \xi = \frac{\lambda_D}{L_{ref}}$$

Where $C_{\pm}$ denotes the dimensionless concentration of cation (+) or anion (-), and C_{ref} is the reference concentration which is typically in the same order as bulk concentration of ions. The electric potential is scaled using thermal voltage (RT/F) since diffusion and chemical reactions are thermally activated processes. Furthermore, ξ is the ratio of Debye screening length (λ_D) to the reference length (L_{ref}) which is typically considered as the distance between electrodes or the size of electrode.

Ions are considered to be inert and subsequently no faradaic reactions occur in our system. Thus the boundary conditions for Eq. (6) and Eq. (7) are zero total flux of ion (including electro-migration and diffusion fluxes). Additionally, Eq. (5) is used to determine the electric potential in the system. For the latter, a fixed value ($\pm FV/2RT$) is considered at the anode (+) and cathode (-) where (V) is the operating electric potential of the electrolytic cell. As described by Bazant [13], it is impossible to satisfy all the boundary conditions assuming a negligible screening length compared to the system size ($\xi \sim 0$). Physically, this assumption is corresponding to electro neutrality ($\rho = 0$) which is always violated at electrochemical interfaces. A numerical solution can only be achieved using a rather larger value of ξ to emphasize the importance of diffuse charge near the electrodes where the electro neutrality condition is not valid. For instance, the value of ξ can be chosen as large as 0.05 for a micro electrochemical system [13]. In this way, the asymptotic behavior of an electrochemical system can be captured.

Simulations are executed unsteadily, but only final steady state results are analyzed. Initial concentrations of ions are calculated assuming a fully dissociated electrolyte. The concentration of CaF_2 is the ratio of density (~ 2600 kg.m^{-3}) to molecular weight (~ 78.07 g.mol^{-1}). The fully dissociated CaF_2 electrolyte ($CaF_2 \leftrightarrow Ca^{2+} + 2F^-$) is consisted of Ca^{2+} and F^- ions in which the concentration of F^- is twice larger than the concentration of Ca^{2+}. The electric permittivity of electrolyte is assumed to be the same as permittivity of free

space since that is unknown for CaF_2 at elevated temperature. Table 1 lists all physical properties required for our calculations.

Table 1. Properties of the system.

T: Bulk temperature (K)	1773
R: Universal gas constant ($J \cdot mol^{-1} \cdot K^{-1}$)	8.314546
F: Faraday constant ($Amp \cdot s \cdot mol^{-1}$)	96485
ε_s: Electric permittivity ($F \cdot m^{-1}$)	8.85418×10^{-12}
V: Low applied voltage (V)	0.005
V: High applied voltage (V)	2
C_{ref}: Reference concentration ($mol \cdot m^{-3}$)	1×10^{5}
L_{ref}: Reference length (m)	1×10^{-6}
λ_D: Debye length (m)	1×10^{-9}
ζ	0.01
ZZ electrolyte	
Z^+: Concentration ($mol \cdot m^{-3}$)	0.333×10^{5}
Z^+: Diffusion coefficient ($m^2 \cdot s^{-1}$)	4×10^{-9}
Z^+: Charge number	+1
Z^-: Concentration ($mol \cdot m^{-3}$)	0.333×10^{5}
Z^-: Diffusion coefficient ($m^2 \cdot s^{-1}$)	4×10^{-9}
Z^-: Charge number	-1
CaF_2 electrolyte	
Ca^{2+}: Concentration ($mol \cdot m^{-3}$)	0.333×10^{5}
Ca^{2+}: Diffusion coefficient ($m^2 \cdot s^{-1}$)	5.66×10^{-9} [14]
Ca^{2+}: Charge number	+2
F^-: Concentration ($mol \cdot m^{-3}$)	0.666×10^{5}
F^-: Diffusion coefficient ($m^2 \cdot s^{-1}$)	4.12×10^{-9} [14]
F^-: Charge number	-1

Results and discussions

A number of simulations were performed by considering two different operating applied potentials. Additionally, two different electrolytes are investigated. Firstly, an arbitrary binary symmetric electrolyte (*ZZ*) is studied in which diffusion coefficients, concentrations, and charge numbers of ions are identical. Secondly, the fully dissociated CaF_2 which is a non-symmetrical binary electrolyte is investigated. Furthermore, responses of electrolytes to the applied potential are compared. Fig. 3 shows the normalized concentration profile of cations (Z^+ or Ca^{2+}) and anions (Z^- or F^-) across the electrolyte at low applied voltage. Note

that, initial concentrations of anions are not the same in Fig. 3(b). As expected, cations move toward the cathode ($X=0$) and anions accumulate near the anode ($X=1$). Once the voltage is applied, ions move to screen the electric field originated from electrodes. Therefore counter-ions (relative to electrode) entering to double layers by electro-migration from the bulk. Concurrently, co-ions leave the double layer entering to the bulk. Due to excess of counter-ions in the double layer, diffusion competes against electro-migration until a uniform equilibrium state is reached. In this way, diffusion layers spread across the electrolytic cell from electrodes. As illustrated in Fig. 3 (c-d), the thickness of diffusion layer can significantly decrease by applying a larger voltage in the system. Here, the electro-migration is dominant that results in double layers filled only with counter-ions. In other words, bulk concentrations of ions significantly decrease so that co-ions completely leave diffusion layers. As illustrated in Fig. 4 (a-b), charge density is divided in three regions: neutral region in the bulk and two electrically charged boundary layers near electrodes. The net bulk charge density remains very small ($\rho \sim 0$) that is known as electro-neutrality condition. Most often, electro-neutrality assumption is used for large scale electrochemical systems. This is an excellent assumption that can significantly simplify investigation of large scale systems. However, it is essential to incorporate the effect of double layers into boundary conditions [13]. As shown in Fig. 4 (b), the thickness of diffusion layer is significantly decreased by applying larger voltage which is consistent with Gouy-Chapman theory [13, 15]. According to the theory, counter-ions have higher tendency to be absorbed than co-ions to be pushed out of the double layer once the electric field is applied. As such, the total charge density of ions increases near the electrode and depletes in the bulk [13]. Furthermore, the charge density remains symmetrical for both *ZZ* and CaF_2 at low applied voltage as indicated in Fig. 4(a). However, the symmetry breaks strongly applying large voltage for CaF_2 electrolyte due to difference in initial concentrations of ions (F^- and Ca^{2+}) as shown in Fig. 4(b).

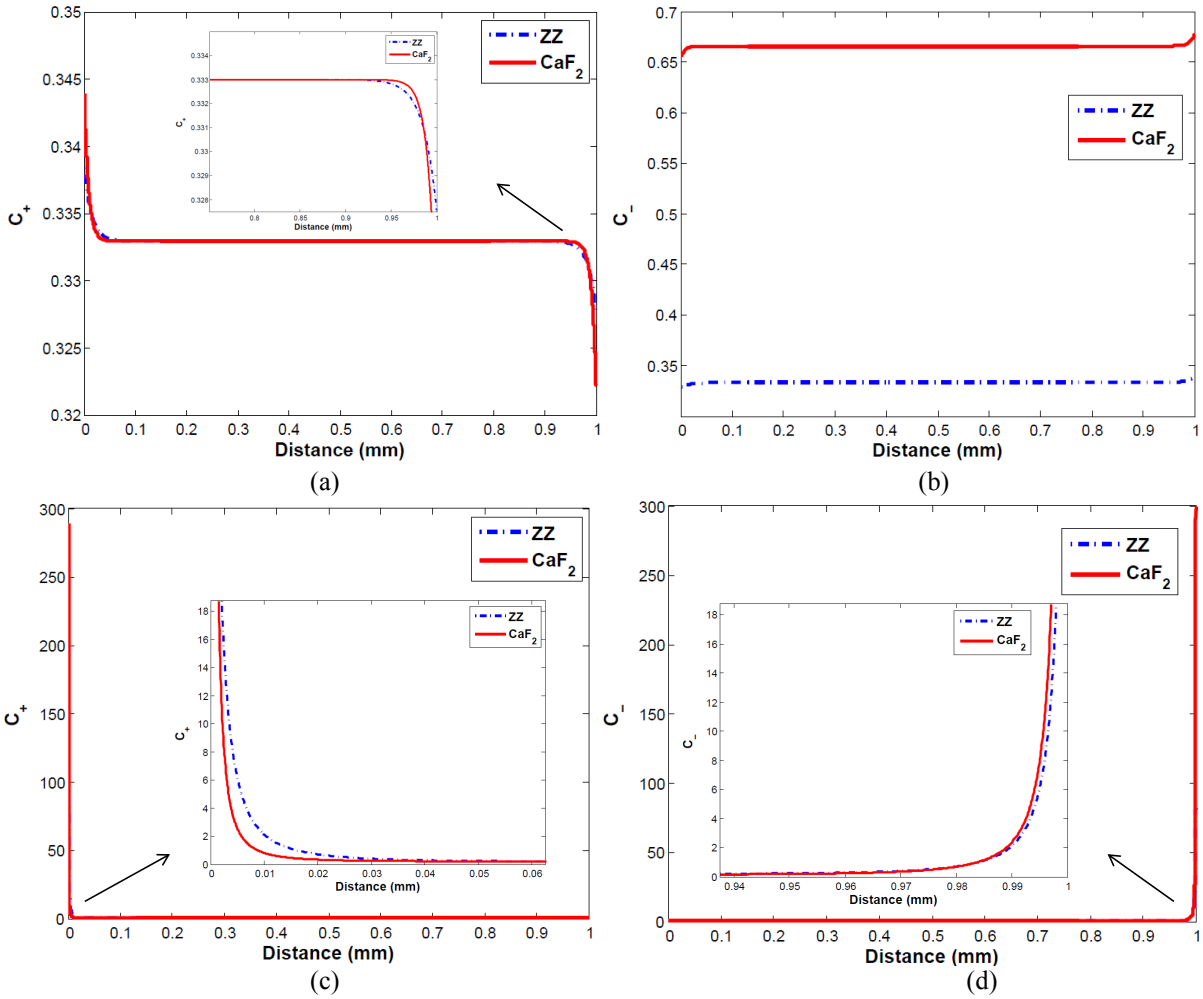

Fig.3. Normalized concentrations of ions are plotted across the electrolyte blocked by cathode ($x=0$) and anode ($x=1$), (a) Cations (Z^+ and Ca^{2+}) at low applied potential (0.005 V), (b) Anions (Z^- and F^-) at low applied potential (0.005 V), (c) Cations (Z^+ and Ca^{2+}) at high applied potential (2 V), (d) Anions (Z^- and F^-) at high applied potential (2 V).

The spatial variation of electric potential is controlled by charge density distribution through Poisson's equation (Eq. 1). Nevertheless, changes in bulk concentration of ions influence the electric potential through the whole electrolyte. In other words, variation in electric potential is not limited near electrodes due to evolution of diffusion layers. The thicknesses of diffusion layers are dependent on the applied potential since electro-migration and diffusion are competing. As shown in Fig. 4(c), the diffusion layer is a narrow region near diffuse charge layer at low applied voltage. Consequently, the potential drop is only near electrodes and the bulk variation of electric potential is negligible. Furthermore, the symmetry of electric potential through the electrolyte is kept independent

of electrolyte whether *ZZ* or CaF_2. In contrast, strong breaking of symmetry in electric potential profile is observed for CaF_2 at large applied potential as illustrated in Fig. 4(d). Additionally, the spatial variation of electric potential is extended to the bulk. The interfacial potential difference near the anode is significantly larger than near the cathode for the CaF_2 electrolyte.

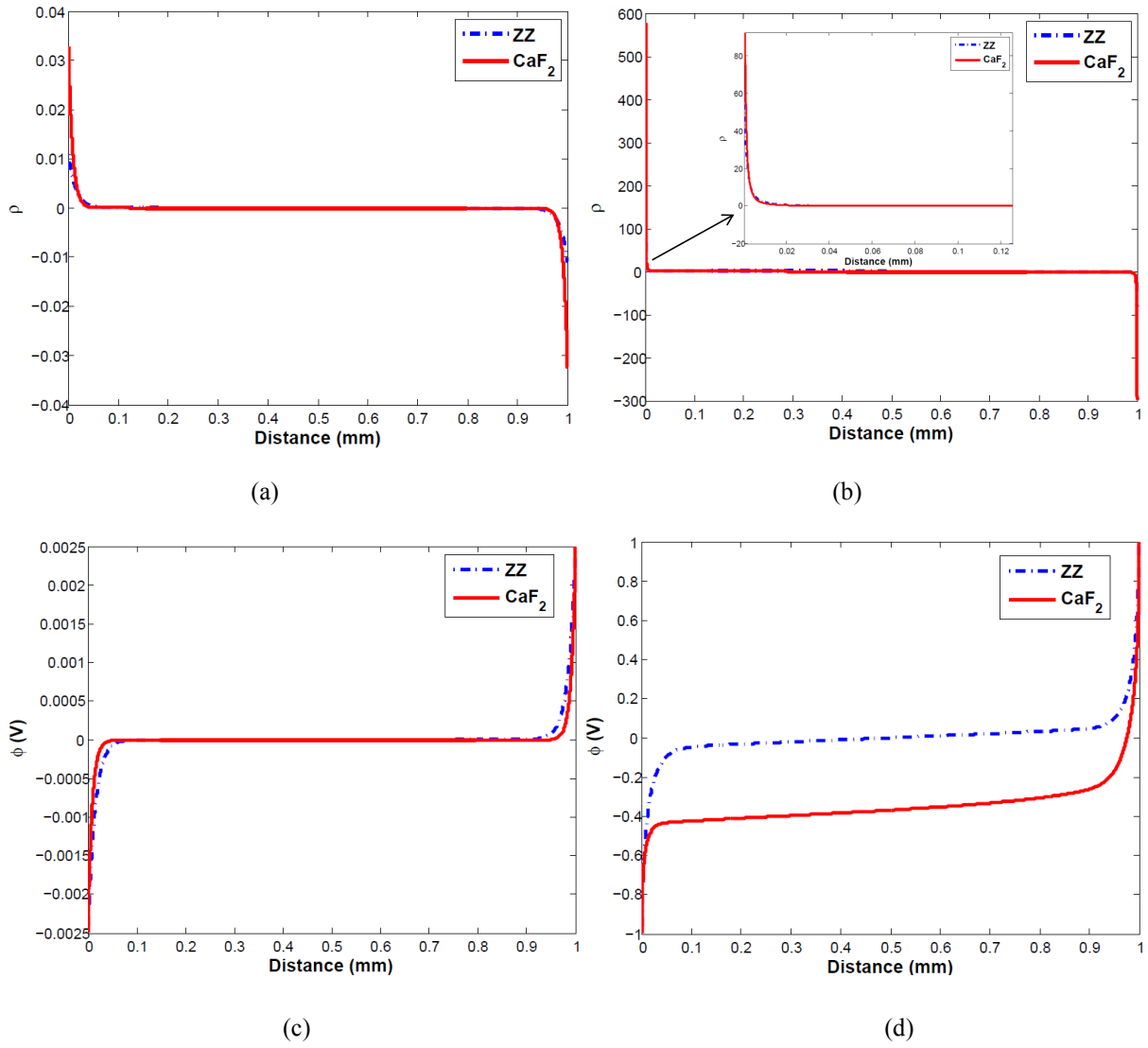

Fig.4. The following parameters are plotted across the electrolytes (*ZZ* or CaF_2) blocked by cathode (*x=0*) and anode (*x=1*), (a) Normalized charge density at low applied voltage (0.005 V), (b) Normalized charge density at high applied voltage (2 V), (c) Electric potential at low applied voltage (0.005 V), (d) Electric potential at high applied voltage (2 V).

It must be noted that a conventional slag is typically composed of CaF_2, Al_2O_3, CaO, SiO_2, and MgO. Therefore, a number of other ions such as O^{2-}, Al^{3+}, Mg^{2+}, and Si^{4+} can play role in electrochemical behavior of the slag. Furthermore, they can participate in Faradaic reactions at electrode surface. Therefore, the model must be further developed to take into account effects of other ions as well as Faradaic reactions on electrical behavior of a conventional slag.

Summary

A numerical study is performed to investigate electrochemical transport of ions in CaF_2 slag as a non-symmetrical binary electrolyte. The behavior of system is compared to an arbitrary binary symmetrical electrolyte (*ZZ*) in which concentration, charge number and diffusion coefficients of ions are identical. Furthermore, the influence of applied potential is studied. The Poisson-Nernst-Planck (PNP) equations considering convection, diffusion, and electro-migration of ions through the electrolyte are solved. The effect of Faradic reactions is not included in the current study. Spatial variations of concentrations of ions, charge density, and electric potential across the electrolyte are compared for *ZZ* and CaF_2 electrolytes. At low applied voltage, the interfacial potential difference near electrodes remains just about the same. Additionally, the diffusion layer is thin resulting in uniform concentration of ions in the bulk. In contrast, the diffusion layer is extended to the bulk of electrolytes at high applied voltage. The symmetrical electrolyte (*ZZ*) has identical potential drop near electrodes independent of magnitude of operating potential. However, significant difference of interfacial potential drop is observed for non-symmetrical electrolyte (CaF_2). For the latter, the anodic interfacial potential drop is much larger than the cathodic one.

Acknowledgement

The authors acknowledge the financial support by the Austrian Federal Ministry of Economy, Family and Youth and the National Foundation for Research, Technology and Development within the framework of the Christian Doppler Laboratory for Advanced Process Simulation of Solidification and Melting.

References

[1] Peover M E 1972 *J. Inst. Metals* **100** 97

[2] Mitchell A and Beynon G 1971 *Metall. Trans.* **2** 3333

[3] Mitchell A and Cameron J 1971 *Metall. Trans.* **2** 3361

[4] Kojima Y, Kato M, Toyoda T, and Inouye M 1975 *Trans. ISIJ* **15** 397

[5] Kharicha A, Wu M, Ludwig A, Ramprecht A, and Holzgruber H 2012 *CFD modeling and simulation in materials processing* (New York: Wiley–Interscience) p 139

[6] Kawakami M, Nagata K, Yamamura M, Sakata N, Miyashita Y, and Goto K S 1977 *Testsu-to-Hagane*, **63** 220

[7] Etienne M 1970 *Ph.D. Thesis* University of British Columbia

[8] Bhat G K and Mitchell A 1969 *Proc. Sec. Symp. On ESR technology*

[9] Whittaker D A, 1968 *Ph.D. Thesis* McMaster University

[10] Golovnev A, Trimper S 2010 *Phys. Lett. A* **374** 2886

[11] Newmann J 2004 *Electrochemical systems*, (New York: Wiley–Interscience)

[12] McNaught A D, and Wilkinson A 1997 *IUPAC, compendium of chemical terminology* (Oxford- Blackwell scientific publication)

[13] Bazant M Z, Thornton K, and Ajdari A 2004 *Phys. Rev. E* **70** 1

[14] Chiho W, and Shunhua X 1993 *ISIJ Int.* **33** 239

[15] Grahame D C 1947 *Chem. Rev.*, **41** 441